DESIGN AND CONSTRUCTION OF FLUORESCENT BIOACTIVE PROBES FOR BIOIMAGING OF TARGETED CELLULAR ORGANELLES

Ph.D. Thesis

By

PRATIBHA KUMARI

DISCIPLINE OF BIOSCIENCE & BIOMEDICAL ENGINEERING

INDIAN INSTITUTE OF TECHNOLOGY INDORE

JULY 2019

DESIGN AND CONSTRUCTION OF FLUORESCENT BIOACTIVE PROBES FOR BIOIMAGING OF TARGETED CELLULAR ORGANELLES

A THESIS

Submitted in partial fulfillment of the requirements for the award of the degree

of

DOCTOR OF PHILOSOPHY

by

PRATIBHA KUMARI

DISCIPLINE OF BIOSCIENCE & BIOMEDICAL ENGINEERING

INDIAN INSTITUTE OF TECHNOLOGY INDORE

JULY 2019

INDIAN INSTITUTE OF TECHNOLOGY INDORE

CANDIDATE'S DECLARATION

I hereby certify that the work which is being presented in the thesis entitled **DESIGN AND CONSTRUCTION OF FLUORESCENT BIOACTIVE PROBES FOR BIOIMAGING OF TARGETED CELLULAR ORGANELLES** in the partial fulfillment of the requirements for the award of the degree of **DOCTOR OF PHILOSOPHY** and submitted in the **DISCIPLINE OF BIOSCIENCE & BIOMEDICAL ENGINEERING, INDIAN INSTITUTE OF TECHNOLOGY INDORE**, is an authentic record of my own work carried out during the time period from DECEMBER 2014 to JULY 2019 under the supervision of Dr. Shaikh M. Mobin, Associate Professor, Indian Institute of Technology Indore.

The matter presented in this thesis has not been submitted by me for the award of any other degree of this or any other institute.

Signature of student with date
PRATIBHA KUMARI

This is to certify that the above statement made by the candidate is correct to the best of my/our knowledge.

Signature of Thesis Supervisor with date
Dr. Shaikh M. Mobin

PRATIBHA KUMARI has successfully given his Ph.D. Oral Examination held on----------

Signature of Chairperson (OEB) Date:

Signature of External Examiner Date:

Signature(s) of Thesis Supervisor(s) Date:

Signature of PSPC Member #1 Date:

Signature of PSPC Member #2 Date:

Signature of Convener, DPGC Date:

Signature of Head of Discipline
Date:

ACKNOWLEDGEMENTS

I am thankful to the creator for his blessings which have allowed me to reach this level of knowledge and exposure in this life.

I would like to acknowledge and extend my deepest gratitude to all who support me and putting their efforts to making things easy and achievable, for completing my thesis.

At the outmost, I would like express my sincere gratitude and warm regards to my supervisor, Dr. Shaikh M. Mobin for constantly guiding me and providing all the necessary facilities along with his expertise, encouragement, and tireless support during my thesis work. His constant motivation allowed me to learn chemistry as well. My sincere appreciation for his enormous effort toward getting the work published in international reputed journals. I also heartily thank him not only for continuous support, constructive suggestions, but also for providing freedom to pursue experiments as per my desire. Moreover, I will always be thankful for constant inspiration to attend conferences/seminars and guidance during research works as well as writing of this thesis.

I would like to convey my gratitude towards Professor Pradeep Mathur (Director of IIT Indore) for excellent research facilities infrastructure and constant stimulating research environment at IIT Indore

Similar profound gratitude goes to our PSPC member Prof. Rajneesh Misra and Prof. Sarika Jalan for carefully monitoring my research progress and helping me with their valuable suggestions and comments for improving my research work.

I am thankful to all the faculties and staff members of discipline of biosciences and biomedical engineering and chemistry, IIT Indore for their support during my research work. I am highly appreciative to staff members of SIC, IIT Indore, especially Mr. Ravinder kumar, Mr. Kinny Pandey, Mr. Ghanshyam

Bhavasar, Mr. Nitin Upadhyay for the characterization facility. I would like to thanks discipline of physics, IIT Indore for RAMAN spectroscopy.

I would like to express my sincere gratitude to IIT Indore and MHRD for providing me fellowship throughout the tenure of my research work.

Special thanks to my group members Dr. Sanjay K. Verma, Dr. Anoop Kumar Saini, Dr. Akbar Mohammad, Dr. Vinay Sharma, Dr. Anoop Kumar Gupta, Dr. Veenu Mishra, Dr. Ajeet Singh, Dr. Archana Chaudhary, Dr. Mohit Saraf, Ms. Shagufi Naz Ansari, Ms. Navpreet Kaur, Ms. Richa Rajak, Mr. Kaushik Natarajan, Mr. Pranav Tiwari, Ms. Topi Ghosh, Mr. Khursheed, Ms. Neha Chaudhary, Mr. Ravinder Kumar, Mr. Pawan Kumar, Ms. Puja Singhvi, and Mr. Praveen Kumar for fruitful suggestion during research work and manuscript writing.

Last but not the least; I would like to thank my family including parents, siblings and my friend Mr. Kumar Vaibhav for unconditional support and constant motivation. I hardly find any words to express my gratitude to them. My thanks to them for their love, support, constant inspiration and sacrifices they have made.

(Pratibha Kumari)

DEDICATED TO MY FAMILY

TABLE OF CONTENTS

ABSTRACT

The work demonstrated in thesis entitled "**DESIGN AND CONSTRUCTION OF FLUORESCENT BIOACTIVE PROBES FOR BIOIMAGING OF TARGETED CELLULAR ORGANELLES**" was initiated in December 2014 in the Discipline of Biosciences and Biomedical Engineering (BSBE), Indian Institute of Technology Indore.

The fluorescence imaging technique has emerged as a powerful way to monitor the amount, localization and movement of biomolecules at the cellular level. The objectives of this thesis are to design and synthesis of various organelles targeting fluorescent probes. The focal points of thesis are as follows:-

1. Design and synthesis and characterization of fluorescent organelles targeting probes.
2. Synthesis of two photon probes for their advance application in bio-imaging and deeper tissue penetration capability.
3. Live cell/tumor spheroid bio-imaging using synthesized probe and compared with standard reference trackers for validating cellular organelles targeting ability of probes.
4. Solid state properties of single crystal explored in terms of unique non-bonding interaction and elastic bending, followed by organelles bio-imaging ability in solution state.
5. Synthesis of biologically active Aroyl-hydrazone based ligands and determines their effectiveness by molecular docking, density function calculation (DFT), DNA and proteins binding.

This thesis contains seven chapters and it begins with a general introduction (**Chapter 1**). Fluorescent probes synthesized for bio-imaging of the target organelles in subsequent chapters (**Chapter 2-5**), Followed by synthesis of

aroyl-hydrazones derivatives for their anti-influenza activities (**Chapter 6**). The thesis outlines the future perspective in the **Chapter 7**.

The introductory chapter (**Chapter 1**) of this thesis illustrates the brief background literature of basic criteria of organelle-targeting fluorescent probes (OTFp). General approaches of organelles targeting fluorescent probe delivery to the organelles. The structure and function of various organelles including lysosomes, endoplasmic reticulum, Golgi apparatus, mitochondria, nucleus etc. have been discussed in detail. The general deign of probes for particular organelles and challenges for organelles targeting probes have also discussed. Moreover, we have described the types and mechanism of reaction such as Schiff base, click reaction which used for probe synthesis. Then the fundamental concepts of molecular electronic transition, fluorescence, and single-photon as well as two-photon microscopy deliberated. The computation study includes molecular docking and density function calculation (DFT). Furthermore, introduction of bending crystal phenomenon has been discussed as well. In solid-state, crystalline materials have wide applications in mechanical actuators, light-emitting diodes (LEDs), phototransistors, photonics, solar cells, and flexible electronics *etc*.

Chapter 2, describes the morphological alteration of lysosomes is a powerful indicator of various pathological disorders. In this regard, a new water soluble fluorescent Schiff-base ligand (**L-lyso**) containing two hydroxyl groups was designed and synthesized. **L-lyso** characterized by NMR, ESI-MS, FTIR, and single crystal diffraction. **L-lyso** exhibits excellent two-photon properties with tracking of lysosomes in live cells as well as in 3D tumor spheroids. Thus, **L-lyso** has an edge over the commercially available expensive LysoTracker probes and also over other reported probes in terms of its long-term imaging, water solubility and facile synthesis.

In **Chapter 3,** a new two-photon, non-cytotoxic, fluorescent probe (**ERLp**) was designed and synthesized in a facile manner and characterized

by various spectroscopic techniques such as NMR, ESI-MS, FTIR, and single crystal diffraction. **ERLp** can selectively track the endoplasmic reticulum with a high Pearson co-localization coefficient (0.91) in live cells and tumor spheroids. Further, ER stress during cell apoptosis and vesicular transport from the ER to the lysosomal compartment were also explored by employing **ERLp**. Therefore, **ERLp** can be used as a potent tool for examining vesicle transport or ER stress associated diseases in real time.

In **Chapter 4**, A novel mesoionic carbene based highly fluorescent Pd(II) complex was synthesized and characterized (NMR, ESI-MS, single crystal diffraction). A recent study advocates that endoplasmic reticulum (ER) dysfunction may be linked to critical neurotrauma and advanced tauopathy. In this regard, targeting the ER warrants urgent attention towards the therapeutic treatment of neurotrauma-related neuro-degeneration. Herein, we describe the synthesis of a new N-heterocyclic mesoionic carbene based highly fluorescent square-planar Pd(II) complex **1**, with a high quantum yield (0.737). Further the probe **1** is a non-toxic probe for selectively labeling the endoplasmic reticulum in live cells.

In **Chapter 5**, we report the unique properties of a new Schiff base ligand (**H_2L**), synthesized and characterized by FTIR, ^{1}H and ^{13}C NMR and LCMS spectroscopy. Further, it has been authenticated by single crystal X-ray diffraction study. In a solid-state, **H_2L** can bend upon externally applied stress which rapidly reverts to its original shape upon relaxation revealing highly flexible and elastic bending properties. The powder XRD and Raman studies indicate high retention of crystallinity and chemical bonds even under stress (bend) conditions which imply that the bending in **H_2L** is purely due to the intermolecular hydrogen bonding C–H$\cdots\pi$ interactions. Moreover, in the solution state, **H_2L** is fluorescent, non-cytotoxic, two-photon excitation ability and selectively labels mitochondria of live cells and tumour spheroids.

In **Chapter 6**, we describe the synthesis and characterization of four new bioactive aroyl-hydrazone derivatives, **L_1–L_4** and their structural as well as biological activities have been explored. The biological activities of **L_1–L_4** have been examined through molecular docking with twelve different proteins which are involved in the propagation of viral/bacterial diseases or proliferation of cancer disease. **L_1** and **L_2** are having a high antiviral activity while **L_3** and **L_4** shows best anticancer activity in terms of their binding energy which was determined by molecular docking studies. **L_1** Shows best binding affinity with Influenza A virus polymerase PB2 subunit with binding energy -11.42 Kcal/Mol and inhibition constant 4.23nM whereas **L_2** strongly bind with the Hepatitis C virus NS5B polymerase with binding energy -10.47 Kcal/Mol and inhibition constant 21.06nM. Ligand **L_3** binds strongly with TGF-beta receptor 1 (Transforming growth factor β–R1) and **L_4** with cancer related EphA2 protein kinases with binding energy -10.61 Kcal/Mol, -10.02 Kcal/Mol and inhibition constant 16.67nM and 45.41nM respectively. In addition to docking with Bovine serum albumin (BSA) and duplex DNA, the experimental results demonstrate the effective binding of **L_1–L_4** with BSA protein and calf thymus DNA (ct-DNA) which is in agreement with the docking results. Furthermore, the geometry optimizations of **L_1–L_4** were performed via density functional theory (DFT). Moreover, all four ligands **(L_1–L_4)** were characterized by NMR, FTIR, ESI-MS, elemental analysis and their molecular structures were validated by single crystal X-ray diffraction studies.

The **Chapter 7** outlines the future perspective of this work.

LIST OF PUBLICATIONS

[1]. **Kumari, P**., Verma, S. K., Mobin, S. M. (2018), Water soluble two-photon fluorescent organic probes for long-term imaging of lysosomes in live cells and tumor spheroids, Chem. Commun., 54, 539-542 (DOI:10.1039/c7cc07812a).

[2]. **Kumari, P**., Verma, S. K., Mobin, S. M. (2019), A facile two-photon fluorescent probe: an endoplasmic reticulum tracker monitoring ER stress and vesicular transport to lysosomes, Chem. Commun., 55, 294-297 (DOI:10.1039/C8CC07429A).

[3]. Verma, S. K., **Kumari, P**., Ansari, S. N., Ansari, M. O., Deori, D., Mobin, S. M. (2018), A novel mesoionic carbene based highly fluorescent Pd(ii) complex as an endoplasmic reticulum tracker in live cells, Dalton Trans., 47, 15646-15650 (DOI:10.1039/c8dt02778a).

[4]. **Kumari, P**., Ansari, S. N., Kumar R., Saini, A. K., Mobin, S. M. (2019), Design and construction of aroyl-hydrazone derivatives: synthesis, crystal structure, molecular docking and their biological activities, Chem. Biodiversity, 16, e1900315 (DOI:10.1002/cbdv.201900315).

[5]. **Kumari, P**., Verma, S. K., Natarajan K., Ansari, S. N., Saini, A. K., Mobin, S. M.(2019), Design and Synthesis of a New Facile Ligand in a Dual Role: Mechanically Elastic Crystal and Selective Mitochondria Target, Cryst. Growth Des., 19, 5483−5490 (DOI: 10.1021/acs.cgd.9b00846).

[6]. Ansari, S. N., Saini, A. K., **Kumari, P.**, Mobin, S. M. (2019), An imidazole derivative-based chemodosimeter for Zn^{2+} and Cu^{2+} ions through "ON–OFF–ON" switching with intracellular Zn^{2+} detection, Inorg. Chem. Front., 6, 736-745 (DOI: 10.1039/C8QI01127C).

[7]. Saini, A. K., **Kumari, P.**, Sharma, V., Mathur, P., Mobin, S. M. (2016), Varying structural motifs in the salen based metal complexes of Co(ii), Ni(ii) and Cu(ii): synthesis, crystal structures, molecular

dynamics and biological activities, Dalton. Trans., 45, 19096-19108 (DOI:10.1039/C6DT03573F).

[8]. Saini, A. K., Saraf, M., **Kumari, P.**, Mobin, S. M. (2018), A highly selective and sensitive chemosensor for l-tryptophan by employing a Schiff based Cu(ii) complex, New J. Chem., 42, 3509-3518 (DOI:10.1039/C7NJ04595F).

[9]. Singh, A., **Kumari, P**., Raghuvanshi, A., Mobin, S. M., Mathur, P. (2018), Ferrocene-substituted bis(ethynyl)anthracene compounds as anticancer agents, Appl. Organomet. Chem., 32, e4071 (DOI:10.1002/aoc.4071).

[10]. Mobin, S. M., Tauqeer, M., Mohammad, A., Mishra, V., **Kumari, P**. (2016), Thiophene-containing thiolato dimers, oxygen inserted Cu(II) complex, crystal structures, molecular docking and theoretical studies, J. Coord. Chem., 69, 2015-2023 (DOI:10.1080/00958972.2016.1192611).

[11]. Gupta, G., **Kumari, P**., Ryu, J. Y., Lee, J., Mobin, S. M., Lee, C. Y. (2019), Mitochondrial Localization of Highly Fluorescent and Photostable BODIPY-Based Ruthenium(II), Rhodium(III), and Iridium(III) Metal Complexes, Inorg. Chem., 58, 8587−8595 (DOI: 10.1021/acs.inorgchem.9b00898).

[12]. Verma, S. K., Ansari, S. N., **Kumari, P**., Mobin, S. M. (2019), Click Reaction Driven Highly Fluorescent Dinuclear Organo-gold(I) Complex Exhibit Dual Role: A Rare Au···H Interactions and as Anti-proliferative Agent, Organometallics, (DOI: 10.1021/acs.organomet.9b00291) (Accepted).

[13]. Sharma, V., Kaur, N., **Kumari, P**., Mobin, S. M. (2019), Unique cervical cancer cells derived carbon dots as promising ER tracker in live cells and 3D tumor spheroids (*Communicated*).

Conferences/Workshop attended and poster presentation

1. "***1st In house symposium on Advances in Bioscience & Bioengineering***" organized by Discipline of Bioscience &Biomedical Engineering, Indian Institute of Technology Indore, 23rd Feb, 2019 (**Poster and Oral Presentation**).

2. *"**IIT Indore- RSC Symposium on Advances in Chemical Sciences**"* organized by Discipline of Chemistry, Indian Institute of Technology-Indore India, 30th Jan 2018 (**Poster Presentation**).

3. ***"Inter-Disciplinary Exploration in Chemistry (I-DEC 2018)"*** organized by IISER Bhopal, 06 -08 Dec, 2018 (**Poster Presentation**).

4. ***"5th Symposium on Advanced Biological Inorganic Chemistr"*** organized by Tata Institute of Fundamental Research (TIFR) and Indian Association for the Cultivation of Science (IACS) Kolkata India, 07th −11th Jan, 2017 (**Poster Presentation**).

5. *"**Frontiers in Inorganic and Organometallics conference**"* organized by Discipline of Chemistry, Indian Institute of Technology-Indore India and CrystEngComm, 14th–15th April 2016 (2nd **Poster Presentation prize**).

6. Workshop on ***"Chemical Biology: The Integration of Chemistry, Biology and Medicine"*** organized by Discipline of Bioscience &Biomedical Engineering, Indian Institute of Technology Indore in association with Purdue University, USA under Global Initiative on Academic Networks (GIAN) sponsored by Ministry of Human Resource and Development (MHRD), India, 12-23 Dec, 2016.

7. GIAN course on "Inorganic Chemistry of Imaging: Magnetic Resonance and Optical Imaging with Coordination Complexes" January 08-12, 2018, conducted by Prof. Janet R. Morrow, University at Buffalo, USA at IIT Indore.

8. "Catalysis by Metal Complexes" a Global Initiative on Academic Networks (GIAN) Course Organized by Discipline of Chemistry, Indian Institute of Technology Indore, an initiatives from MHRD, New Delhi, from November 21−26, 2016.

LIST OF ABBREVIATIONS

DAPI	4',6-diamidino-2-phenylindole
ESI-MS	Electrospray ionization mass spectrometry
HRMS	High Resolution Mass Spectrometry
PXRD	Powder X-ray diffraction
FTIR	Fourier-transform Infrared spectroscopy
SCXRD	Single crystal X-ray diffractometer
UV light	Ultraviolet light
NMR	Nuclear magnetic resonance spectroscopy
DFT	Density functional theory
HOMO	Highest occupied molecular orbitals
LUMO	Lowest unoccupied molecular orbitals
PET	Photo–induced electron transfer
THF	Tetrahydrofuran
$CHCl_3$	Chloroform
MeOH	Methanol
EtOH	Ethanol
KBr	Potassium bromide
ACN	Acetonitrile

DMSO	Dimethyl sulfoxide
$CDCl_3$	Deuterated chloroform
DMSO-d_6	Deuterated dimethyl sulfoxide
DMF	Dimethylformamide
RT	Room temperature
DNA	Deoxyribonucleic acid
RNA	Ribonucleic acid
EtBr	Ethidium bromide
EtBr–DNA	Ethidium bromide bound DNA
MTT	3-(4,5-dimethylthiazol-2-yl)-2,5-diphenyltetrazolium bromide
TPEN	N,N,N0,N0-tetrakis(2-pyridylmethyl) -ethylenediamine
HeLa	Cervical cancer cell line
DU145	Human prostate cancer cell line
MCF–7	Breast cancer cell line
A375	Skin melanoma cell line
A549	Human lung carcinoma
HEK293	Human embryonic kidney cell line
NIH 3T3	Mouse embryo fibroblast cell line

HL-7720	Human liver cell line
HCV	Hepatitis C virus
TGF-β	Transforming growth factor-beta
MEM	Minimum essential medium
DMEM	Dulbecco's Modified Eagle Medium
TLC	Thin-layer chromatography
PBS	Phosphate-buffered saline
WHO	World Health Organization
Trp	Tryptophan
BSA	Bovine serum albumin
CT–DNA	Calf Thymus–DNA
IC_{50}	Half maximal inhibitory concentration
K_q	Quenching constant
K_b	Binding constant
K_{sv}	Stern–Volmer quenching constant
SiO_2	Silicon dioxide
TP	Two-Photon
OPM	One-photon microscopy
TPM	Two-photon microscopy

ROI	Region of interest
MCTS	Multicellular tumor spheroid
LTR	LysoTracker Red
LTG	LysoTracker Green
MTR	MitoTracker Red
ER	Endoplasmic reticulum
R_r	Pearson's colocalisation coefficient
(°)	degree
Å	Angstrom
µm	Micrometer
nm	nanometer
µM	Micromolar
nM	Nanomolar
λ_{ex}	Excitation wavelength
λ_{em}	Emission wavelength

LIST OF SCHEMES

LIST OF FIGURES

LIST OF TABLES

LIST OF CHARTS

Annexure 1

CHAPTER 2

CHAPTER 3

CHAPTER 4

CHAPTER 5

CHAPTER 6

CHAPTER 1

Introduction

1.1. Cellular organelle bio-imaging:

Cells are the structural and functional unit of all life on the biosphere. Various cellular organelles are found in eukaryotes such as lysosomes, endoplasmic reticulum and Golgi apparatus, mitochondria, nucleus play an essential role in performing normal functions of cells *[1]* **(Figure 1.1)**. Organelle dysfunction causes the number of diseases such as Parkinson's diseases, Cancer, diabetes, Alzheimer's diseases *etc [2-5]*. Therefore organelles are of greater interest; not only for bio-imaging them and tracking their morphological alteration in real time which can enhance our understanding of how organelles function, but also considered as a potential therapeutic target for the treatment of many diseases.

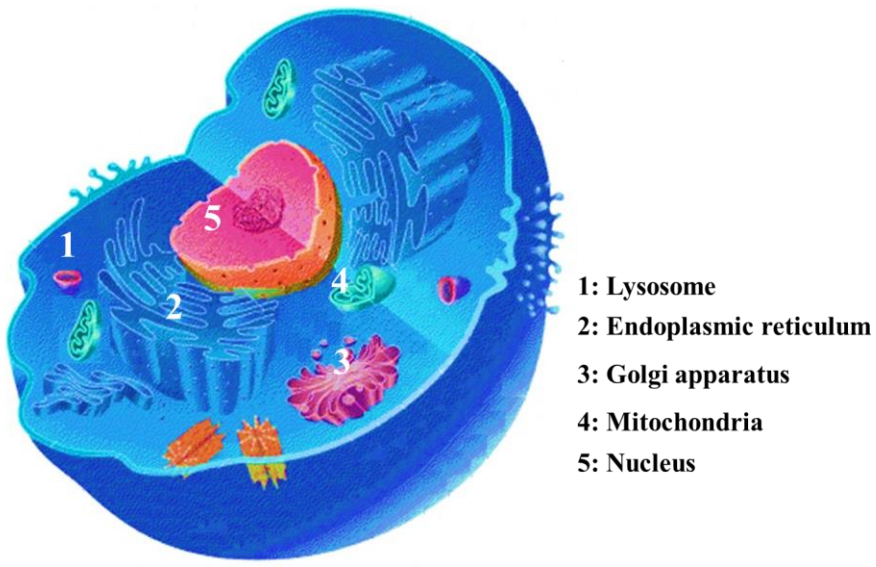

Figure 1.1. Schematic representation of cellular organelles (lysosome, endoplasmic reticulum, golgi apparatus, mitochondrion and nucleus) in a cell.

Recently, fluorescence imaging technique has emerged as a powerful way to monitor the amount, localization and movement of biomolecules at the cellular level *[6-7]*. Small molecule fluorescent probes

have found extensive applications in diverse fields, including drug discovery, clinical diagnosis, and chemical biology *[8-10]*. Keeping this in mind, organelles targeting ligands or metal complexes have attracted worldwide attention in recent years *[11]*.

1.1.1. The basic criteria of organelle-targeting probes:

Few criteria should be considered during the design and synthesis of organelles targeting fluorescent probe (OTFp) for their practical applications. (i) The probes should be chemically stable and synthetically accessible; (ii) easily and rapidly pass through the plasma membrane and organelle's membranes; (iii) show negligibly toxic to cells; (iv) not alter the endogenous metabolism of live cells; (v) remain inside the target organelle, react efficiently and selectively with the analytes of interest; (vi) exhibit measurable changes in the signal.

1.1.2. Organelle-targeting synthetic probes:

The organelle-targeting moieties can be peptides or small molecules. But in the case of peptides, its effectiveness as targeting moieties affected since it can be degraded by enzymes. However, small molecules remain unaffected by enzymes. Synthetic probes pose numerous advantages over other probes. Due to their synthetic nature, they are often available in large quantities and more cost-effective than antibodies. Unlike the fluorescent proteins, their application in cells does not require any transformation or genetic manipulation, which further allows their use where tedious transfection techniques are not practical or impossible *[1, 12]*. Synthetic probes are prepared with a wide range of targeting features inserted into them. Therefore synthetic organic probes are extensively used for visualizing various organelles and some of the probes have been commercialized **(Table 1.1)**.

Table 1.1. Some commercially available organic dyes for organelle targeted imaging.

Organelles	Organic dyes
Lysosome	LysoTracker® Blue DND-22 , LysoTracker® Blue-White DPX, LysoTracker® Green DND-26, LysoTracker® Red DND-99,
Mitochondrion	MitoTracker® Green FM, MitoTracker® Orange, MitoTracker® Red FM, MitoTracker® Deep Red
Endoplasmic Reticulum (ER)	ER-Tracker™ BlueWhite DPX, ER-Tracker™ Green, ER-Tracker™ Red
Nuclear	Hoechst 33342, DAPI

1.1.3. General approaches of OTFp delivery to the organelles:

Generally, for the delivery of fluorescent probes into organelles, there are two main strategies have been employed: (i) The direct one-step strategy and (ii) the indirect two-step strategy.

In the direct one-step strategy, organelles targeting fluorescent probe (OTFp) either bear organelle-anchoring moiety within the probe or it can covalently be attached to extra organelle-anchoring motifs **(Figure 1.2a).** In this case, fluorophores equipped with an anchoring moiety that has the capacity to drives the whole molecule into the desired target organelle. For example, molecules containing unprotonated amino bases are accumulated in lysosomes while triphenylphosphonium (TPP) accumulate inside the mitochondria *[13-14]*. Moreover, the probes can also consist of analyte-responding moiety. When the analyte-responding moiety meets the analytes of interest within particular organelle, thereby leading to fluorescence turn On/Off or changes in fluorescence signal.

In the indirect two-step strategy, a high-affinity receptor or an enzyme is first expressed on the organelles; the fluorescent probe consisting of receptor binding unit or substrate for enzyme; which can react with the receptor/enzyme and form a covalent bond with the protein of interest, thus being selectively retained within the desired organelle. Additionally, the fluorescent probe also carries an analyte-responding motif. The probe will exhibit changes in the fluorescence signal upon integration with the analyte of interest **(Figure 1.2b)**. The protein-bound nature limits the free movement of the probes. This strategy may lack effectiveness in the case of signaling molecules that float within the cellular environment.

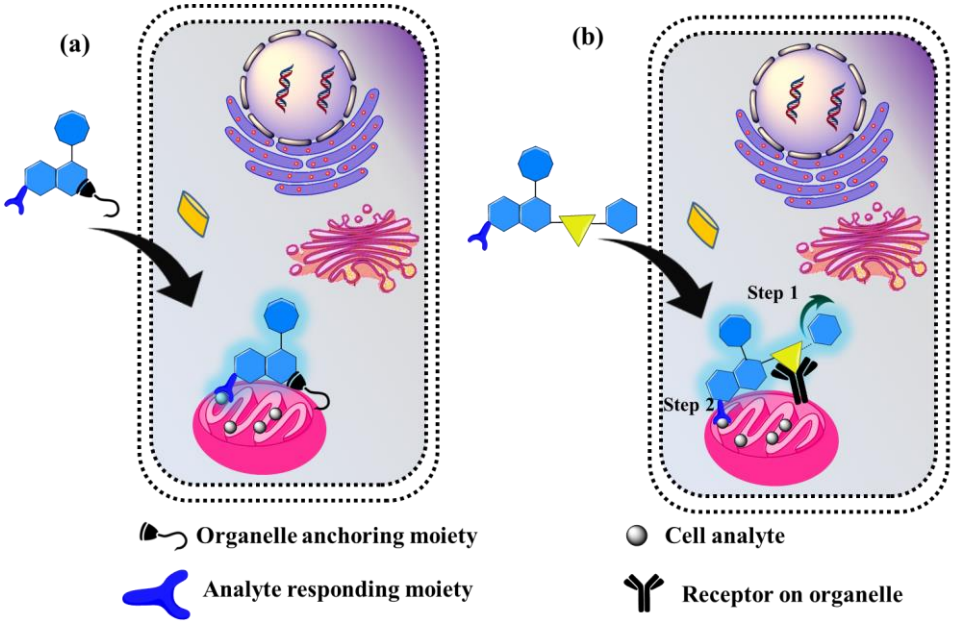

Figure 1.2. (a) Organelle targeting fluorescent probe (OTFp) delivery based on the direct one-step strategy. **(b)** OTFp based on the indirect two-step strategy.

1.2. Structure and function of Lysosomes:

Foreign materials, malfunctioning organelles, and obsolete biomolecules hamper cell growth and proper functioning of lysosomes. The acid hydrolases (present in lysosomes) play a significant role in degrading these molecules. The acid hydrolases are genetically encoded by nuclear DNA, produced in the ribosomes on the rough endoplasmic reticulum and tagged by mannose-6-phosphate (M6P) in the cis-Golgi. To prevent cellular damages by acid hydrolases release, they are protected by the M6P receptor (M6PR) protein in the Trans-Golgi. From the trans-Golgi network, the vesicles containing acid hydrolases transferred to the late endosomes *[15]*. Within the medium acidic environment of late endosomes (pH 5.5), M6PR release hydrolase enzymes in the lysosomes (pH 4.5), packed in the vesicles back to Golgi for recycling **(Figure 1.3)** *[16]*.

The lysosomes are single layer compartment; ubiquitously present in almost all eukaryotic cells, often described as the stomach of the cells. The lysosomes, as well as endosomes, maintained low pH value 4.5, which is facilitated by a number of proton pumps, including vacuolar-type H^+-ATPase. Adenosine Triphosphate (ATP) used as the energy source to supply the protons into the lysosome or endosome membrane. When the acid hydrolases enter in the lysosomes, they are activated by the low pH value and play a pivotal role in degrading bio-macromolecules delivered by different pathways (endocytosis, phagocytosis, and autophagy) into smaller fragments, which are then exported out of the lysosomes *[17-18]* as depicted in **Figure 1.3.**

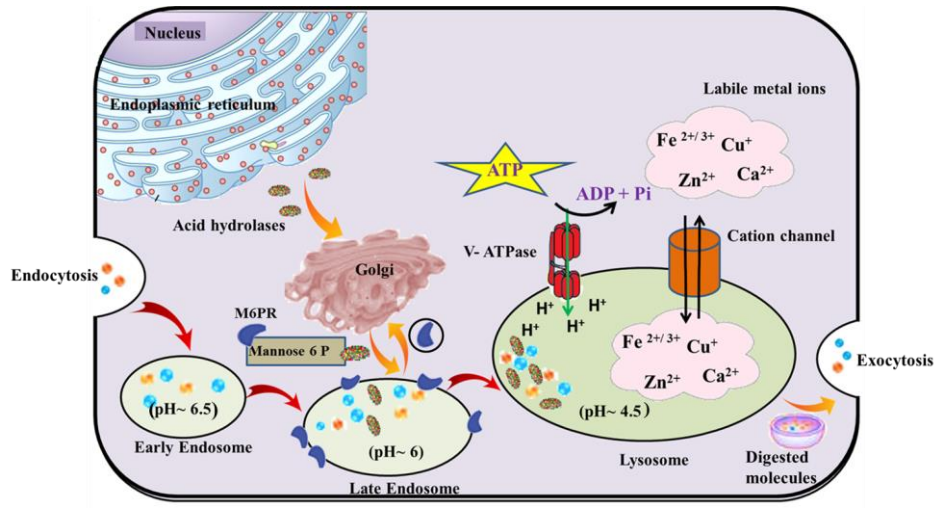

Figure 1.3. Structure and function of lysosome of cell.

More than 60 types of acid hydrolases present in lysosomes which includes specific peptidases lipases, membrane proteinase, sulfatases, proteases, phosphatases, nucleases, glycosidase, *etc*. to degrade bio-macromolecules which includes obsolete biomolecules, malfunctioning organelles, and foreign species *[19-21]*. Besides their role in terminal garbage disposal compartment of cells, lysosomes also perform a critical role in a number of key life activities including metabolism, cell migration, cell antigen processing, apoptosis, intracellular transportation, plasma membrane repair, and cholesterol homeostasis *[21]* as shown in **Figure 1.4.** Lysosomes also govern cell division, growth, and differentiation. It emerged as a sophisticated signaling hub in controlling nutrient response and growth/hormone signaling *[22-23]*. The master mechanistic regulating target of rapamycin complex 1 kinase is stimulated on lysosomes in response to growth and nutrient factor *[24]*. Lysosomes enable autophagy (self-eating) process which is necessary for stress adaptation. Lysosomal dysfunction causes several diseases including neurodegenerative disorders, silicosis, lysosomal storage disease, cardiovascular disorders, cancer and inflammation and age-related diseases *[25]*.

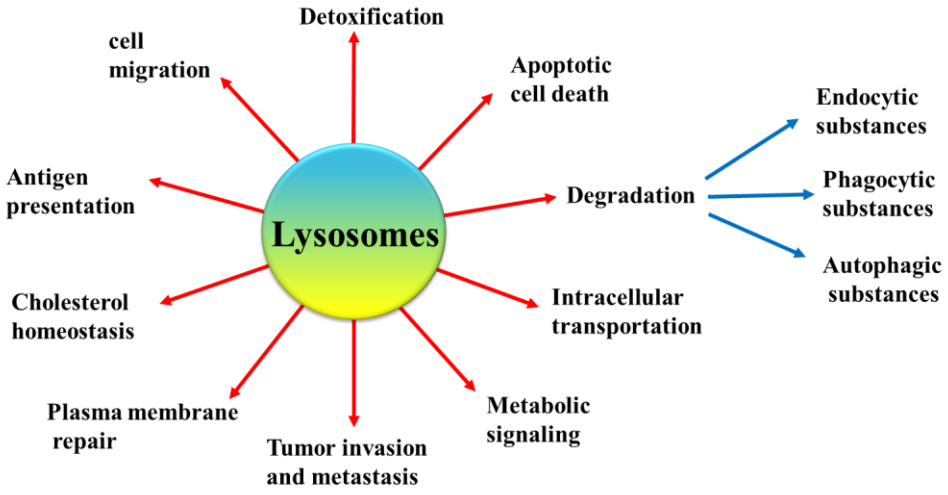

Figure 1.4. Representation of functional aspects of lysosome.

1.2.1. Possible pathways for probe to accumulate into lysosomes:

There are mainly four possible ways by which amine-containing molecules can gather into lysosomes. Three of the pathways involve direct transfer from of probe from the cell cytosol to lysosomes. (i) Passive diffusion (most common), (ii) autophagocytosis (with subsequent fusion with lysosomes) and (iii) by drug transporter protein which is associated with lysosomal membranes and orientated in such a way as to facilitate the transport of probe into the lumen space. (iv)The fourth possible pathway is endocytosis; large and/or membrane impermeable compounds sequestration occurs from the extracellular fluid by this mechanism *[26]*.

1.2.2. General deign of lysosome targeting probe (basic amines):

Small molecules below 1 kDa were able to diffuse easily through the cell bilayer membrane *[27]*. Probes which can anchors to the lysosomes or any other acidic organelles are prepared with lipophilic weakly basic amines moieties. The pH value of the cytosol of cells is typically around neutrality *[28]*. The weekly basic amines having pKa values around 8 thus in cytosol they exist predominantly in

their free base form **(b)**. Once the basic probes cross lipid bilayers of lysosomes, they become positively charged due to protonation of amines (BH^+) in an acidic environment. The protonated species is relatively membrane impermeable and unable to diffuse out of the organelle so remain trapped inside the organelles. A simplified model of this mechanism is shown in **(Figure 1.5)**. As long as low pH maintained in the lysosomes, the base will continuously accumulate and attain very high concentration at steady state relative to concentrations in the cytosol.

The concentrations of probes were at least 1000 times higher in lysosomes than its concentration in the cell culture media. The lysosomes could not have such a reserve of protons or extensive buffer capacity to allow for such extensive accumulations. Lysosomes maintain a lower pH value (acidic conditions) than the cytoplasm using proton-importing machinery **(Figure 1.5)** i.e V-type ATPases proton pump import proton using ATP as an energy source *[29]*. Most of the reported lysosomes targeted fluorescent probes (LyTFps) and endosome targeted (EndTFps) that function only under acidic conditions takes advantage of the low pH value of these digestive organelles.

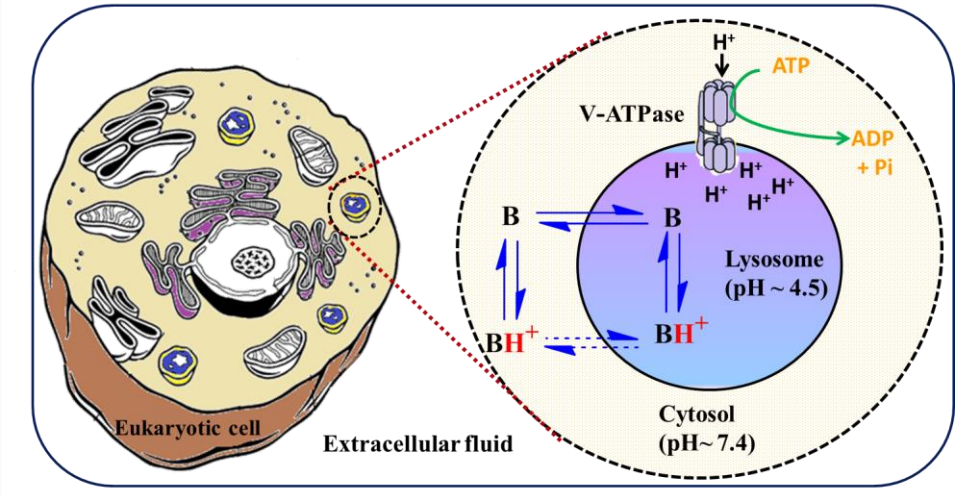

Figure 1.5. Illustration of the mechanistic basis for pH partitioning is driven by accumulation of weakly basic amines into lysosomes. Where free base form **(b)**, ionized state (BH^+).

There is an additional mechanism for accumulation of probes in the lysosome. A relatively significant residual binding of cationic probes to lysosomal membranes through interactions with acidic glycolipids and acidic polysaccharides, which are quite an abundant component of lysosomal lipid bilayers *[26a]*.

Lysosomotropic agents refer to any molecule that sequestered into lysosomes, regardless of the pathway. There are numerous uses of lysosomotropic agents such as in pH meters, pharmaceuticals, and the fluorescent probes for lysosome imaging *[26a]*. The Probes designed for targeting other acidic organelles such as autophagosomes or endosomes share similar features as those for lysosomes, but because of their distinct pH environments, special tuning is required in that case. On the basis of this mechanism, various commercial fluorescent probes for lysosome have been developed, such as LysoTracker blue ($\lambda_{ex}/\lambda_{em}$ = 373⁄422), LysoTracker yellow ($\lambda_{ex}/\lambda_{em}$ = 465⁄535), LysoTracker green ($\lambda_{ex}/\lambda_{em}$ = 504⁄511) and LysoTracker red ($\lambda_{ex}/\lambda_{em}$ = 577⁄590), which share the same lipophilic basic amino moiety but have different excitation and emission wavelengths *[26b]* as depicted in **Scheme 1.1.**

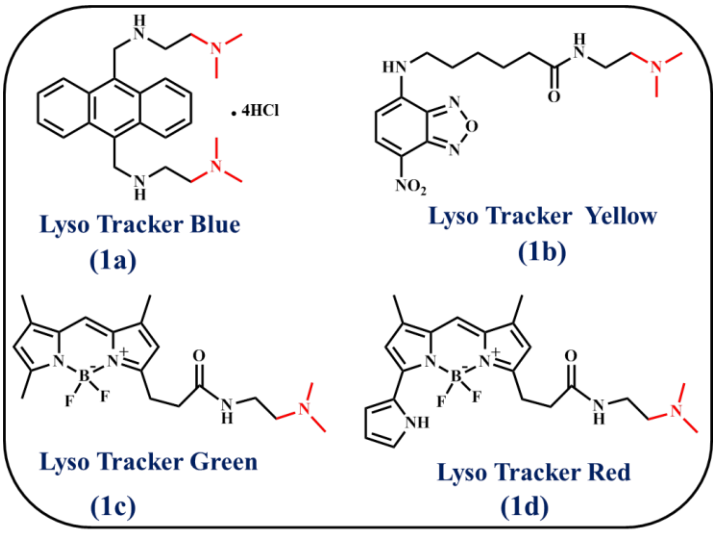

Scheme 1.1. Structures of commercial available LysoTrackers. Lysosome targeting motif is red.

1.2.3. The general methods to design probes for lysosome and sense lysosomal signaling molecule:

There are many small signaling molecules involved in the functions of lysosomes, such as NO, HClO, *etc*. Typically, lysosomal sensor probes were designed by using lysosome anchoring agents (a masked fluorophore is linked to a weak base) as the targeting unit and activation sensor moiety for sensing the analyte of interest. Preferably, before reaching the target organelles, the probes stay in the fluorescence "off" state in order to minimize the background interference and improve the signal-to-noise ratio. Once the activation sensor moiety comes in contact with analytes, their interaction quickly unmasks the fluorophore and the fluorescence "On" signals appears. Most of the lysosomal sensor probes are AND logical gates, which can only illuminate when they are activated by both protons (H^+) and the analytes of interest *[30]*. There are also some reports that utilize the autophagic or endocytic pathway for the selective delivery of OTFps. Recently, Fan *et al. [31]* reported a lysosome-targeting and polarity-specific fluorescent probe CPM **(2a, Scheme 1.2)** for cancer diagnosis and imaging. The confocal imaging co-localization experiment with commercially available Lysotracker green dyes was performed to indicate its localized in the lysosomes **(Figure 1.6)**

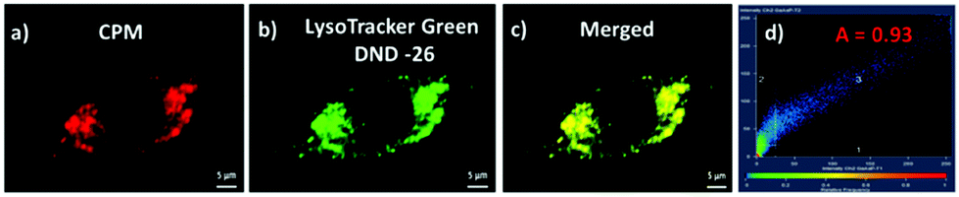

Figure 1.6. (a) Confocal images of 5 μM **CPM. (b)** LysoTracker Green DND-26 (1 μM) co-stained in SMMC-7721 cells. **(c)** Merged image. (d) The correlation of **CPM** and LysoTracker Green DND-26 intensities (A = 0.93). **CPM** λ_{ex} = 458 nm and λ_{em} = 560 - 650 nm; LysoTracker Green DND-26 λ_{ex} = 488 nm, λ_{em} =. 500 – 550 nm. Scale bar: 5 μm [31].

1.2.4. Lysosome targeting probe for Metal Ions sensing:

Lysosomes play a major role in the intracellular regulation and homeostasis of iron *[32-33]*. Lysosomal iron controls the sensitivity of the cells to oxidants *[34]*. Fakih et al. *[35]* synthesized a fluorescent turn "Off" probes by incorporating a basic 1-dimethylethylamine moiety **(2b, Scheme 1.2)** and another more iron sensitive *[36]* SF34 **(2c, Scheme 1.2)** to monitor the endosomal/lysosomal iron. These probes are highly sensitive to the lysosomal iron status in response to clinically used chelators, such as desferrioxamine, deferiprone and deferasirox as demonstrated by Confocal imaging experiments.

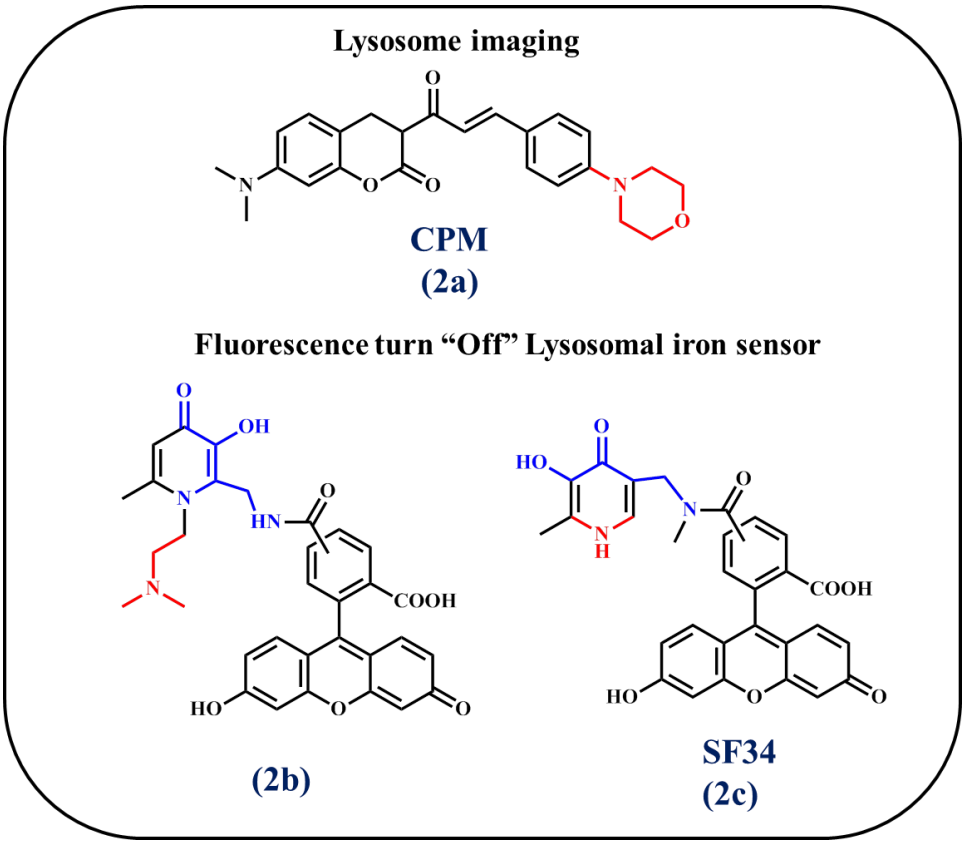

Scheme 1.2. Structures of lysosome-targeting fluorescent probe as well as turn "Off" probes for iron ions. Lysosome targeting motif highlighted red and metal binding motif highlighted blue.

Fluorescence quenching by Fe^{2+}/Fe^{3+} due to its paramagnetic nature, but fluorescent turn "On" probes by Fe^{2+}/Fe^{3+} for lysosome-targeting were lacking. Recently, ring opening of rhodamine was used as the basis to design iron turn "On" probes. The probe 3a **(Scheme 1.3)** displayed insignificant fluorescence when its ring in closed form. However in the presence of Fe^{3+}, ring-open complex form as iron species coordinated with the diacetohydrazide moiety *[37]*. The phenylamines attached to the xanthene scaffold to facilitate this probe localization in acid organelles (endosomes or lysosomes) of live HeLa cells. The intracellular fluorescence turn "On" response might arise from either endogenous labile Fe^{3+} or excessive H^+ in the lysosomes. The low pH value can also trigger the turning "On" the response of a probe by just opening their rings. Another report on the fluorescent turn "On" RPE probe **(3b, Scheme 1.3)** for labile lysosomal Fe^{3+} *[38]*.

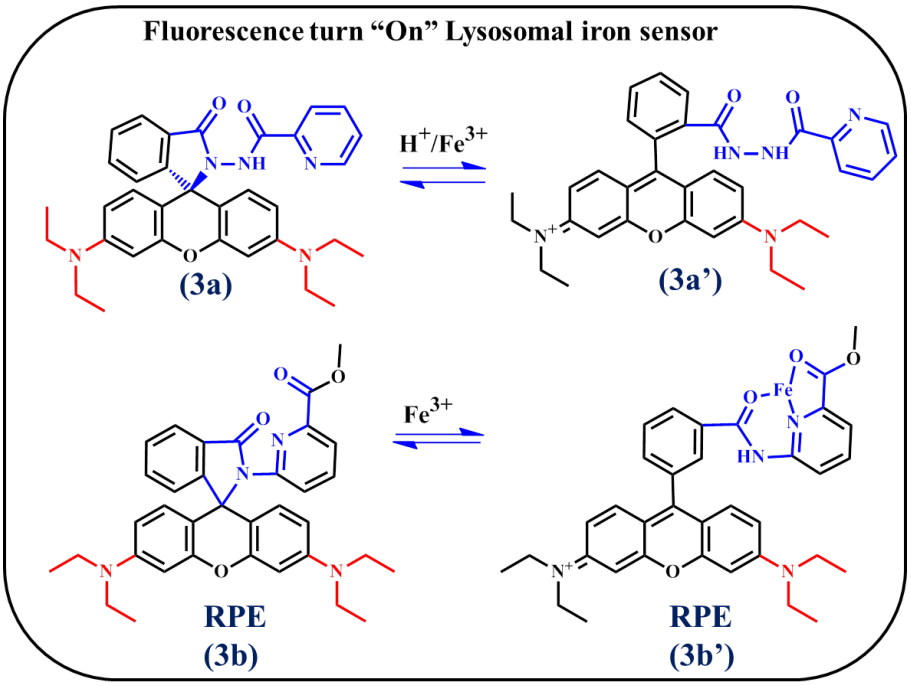

Scheme 1.3. Structures of lysosome-targeting fluorescent turn "On" probes for iron ions. Lysosome targeting motif highlighted red and metal ion binding motif highlighted blue.

Zinc ions generally, mediate the autophagy pathway, but excess zinc ions interrupt the normal enzymatic functions of the lysosome, resulting in the accumulation of a large number of malfunctioning proteins *[39]*. Jiang research group in 2012 *[40]*, construct a lysosome-targeting fluorescent probe DQZn4 for detecting Zn^{2+} **(4a, Scheme 1.4)**. DQZn4 consist of both lysosomal anchoring group (dimethylethylamino) as well as the fluorescence reporter (quinoline scaffold) responded to Zn^{2+}. DQZn4 exhibited fluorescence signal enhancements due to photoinduced electron transfer (PeT) mechanism and a ratiometric signal with a blue-shift due to intramolecular excited states variation.

Another research group reported probe LysoZn-1 **(4b, Scheme 1.4)** for Zn^{2+} *[41]*. This probe was designed by attaching lysosome-targeting moiety (2-morpholinoethylamine) to a known Zn^{2+} probe (styryl-BODIPY-DPA scaffold). Fluorescence signals enhancement upon binding with Zn2+. Successively, the FRET-based probe **4c** *[42]* shown in **Scheme 1.4** and the two-photon probe (λ_{ex} 900 nm) **4d** *[43]* depicted in **Scheme 1.4** were also reported for sensing and imaging of endogenous zinc ions in lysosomes **(Figure 1.7)**.

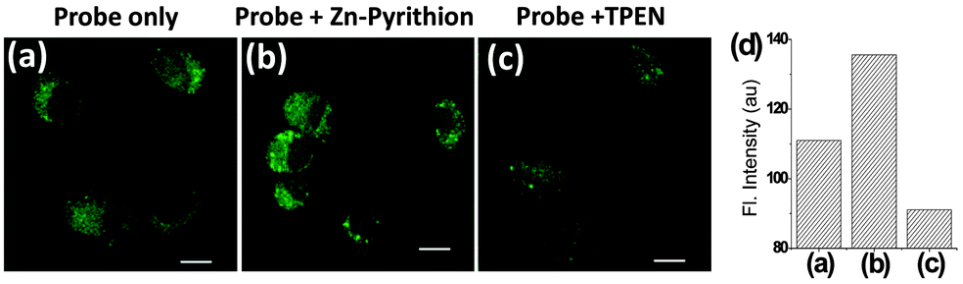

Figure 1.7. TPM imaging of Zn(II) ions in live NIH 3T3 cells: **(a)** the cells were treated with **4d** only (30 μM, 30 min); **(b)** the cells were treated with **4d** (30 μM, 30 min) followed by incubation with $Zn(ClO_4)_2$ and pyrithione (1 : 1) mixture (60 μM 10min); **(c)** the cells were incubated with **4d** (30 μM, 30 min); then incubation with (150 μM, 10 min) TPEN chelator. Scale bar: 10 μm. (d) Relative intensity plot of the respective TPM images are depicted in (a–c). [43]

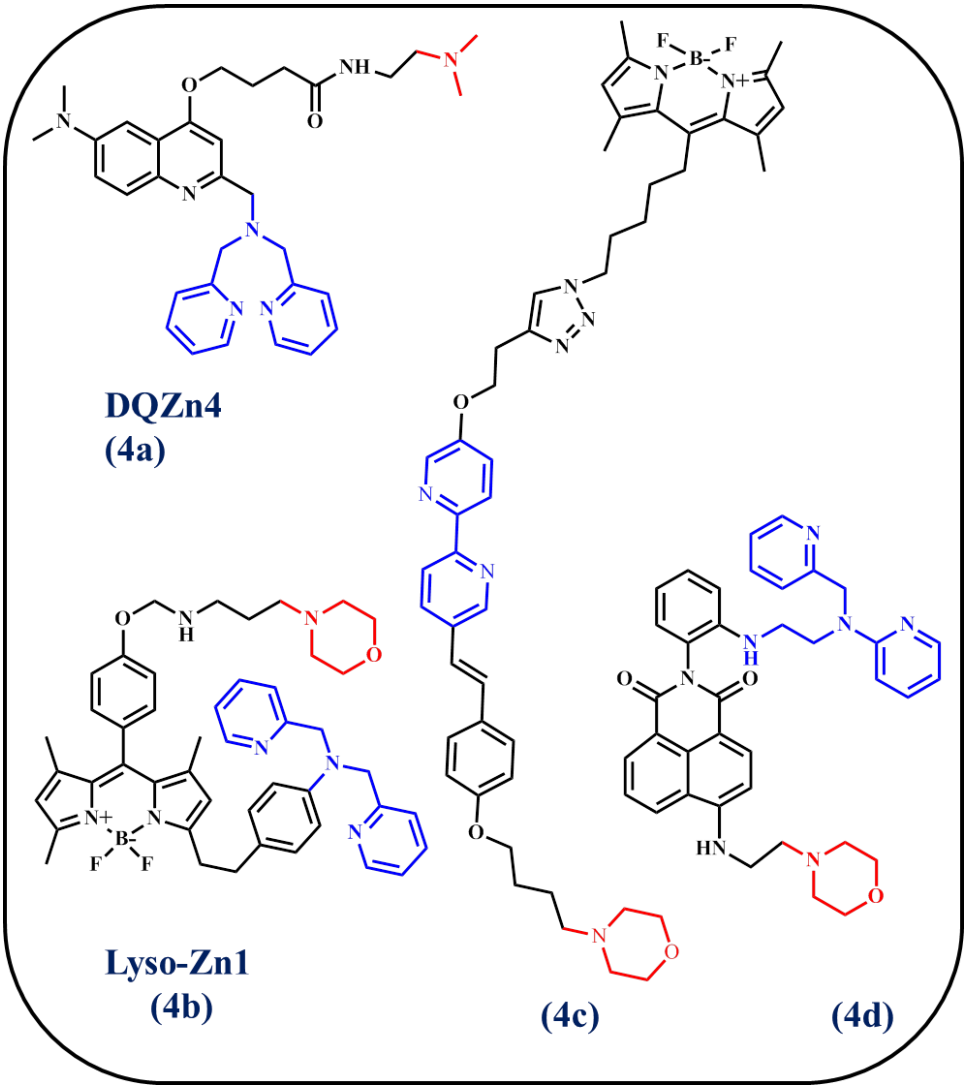

Scheme 1.4. Structures of lysosome-targeting fluorescent turn "On" probes for Zinc ions. Lysosome targeting motif highlighted red and zinc ion binding motif highlighted blue.

The Pearson's co-localization coefficient of the probe *[43]* **4d (Scheme 1.4)** describes the correlation of the intensity distributions to characterize the degree of overlap (0.87) of **4d** with commercially available lysotracker deep red **(Figure 1.8)**, was calculated to be by using the LAS AF software.

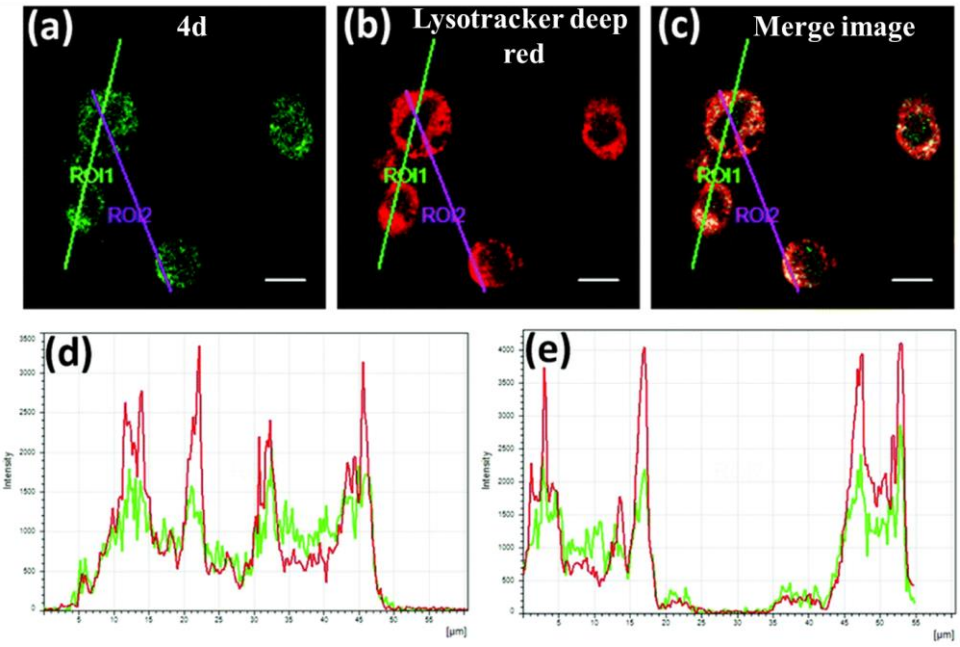

Figure 1.8. Co-localization of fluorescence of **4d** (as Zn^{2+} sensor) with LysoTracker Deep Red in NIH 3T3 cells: **(a)** TPM images of cells co-incubated with probe **4d** (30 μM) followed by $Zn(ClO_4)_2$ and pyrithione (1 : 1) solution (60 μM), λ_{ex} = 900 nm, λ_{em} = 500–630 nm. **(b)** OPM images of cells treated with LysoTracker Deep Red (1 μM) for 10 min at 37 ºC, λ_{ex} = 633 nm, λ_{em} = 670–750 nm. **(c)** Merged images. Scale bar: 10 μm. (d and e) Intensity profiles measured across the NIH 3T3 cells: **(d)** ROI 1 and **(e)** ROI 2. [43]

In spite of lysosomes involve in iron and zinc metabolism, they also contribute in copper homeostasis *[44-45]*. Excessive accumulation of copper in lysosomes will leads to leakage of acid hydrolases and lysosomal lipid peroxidation which further cause hepatocyte necrosis *[46-47]*. Therefore for the sensing and imaging of Cu^{2+} in lysosomes, cyanine7 based scaffold was used for the design and synthesis of NIR (Near Infrared) fluorescent turn "On" probe by Tang et.al. **(5a, Scheme 1.5)** *[48]*. Another rhodamine-based fluorescent turn "On" lysosomal Cu^{2+} sensing probe RHAT **(5b, Scheme 1.5)** was synthesized by same the group *[49]*. 134 The probe can target specifically to lysosomes **(Figure 1.9)**.

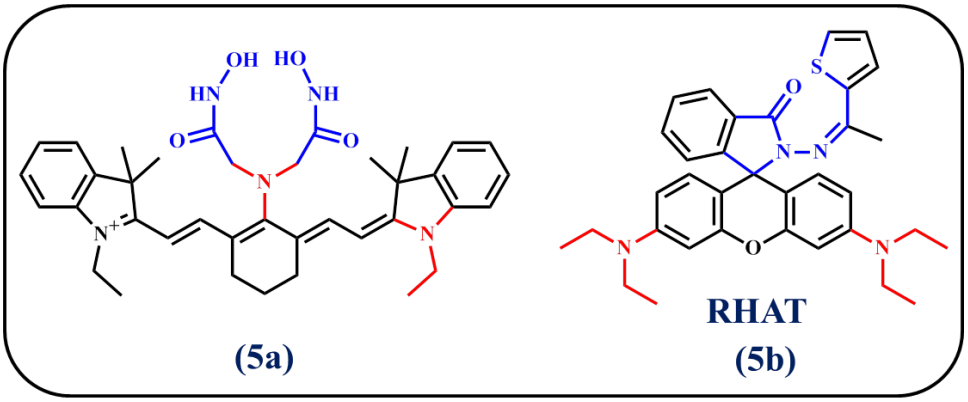

Scheme 1.5. Structures of lysosome-targeting fluorescent turn "On" probes for cupper ions. Lysosome targeting motif highlighted red and cupper ion binding motif highlighted blue.

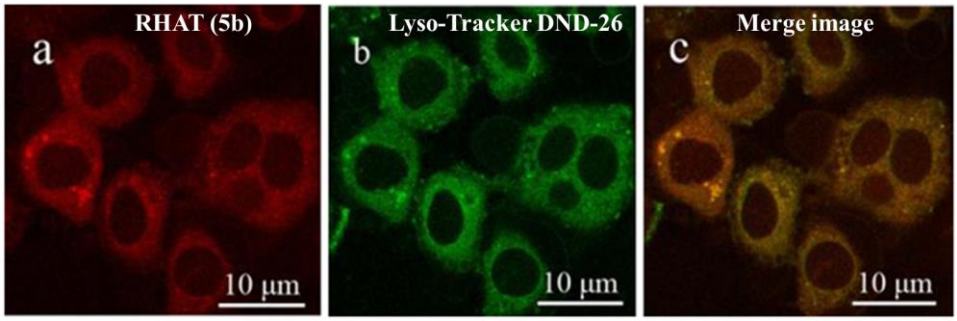

Figure 1.9. (a) HL-7720 cells treated with Cu^{2+} (30 μM, 30 min at 37°C), then 15 μM RHAT **(5b)** for 15 min. **(b)** Addition of 50 nM Lyso-Tracker DND-26 for 10 min. **(c)** merge image of **(a)** and **(b)**. [49]

The thiophene-substituted hydrazide moiety of the probe RHAT **(5b, Scheme 1.5)** leads to selective response to Cu^{2+}. The high sensitivity of the rhodamine ring-opening process allowed them in imaging of drug-induced fluctuations of Cu^{2+} level in live cells **(Figure 1.10).**

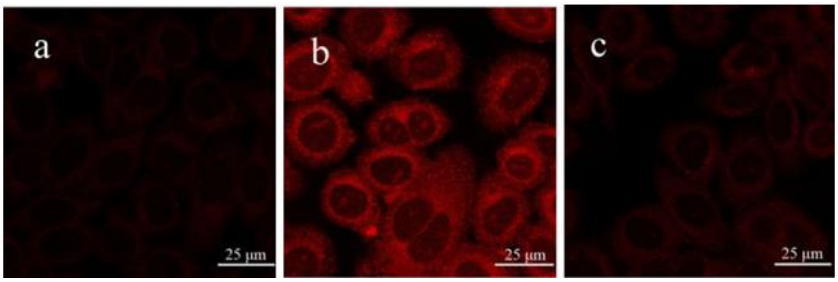

Figure 1.10. Confocal fluorescence images of RHAT **(5d)** showing Cu^{2+} ions sensing in live HL-7720 cells. **(a)** Cells incubated with 15 μM RHAT **(5d)** for 15 min at 37 ºC. **(b)** The cells were pretreated with Cu^{2+} (30 μM ,30 min at 37 ºC), then were incubated with 15 μM RHAT **(5d)** for 15 min. **(c)** RHAT-supplemented cells pretreated with 30 μM Cu^{2+}, then treated with 50 μM chelator TPEN. [49]

1.2.5. Lysosome targeting probe for detecting H_2O_2:

Another critical reactive species is lysosomal H_2O_2, which is associated with apoptosis and autophagy in normal and pathological processes *[50-51]*. To further explore its cellular functions, Song et al. designed the lysosome-targeting fluorescent turn "On" probe ZP1Fe2 **(6a, Scheme 1.6)** for H_2O_2 . The bioredox reaction was introduced to remove the iron complex from the xanthene ring *[52]*. The amino chelator and the slightly basic phenolic acid moieties are likely to be lysosome targeting group, but further required clarification. In 2013, Jing and Zhang group is developed a new two-photon probe J-S **(6b, Scheme 1.6)** for lysosomal H_2O_2 imaging in live cells *[53]*. J-S selective exhibited turn "On" fluorescence signal in response to H_2O_2, in the presence of enzyme myeloperoxidase (MPO). In the absence of the enzyme, the probe was distributed in the cytosol. The thiomorpholine moiety reaction with H_2O_2 allowed the probe to detect and imaging of exogenous or endogenous (lysosomal) H_2O_2 *[53]*.

In 2015, Yoon group *[54]* reported naphthalimide based fluorescent probe **6c** for H_2O_2 detection. The probe consists of lysosome anchor moiety (aminoethylmorpholine) and an H_2O_2-responding motif (boronate moiety) **(6c, Scheme 1.6).** This probe detects both endogenously

generated and exogenously added reactive species, although the addition of an H_2O_2 scavenger quenched the fluorescence response.

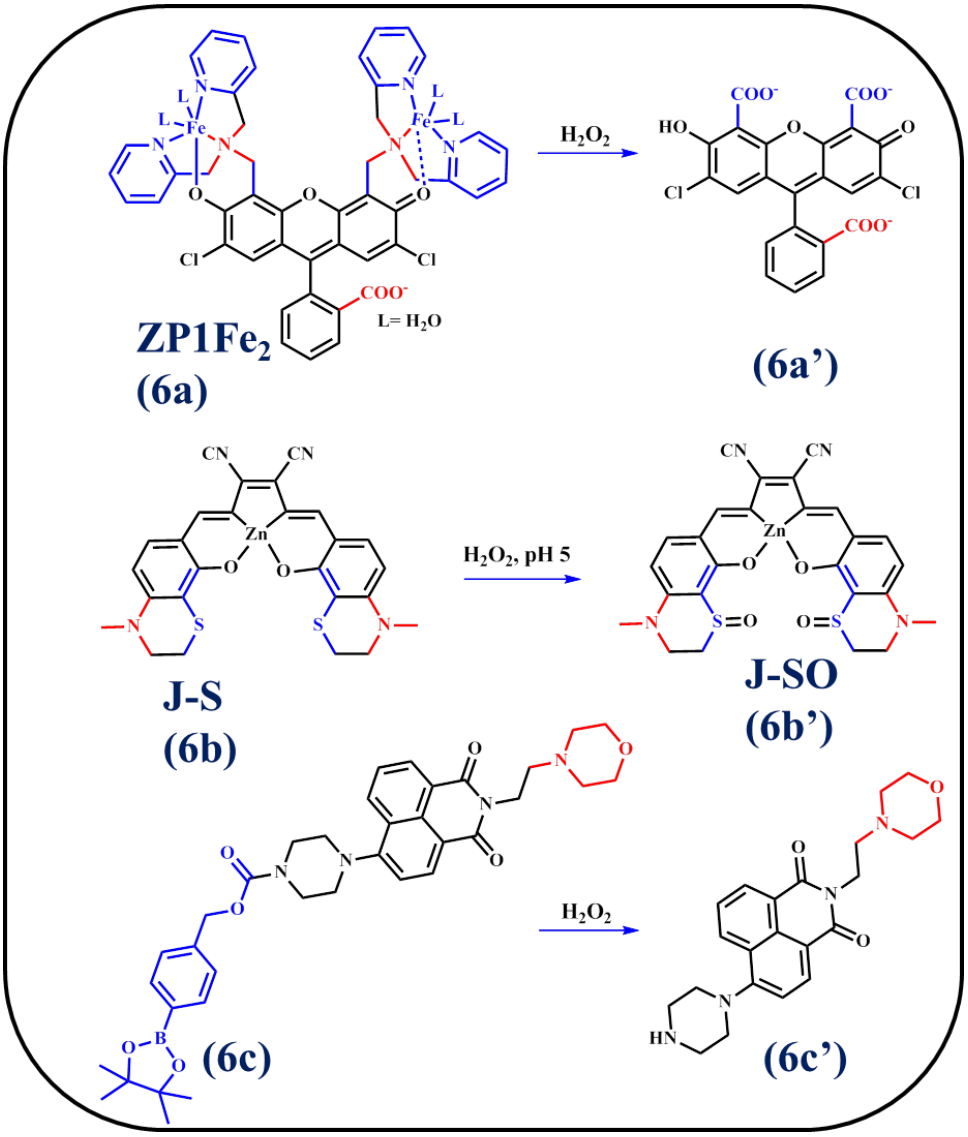

Scheme 1.6. Structures of lysosome targeting fluorescent probes for sensing H_2O_2 in live cells. Lysosome targeting motif highlighted red and H_2O_2 sensing motif highlighted blue.

1.2.6. Lysosome targeting probe for sensing HOCl molecules:

Hypochlorous acid (HOCl) is one of the end products of H_2O_2 metabolism. It plays an important role as signaling molecule as well as a scavenger for cell debris. HOCl also plays important roles in regulating inflammation and cellular apoptosis. In 2015, Yuan *et al. [55]* designed a ruthenium (II) complex based probe Ru-Fc **(7a, Scheme 1.7)** that precisely detects lysosomal HOCl. the probe was weakly fluorescent in the absence of interaction with HOCl, due to photoinduced electron transfer (PET) from the ferrocene quencher to the ruthenium complex. The fluorescence emission is restored from the complex when HOCl cleaves the linker between the ferrocene and ruthenium complex. Notably, Ru-Fc probe localized in the lysosome by the caveolae-mediated endocytic pathway, as confirmed by performing endocytosis inhibitor assays. Due to its relatively large size, it not enters in lysosome by free diffusion. In addition, Ru-Fc probe was visualizing endogenous HOCl species in live cells, as well as in live Daphnia magna and zebrafish. In the same year, Li and co-workers reported a fluorescent probe **(7b, Scheme 1.7)** for lysosomal HOCl response, based on a selenide switch.*[56]* [147] Yuan *et al. [57]* reported LYSO-TP **(7c, Scheme 1.7)**, for detecting endogenous lysosomal HOCl (nanomolar range) in stimulated macrophage cells *[57]*

1.2.7. Lysosome targeting probe for detecting reactive species and thiols:

Nitric oxide (NO) is a cellular signaling molecule *[58]*, 60 affects the lysosome's autophagy processes *[59]*. [141] The Xiao and its coworker *[60]*142 constructed a two-photon fluorescent probe Lyso-NINO **(8, Scheme 1.8)** for detecting and imaging of lysosomal NO activities in real time. This probe consists of a lysosome-targeting moiety (aminoethyl morpholine), NO-capturing moiety (o-phenylenediamine), and the two-photon fluorophore (naphthalimide). Lyso-NINO displayed selective turn

"On" fluorescence response to NO over other reactive oxygen species in the nanomolar range. It could capture endogenous NO in lysosomes in live cells.

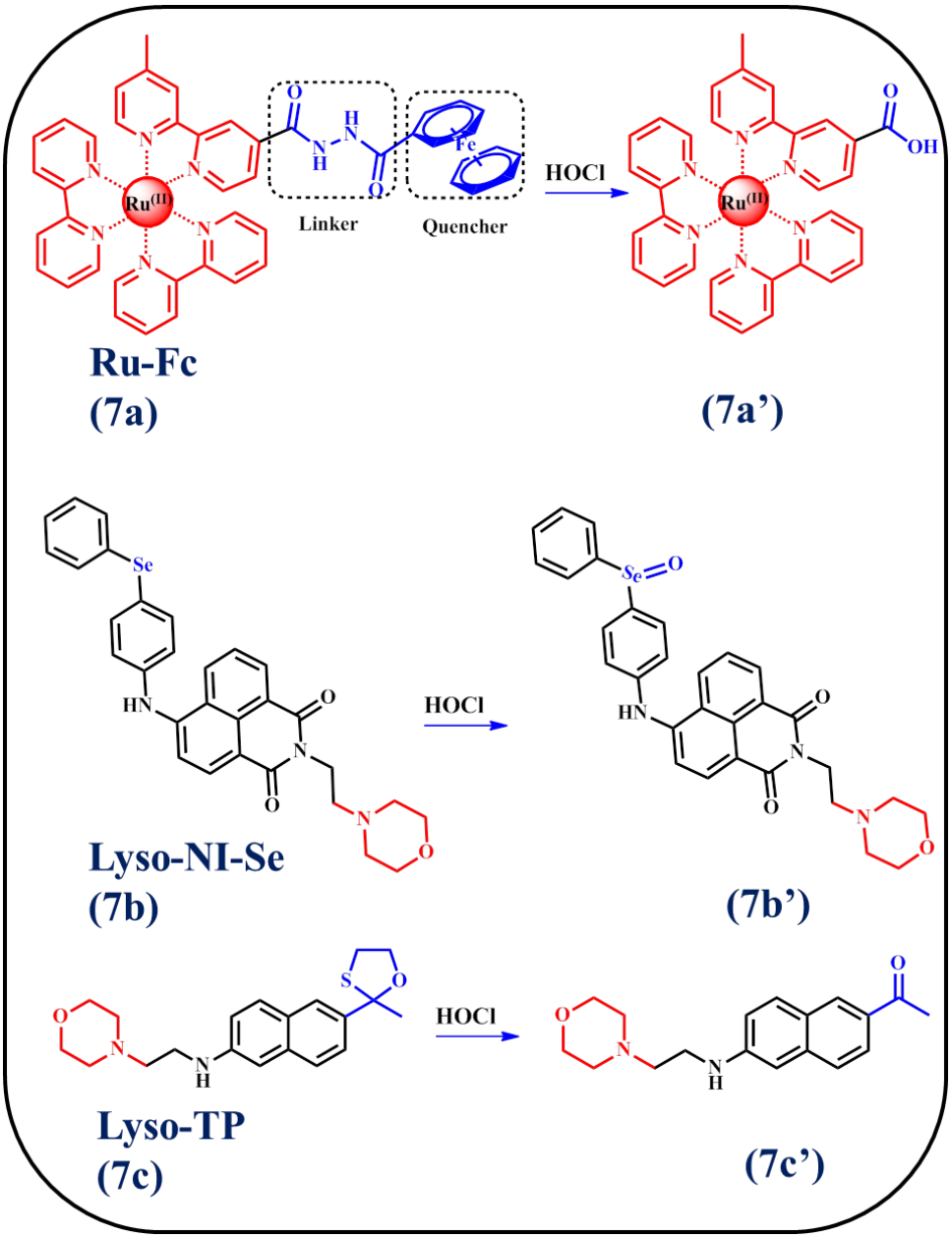

Scheme 1.7. Structures of lysosome-targeting fluorescent turn probes for HOCl sensing in live cells. Lysosome targeting motif highlighted red and H_2O_2 sensing motif highlighted blue.

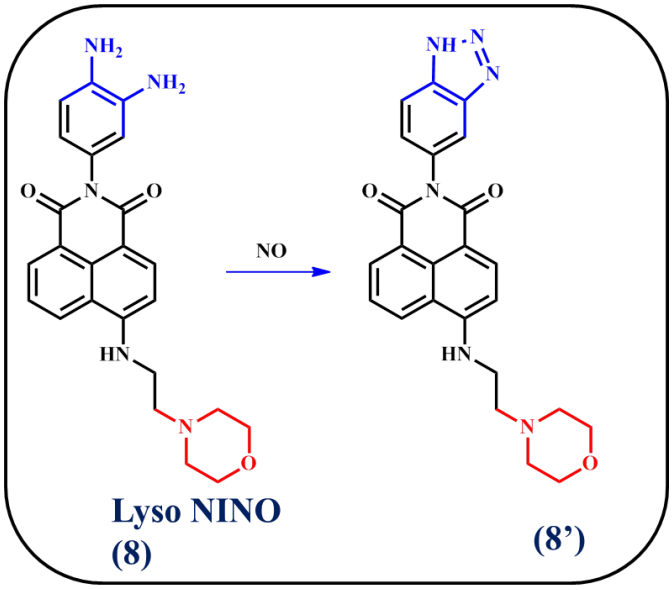

Scheme 1.8. Structures of lysosome-targeting fluorescent turn "On" probes for Nitric oxide (NO) sensing in live cells. Lysosome targeting motif highlighted red and NO sensing motif highlighted blue.

Hydrogen sulfide (H_2S) is endogenously produced by the enzymes such as cystathionine γ-lyase and cystathionine β-synthase. It is an important gas transmitter for various physiological processes. It may act as an antioxidant and signaling agent in the brain, lung, blood, kidney, spleen, liver, *etc*. However abnormal regulation leads to diseases *[61]*. The cellular functions of H_2S remain under debate and attracts researcher attention *[62]*. To elucidate the role of H_2S in lysosomes, in 2013 Xu et al. reported naphthalimide-based probe Lyso-NHS **(9a, Scheme 1.9)**, which can determine H_2S species inside the lysosomes of living cells. Morpholine moiety of Lyso-NHS allows its localization in lysosomes whereas rapid thiolysis of the dinitrophenyl ether (fluorescence quencher under physiological conditions) by H_2S turn "On" fluorescence response *[63]* Successively, they developed another lysosome localizing probe Lyso-AFP **(9b, Scheme 1.9)** based on the reduction of an azide moiety by H_2S leads to turn "On" fluorescence response *[64]*. Another group

reported **9c** **(Scheme 1.9)** as lysosome-targeting H_2S probes *[65]*. Two-photon lysosome-targeting H_2S probes TP-PMVC was designed by Lin *et al*. *[66]* Pyridine moiety (pKa ≈ 5.0) was used for lysosomal localization, and the indolenium unit was selected as the site for H_2S owing to its electrophilic character **(9d, Scheme 1.9)**.

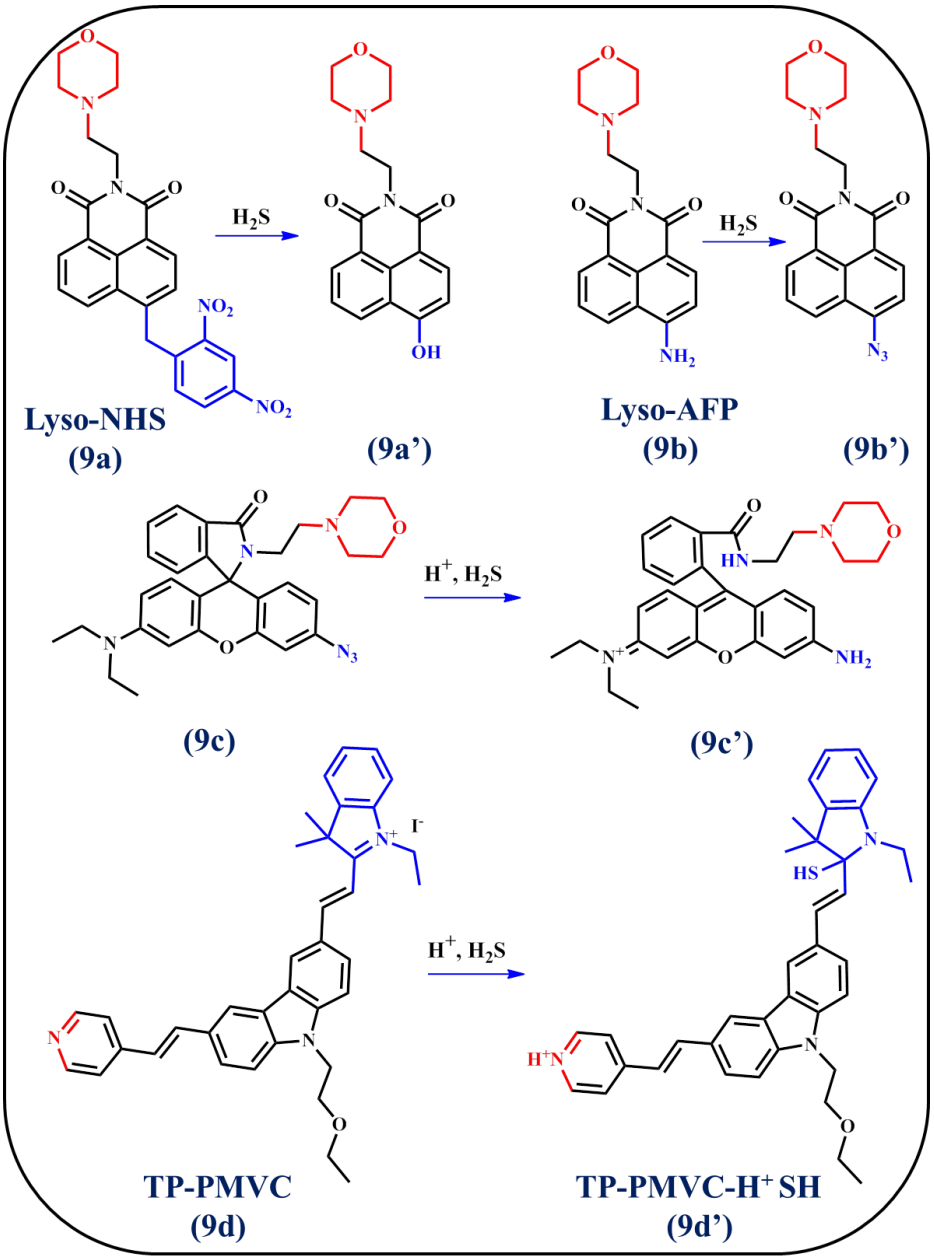

Scheme 1.9. Structures of lysosome-targeting fluorescent turn "On" probes for targeting lysosomal H_2S in live cells. Lysosome targeting motif highlighted red and H_2S sensing motif highlighted blue.

1.2.8. Challenges for lysosome targeting probes:

Although some progress has been done for the development of lysosome targeting probes on the basis of unique acidic matrix of lysosome, some challenges are still remains:

(i) Lysosome targeting probe for sensing of some reactive biomolecules such as Ca^{2+}, Mg^{2+}, and various hydrolases are not reported till date. These biomolecules are paly an important role for functions of lysosome and cell survival.

(ii) Some lysosomes targeting probes are prone to degradation by the considerable amounts of hydrolase enzymes in lysosomes, which cause diminished fluorescence signal and consequently the detection became unsatisfactory for their application in live cells imaging *[17]*.

(iii) Most reported lysosome targeting probe consist of basic moieties However, their long-term incubation within lysosomes could induce an increase in the pH value (alkalization), resulting to cell death *[26b]*.

1.3. Structure and function of ER and Golgi apparatus:

The endoplasmic reticulum (ER) and Golgi apparatus are types of organelles found in most eukaryotic cells. Proteins are crucial for cellular architecture and functions. Structurally, both the endoplasmic reticulum (ER) and Golgi apparatus are a network of sac-like structures known as cisternae found throughout the cell and some ER connected to the nucleus through the nuclear pore. The rough ER (ribosomes attached to its surface) functions as a synthesis and packaging of proteins with the help of ribosomes, mRNA, and tRNA. After the synthesis of nascent protein, they are then folded within the rough ER to produce functional 3D protein structures *[67]*. Further proteins are transported to their respective locations *via* the Golgi apparatus **(Figure 1.11)**. On the other hand, smooth ER acts as a storage organelle. It plays an essential role in the synthesis and storage of lipids and steroids. It mainly considers as signaling station; for example, calcium signaling, as it contains the largest calcium pools within the cell *[68]*. Calcium signaling is crucial for the movement of muscle cells. Smooth ER receives and monitors other signaling molecules including sterols, nucleotides, reactive oxygen species (ROS) and various enzymes. Correspondingly, they activate transcription factors cascades *[69-70]*. In addition to the synthesis of a large number of proteins (enzyme precursors, digestive enzymes, *etc*.), lipids and carbohydrates, the ER plays an important metabolic role in cells *[71]*.

Once protein properly folded in rough ER, they are wrapped into vesicles (lipid bilayer membrane) and transported to the cis face of Golgi apparatus (cis face toward ER while trans face away) *[72]*. Here proteins processing take place including various modification procedures such as sulfation, methylation, glycosylation, phosphorylation, *etc*. *[73]*. The proteins modification including its tagging, that allows them to target their respective destinations. For example, the proteins are tagged with mannose-6-phosphate (M6P) in the case of lysosomal acid hydrolases for

their transportation to the lysosomes *[74]*. Therefore, the rough ER and the Golgi apparatus together secure the synthesis, processing and transportation of bio-macromolecules **(Figure 1.11).**

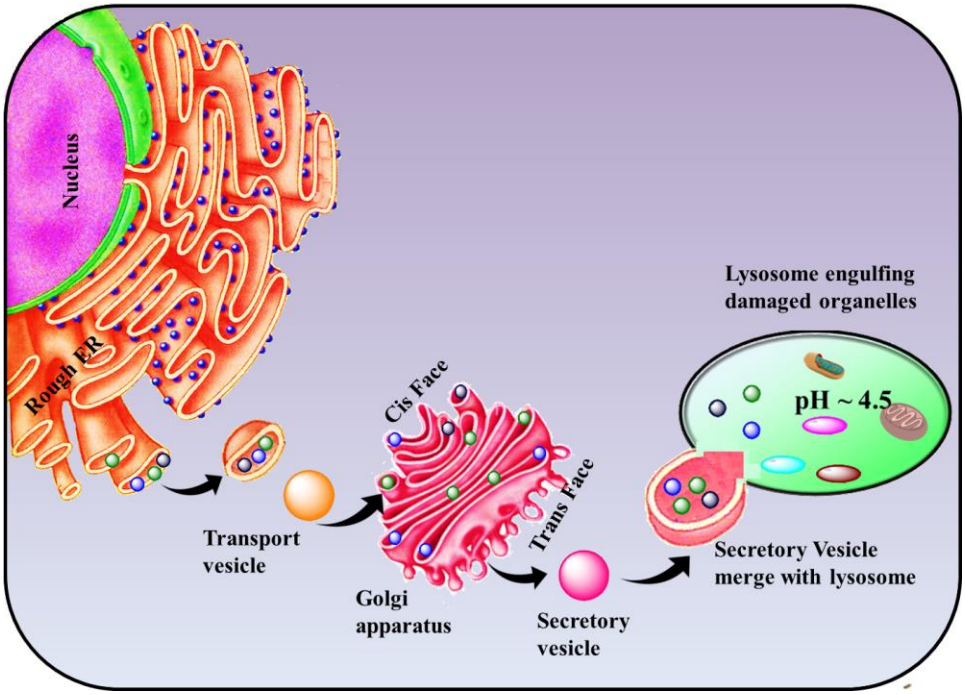

Figure 1.11. Structure and function of ER and Golgi apparatus, vesicles transport from ER to lysosome *via* Golgi apparatus.

1.3.1. General feature of ER-Targeting fluorescent probes:

For the large lipophilic membrane of the ER, selective ER reagents share some common features with the ER trackers: they are amphipathic, lipophilic cationic dyes with the moderate-sized conjugated ligand. Some commercially available dye for ER such as ER-Tracker™ Bluewhite DPX *[75]*, ER-Tracker™ Green (BODIPY™ FL Glibenclamide), ER-Tracker™ Red (BODIPY™ TR Glibenclamide) **(Scheme 1.10)**. Glibenclamide (glyburide) binds to the sulphonylurea receptors of ATP sensitive K channels which are prominent on ER; the pharmacological activity of glibenclamide could potentially affect ER function. Variable

expression of sulphonylurea receptors in some specialized cell types may result in non-ER labeling.

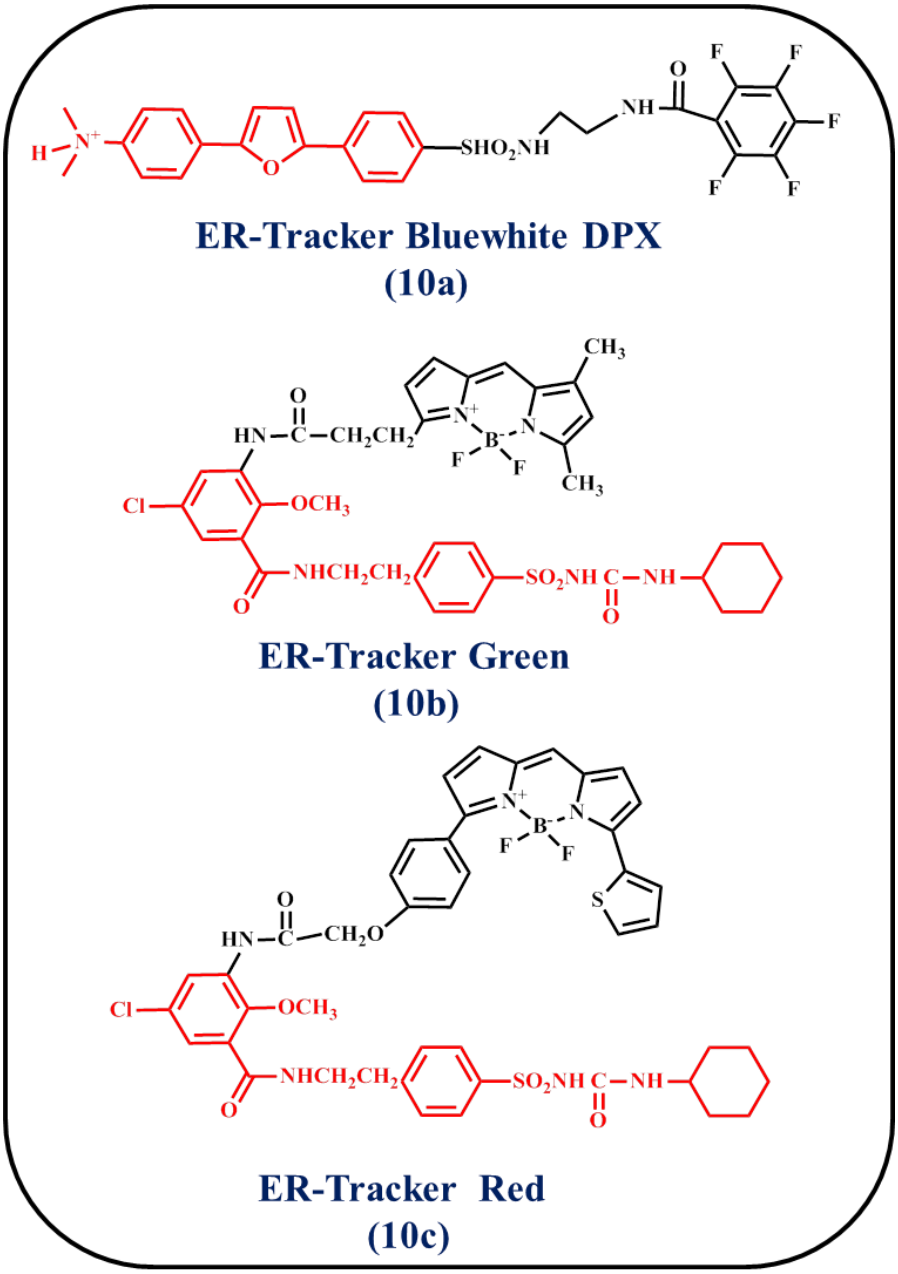

Scheme 1.10. Structure of commercially available ER-tracking dyes. Red color denoted ER targeting lipophilic moiety.

In 2010, the Che *et al. [76]* reported the new ER reagent **11a**, which consists of a cytotoxic artemisinin derivative conjugated with a

fluorescent dansyl moiety **(11a, Scheme 1.11)**. The co-localization experiment with commercially available organelle-specific dyes indicated that this probe located at the ER. However, whether artemisinin and its derivatives could specifically target the ER or not, is still controversial. In 2015, Peterson research group developed fluorinated hydrophobic rhodols derivative fluorophores that allow the delivery of small molecules for targeting ER-associated proteins and pathways *[77]*. Compound **11b (scheme 1.11)** was designed by incorporate fluorine atoms at the 2'- and 7'-positions of rhodol and the polar carboxylate of rhodol was substituted with a hydrophobic methyl group to favor association with cellular membranes of ER. Another compound rhodol nitrofuran **(11c, scheme 1.11)** was also designed by introducing 5-nitrofuran-2-acrylaldehyde hydrazine to target the p97 protein of the ER *[77]*. Kim et al. *[78]* in 2016 reported ERp probe **(11d, scheme 1.11)** preference for ER accumulation may be due to its lipophilic in nature considering that the lipophilic molecules can be commonly metabolized in ER.

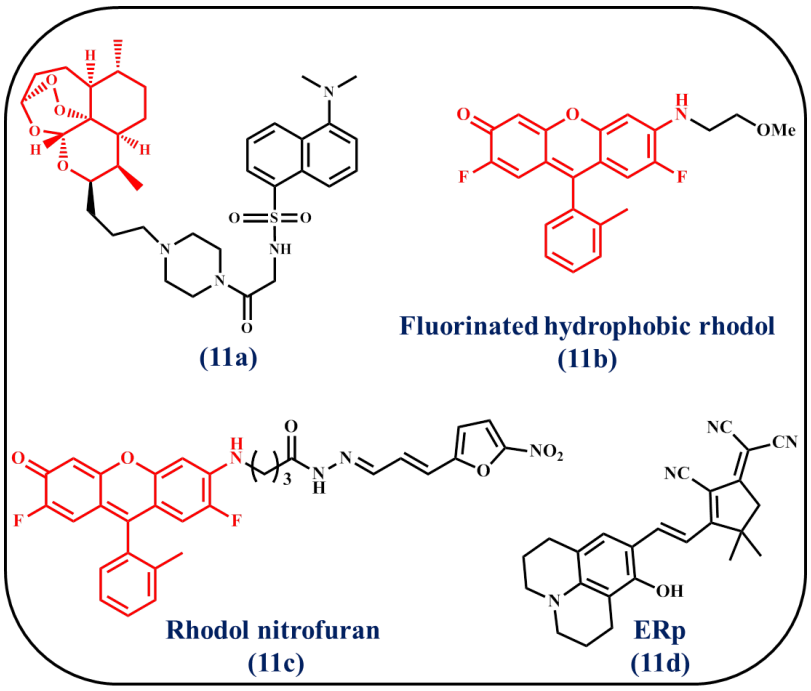

Scheme 1.11. Various newly developed ER-tracking probes. Red color represent lipophilic moiety for ER targeting.

The confocal imaging co-localization experiment with commercially available organelle-specific dyes indicated that these probes are localized in the ER **(Figure 1.12).** The **ERp** probe **(11d, scheme 1.11)** can monitor the dynamic change of the ER structure *[78]*. Tubulin is the main cytoskeleton associated with a smooth endoplasmic reticulum structure for their normal functions. Tunicamycin induces the ER stress by blocking *N*-glycosylation of newly synthesized proteins in the ER **(Figure 1.13)**.

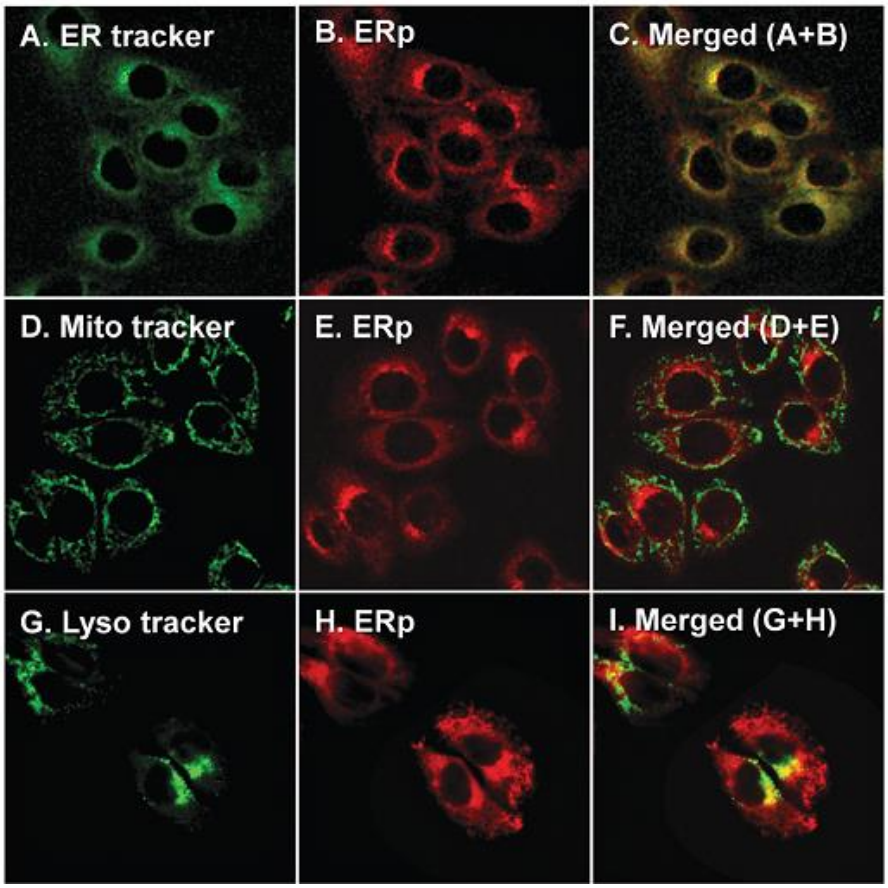

Figure 1.12. Co-localization experiment of **ERp** (2.5 μM) with several organelles pecific trackers in Hela cells. The panels (B, E and H) show the fluorescence imaging of **ERp** (λ_{ex}=543 nm with an LP 650 nm emission filter). The panels (A, D and G) show the images of ER-, Mito- and Lyso-Tracker (λ_{ex}= 488 nm with a BP 505–550 nm filter for all), respectively. The panels (C, F and I) show the images of A + B, D + E, and G + H merging, respectively. [78]

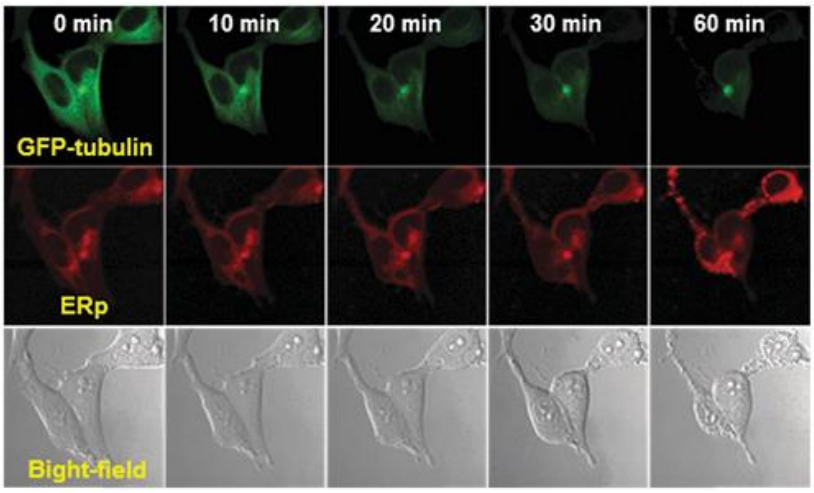

Figure 1.13. Fluorescence images of HeLa cells using tunicamycin (40 μg ml^{-1}) treated for 3 h before **ERp** (2.5 μM) for 20 min. GFP-tubulin (C-10613; Thermo) has to be incubated overnight at 37 ºC before the experiment. λ_{ex} = 488 nm, λ_{em} = 500–560 nm (GFP-tubulin); λ_{ex} = 633 nm and λ_{em} = 660–700 nm (**ERp**). [78]

1.3.2. ER targeting probe for Metal Ions sensing:

Metal ions mainly Ca^{2+} and Zn^{2+} are required for the proper functioning of the ER. In 2013, Lippard research group reported a fluorescent red emitting sensor, ZBR1 **(12a, Scheme 1.12)** to monitor labile Zn^{2+} ions in the ER, based on a benzoresorufin fluorophores functionalized with pyridine and pyrazine-containing metal chelators *[79]*. ZBR1 turns "On" probe upon binding with Zn^{2+} ion in live cells. Additionally, ZBR1 was also used for the monitoring of peroxynitrite-induced depletion of labile zinc (fluorescence intensity decrease) within the ER of neural stem cells.

In 2014, Kim and co-workers reported an ER targeting fluorescent probe for Cu^{2+} ions *[80]*. The probe was designed by incorporating an ethylene glycol chain into a naphthalimide fluorophore **(12b, Scheme 1.12)** due to ER localization capacity of lipophilic or glycosylated compounds. Co-localization result (using confocal microscopy) indicated

that this probe selectively localized into the ER, instead of other organelles in live-cell *[80]*.

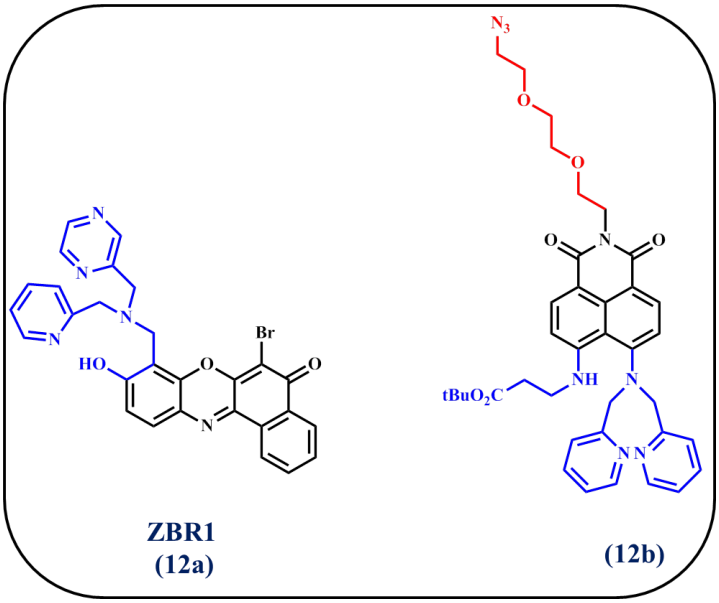

Scheme 1.12. ER-targeting fluorescent probes for metal ion sensing in ER of live cells Zn^{2+} (**12a**), Cu^{2+} (**12b**). Blue color represents metal binding moiety and red color for ER targeting lipophilic moiety.

1.3.3. ER-Targeting probe monitor vesicle transport from ER to Lysosome:

In 2014, Kim and Kang research group *[81]* reported an amidine-based two-photon fluorescent probe ELP1 **(13, Scheme 1.13)** for monitoring vesicle transport from the ER to lysosome in live cells. Amidine containing small-molecule could be selectively localized to protein-rich organelles, such as the ER and Golgi.

The amino group at position 2 of naphthalene was introduced in order to design a two-photon excitable probe. This leads to a push–pull dipole, as the amidine moiety is cationic in a physiological medium, causing an efficient intramolecular charge transfer (ICT) character that is a necessity for strong efficiency in two-photon excitation. Hence, the amidine group and monomethyl amine might be responsible for ELP1 (**13**) to reside in the ER. Further two-photon microscopy imaging studies

revealed that the probe initially localized in the ER and subsequently transported to the lysosome through vesicular transport *[81]* as shown in **Figure 1.14**.

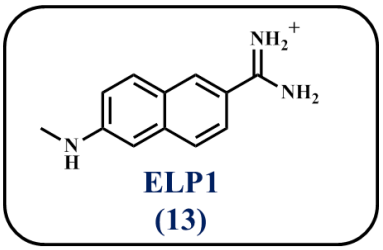

Scheme 1.13. ER-targeting fluorescent probe, monitor vesicle transport ER to lysosome.

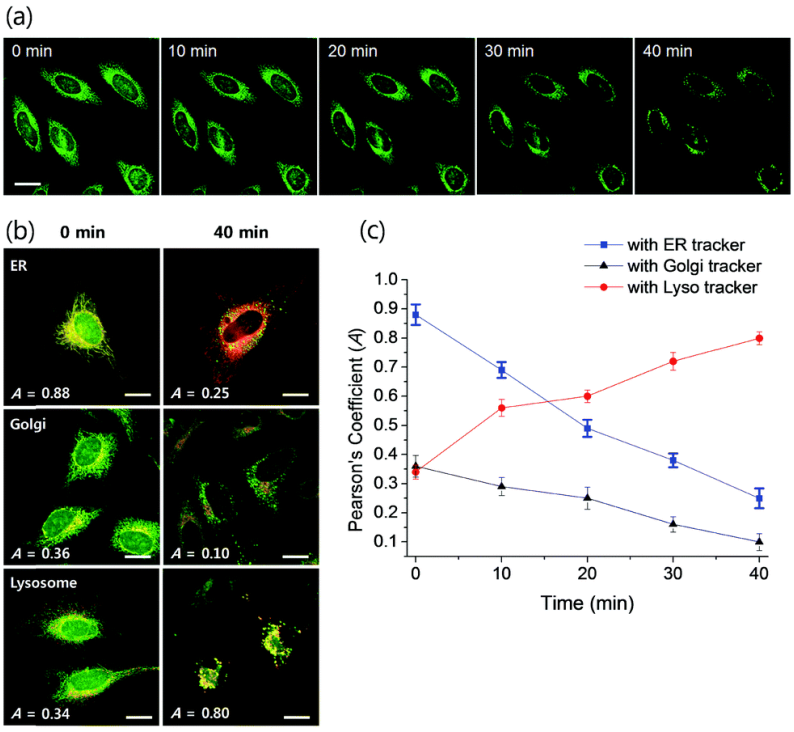

Figure 1.14. Co-localization images of **ELP1** with various organelles trackers displaying vesicle transport from ER to Lysosomes. **(a)** Time course TPM images of HeLa cells labeled with 2.0 μM **ELP1**. **(b)** Time course merged images of HeLa cells co-labeled with 2.0 μM **ELP1** (green fluorescence, TPM images) and organelle markers (red fluorescence, OPM images; 1.0 μM ER-Tracker Red for ER, 5.0 μM BODIPY TR ceramide complexed to BSA for Golgi, 1.0 μM LysoTracker Red DND-99 for lysosome). **(c)** Graph of the Pearson's co-localization coefficient value with different trackers. Scale bars = **(a)** 45 μm and **(b)** 20 μm, respectively. [81]

1.3.4. Fluorescent Probes Targeting the Golgi apparatus:

Golgi apparatus plays a crucial role in protein labeling and transportation; it mediates the intracellular transport and storage of metal ions *[82]*. Tsien research group *[83]* developed fluorescent turn "On" probe Zinpyr-1 **(14a, Scheme 1.14)**, which mostly localized in the Golgi apparatus or Golgi-apparatus associated vesicles. In 2015, Kim and co-workers reported a two-photon fluorescent probe SZnC **(14b, Scheme 1.14)** for Zn^{2+} and specifically localized in Golgi-apparatus *[84]*. This probe can be employed to monitor zinc ions fluctuations in real time.

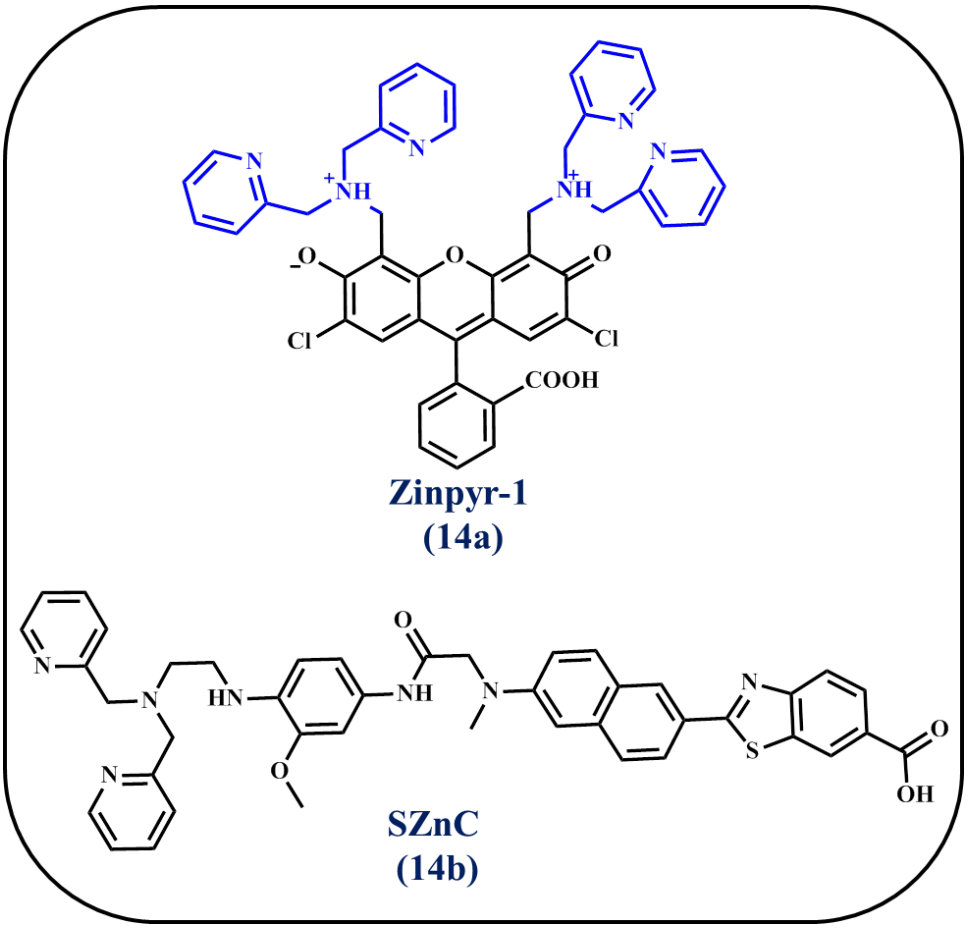

Scheme 1.14. Golgi-apparatus targeting fluorescent turn "On" probes for Zn^{2+} ions.

1.3.5. Challenges of Fluorescent Probes for Targeting the ER/Golgi Apparatus:

Although a few probes/trackers have been developed that can target the ER and Golgi apparatus and the certain rules these probes follow have been summarized but the molecular mechanism of localization remains unclear. For the design of reliable and reproducible ER/Golgi apparatus-targeting agents more studies are required.

In general, for the development of any organelle-targeting luminescent probe, a targeting moiety that is specific to the particular organelle plays a crucial role in driving the probe to its destination. In the case of the ER and Golgi apparatus, appending moieties of their respective known target agent, ER-Tracker Blue/White DPX and Golgi tracker red were not successful; partially because of these moieties lost their specificity when attached to other fluorophores.

1.4. Structure and function of mitochondria:

Mitochondria are the major sources of energy for all living eukaryotic cells *[85]*. Energy derived from the breakdown of carbohydrates and fatty acids which is converted to adenosine triphosphate (ATP) by process of oxidative phosphorylation. ATP acts as fuels for numerous cellular activities, including cell division, synthesis of biomolecules and metabolism *[86]*.

The mitochondrion consists of double-membrane, outer and inner, which are structurally and functionally distinct. The outer membrane is porous and permeable and an inner membrane is highly invaginated, folded into cristae in order to increase the membrane's surface area **(Figure 1.15)** *[87a]*. The chemical environment of inter-membrane space is similar to the cytoplasmic environment since the outer mitochondrion membrane is permeable to molecules smaller than 6 kD; which allows chemical exchange between the mitochondria and cytoplasm *[87b]* shown in **Figure 1.15**.

The inner membrane forms an effective barrier to even small molecules, ions and matrix is present inside the inner membrane where most of the mitochondrial activities take place. The inner membrane of mitochondrion consists of various proteins/enzymes, including oxidoreductases which carry out redox reactions and electron transfer, carrier proteins, and synthases for the biomolecules synthesis *[88]*. The oxidative phosphorylation process is performed inside the inner membrane and the proton pumped outward which induces a proton gradient results in a slightly basic environment inside the matrix. Furthermore, the movement of positive charges induces a membrane potential that is considerably larger than that of any other organelle membrane potential *[89]*.

The whole oxidative phosphorylation process along with ATP production is known as mitochondrial respiration *[90]* depicted in **Figure 1.15**. Various signaling molecules are required to coordinate the regular

functions of mitochondrial respiration including various metal ions (Zn^{2+}, Ca^{2+}, Cu^{+} and $Fe^{2+/3+}$) *[91]* as well as reactive oxygen/sulfur/ nitrogen species (ROS/RSS/RNS) *[92-93]*. Further to suppress the inevitable oxidative stress arising during respiration, there is a series of reducing mechanisms coordinated by thioredoxin (Trx) reductases and glutathione (GSH) reductases.

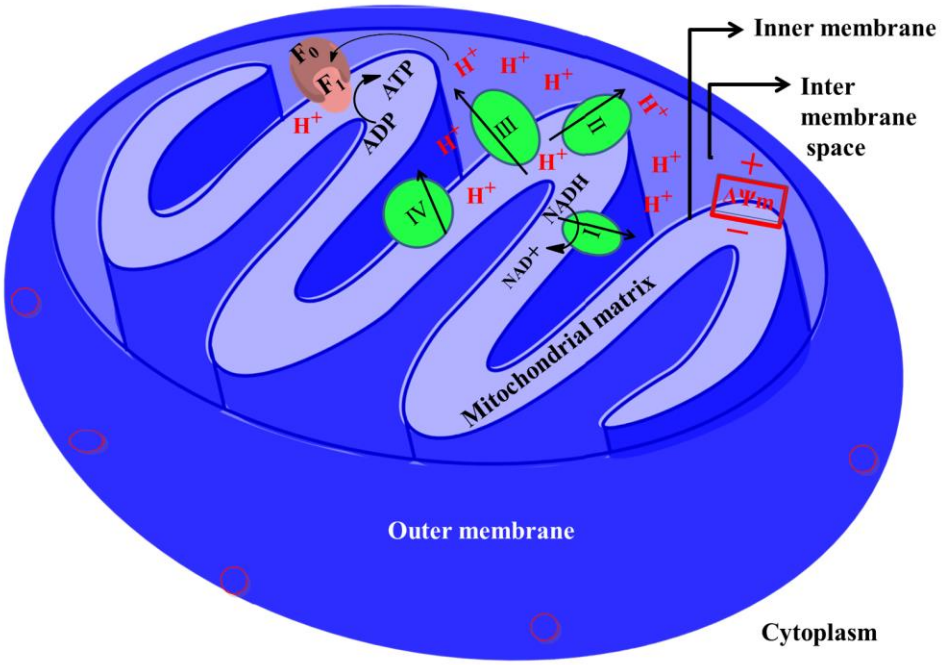

Figure 1.15. General components and biological processes within mitochondria.

1.4.1. The general methods to design mitochondria tracking probe:

During mitochondrial oxidative phosphorylation, proton pumping happened which results in strong negative membrane potential (108−158 mV) generated within the mitochondrial matrix *[94]*. Consequently, cations with strong lipophilicity have the capacity to transport across the phospholipid bilayer of the inner membrane and sequestered inside the matrix at a ratio of more than 10:1 as compared to other organelles, driven by the potential gradient of the membrane *[95]*. Most of the fluorescent probes bearing lipophilic cations gathered within the mitochondrial matrix of live cells, therefore various lipophilic cationic dyes, such as indole,

cyanine, and rhodamine display strong attraction to the mitochondria *[95-97]*.

Various MitoTracker series *[26b]* have been optimized and commercialized **(15a–15d, Scheme 1.15),** since they consist of lipophilic scaffolds and possess overall positive charge so that easily across the mitochondrial membrane of live cells. Their accumulation is dependent upon membrane mitochondrial potential.

There are many other fluorescent scaffolds such as fluorescein, BODIPY, coumarin, *etc*. are neutral in their original states. Even though these fluorophores reveal outstanding photo-physical properties but they didn't show a preference for mitochondria than other organelles. To address this issue, the neutral fluorescent probe can be modified by extension with a universal lipophilic cationic moiety.

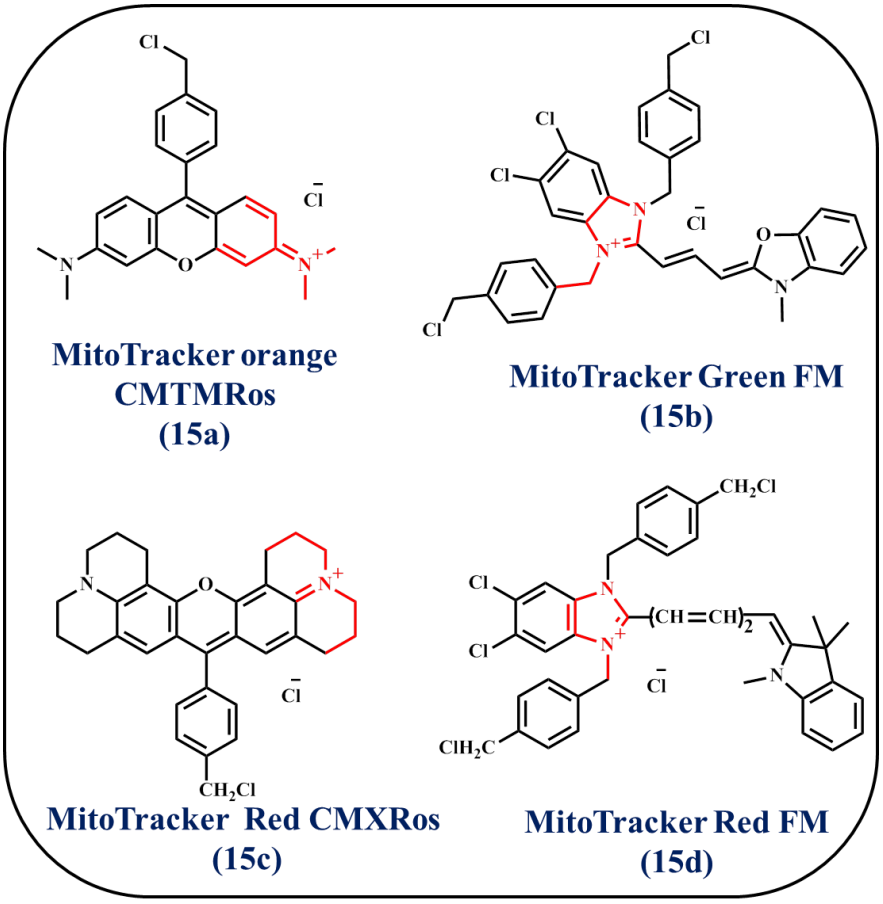

Scheme 1.15. Structures of commercially available MitoTrackers.

The Extension moiety can drive the probe selectively into the mitochondria **(16a–16c, Scheme 1.16).** Some potent mitochondria-targeting agents have been reported which includes triphenylphosphonium (TPP) *[89]*, MKT-077derivatives *[98]* and Flupirtine derivatives *[99]*. TPP is an organic cationic salt (positive charge on the phosphonium ion surrounded by three lipophilic phenyl groups) which was initially used to deliver drugs to mitochondria. Later large a number of mitochondria staining probes have been developed by the incorporation of TPP into fluorophores; TPP rapidly crosses mitochondrial membranes and enriches several folds within the mitochondrial matrix *[89]*. However, mitochondrial membrane potential affected by the positive charge on TPP which subsequently causes membrane rupture and disruption of the microenvironment *[100]*. Therefore, the mitochondrial-targeting strategy needs to further optimization.

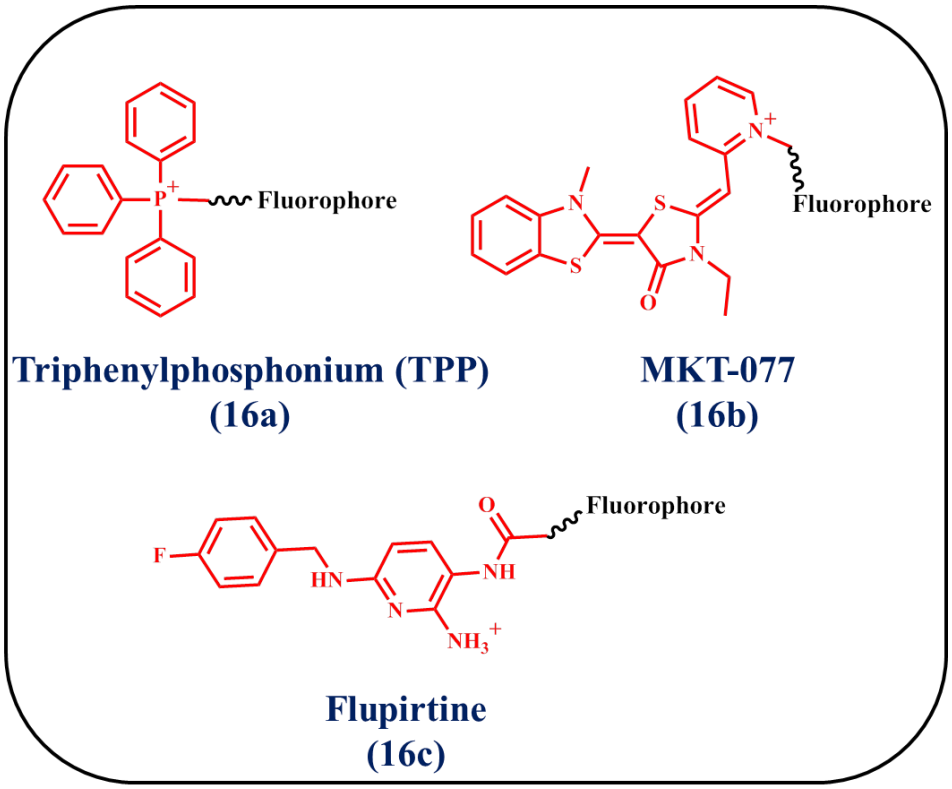

Scheme 1.16. Design of the mitochondria-targeting fluorescent probes based on anchoring groups.

In addition to the lipophilic cationic vectors, there are some natural and synthetic peptides have been developed to display mitochondria-targeting ability. For example, by exploiting the mitochondrial import machinery, positively charged signal peptides (amphipathic α-helix at the N-terminus) will be able to recognize the translocase present in mitochondrial inner membrane, thus allowing the easy delivery of cargo molecules, most commonly fluorescent proteins into the mitochondrial matrix *[101]*. From the natural system, researchers get encouraged and have refined the long-chain polypeptides; to obtain the functioning moieties, most of which are cationic amino acids incorporated either (e.g. lysine, arginine) or hydrophobic moiety (e.g. cyclohexylalanine, phenylalanine). In Arginine based functional peptides **(17, Scheme 1.17)** there are several positive charges are balanced by the long amphiphilic chain of amino acids; hence, warrants both to cross the phospholipid bilayer (lipophilicity) as well as biocompatibility *[30, 102-103]*.

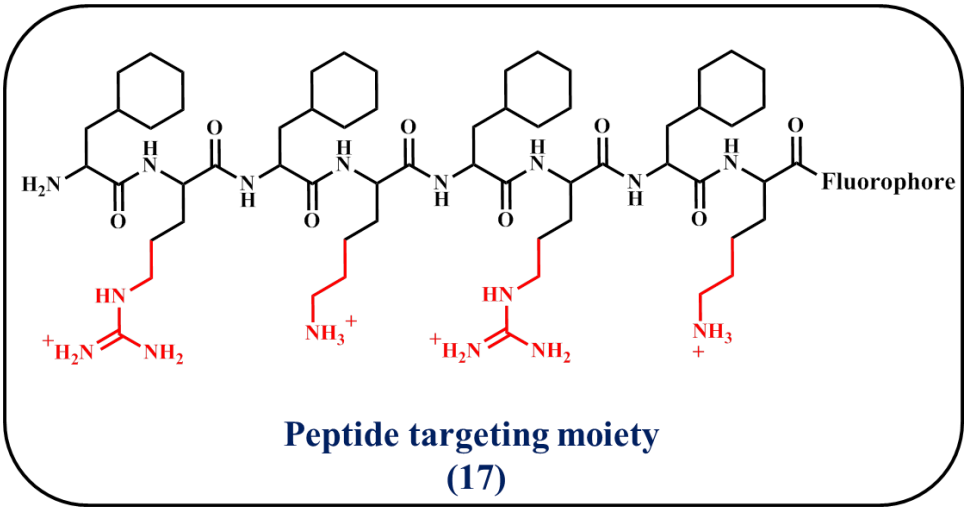

Scheme 1.17. Representative structure of a synthetic mitochondria-penetrating peptide.

1.4.2. Challenges for mitochondria tracking probes

(i) Even though lipophilic cationic dyes can stain mitochondria; however, once the mitochondrial membrane potential lost during cell apoptosis, or due to drug treatment cationic probes washed out of the organelle *[104, 26b]*.

(ii) There are numerous analytes present within the mitochondria; most of analytes exist in nanomolar concentration. Hence the sensitivity of mitochondria targeting probes needs to be significantly improved *[105]*.

1.5. Structure and function of nucleus

The nucleus is considered as the heart of cell and found in all eukaryotic cells. It contains hereditary material (DNA); controls transcription (RNA synthesis), protein expression, reproduction and cell growth *[106]*shown in **Figure 1.16**. It is enclosed by double-layer phospholipid bilayers membranes which separate the nuclear contents from the cytoplasm. The outer nucleus membrane is continuous with rough endoplasmic reticulum. The ribosomes synthesized in the nucleus are transported to the ER, where they carried out protein synthesis. Both outer and inner membranes of nucleus are joined at nuclear pores which consist of several proteins/enzymes known as nucleoporins. Nuclear pores regulate the passage of materials between the nucleus and cytoplasm. It allows free passage of water-soluble small molecules, such as H_2O_2, calcium and other signaling molecules. However, large biomolecules, such as proteins, nucleic acids, and ribosomes require energy dependent transporters to cross the nuclear membrane *[106]*. The importins transporters facilitate the import of biomolecules from cytoplasm, while exportins allow export of biomolecules out of nucleus **(Figure 1.16)**.

The nuclear membrane also surrounds the nucleolus including genetic information. The nucleolus is composed of proteins and RNA and produces ribosomes to be transferred to the ER for the synthesis of

proteins. In contrast, during cell division, various DNA chains became compact and form chromosomes which mixed and recombine in order to ensure genetic diversity **(Figure 1.16)**.

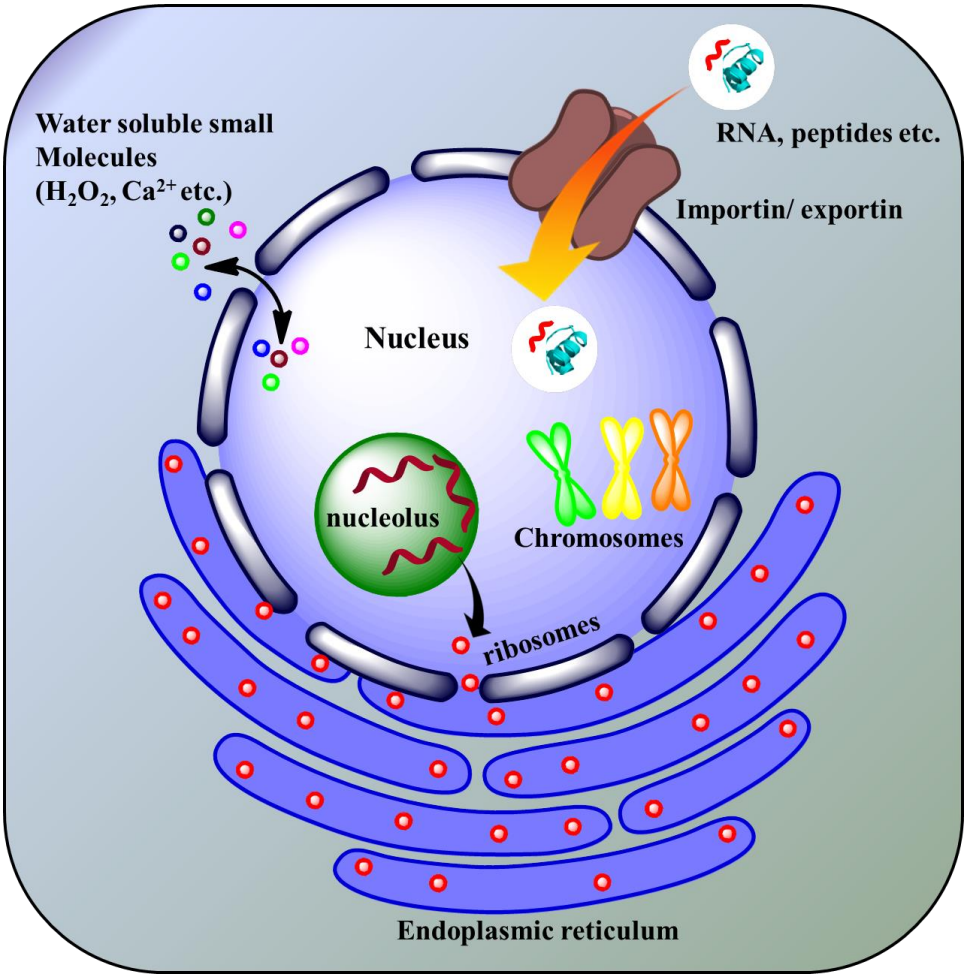

Figure 1.16. General components and biological processes within the nucleus.

1.5.1. The general methods to design nucleus tracking probe:

Interruption of the genetic materials leads to cell death or even the progression of cancer. There is greater demand to visualize and understand the functions of the nucleus. This has triggered immense curiosity in the development of nucleus targeting fluorescent probes. Phosphate groups present in the DNA backbone carry negatively-charged oxygen molecules which giving overall negative charge to the phosphate-sugar backbone

of DNA **(Figure 1.17)**. Therefore, the cationic dyes can bind to negatively charged DNA driven by electrostatic forces; several nucleus imaging probes have been designed and developed accordingly *[107]*.

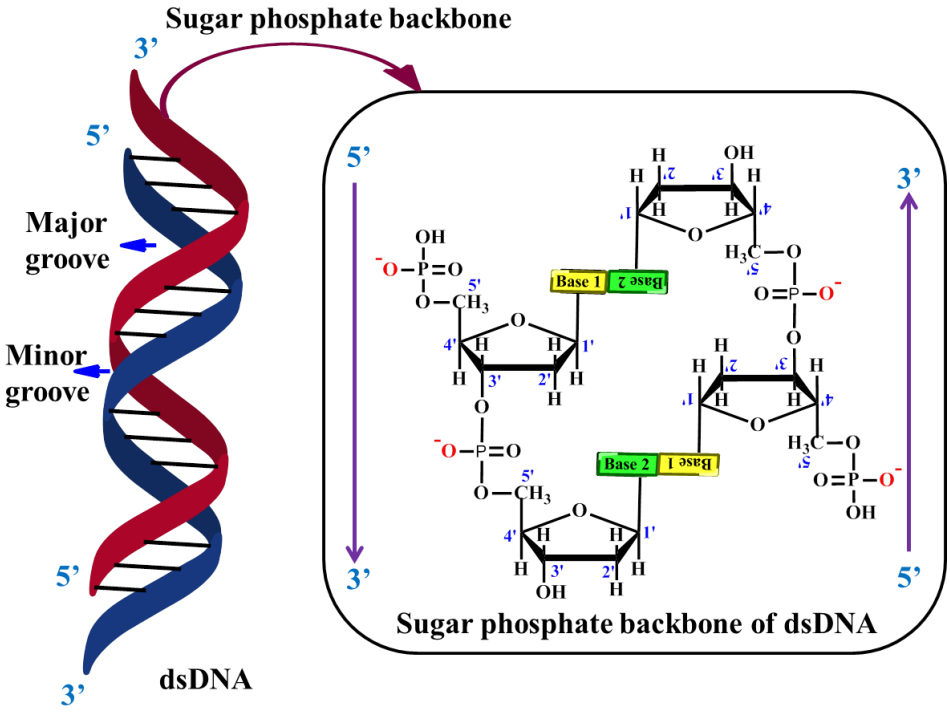

Figure 1.17. Structure of double stranded DNA and negatively charged sugar phosphate of DNA.

Commercially available nucleus staining dye such as DAPI and Hoechst 33342 **(18a and 18b, Scheme 1.18)**, are presumed to bind in the minor groove of the double-stranded DNA. Common features of nucleus targeting probes include short hydrophobic chains, cationic characters, and a planar aromatic system. This results in their weak interaction with lipids and proteins, hence allowing their uninterrupted movement into nuclei of cells *[107-108]*. Further short peptide chains are known as nuclear localization signals (NLS) which have strong interaction with importins transporter, developed as potent nucleus-anchoring motifs. The vehicles bearing NLS bind with importins and actively transported into the nucleus *[109]*.

Several fluorescent probes for dsDNA have been reported till date. However, very few probes with negligible toxicity and many of them do not permeate into the nucleus of live cells *[110-111]*.

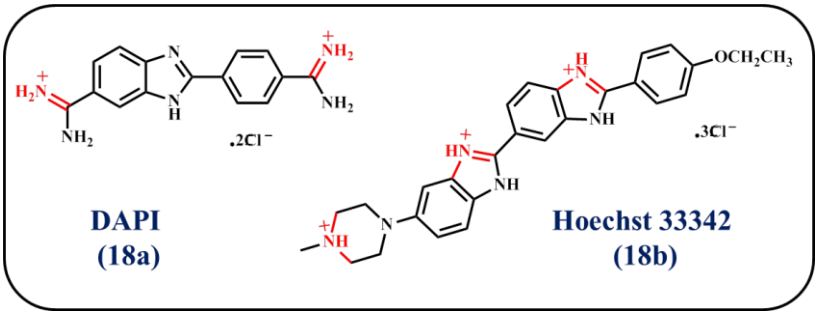

Scheme 1.18. Structures of commercial available nucleus staining dyes DAPI and Hoechst 33342

In 2009, Chang *et al. [112]* reported a green fluorescent probe **C61 (19a, Scheme 1.19)** to detect nuclear dsDNA in both live and fixed cells. Fluorescence intensity enhancement occurs upon binding of C61with dsDNA. Although the excitation and emission maxima wavelengths are still relatively short ($\lambda_{ex}/\lambda_{em}$ = 425/540 nm). In 2011, Peng research group *[113]* reported the thiazole orange (TO-3) analog DEAB-TO-3 as a red fluorescent probe **(19b, Scheme 1.19**, $\lambda_{ex}/\lambda_{em}$ = 626/649 nm) with a (diethylamino)butyl substituent group for DNA staining of live cells. This probe revealed fluorescence enhancement (97.3-fold) upon binding in the groove of native DNA but in case of RNA, it shows 6 fold difference and with BSA negligible response.

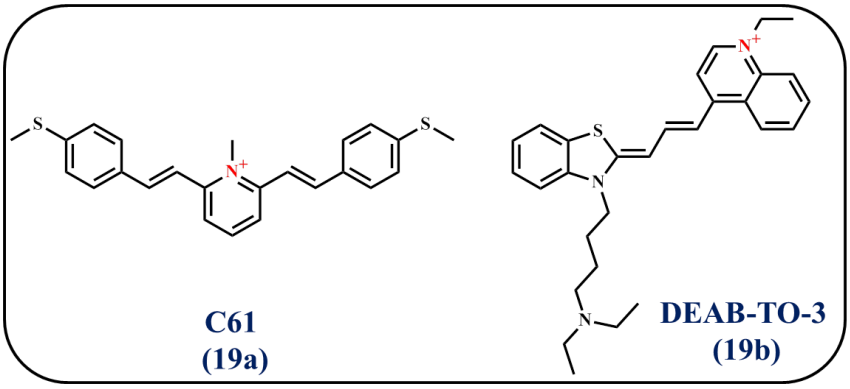

Scheme 1.19. Structures of nucleus targeting probe for ds-DNA.

1.5.2. Nucleolus targeting probes:

Wong research group in 2015, developed two-photon probe MPI **(20a, Scheme 1.20),** by employing an indole-based positively charged cyanine which is highly selective for the ribosomal RNA (rRNA) imaging in the nucleolus of live cells *[114]*. Due to its small size and relative hydrophilicity allows it to penetrate deeply into the nucleus and the positive charge enables its interaction with the RNA chain. In the same year, Chow *et al*. *[115]* designed and developed a new RNA-selective fluorescent probe Styryl-TO **(20b, Scheme1.20)** by integrating thiazole orange and a p-(methylthio)styryl moiety for nucleolus RNA staining in live cells.

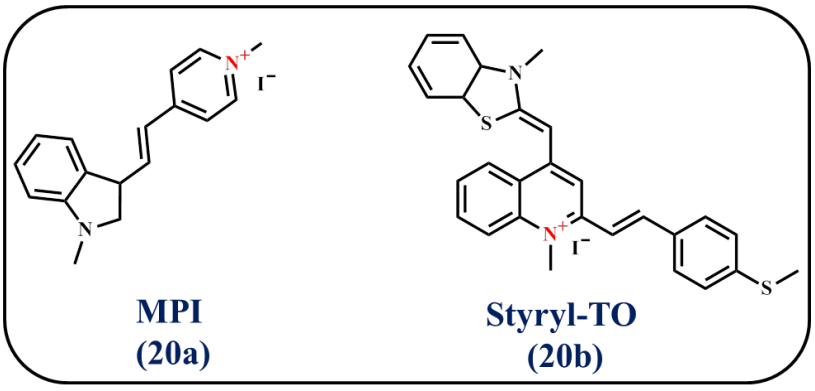

Scheme 1.20. Structure of a fluorescent probes for staining nucleolus rRNA in live cells.

1.5.3. Challenges for nucleus targeting probe:

The selectivity of nucleus targeting probes is controlled by their competitive sequestration within the nucleus as compared to any other cellular organelles. There are several reports indicated that even minute changes in the structures of nucleus targeting dye could completely eliminate their selectivity, consequently further complicating the situation *[116-117]*.

1.6. Photo-induced electron transfer (PET) mechanism of sensor:

Electron transfer reactions play a significant role both in chemistry and biology. An electron transfer reaction involves the transfer of an electron from a 'donor' to an 'acceptor'. Electron transfer reaction can occur photochemically known as photoinduced electron transfer (PET) reactions. PET-based sensors are usually consisting of a fluorophore which connected *via* a spacer to a receptor group which carries at least one non-bonding electron pair *[118]* depicted in **Figure 1.18**.

In the excitation state of the fluorophore, an electron goes from to highest occupied molecular orbital (HOMO) to lowest unoccupied molecular orbital (LUMO) followed by charge recombination and get back to the ground state with the release of a large amount of energy as fluorescence emission. However, if the HOMO orbital of another part of fluorophores i.e receptor lies between the HOMO and LUMO levels of the excited fluorophore, then there is electron from the HOMO orbital of receptor transfer to the half occupied HOMO of the excited fluorophore, consequently non-radiative decay process occurs which leads to fluorescence quenching (**Scheme 1.21a**). On the other hand, in the bound state with an analyte, the PET process is arrested by the arrival of the analyte at the receptor site. The arrest can be easily seen by considering H^+ as the analyte. In this case, the energy of HOMO of the receptor is less than the HOMO and LUMO levels of the excited fluorophore, due to an increase in the redox potentials (**Scheme 1.21b**). This process restricts the electron transfer and enables the fluorescence from the fluorophore *[118]*.

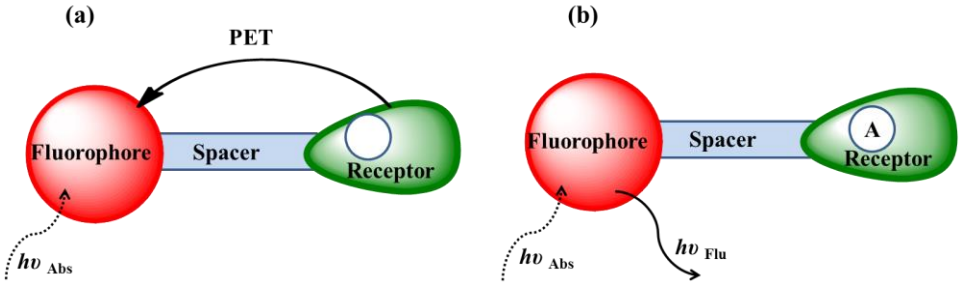

Figure 1.18. (a) An electron transfer from the analyte-free receptor to the photo-excited fluorophore resulting fluorescence 'off' state of sensor. **(b)** The electron transfer from the analyte-bound receptor is blocked causing the fluorescence 'on' state of the sensor.

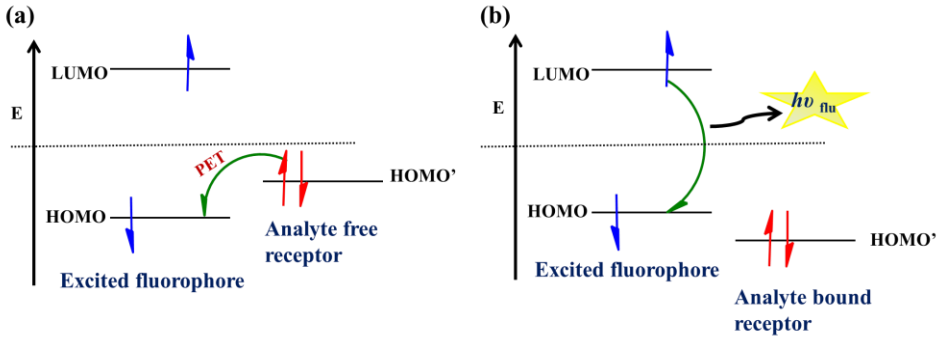

Scheme 1.21. Molecular orbital energy diagrams of PET process **(a)** the analyte-free situation and **(b)** the analyte-bound situation.

1.7. Type of reactions and mechanisms:

There are various types of reaction used for the synthesized of biologically active compounds, some of them described below.

1.7.1. Schiff base reaction:

Schiff base named after Hugo Schiff. It is a subclass of imines and its general structure R2C=NR' (R'≠H). Schiff base ligand can be synthesized by the condensation reaction of an aldehyde or ketone with a primary amine *[119]* shown in **scheme 1.22**.

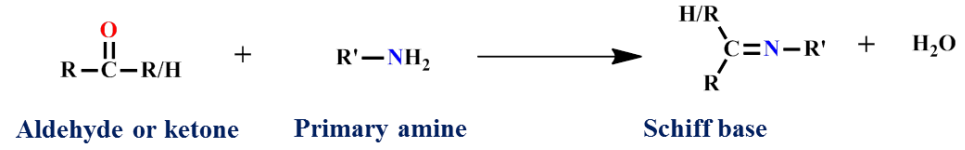

Scheme 1.22. Schiff base synthesized by the condensation reaction.

R denotes an alkyl or an aryl group **(scheme 1.22)**. Aryl substituents Schiff bases are comparatively more stable and readily synthesized than alkyl substituents Schiff bases due to effective conjugation.

The Schiff base formation mechanism is based on the theme of nucleophilic addition to the carbonyl group. Here amine acts as a nucleophile. Amine reacts with the aldehyde or ketone, form an unstable intermediate compound known as hemiaminal (or carbinolamine) followed by dehydration to generate an imine. The reaction catalyzed by acid or base **(scheme 1.23)**. Since the hemiaminal is an alcohol, it undergoes acid catalyzed dehydration *[119]*.

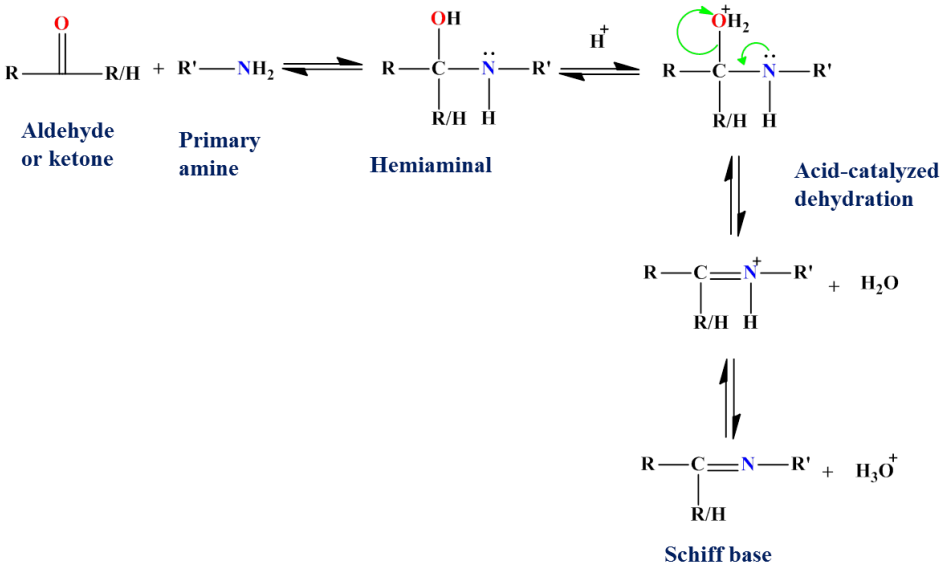

Scheme 1.23. Schiff base formation general mechanism.

Moreover, reaction of carbonyl (aldehyde/ ketone) with hydrazine gives a hydrazone ($R_1HC{=}NNH_2$ or $R_1R_2C{=}NNH_2$). Hydrazine is more

nucleophilic than a regular amine due to a presence of the adjacent nitrogen **(Scheme 1.24)**.

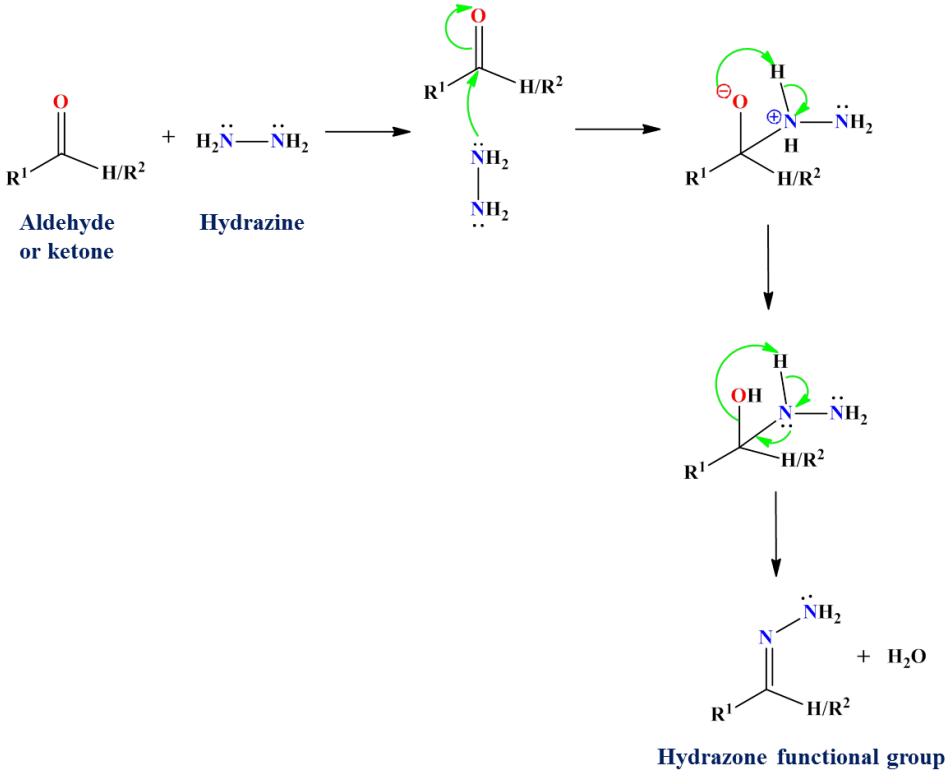

Scheme 1.24. Hydrazone formation general mechanism.

Nowadays, there is growing interest in developing new drugs which is based on the aroyl-hydrazone skeleton, Ar–CH=N–NH–C(=O)–Ar′ (Ar = aromatic ring) *[120-121]*. Basically hydrazones are organic ligands consisting of –NH–N=CH– group. Addition donor site like C=O increase the flexibility and versatility of compound; enhance their biological properties for therapeutic application *[121]*.

Schiff bases are used as catalysts, pigments and dyes, and as polymer stabilizers. They exhibit extensive biological activities, comprising antiviral, antibacterial, antifungal, anti-proliferative, antimalarial, antipyretic and anti-inflammatory properties. The imine group present in Schiff bases is critical for their various biological activities *[122]*.

1.7.2. Click reaction:

Huisgen discovered Click chemistry. Click reaction is the Huisgen copper-catalyzed coupling reaction of terminal azide with terminal alkyne to form a 5-membered 1,2,3-triazole unit *[123-124]* shown in **Scheme 1.25**. Click reaction mostly used in the polymer chemistry. Click reaction occurs in virtually any solvent, including aqueous solvent systems and provide high yield end product. This reaction is highly specific and very efficiently occurs in any solvent, including aqueous solvent. It generates negligible and harmless by-products, and highly thermodynamic energy which drives reaction irreversibly to high yield of a single reaction product *[123]*.

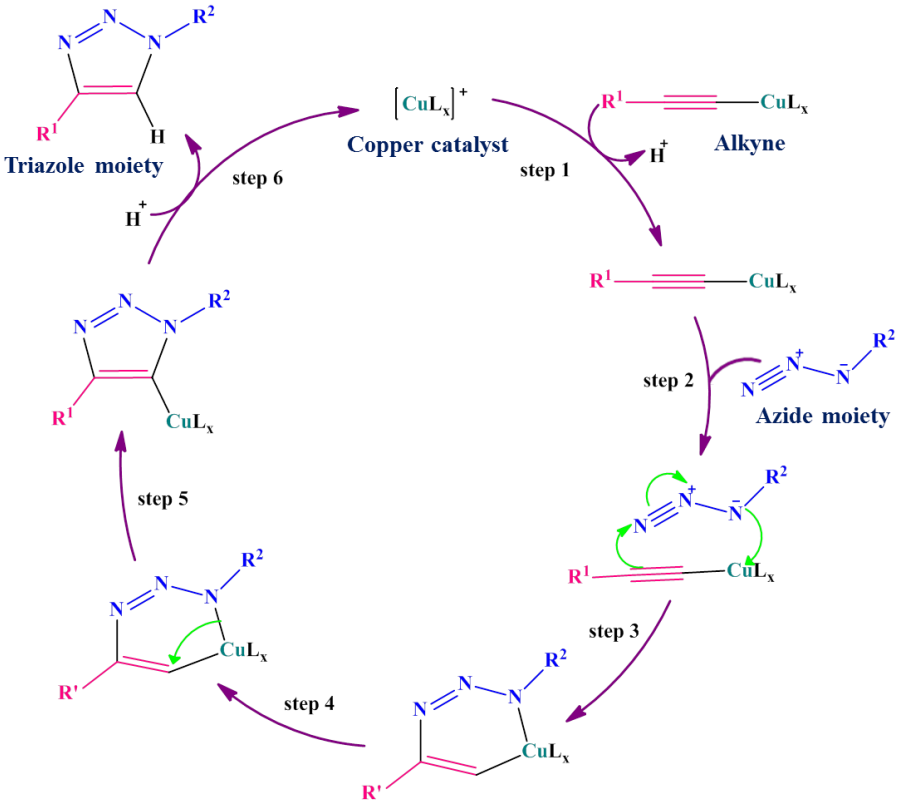

Scheme 1.25. Copper-catalyzed click reaction (Hüisgen cyclization of azide and alkyne to form a 5-membered triazole ring)

Nowadays, click reactions very efficiently used in joining a biomolecule and a reporter molecule. Unnatural amino acids containing

reactive groups incorporated to the proteins by using this novel reaction and also used in the modification of nucleotides. Click reaction further used in the various biomimetic applications and pharmacological drug design *[125]*.

1.7.2.1. Transition metal carbene-complex:

Recently, mesoionic carbene (MIC) ligand moiety is more focus in metal complexes as alternative of N-heterocyclic carbene (NHC), which is widely developed and utilized for functional materials and bioactivity. One of the most fascinating features of MIC is that strong dipole moment in its five membered rings exists in the resonance as compared with the NHC *[124]* depicted in **scheme 1.26.**

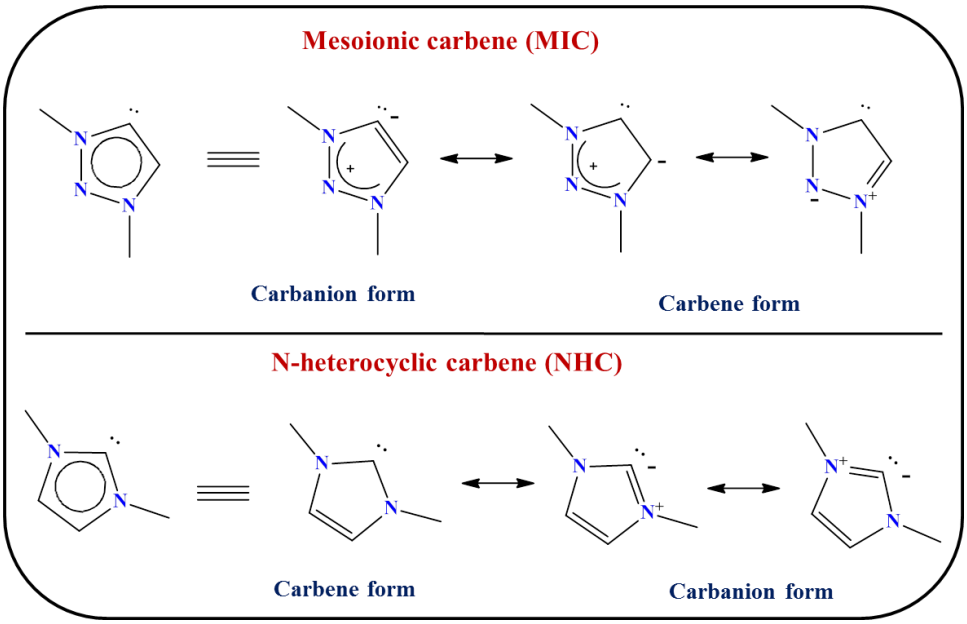

Scheme 1.26. Resonance structure of mesoionic carbene (MIC) and N-hetrocyclic carbine (NHC)

The highly polarized carbon atom of nitrogen-rich triazole allowing the complexation of anions by halogen and hydrogen bonding,

and in the case of the triazolium salts, *via* charge-assisted halogen and hydrogen bonds.

Moreover, the triazole moiety allows numerous N-coordination and by anionic, neutral, or cationic nitrogen donors. Also, CH-deprotonation of the triazole and the triazolium generate powerful carbanionic and mesoionic carbene donors, respectively for C-coordination *[124]* shown in **Scheme 1.27**.

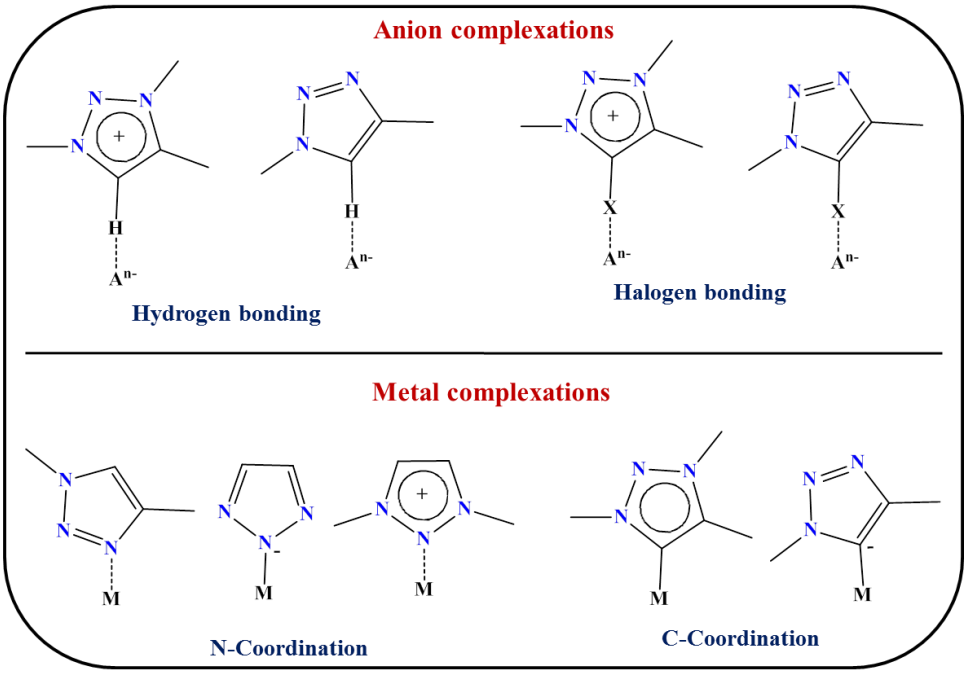

Scheme 1.27. Selected supramolecular interactions of 1,2,3-triazoles and their derivatives.

1.8. Molecular electronic transition and fluorescence

1.8.1. Molecular electronic transition of probe:

Molecular electronic transitions occur when the electrons of molecule are getting excited from lower energy level to a higher energy level. Electrons occupying a highest occupied molecular orbital (HOMO) of a sigma bond can excited and moved to the lowest unoccupied molecular orbital (LUMO) of sigma bond ($\sigma \rightarrow \sigma^*$ transition). Similarly an electron from a π-bonding orbital promoted to an antibonding π^* orbital ($\pi \rightarrow \pi^*$ transition). The loan pair of electron of auxochromes depicted as 'n' also transited to higher energy level like aromatic pi bond transitions *[126]* shown in **Figure 1.19.**

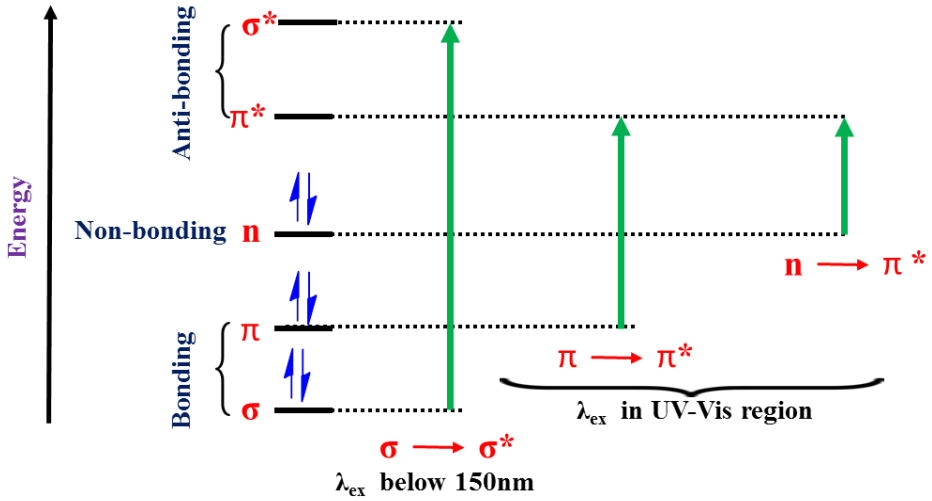

Figure 1.19. Representation of molecular electronic transitions state of electrons.

1.8.2. Principles of fluorescence:

When the fluorescent molecule in their ground state absorbs light energy (photons), which leads to alterations in the electronic, rotational and vibrational states of the molecule. The absorbed energy moves an electron to an excited state (away from the nucleus) within femtoseconds. Once the molecule gets excited several different pathways were used to eventually lose the absorbed energy and return back to their ground state

(Figure 1.20). During internal conversion, there is a transition between electron orbital states (such as S_2 to S_1) *[127]*. Internal conversions allow isoenergetic transitions, so no energy is lost during this transition. However, the extra energy is eventually shed through vibrational relaxation. In the vibrational relaxation process, the vibrational energy of the fluorophore is shifted to neighboring molecules *via* direct interactions. In aqueous medium, water is the probable energy recipient. Importantly, vibrational relaxation does not emit any photons. Both the Internal conversion as well as vibrational relaxation takes place in picoseconds and usually bring the molecule back to the lowest energy level of S_1. Finally, the molecule comes back to the ground state (S_1 to S_0) with the release of energy (fluorescence emission) *[127]*.

Another pathway of energy loss happens after intersystem crossing by the forbidden transition to the triplet state **(Figure 1.20)**. In some fluorophore, triplet state vibrational energy stages overlap with the lowest energy stage in S_1. This overlapping further favors intersystem crossing followed by internal conversion to the lowest energy level of T_1. The triplet state molecule does not easily come back to the singlet ground state (S_0), because this transition requires the triplet outer electron to again undergo a forbidden transition. Even though some triplet-state molecule reaches the ground state without the emission of any light, but in many cases, light emission occurred known as phosphorescence and it takes place within microseconds. If another photon is absorbed, triplet-triplet transitions can transfer the electron into higher triplet states, hence further delaying light emission. The triplet-state molecules can undergo photochemical reactions that lead to irreversible bleaching and phototoxicity *[127]*.

Some fluorophores are employed for the specific labeling of cellular structure and visualized with the help of fluorescence microscopy. These fluorophores are ideal for fluorescence microscopy since the energy

differences between excited state and ground state orbitals of fluorophores are small enough that comparatively low-energy photons of the visible region can be used to excite electrons from the ground state to excited states *[127].*. Generally, the higher number of conjugated bonds in the molecule, the lower excitation energy and longer wavelength of photon required (E=*hc*/λ).

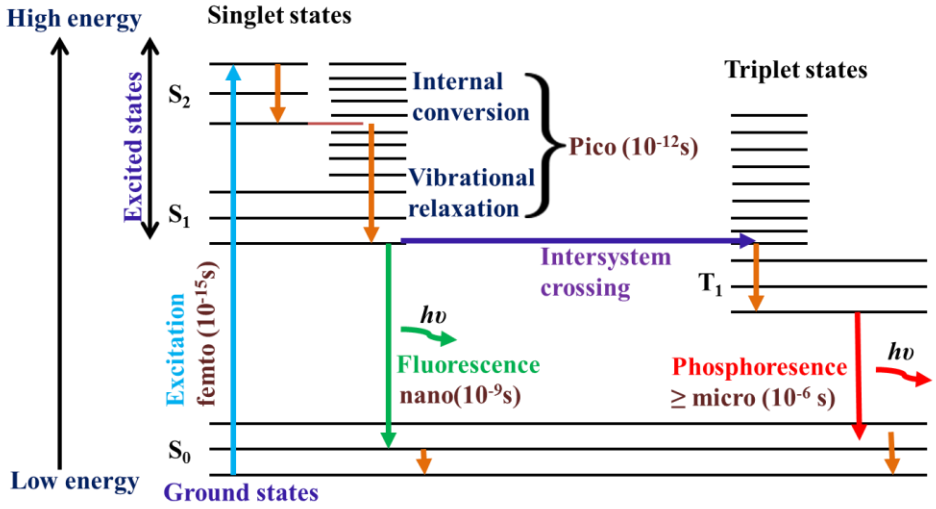

Figure 1.20. Jablonski diagram illustrates the energy states of a molecule and the times elapsed in various steps (excitation, fluorescence emission and phosphorescence).

1.8.3. One-photon and two-photon fluorescence study:

The time it takes a molecule to transition from the ground state to an excited state is extremely brief, on the order of femtoseconds. Whereas one photon of the appropriate energy typically causes this transition, it is also possible for multiple photons to add their energy to bring a molecule to the excited state. For example, if two photons with half the energy (that is, twice the wavelength) of that needed to reach the excited state imposes on a molecule at the same time (within a time interval less than 10^{-18} s) *[128]*, their energies can be added and excite molecule that termed as two-photon excitation **(Figure 1.21).**

Two-Photon Microscopy (TPM) is a powerful technique and superior over one-photon microscopy. (i) It retains all of the advantages of a one-photon (confocal) microscopy and prevents out of focus photobleaching and photodamage of the sample *[128]*. (ii) By using the same fluorophores and the sample, two-photon excitation can image more efficiently and six-fold deeper penetrated inside tissue sample than confocal microscopy. The excitation photons are not absorbed as they pass through the sample until they reach the focal spot *[129]*. (iii) Two-photon microscopy used infrared excitation wavelengths which are least absorbed by the sample and very little affected by the scattering phenomenon. Also, longer integration times or increased number of scans can be frequently used in a time-lapse experiment using Two-photon microscopy, without experiencing photobleaching or photodamage as generally did by UV excitation wavelength *[128]*.

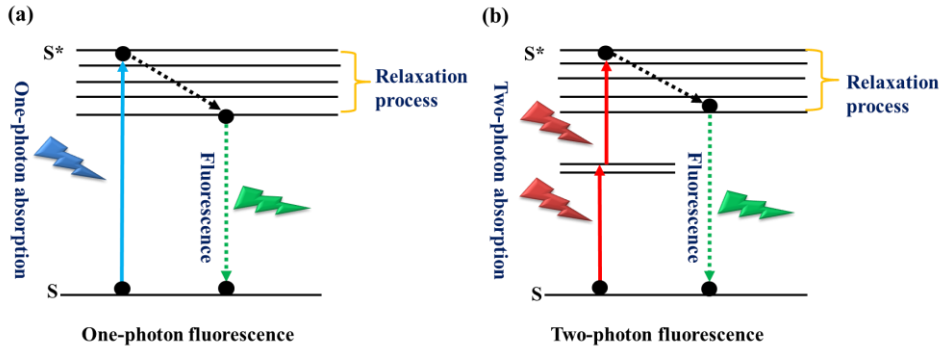

Figure 1.21. Jablonski diagram displaying one-photon vs. two-photon excitation of a molecule, and the subsequent fluorescence emission.

1.9. Computational studies on organic ligands:

The theoretical study was performed employing efficient computer programs to calculate the structures and properties of molecule, interaction of synthetic compound with biomolecules such as protein, DNA *etc*.

1.9.1. Molecular docking:

Molecular docking is a computational (*in silico)* technique which can predict the preferable orientation of one molecule to another when bound together to form stable complex. The association of biopolymers (protein, DNA and RNA) with small molecules plays an important role in signal transduction. Therefore the relative orientation of two interacting partners may affect strength and type of signal production. Molecular docking is convenient for predicting both strength as well as type signal produces. It is very promising platform in structural molecular biology and computer-based rational drug design. The docking results provide binding conformation of ligand with appropriate target and provide 3D structure of biopolymers with the associated target ligand **(Scheme 1.28)**. It enhanced our understanding in term of binding affinity as well as mode of interactions of protein or nucleic acid with ligands *[130]*.

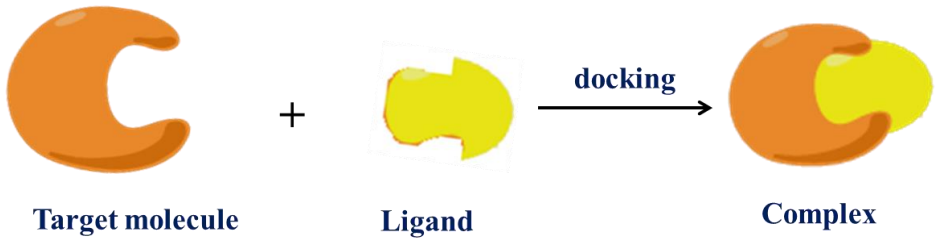

Scheme 1.28. Molecular docking of ligand with target molecule.

Molecular docking is an attractive platform to understand the drug-DNA/protein interactions to analysis the exact binding sites in three dimensional structures. Mostly non-covalent interactions prevalent in docking study, which include H-bonding, electrostatic, hydrophobic, Van

der Waals interactions, *etc*. Docking plays a crucial role in the recognition of active binding site in nucleic acid/protein novel therapeutic drugs. Arif *et al. [131]* performed molecular docking studies of phthalimide derivative **1 (Figure 1.22)** with duplex DNA having sequence d(CGCGAATTCGCG)$_2$. The minimum energy conformation is most energetically favorable and the docked structures are represented in **Figure 1.23**. Docking results revealed compound **1** best binding in the minor groove of DNA.

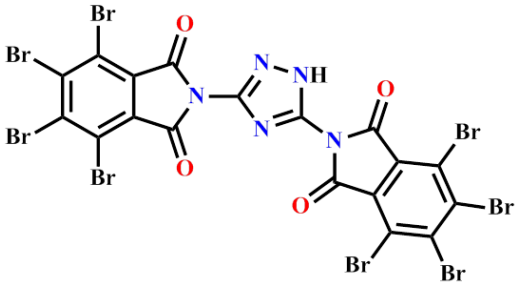

Figure 1.22. structure of compound **1**.

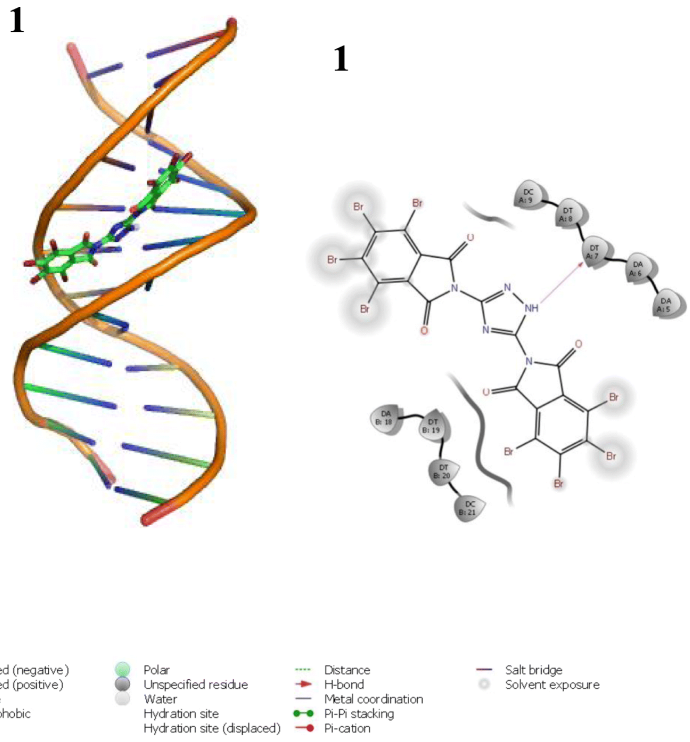

Figure 1.23. Molecular docking of the phthalimide derivative 1 with DNA. [131]

Studies based on binding of ligands with proteins are nowadays becoming ever more significant for the interpretation of transport and metabolism processes. Dandawate *et al*. *[132]* performed molecular docking studies of plumbagin **1 (22a, scheme 1.29)** and plumbagin hydrazides compounds **2-4**, **(22b-22e, scheme 1.29)** into the active site of p50 subunit of NF-κB protein.

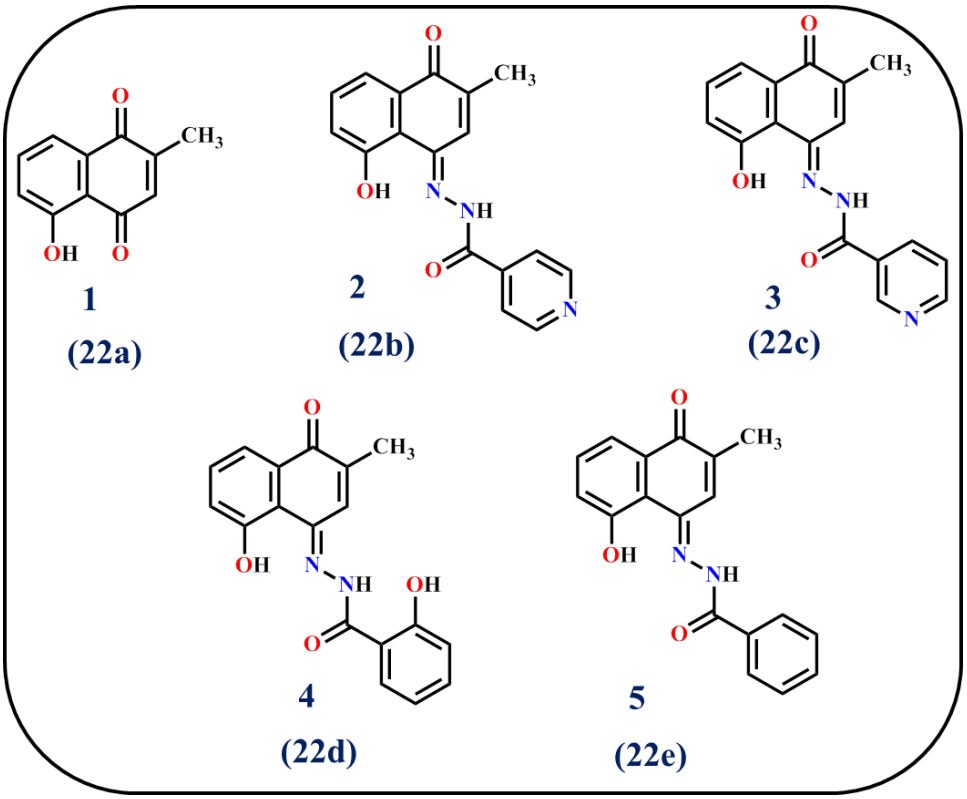

Scheme 1.29. Structure of plumbagin (**1**) and plumbagin hydrazides (**2**–**5**)

The molecular docking result confirms that hydrazide substitution allowing additional hydrogen bonding interactions with NF-κB protein. The binding energies of **1-5** compounds are in the range of 7.43-7.88 kcal/mol. The hydrazide substitution compounds have higher binding energy than the parent plumbagin compound. This indicate that the tight binding in the active site of p50-subunit of NF-kB protein promoted through H-bonding interaction with Gly66 (1.784 Å), Gly66 (1.832 Å),

His64 (2.191 Å) residues, respectively **(Figure 1.24).** These compounds bind in the active site of NF-κB and inhibit its expression which may be further responsible for the enhanced anti-proliferative activity *[132]*.

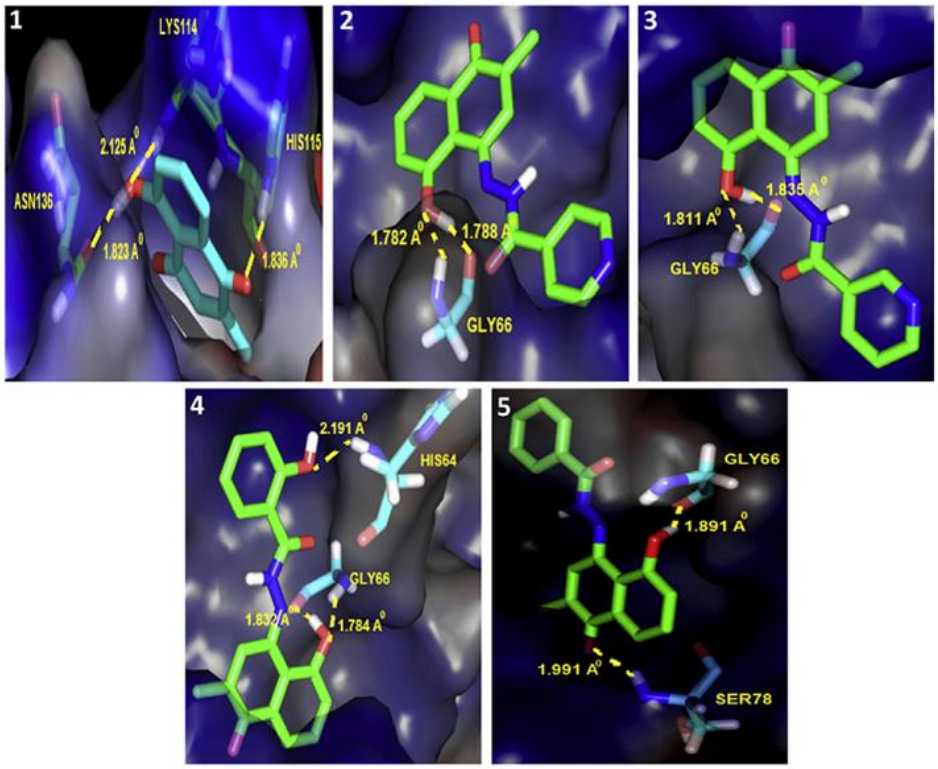

Figure 1.24. Molecular docking of plumbagin (**1**) and plumbagin hydrazides (**2-5**) into the active site of p50 subunit of NF-kB protein. [132]

1.9.2. Density functional theory (DFT):

Electronic structure calculations play an important role in the deep understanding of chemical structure and reactivity. Density functional theory (DFT) is a very popular and versatile computational quantum mechanical modeling technique used in the calculation of the electronic structure. DFT requires the calculation of the total electron density and technically does not need a wave function. However, in practical, DFT commonly uses electron density to calculate some parts of the energy and the wave function to calculate other parts of the energy. The normalized wave function and total electron density can be

interrelated *[133]*. The electronic properties of a many-electron system can be determined by using functionals (functions of another function); in this case, the spatially dependent electron density. Therefore, the name density functional theory comes from the use of functionals of the electron density.

According to the frontier molecular orbital theory, the energy of HOMO (measures the electron donating character of a compound) and LUMO (measures its electron accepting character) orbital levels are very significant factors that affected bioactivity and play a vital role in various pharmacological processes *[134]*. The frontier orbital energy can also provide some valuable information for the active mechanism. Nowadays, DFT calculation is most extensively used due to its accuracy and less time consumption *[135]*.

In 2019, Ying Cui *et al*. *[136]* reported 2-thiazolyl-hydrazone derivatives showing *in vitro* neuraminidase inhibitory activity against influenza virus H1N1. They performed DFT calculation of **2g (23a, Scheme 1.30**) and compared their electronic structure as well as energy with Oseltamivir (**23b, 23c, Scheme 1.30**), which is medically approved drug for controlling influenza diseases.

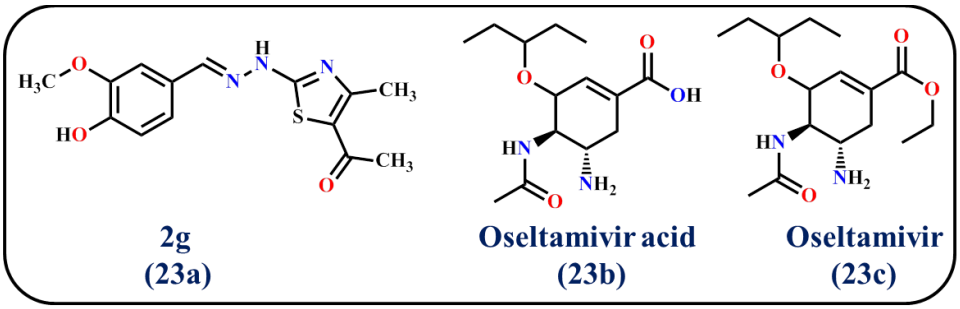

Scheme 1.30. Structure of 2-thiazolyl-hydrazone derivative (2g) and Oseltamivir (anti-influenza drug.)

The HOMO orbital of compound **2g** is distributed at the carbonyl group whereas the LUMO orbital is mostly concentrated at the nitrogen atom of the thiazole ring and the carbon atom between the sulfur atom and

the nitrogen atom. HOMO orbitals oseltamivir acid or oseltamivir are distributed at the acetamide bond, particularly at the carbonyl group of the acetamide bond whereas their LUMO orbitals mostly concentrated at the carbonyl group of the carboxyl or ester group respectively **(figure 1.25).** The energy-level difference (ΔE) of 2g is much closer to that of oseltamivir acid and oseltamivir *[136]*.

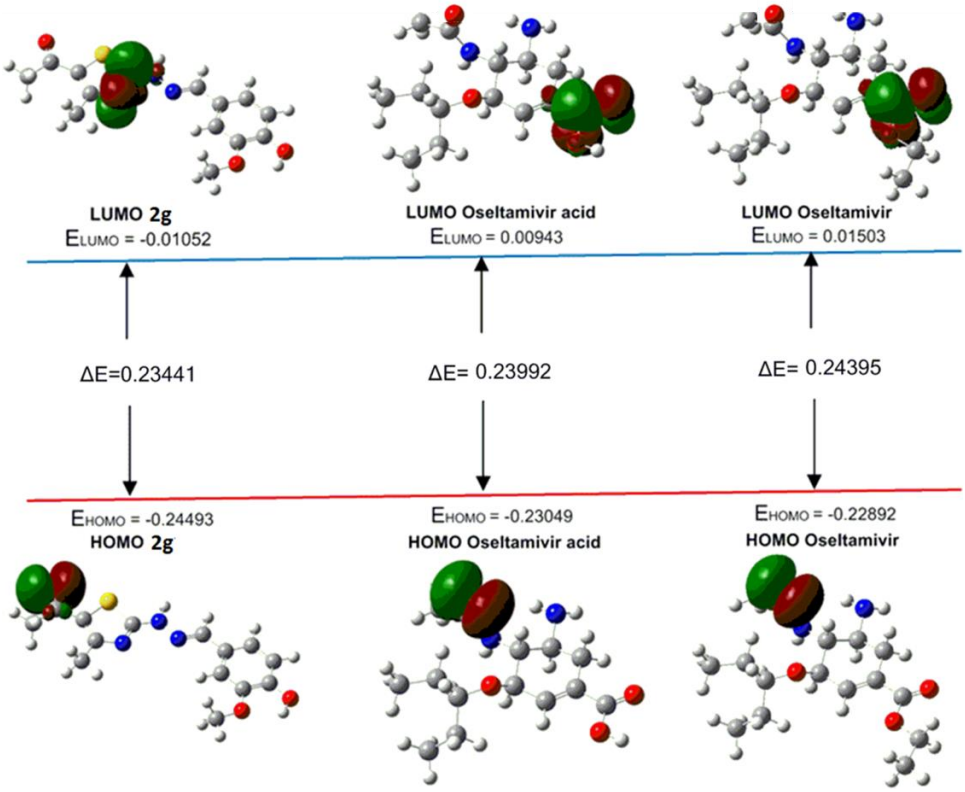

Figure 1.25. Frontier molecular orbital energy level and distribution in compound 2g, Oseltamivir acid, and Oseltamivir. . [136]

The HOMO orbital distribution of compound **2g** and oseltamivir acid is almost identical on the structure of carbonyl. Moreover, the direction of electron transfer's pattern in compound **2g** and oseltamivir acid from the HOMO to the LOMO orbit is also agreement. The electron-withdrawing groups on the benzene ring are more helpful to electron transfer, which shows a similar effect of the oseltamivir carboxyl group

(Figure 1.26). Thus, to some extent, the DFT calculation can explain the reason behind why the target compounds have anti-influenza activities *[136]*.

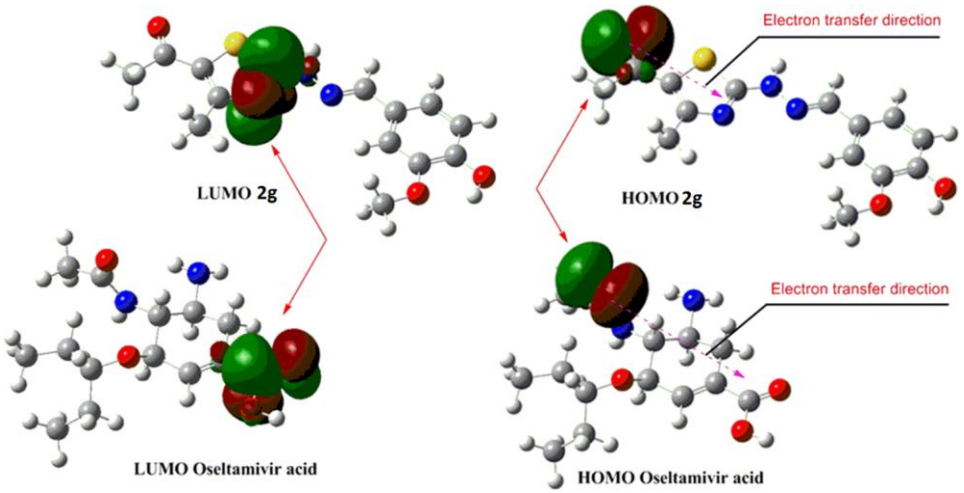

Figure 1.26. Comparison of the frontier orbital distribution and the direction of electron transfer of compound 2g and oseltamivir acid. [136]

1.10. Flexible organic crystals:

The use of multi-talented materials has been of great interest to the researchers considering the vast array of potential applications and good economic viability.

Conversion of energy into motion is a well-known process in nature. Dynamic molecule crystals which can jump, twist, burst and curl are efficient macro/micro/nanoenergy-based transducer of light to kinetic energy of mechanical motion. Ordered molecular crystals that bend, twist, or coil like soft materials such as polymers, elastomers are unusual crystals *[137]*. Multifunctional materials have wide application and economic viability. Either plastic or elastic deformation of an organic crystal can happened *[138]*. Upon the application of mechanical stress plastic material undergoes irreversible permanent distortion; while elastic materials undergo reversible distortion. Recently, Alimi *et al. [138]*

reported hand twisted 4-bromobenzonitrile crystals revealed highly flexible plastic bending characteristic.

The plasticity and elasticity of the crystals based on the following building blocks: vanillin derivatives, Schiff bases, polyhalogenated N-benzylideneanilines, pyrimidine, naphthalene diimide derivatives, organic co-crystals, ester spacer based molecules, and azine based molecules *[139-141]*. In 2015, Ghosh *et al. [142]* reported a series of polyhalogenated N-Benzylideneanilines based elastic organic crystals. Crystal structure analysis of compounds EC1-EC7 demostrated that they are closely related to each other and polymorphism was not observed in any of the crystals (**Scheme 1.31**).

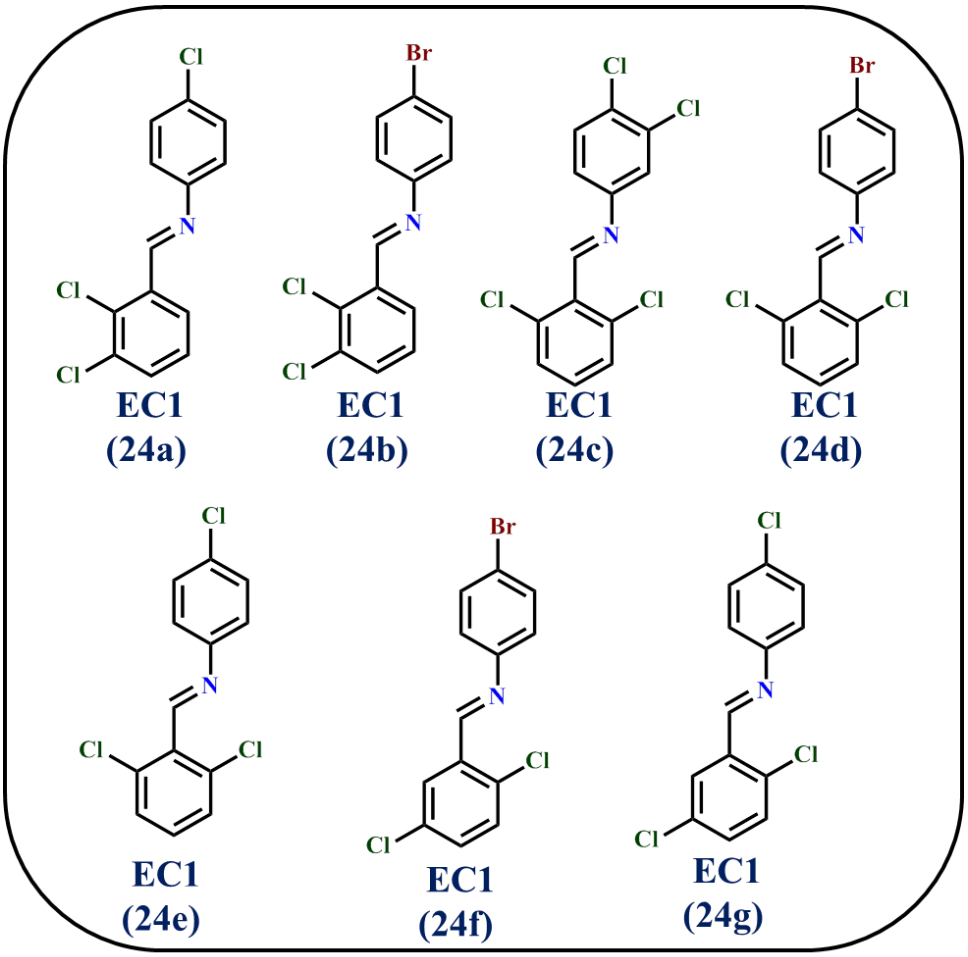

Scheme 1.31. Structure of organic compounds, which give elastic bendable crystals.

Anoop et al. *[140]* developed azine based (H_3L) elastic bending crystal in solid state and Al^{3+} sensing studies (Fluorescence turn "On") in solution state **(Figure 1.27).**

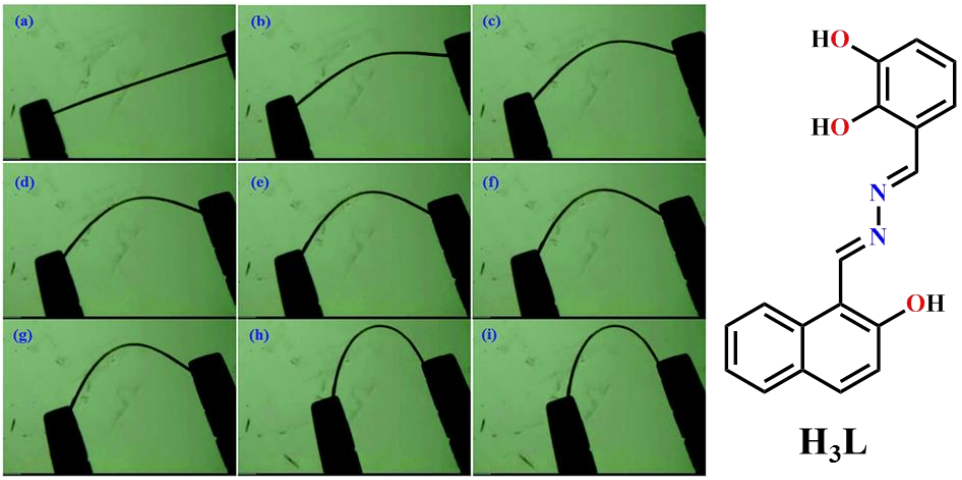

Figure 1.27. The different elastic stages in the successive bending in H_3L. [140]

Organic flexible materials have various applications in organic light-emitting diodes, artificial muscles, transistors, mechanical actuators, explosives, solar cells and optoelectronics *[143]*.

1.11 References

[1]. Satori, C. P., Henderson, M. M., Krautkramer, E. A., Kostal, V., Distefano, M. M., Arriaga, E. A. (2013), Bioanalysis of Eukaryotic Organelles, Chem. Rev., 113, 2733-2811 (DOI: 10.1021/cr300354g).

[2]. Tofaris, G. K. (2012), Lysosome-dependent pathways as a unifying theme in Parkinson's disease, Mov. Disord, 27, 1364-1369 (DOI: 10.1002/mds.25136).

[3]. Ju, L., Han, J., Zhang, X., Deng, Y., Yan, H., Wang, C., Li, X., Chen, S., Alimujiang, M., Li, X., Fang, Q., Yang, Y., Jia, W. (2019), Obesity-associated inflammation triggers an autophagy–lysosomal response in adipocytes and causes degradation of perilipin 1, Cell Death Dis., 10, 121 (DOI: 10.1038/s41419-019-1393-8).

[4]. Lawrence, R. E., Zoncu, R. (2019), The lysosome as a cellular centre for signalling, metabolism and quality control, Nat. Cell Biol., 21, 133-142 (DOI: 10.1038/s41556-018-0244-7).

[5]. Hoye, A. T., Davoren, J. E., Wipf, P., Fink, M. P., Kagan, V. E. (2008), Targeting mitochondria, Acc. Chem. Res., 41, 87-97 (DOI: 10.1021/ar700135m).

[6]. Verwilst, P., Sunwoo, K., Kim, J. S. (2015), The role of copper ions in pathophysiology and fluorescent sensors for the detection thereof, Chem. Commun., 51, 5556-5571 (DOI: 10.1039/c4cc10366a).

[7]. Ghoroghchian, P. P., Therien, M. J., Hammer, D. A. (2009), In vivo fluorescence imaging: a personal perspective, Wiley Interdiscip. Rev. Nanomed. Nanobiotechnol., 1, 156-167 (DOI: 10.1002/wnan.7).

[8]. Benson, R. A., McInnes, I. B., Brewer, J. M., Garside, P. (2015), Cellular imaging in rheumatic diseases, Nat. Rev. Rheumatol., 11, 357-367 (DOI: 10.1038/nrrheum.2015.34).

[9]. Qian, X., Xu, Z. (2015), Fluorescence imaging of metal ions implicated in diseases, Chem. Soc. Rev., 44, 4487-4493 (DOI: 10.1039/c4cs00292j).

[10]. Cotruvo, J. J. A., Aron, A. T., Ramos-Torres, K. M., Chang, C. J. (2015), Synthetic fluorescent probes for studying copper in biological systems, Chem. Soc. Rev., 44, 4400-4414 (DOI: 10.1039/C4CS00346B).

[11]. Thomas, J. A. (2015), Optical imaging probes for biomolecules: an introductory perspective, Chem. Soc. Rev., 44, 4494-4500 (DOI: 10.1039/C5CS00070J).

[12]. Tantama, M., Hung, Y. P., Yellen, G. (2011), Imaging Intracellular pH in Live Cells with a Genetically Encoded Red Fluorescent Protein Sensor, J. Am. Chem. Soc., 133, 10034-10037 (DOI: 10.1021/ja202902d).

[13]. Villamil Giraldo, A. M., Appelqvist, H., Ederth, T., Ollinger, K. (2014), Lysosomotropic agents: impact on lysosomal membrane permeabilization and cell death, Biochem . Soc. Trans., 42, 1460-1464 (DOI: 10.1042/bst20140145).

[14]. Dickinson, B. C., Srikun, D., Chang, C. J. (2010), Mitochondrial-targeted fluorescent probes for reactive oxygen species, Curr. Opin. Chem. Biol., 14, 50-56 (DOI: 10.1016/j.cbpa.2009.10.014).

[15]. Collawn, J. F., Kuhn, L. A., Liu, L. F., Tainer, J. A., Trowbridge, I. S. (1991), Transplanted LDL and mannose-6-phosphate receptor internalization signals promote high-efficiency endocytosis of the transferrin receptor, Embo j., 10, 3247-3253 (PMID: 1655415)

[16]. Rink, J., Ghigo, E., Kalaidzidis, Y., Zerial, M. (2005), Rab conversion as a mechanism of progression from early to late endosomes, Cell, 122, 735-749 (DOI: 10.1016/j.cell.2005.06.043).

[17]. Luzio, J. P., Pryor, P. R., Bright, N. A. (2007), Lysosomes: fusion and function, Nat. Rev. Mol. Cell Biol., 8, 622-632 (10.1038/nrm2217).

[18]. Saftig, P., Klumperman, J. (2009), Lysosome biogenesis and lysosomal membrane proteins: trafficking meets function, Nat. Rev. Mol. Cell Biol., 10, 623-635 (DOI: 10.1038/nrm2745).

[19]. Sharma, A., Vaghasiya, K., Ray, E., Verma, R. K. (2018), Lysosomal targeting strategies for design and delivery of bioactive for therapeutic interventions, J. Drug Targeting, 26, 208-221 (DOI: 10.1080/1061186X.2017.1374390).

[20]. Luzio, J. P., Hackmann, Y., Dieckmann, N. M., Griffiths, G. M. (2014), The biogenesis of lysosomes and lysosome-related organelles, Cold. Spring Harb. Perspect. Biol., 6, a016840 (DOI: 10.1101/cshperspect.a016840).

[21]. Qiu, K., Huang, H., Liu, B., Liu, Y., Huang, Z., Chen, Y., Ji, L., Chao, H. (2016), Long-Term Lysosomes Tracking with a Water-Soluble Two-Photon Phosphorescent Iridium(III) Complex, ACS Appl. Mater. Interfaces, 8, 12702-12710 (DOI: 10.1021/acsami.6b03422).

[22]. Meszaros, G., Pasquier, A., Vivot, K., Goginashvili, A., Ricci, R. (2018), Lysosomes in nutrient signalling: A focus on pancreatic beta-cells, Diabetes Obes. Metab., 20 Suppl 2, 104-115 (DOI: 10.1111/dom.13389).

[23]. Wang, F., Gomez-Sintes, R., Boya, P. (2018), Lysosomal membrane permeabilization and cell death, Traffic, 19, 918-931 (DOI: 10.1111/tra.12613).

[24]. Hesketh, G. G., Wartosch, L., Davis, L. J., Bright, N. A., Luzio, J. P. (2018), The Lysosome and Intracellular Signalling, Prog. Mol. Subcell. Biol., 57, 151-180 (DOI: 10.1007/978-3-319-96704-2_6).

[25]. Appelqvist, H., Waster, P., Kagedal, K., Ollinger, K. (2013), The lysosome: from waste bag to potential therapeutic target, J. Mol. Cell Biol., 5, 214-226 (DOI: 10.1093/jmcb/mjt022).

[26]. **(a)** Kaufmann, A. M., Krise, J. P. (2007), Lysosomal sequestration of amine-containing drugs: analysis and therapeutic implications, J. Pharm. Sci., 96, 729-746 (DOI: 10.1002/jps.20792); **(b)** Johnson, I., Spence, M. T. Z., (2010) The Molecular Probes HandbookA Guide to Fluorescent Probes and Labelling Technologies, 11th ed., Life Technologies, Carlsbad.

[27]. Tekpli, X., Rivedal, E., Gorria, M., Landvik, N. E., Rissel, M., Dimanche-Boitrel, M. T., Baffet, G., Holme, J. A., Lagadic-Gossmann, D. (2010), The B[a]P-increased intercellular communication via translocation of connexin-43 into gap junctions reduces apoptosis, Toxicol. Appl. Pharmacol., 242, 231-240 (DOI: 10.1016/j.taap.2009.10.012).

[28]. Simon, S., Roy, D., Schindler, M. (1994), Intracellular pH and the control of multidrug resistance, Proc. Natl. Acad. Sci. U S A, 91, 1128-1132 (DOI: 10.1073/pnas.90.3.1128)

[29]. Terman, A., Kurz, T., Gustafsson, B., Brunk, U. T. (2006), Lysosomal labilization, IUBMB life, 58, 531-539 (DOI: 10.1080/15216540600904885).

[30]. Xu, W., Zeng, Z., Jiang, J. H., Chang, Y. T., Yuan, L. (2016), Discerning the Chemistry in Individual Organelles with Small-Molecule Fluorescent Probes, Angew. Chem. Int. Ed. Engl., 55, 13658-13699 (DOI: 10.1002/anie.201510721).

[31]. Fan, L., Wang, X., Ge, J., Li, F., Wang, X., Wang, J., Shuang, S., Dong, C. (2019), A lysosome-targeting and polarity-specific

fluorescent probe for cancer diagnosis, Chem. Commun., 55, 4703-4706 (DOI: 10.1039/C9CC00962K).

[32]. La, A., Nguyen, T., Tran, K., Sauble, E., Tu, D., Gonzalez, A., Kidane, T. Z., Soriano, C., Morgan, J., Doan, M., Tran, K., Wang, C. Y., Knutson, M. D., Linder, M. C. (2018), Mobilization of iron from ferritin: new steps and details, Metallomics, 10, 154-168 (DOI: 10.1039/c7mt00284j).

[33]. Havelaar, A. C., de Gast, I. L., Snijders, S., Beerens, C. E., Mancini, G. M., Verheijen, F. W. (1998), Characterization of a heavy metal ion transporter in the lysosomal membrane, FEBS Lett., 436, 223-227.(DOI: 10.1016/S0014-5793(98)01133-8)

[34]. Kurz, T., Terman, A., Gustafsson, B., Brunk, U. T. (2008), Lysosomes and oxidative stress in aging and apoptosis, Biochim. Biophys. Acta., 1780, 1291-1303 (DOI: 10.1016/j.bbagen.2008.01.009).

[35]. Fakih, S., Podinovskaia, M., Kong, X., Collins, H. L., Schaible, U. E., Hider, R. C. (2008), Targeting the lysosome: fluorescent iron(III) chelators to selectively monitor endosomal/lysosomal labile iron pools, J. Med. Chem., 51, 4539-4552 (DOI: 10.1021/jm8001247).

[36]. Fakih, S., Podinovskaia, M., Kong, X., Schaible, U. E., Collins, H. L., Hider, R. C. (2009), Monitoring intracellular labile iron pools: A novel fluorescent iron(III) sensor as a potential non-invasive diagnosis tool, J. Pharm. Sci., 98, 2212-2226 (DOI: 10.1002/jps.21583).

[37]. Chartres, J. D., Busby, M., Riley, M. J., Davis, J. J., Bernhardt, P. V. (2011), A turn-on fluorescent iron complex and its cellular uptake, Inorg. Chem., 50, 9178-9183 (DOI: 10.1021/ic201495r).

[38]. Wei, Y., Aydin, Z., Zhang, Y., Liu, Z., Guo, M. (2012), A turn-on fluorescent sensor for imaging labile Fe(3+) in live neuronal cells at

subcellular resolution, Chembiochem, 13, 1569-1573 (DOI: 10.1002/cbic.201200202).

[39]. Lee, S. J., Koh, J. Y. (2010), Roles of zinc and metallothionein-3 in oxidative stress-induced lysosomal dysfunction, cell death, and autophagy in neurons and astrocytes, Mol. Brain, 3, 30 (DOI: 10.1186/1756-6606-3-30).

[40]. Xue, L., Li, G., Zhu, D., Liu, Q., Jiang, H. (2012), Rational design of a ratiometric and targetable fluorescent probe for imaging lysosomal zinc ions, Inorg. Chem., 51, 10842-10849 (DOI: 10.1021/ic301307v).

[41]. Zhu, H., Fan, J., Zhang, S., Cao, J., Song, K., Ge, D., Dong, H., Wang, J., Peng, X. (2014), Ratiometric fluorescence imaging of lysosomal Zn2+ release under oxidative stress in neural stem cells, Biomater. Sci., 2, 89-97 (DOI: 10.1039/C3BM60186B).

[42]. Sreenath, K., Yuan, Z., Allen, J. R., Davidson, M. W., Zhu, L. (2015), A fluorescent indicator for imaging lysosomal zinc(II) with Forster resonance energy transfer (FRET)-enhanced photostability and a narrow band of emission, Chemistry, 21, 867-874 (DOI: 10.1002/chem.201403479).

[43]. Lee, H. J., Cho, C. W., Seo, H., Singha, S., Jun, Y. W., Lee, K. H., Jung, Y., Kim, K. T., Park, S., Bae, S. C., Ahn, K. H. (2016), A two-photon fluorescent probe for lysosomal zinc ions, Chem. Commun., 52, 124-127 (DOI: 10.1039/c5cc06976a).

[44]. Gitlin, J. D. (2014), Copper homeostasis: specialized functions of the late secretory pathway, Dev. Cell, 29, 631-632 (DOI: 10.1016/j.devcel.2014.06.002).

[45]. Pena, K., Coblenz, J., Kiselyov, K. (2015), Brief exposure to copper activates lysosomal exocytosis, Cell calcium, 57, 257-262 (DOI: 10.1016/j.ceca.2015.01.005).

[46]. Asada, H., Kojima, M., Nagahara, T., Goto-Koshino, Y., Chambers, J. K., Nakagawa, T., Yokoyama, N., Uchida, K., Tsujimoto, H., Ohno, K. (2019), Hepatic copper accumulation in a young cat with familial variations in the ATP7B gene, J. Vet. Intern. Med., 33, 874-878 (DOI: 10.1111/jvim.15399).

[47]. Klein, D., Lichtmannegger, J., Heinzmann, U., Muller-Hocker, J., Michaelsen, S., Summer, K. H. (1998), Association of copper to metallothionein in hepatic lysosomes of Long-Evans cinnamon (LEC) rats during the development of hepatitis, Eur. J. Clin. Invest., 28, 302-310 (DOI: 10.1046/j.1365-2362.1998.00292.x)

[48]. Li, P., Duan, X., Chen, Z., Liu, Y., Xie, T., Fang, L., Li, X., Yin, M., Tang, B. (2011), A near-infrared fluorescent probe for detecting copper(II) with high selectivity and sensitivity and its biological imaging applications, Chem. Commun., 47, 7755-7757 (DOI: 10.1039/c1cc11885d).

[49]. Li, P., Zhou, H., Tang, B. (2012), A lysosomal-targeted fluorescent probe for detecting Cu2+, J. Photochem. Photobiol., A, 249, 36-40 (DOI: 10.1016/j.jphotochem.2012.08.020).

[50]. He, J., Zhang, X., Lian, C., Wu, J., Fang, Y., Ye, X. (2019), KEAP1/NRF2 axis regulates H2O2-induced apoptosis of pancreatic beta-cells, Gene, 691, 8-17 (DOI: 10.1016/j.gene.2018.11.100).

[51]. Mantzaris, M. D., Bellou, S., Skiada, V., Kitsati, N., Fotsis, T., Galaris, D. (2016), Intracellular labile iron determines H2O2-induced apoptotic signaling via sustained activation of ASK1/JNK-p38 axis, Free Radic. Biol. Med., 97, 454-465 (DOI: 10.1016/j.freeradbiomed.2016.07.002).

[52]. Song, D., Lim, J. M., Cho, S., Park, S. J., Cho, J., Kang, D., Rhee, S. G., You, Y., Nam, W. (2012), A fluorescence turn-on H2O2 probe exhibits lysosome-localized fluorescence signals, Chem. Commun., 48, 5449-5451 (DOI: 10.1039/c2cc31632c).

[53]. Jing, J., Zhang, J.-L. (2013), Combining myeloperoxidase (MPO) with fluorogenic ZnSalen to detect lysosomal hydrogen peroxide in live cells, Chem. Sci., 4, 2947-2952 (DOI: 10.1039/C3SC50807B).

[54]. Kim, D., Kim, G., Nam, S. J., Yin, J., Yoon, J. (2015), Visualization of endogenous and exogenous hydrogen peroxide using a lysosome-targetable fluorescent probe, Sci. Rep., 5, 8488 (DOI: 10.1038/srep08488).

[55]. Cao, L., Zhang, R., Zhang, W., Du, Z., Liu, C., Ye, Z., Song, B., Yuan, J. (2015), A ruthenium(II) complex-based lysosome-targetable multisignal chemosensor for in vivo detection of hypochlorous acid, Biomaterials, 68, 21-31 (DOI: 10.1016/j.biomaterials.2015.07.052).

[56]. Qu, Z., Ding, J., Zhao, M., Li, P. (2015), Development of a selenide-based fluorescent probe for imaging hypochlorous acid in lysosomes, J. Photochem. Photobiol., A, 299, 1-8 (DOI: 10.1016/j.jphotochem.2014.10.015)

[57]. Yuan, L., Wang, L., Agrawalla, B. K., Park, S.-J., Zhu, H., Sivaraman, B., Peng, J., Xu, Q.-H., Chang, Y.-T. (2015), Development of Targetable Two-Photon Fluorescent Probes to Image Hypochlorous Acid in Mitochondria and Lysosome in Live Cell and Inflamed Mouse Model, J. Am. Chem. Soc., 137, 5930-5938 (DOI: 10.1021/jacs.5b00042).

[58]. Yoo, Y. M., Jung, E. M., Ahn, C., Jeung, E. B. (2018), Nitric oxide prevents H2O2-induced apoptosis in SK-N-MC human neuroblastoma cells, Int. J. Biol. Sci., 14, 1974-1984 (DOI: 10.7150/ijbs.28050).

[59]. Sarkar, S., Korolchuk, V. I., Renna, M., Imarisio, S., Fleming, A., Williams, A., Garcia-Arencibia, M., Rose, C., Luo, S., Underwood, B. R., Kroemer, G., O'Kane, C. J., Rubinsztein, D. C. (2011),

Complex inhibitory effects of nitric oxide on autophagy, Mol. Cell, 43, 19-32 (DOI: 10.1016/j.molcel.2011.04.029).

[60]. Yu, H., Xiao, Y., Jin, L. (2012), A lysosome-targetable and two-photon fluorescent probe for monitoring endogenous and exogenous nitric oxide in living cells, J. Am. Chem. Soc., 134, 17486-17489 (DOI: 10.1021/ja308967u).

[61]. Olas, B. (2015), Hydrogen sulfide in signaling pathways, Clin. Chim. Acta., 439, 212-218 (DOI: 10.1016/j.cca.2014.10.037).

[62]. Kashfi, K., Olson, K. R. (2013), Biology and therapeutic potential of hydrogen sulfide and hydrogen sulfide-releasing chimeras, Biochem. Pharmacol., 85, 689-703 (DOI: 10.1016/j.bcp.2012.10.019).

[63]. Liu, T., Xu, Z., Spring, D. R., Cui, J. (2013), A lysosome-targetable fluorescent probe for imaging hydrogen sulfide in living cells, Org. Lett., 15, 2310-2313 (DOI: 10.1021/ol400973v).

[64]. Qiao, Q., Zhao, M., Lang, H., Mao, D., Cui, J., Xu, Z. (2014), A turn-on fluorescent probe for imaging lysosomal hydrogen sulfide in living cells, RSC Adv., 4, 25790-25794 (DOI: 10.1039/C4RA03725A).

[65]. Yang, S., Qi, Y., Liu, C., Wang, Y., Zhao, Y., Wang, L., Li, J., Tan, W., Yang, R. (2014), Design of a simultaneous target and location-activatable fluorescent probe for visualizing hydrogen sulfide in lysosomes, Anal. Chem., 86, 7508-7515 (DOI: 10.1021/ac501263d).

[66]. Liu, Y., Meng, F., He, L., Liu, K., Lin, W. (2016), A dual-site two-photon fluorescent probe for visualizing lysosomes and tracking lysosomal hydrogen sulfide with two different sets of fluorescence signals in the living cells and mouse liver tissues, Chem. Commun., 52, 7016-7019 (DOI: 10.1039/c6cc02368a).

[67]. Pedrazzini, E., Vitale, A. (2018), Protein Biosynthesis and Maturation in the ER, Methods Mol. Biol., 1691, 179-189 (DOI: 10.1007/978-1-4939-7389-7_14).

[68]. Mattson, M. P., LaFerla, F. M., Chan, S. L., Leissring, M. A., Shepel, P. N., Geiger, J. D. (2000), Calcium signaling in the ER: its role in neuronal plasticity and neurodegenerative disorders, Trends Neurosci., 23, 222-229. (DOI: 10.1016/S0166-2236(00)01548-4)

[69]. Lur, G., Haynes, L. P., Prior, I. A., Gerasimenko, O. V., Feske, S., Petersen, O. H., Burgoyne, R. D., Tepikin, A. V. (2009), Ribosome-free terminals of rough ER allow formation of STIM1 puncta and segregation of STIM1 from IP(3) receptors, Curr. Biol., 19, 1648-1653 (DOI: 10.1016/j.cub.2009.07.072).

[70]. Ali, E. S., Petrovsky, N. (2019), Calcium Signaling As a Therapeutic Target for Liver Steatosis, Trends Endocrinol. Metab., 30, 270-281 (DOI: 10.1016/j.tem.2019.02.005).

[71]. Mandl, J., Meszaros, T., Banhegyi, G., Hunyady, L., Csala, M. (2009), Endoplasmic reticulum: nutrient sensor in physiology and pathology, Trends Endocrinol. Metab., 20, 194-201 (DOI: 10.1016/j.tem.2009.01.003).

[72]. O'Donnell, J., Maddox, K., Stagg, S. (2011), The structure of a COPII tubule, J. Struct. Biol., 173, 358-364 (DOI: 10.1016/j.jsb.2010.09.002).

[73]. Tie, H. C., Ludwig, A., Sandin, S., Lu, L. (2018), The spatial separation of processing and transport functions to the interior and periphery of the Golgi stack, eLife, 7, e41301 (DOI: 10.7554/eLife.41301).

[74]. Markmann, S., Krambeck, S., Hughes, C. J., Mirzaian, M., Aerts, J. M., Saftig, P., Schweizer, M., Vissers, J. P., Braulke, T., Damme, M. (2017), Quantitative Proteome Analysis of Mouse Liver Lysosomes Provides Evidence for Mannose 6-phosphate-

independent Targeting Mechanisms of Acid Hydrolases in Mucolipidosis II, Mol. Cell Proteomics, 16, 438-450 (DOI: 10.1074/mcp.M116.063636).

[75]. Colston, J., Horobin, R., Rashid-Doubell, F., Pediani, J., Johal, K. (2003), Why fluorescent probes for endoplasmic reticulum are selective: an experimental and QSAR-modelling study, Biotech. Histochem., 78, 323-332 (DOI: 10.1080/10520290310001646659).

[76]. Liu, Y., Lok, C. N., Ko, B. C., Shum, T. Y., Wong, M. K., Che, C. M. (2010), Subcellular localization of a fluorescent artemisinin derivative to endoplasmic reticulum, Org Lett, 12, 1420-1423 (DOI: 10.1021/ol902890j).

[77]. Meinig, J. M., Fu, L., Peterson, B. R. (2015), Synthesis of Fluorophores that Target Small Molecules to the Endoplasmic Reticulum of Living Mammalian Cells, Angew. Chem. Int. Ed. Engl., 54, 9696-9699 (DOI: 10.1002/anie.201504156).

[78]. Kim, H. R., Kumar, R., Kim, W., Lee, J. H., Suh, M., Sharma, A., Kim, C. H., Kang, C., Seung Kim, J. (2016), A far-red, photo- and bio-stable fluorescent marker selective to the endoplasmic reticulum and its application to tunicamycin-treated HeLa cells, Chem. Commun., 52, 7134-7137 (DOI: 10.1039/c6cc02330d).

[79]. Lin, W., Buccella, D., Lippard, S. J. (2013), Visualization of peroxynitrite-induced changes of labile Zn2+ in the endoplasmic reticulum with benzoresorufin-based fluorescent probes, J. Am. Chem. Soc., 135, 13512-13520 (DOI: 10.1021/ja4059487).

[80]. Lee, Y. H., Park, N., Park, Y. B., Hwang, Y. J., Kang, C., Kim, J. S. (2014), Organelle-selective fluorescent Cu2+ ion probes: revealing the endoplasmic reticulum as a reservoir for Cu-overloading, Chem. Commun., 50, 3197-3200 (DOI: 10.1039/c4cc00091a).

[81]. Lee, H. W., Cho, M. K., Kim, H. R., Lim, C. S., Kang, C., Kim, H. M. (2017), Visualization of vesicular transport from the

endoplasmic reticulum to lysosome using an amidine derived two-photon probe, Chem. Commun., 53, 6097-6100 (DOI: 10.1039/c7cc01518f).

[82]. Shull, G. E., Miller, M. L., Prasad, V. (2011), Secretory pathway stress responses as possible mechanisms of disease involving Golgi Ca2+ pump dysfunction, Biofactors, 37, 150-158 (DOI: 10.1002/biof.141).

[83]. Walkup, G. K., Burdette, S. C., Lippard, S. J., Tsien, R. Y. (2000), A New Cell-Permeable Fluorescent Probe for Zn2+, J. Am. Chem. Soc., 122, 5644-5645 (DOI: 10.1021/ja000868p).

[84]. Singh, H., Lee, H. W., Heo, C. H., Byun, J. W., Sarkar, A. R., Kim, H. M. (2015), A Golgi-localized two-photon probe for imaging zinc ions, Chem. Commun., 51, 12099-12102 (DOI: 10.1039/c5cc03884g).

[85]. Smith, R. A., Hartley, R. C., Cocheme, H. M., Murphy, M. P. (2012), Mitochondrial pharmacology, Trends Pharmacol. Sci., 33, 341-352 (DOI: 10.1016/j.tips.2012.03.010).

[86]. Kramer, P., Bressan, P. (2018), Our (Mother's) Mitochondria and Our Mind, Perspect. Psychol. Sci., 13, 88-100 (DOI: 10.1177/1745691617718356).

[87]. **(a)** Henze, K., Martin, W. (2003), Evolutionary biology: essence of mitochondria, Nature, 426, 127-128 (DOI: 10.1038/426127a); **(b)** Alberts, B., Johnson, A., Lewis, J., Raff, M., Roberts, K., Walter, P., 2008 Molecular Biology of the Cell, 5th ed., Garland Science,New York.

[88]. Herrmann, J. M., Neupert, W. (2000), Protein transport into mitochondria, Curr. Opin. Microbiol., 3, 210-214. (DOI: 10.1016/S1369-5274(00)00077-1)

[89]. Zielonka, J., Joseph, J., Sikora, A., Hardy, M., Ouari, O., Vasquez-Vivar, J., Cheng, G., Lopez, M., Kalyanaraman, B. (2017),

Mitochondria-Targeted Triphenylphosphonium-Based Compounds: Syntheses, Mechanisms of Action, and Therapeutic and Diagnostic Applications, Chem. Rev., 117, 10043-10120 (DOI: 10.1021/acs.chemrev.7b00042).

[90]. Shaw, D. S., Meitha, K., Considine, M. J., Foyer, C. H. (2017), Mitochondrial Respiration and Oxygen Tension, Methods Mol. Biol., 1670, 97-113 (DOI: 10.1007/978-1-4939-7292-0_11).

[91]. McCormick, S. P., Moore, M. J., Lindahl, P. A. (2015), Detection of Labile Low-Molecular-Mass Transition Metal Complexes in Mitochondria, Biochemistry, 54, 3442-3453 (DOI: 10.1021/bi5015437).

[92]. Li, X., Fang, P., Yang, W. Y., Chan, K., Lavallee, M., Xu, K., Gao, T., Wang, H., Yang, X. (2017), Mitochondrial ROS, uncoupled from ATP synthesis, determine endothelial activation for both physiological recruitment of patrolling cells and pathological recruitment of inflammatory cells, Can. J. Physiol. Pharmacol., 95, 247-252 (DOI: 10.1139/cjpp-2016-0515).

[93]. Zou, D., Li, J., Fan, Q., Zheng, X., Deng, J., Wang, S. (2019), Reactive oxygen and nitrogen species induce cell apoptosis via a mitochondria-dependent pathway in hyperoxia lung injury, J. Cell Biochem., 120, 4837-4850 (DOI: 10.1002/jcb.27382).

[94]. Gerencser, A. A., Chinopoulos, C., Birket, M. J., Jastroch, M., Vitelli, C., Nicholls, D. G., Brand, M. D. (2012), Quantitative measurement of mitochondrial membrane potential in cultured cells: calcium-induced de- and hyperpolarization of neuronal mitochondria, J. Physiol., 590, 2845-2871 (DOI: 10.1113/jphysiol.2012.228387).

[95]. Murphy, M. P. (2008), Targeting lipophilic cations to mitochondria, Biochim Biophys. Acta., 1777, 1028-1031 (DOI: 10.1016/j.bbabio.2008.03.029).

[96]. Onoe, S., Temma, T., Shimizu, Y., Ono, M., Saji, H. (2014), Investigation of cyanine dyes for in vivo optical imaging of altered mitochondrial membrane potential in tumors, Cancer Med., 3, 775-786 (DOI: 10.1002/cam4.252).

[97]. Antonenko, Y. N., Avetisyan, A. V., Cherepanov, D. A., Knorre, D. A., Korshunova, G. A., Markova, O. V., Ojovan, S. M., Perevoshchikova, I. V., Pustovidko, A. V., Rokitskaya, T. I., Severina, II, Simonyan, R. A., Smirnova, E. A., Sobko, A. A., Sumbatyan, N. V., Severin, F. F., Skulachev, V. P. (2011), Derivatives of rhodamine 19 as mild mitochondria-targeted cationic uncouplers, J. Biol. Chem., 286, 17831-17840 (DOI: 10.1074/jbc.M110.212837).

[98]. Koya, K., Li, Y., Wang, H., Ukai, T., Tatsuta, N., Kawakami, M., Shishido, Chen, L. B. (1996), MKT-077, a novel rhodacyanine dye in clinical trials, exhibits anticarcinoma activity in preclinical studies based on selective mitochondrial accumulation, Cancer Res, 56, 538-543 (PMID: 8564968)

[99]. Schluter, T., Struy, H., Schonfeld, P. (2000), Protection of mitochondrial integrity from oxidative stress by the triaminopyridine derivative flupirtine, FEBS Lett, 481, 42-46. (DOI: 10.1016/S0014-5793(00)01923-2)

[100]. Trnka, J., Elkalaf, M., Andel, M. (2015), Lipophilic triphenylphosphonium cations inhibit mitochondrial electron transport chain and induce mitochondrial proton leak, PloS one, 10, e0121837 (DOI: 10.1371/journal.pone.0121837).

[101]. Heinemeyer, T., Stemmet, M., Bardien, S., Neethling, A. (2019), Underappreciated Roles of the Translocase of the Outer and Inner Mitochondrial Membrane Protein Complexes in Human Disease, DNA Cell Biol., 38, 23-40 (DOI: 10.1089/dna.2018.4292).

[102]. Horton, K. L., Stewart, K. M., Fonseca, S. B., Guo, Q., Kelley, S. O. (2008), Mitochondria-penetrating peptides, Chem. Biol., 15, 375-382 (DOI: 10.1016/j.chembiol.2008.03.015).

[103]. Yousif, L. F., Stewart, K. M., Horton, K. L., Kelley, S. O. (2009), Mitochondria-penetrating peptides: sequence effects and model cargo transport, Chembiochem, 10, 2081-2088 (DOI: 10.1002/cbic.200900017).

[104]. Neto, B. A. D., Corrêa, J. R., Silva, R. G. (2013), Selective mitochondrial staining with small fluorescent probes: importance, design, synthesis, challenges and trends for new markers, RSC Adv., 3, 5291-5301 (DOI: 10.1039/C2RA21995F).

[105]. Wang, X. H., Peng, H. S., Yang, L., You, F. T., Teng, F., Hou, L. L., Wolfbeis, O. S. (2014), Targetable phosphorescent oxygen nanosensors for the assessment of tumor mitochondrial dysfunction by monitoring the respiratory activity, Angew. Chem. Int. Ed. Engl., 53, 12471-12475 (DOI: 10.1002/anie.201405048).

[106]. Lamond, A. I., Earnshaw, W. C. (1998), Structure and Function in the Nucleus, Science, 280, 547 (DOI: 10.1126/science.280.5363.547).

[107]. Horobin, R. W., Stockert, J. C., Rashid-Doubell, F. (2006), Fluorescent cationic probes for nuclei of living cells: why are they selective? A quantitative structure-activity relations analysis, Histochem. Cell Biol., 126, 165-175 (DOI: 10.1007/s00418-006-0156-7).

[108]. Zheng, M. L., Fujita, K., Chen, W. Q., Smith, N. I., Duan, X. M., Kawata, S. (2011), Comparison of staining selectivity for subcellular structures by carbazole-based cyanine probes in nonlinear optical microscopy, Chembiochem, 12, 52-55 (DOI: 10.1002/cbic.201000593).

[109]. Wu, J., Zou, Y., Li, C., Sicking, W., Piantanida, I., Yi, T., Schmuck, C. (2012), A molecular peptide beacon for the ratiometric sensing of nucleic acids, J. Am. Chem. Soc., 134, 1958-1961 (DOI: 10.1021/ja2103845).

[110]. Hong, Y., Chen, S., Leung, C. W., Lam, J. W., Tang, B. Z. (2013), Water-soluble tetraphenylethene derivatives as fluorescent "light-up" probes for nucleic acid detection and their applications in cell imaging, Chem. Asian J., 8, 1806-1812 (DOI: 10.1002/asia.201300065).

[111]. Feng, X. J., Wu, P. L., Bolze, F., Leung, H. W., Li, K. F., Mak, N. K., Kwong, D. W., Nicoud, J. F., Cheah, K. W., Wong, M. S. (2010), Cyanines as new fluorescent probes for DNA detection and two-photon excited bioimaging, Org. Lett., 12, 2194-2197 (DOI: 10.1021/ol100474b).

[112]. Feng, S., Kim, Y. K., Yang, S., Chang, Y. T. (2010), Discovery of a green DNA probe for live-cell imaging, Chem. Commun., 46, 436-438 (DOI: 10.1039/b916858c).

[113]. Peng, X., Wu, T., Fan, J., Wang, J., Zhang, S., Song, F., Sun, S. (2011), An effective minor groove binder as a red fluorescent marker for live-cell DNA imaging and quantification, Angew Chem Int Ed Engl, 50, 4180-4183 (DOI: 10.1002/anie.201007386).

[114]. Guo, L., Chan, M. S., Xu, D., Tam, D. Y., Bolze, F., Lo, P. K., Wong, M. S. (2015), Indole-based cyanine as a nuclear RNA-selective two-photon fluorescent probe for live cell imaging, ACS Chem. Biol., 10, 1171-1175 (DOI: 10.1021/cb500927r).

[115]. Lu, Y. J., Deng, Q., Hu, D. P., Wang, Z. Y., Huang, B. H., Du, Z. Y., Fang, Y. X., Wong, W. L., Zhang, K., Chow, C. F. (2015), A molecular fluorescent dye for specific staining and imaging of RNA in live cells: a novel ligand integration from classical thiazole

orange and styryl compounds, Chem. Commun., 51, 15241-15244 (DOI: 10.1039/c5cc05551b).

[116]. Shen, X., Jiang, Q., Wang, J., Dai, L., Zou, G., Wang, Z. G., Chen, W. Q., Jiang, W., Ding, B. (2012), Visualization of the intracellular location and stability of DNA origami with a label-free fluorescent probe, Chem. Commun., 48, 11301-11303 (DOI: 10.1039/c2cc36185j).

[117]. De Meulenaere, E., Chen, W.-Q., Van Cleuvenbergen, S., Zheng, M.-L., Psilodimitrakopoulos, S., Paesen, R., Taymans, J.-M., Ameloot, M., Vanderleyden, J., Loza-Alvarez, P., Duan, X.-M., Clays, K. (2012), Molecular engineering of chromophores for combined second-harmonic and two-photon fluorescence in cellular imaging, Chem. Sci., 3, 984-995 (DOI: 10.1039/C2SC00771A).

[118]. de Silva, A. P., Moody, T. S., Wright, G. D. (2009), Fluorescent PET (Photoinduced Electron Transfer) sensors as potent analytical tools, Analyst, 134, 2385-2393 (DOI: 10.1039/B912527M).

[119]. Cordes, E. H., Jencks, W. P. (1962), On the Mechanism of Schiff Base Formation and Hydrolysis, J. Am. Chem. Soc., 84, 832-837 (DOI: 10.1021/ja00864a031).

[120]. Ramachandran, E., Gandin, V., Bertani, R., Sgarbossa, P., Natarajan, K., Bhuvanesh, N. S. P., Venzo, A., Zoleo, A., Glisenti, A., Dolmella, A., Albinati, A., Marzano, C. (2018), Synthesis, characterization and cytotoxic activity of novel copper(II) complexes with aroylhydrazone derivatives of 2-Oxo-1,2-dihydrobenzo[h]quinoline-3-carbaldehyde, J. Inorg. Biochem., 182, 18-28 (DOI: 10.1016/j.jinorgbio.2018.01.016).

[121]. Zhang, M., Xian, D.-M., Li, H.-H., Zhang, J.-C., You, Z.-L. (2012), Synthesis and Structures of Halo-Substituted

Aroylhydrazones with Antimicrobial Activity, Aust. J. Chem., 65, 343-350. (DOI: 10.1071/CH11424)

[122]. da Silva, C. M., da Silva, D. L., Modolo, L. V., Alves, R. B., de Resende, M. A., Martins, C. V. B., de Fátima, Â. (2011), Schiff bases: A short review of their antimicrobial activities, J. Adv. Res., 2, 1-8 (DOI: 10.1016/j.jare.2010.05.004)

[123]. Liang, L., Astruc, D. (2011), The copper(I)-catalyzed alkyne-azide cycloaddition (CuAAC) "click" reaction and its applications. An overview, Coord. Chem. Rev., 255, 2933-2945 (DOI: 10.1016/j.ccr.2011.06.028).

[124]. Schulze, B., Schubert, U. S. (2014), Beyond click chemistry - supramolecular interactions of 1,2,3-triazoles, Chem. Soc. Rev., 43, 2522-2571 (DOI: 10.1039/c3cs60386e).

[125]. Hein, C. D., Liu, X. M., Wang, D. (2008), Click chemistry, a powerful tool for pharmaceutical sciences, Pharm. Res., 25, 2216-2230 (DOI: 10.1007/s11095-008-9616-1).

[126]. Kasha, M., Rawls, H. R. (1968), Correlation of orbital classification of molecular electronic transitions with transition mechanism: the aromatic amines*, Photochem. Photobiol., 7, 561-569 (DOI: 10.1111/j.1751-1097.1968.tb08038.x).

[127]. Lichtman, J. W., Conchello, J.-A. (2005), Fluorescence microscopy, Nat. Methods, 2, 910 (DOI: 10.1038/nmeth817).

[128]. Ustione, A., Piston, D. W. (2011), A simple introduction to multiphoton microscopy, J. Microsc., 243, 221-226 (DOI: 10.1111/j.1365-2818.2011.03532.x).

[129]. Helmchen, F., Denk, W. (2005), Deep tissue two-photon microscopy, Nat Methods, 2, 932-940 (10.1038/nmeth818).

[130]. Morris, G. M., Lim-Wilby, M. (2008), Molecular docking, Methods, Mol. Biol, 443, 365-382 (DOI: 10.1007/978-1-59745-177-2_19).

[131]. Arif, R., Nayab, P. S., Akrema, Abid, M., Yadava, U., Rahisuddin (2019), Investigation of DNA binding and molecular docking propensity of phthalimide derivatives: in vitro antibacterial and antioxidant assay, J. Anal. Sci. Technol., 10, 19 (DOI: 10.1186/s40543-019-0177-1).

[132]. Dandawate, P., Khan, E., Padhye, S., Gaba, H., Sinha, S., Deshpande, J., Venkateswara Swamy, K., Khetmalas, M., Ahmad, A., Sarkar, F. H. (2012), Synthesis, characterization, molecular docking and cytotoxic activity of novel plumbagin hydrazones against breast cancer cells, Bioorg. Med. Chem. Lett., 22, 3104-3108 (DOI: 10.1016/j.bmcl.2012.03.060).

[133]. Baseden, K. A., Tye, J. W. (2014), Introduction to Density Functional Theory: Calculations by Hand on the Helium Atom, J. Chem. Educ., 91, 2116-2123 (DOI: 10.1021/ed5004788).

[134]. Farag, A. M., Fahim, A. M. (2019), Synthesis, biological evaluation and DFT calculation of novel pyrazole and pyrimidine derivatives, J. Mol. Struct., 1179, 304-314 (DOI: 10.1016/j.molstruc.2018.11.008).

[135]. Issaoui, N., Ghalla, H., Muthu, S., Flakus, H. T., Oujia, B. (2015), Molecular structure, vibrational spectra, AIM, HOMO-LUMO, NBO, UV, first order hyperpolarizability, analysis of 3-thiophenecarboxylic acid monomer and dimer by Hartree-Fock and density functional theory, Spectrochim. Acta A Mol. Biomol. Spectrosc., 136 Pt C, 1227-1242 (DOI: 10.1016/j.saa.2014.10.008).

[136]. Cui, M.-Y., Nie, J.-X., Yan, Z.-Z., Xiao, M.-W., Lin, D., Ye, J., Hu, A.-X. (2019), Design, synthesis, bioactivity, and DFT calculation of 2-thiazolyl-hydrazone derivatives as influenza neuraminidase inhibitors, Med. Chem. Res., (DOI: 10.1007/s00044-019-02343-3).

[137]. Hayashi, S., Asano, A., Kamiya, N., Yokomori, Y., Maeda, T., Koizumi, T. (2017), Fluorescent organic single crystals with elastic bending flexibility: 1,4-bis(thien-2-yl)-2,3,5,6-tetrafluorobenzene derivatives, Sci. Rep., 7, 9453 (DOI: 10.1038/s41598-017-09848-0).

[138]. Alimi, L. O., Lama, P., Smith, V. J., Barbour, L. J. (2018), Hand-twistable plastically deformable crystals of a rigid small organic molecule, Chem. Commun., 54, 2994-2997 (DOI: 10.1039/C8CC00775F).

[139]. Saha, S., Desiraju, G. R. (2016), Using structural modularity in cocrystals to engineer properties: elasticity, Chem. Commun., 52, 7676-7679 (DOI: 10.1039/C6CC03226E).

[140]. Saini, A. K., Natarajan, K., Mobin, S. M. (2017), A new multitalented azine ligand: elastic bending, single-crystal-to-single-crystal transformation and a fluorescence turn-on Al(iii) sensor, Chem Commun (Camb), 53, 9870-9873 (10.1039/c7cc04392a).

[141]. Naumov, P., Chizhik, S., Panda, M. K., Nath, N. K., Boldyreva, E. (2015), Mechanically Responsive Molecular Crystals, Chem. Rev., 115, 12440-12490 (DOI: 10.1021/acs.chemrev.5b00398).

[142]. Ghosh, S., Mishra, M. K., Kadambi, S. B., Ramamurty, U., Desiraju, G. R. (2015), Designing elastic organic crystals: highly flexible polyhalogenated N-benzylideneanilines, Angew. Chem. Int. Ed. Engl., 54, 2674-2678 (DOI: 10.1002/anie.201410730).

[143]. Krishna, G. R., Devarapalli, R., Lal, G., Reddy, C. M. (2016), Mechanically Flexible Organic Crystals Achieved by Introducing Weak Interactions in Structure: Supramolecular Shape Synthons, J. Am. Chem. Soc., 138, 13561-13567 (DOI: 10.1021/jacs.6b05118).

CHAPTER 2

Two-photon Fluorescent Organic Probe for Imaging of Lysosomes in Live Cells and Tumor Spheroids

2.1. Introduction

Lysosomes are acidic, membrane-bound organelles considered as ‘‘stomachs’’ of the cells, which degrade macromolecules delivered by endocytosis and intracellular materials with the help of multiple acid hydrolases *[1-5]*. Lysosomes play an important role in many physiological activities such as cell migration, cell signaling, cholesterol homeostasis, initiation of apoptosis and tissue remodeling *[6-11]*. Lysosomal dysfunction causes various diseases including lysosomal storage diseases such as Tay-Sachs *[12-13]*, progression of cancer *[14-15]*, neurodegenerative diseases such as Parkinson’s disease, Gaucher disease and others *[16-18]*. Thus, the ability to visualize lysosomal morphology is essential in order to understand the biological functions of lysosomes. LysoTracker probes such as Neutral Red (NR), DND-189, and DND-99 are expensive fluorescent dyes that have the tendency to specifically label lysosomes. However, these dyes have some limitations: (i) prolonged accumulation of LysoTracker probes in the intracellular environment increases the cellular pH, causing fluorescent dye quenching as well as physiological and morphological changes in the lysosomes and (ii) the low photostability limits their use for long term tracking of lysosomes to observe dynamic changes in lysosomal morphology in a stipulated time *[19-24]*.

So far reports on long term imaging of lysosomes have been based on some metal-complexes *[25-27]*, BODIPY moieties *[28-29]*, complex organic or dextran-conjugated fluorophores *[30-34]*, **(Chart 2.1)** and

inorganic nanocomposites *[35-36]* but all these involve a tedious multistep synthetic process. Also, these emerging lyso-probes and nanoparticles may suffer from toxic impacts *[37]*. For example, the SiO_2 particles are well known to cause damage to the lysosomal membranes *[38]*. Moreover, the dextran based fluorescence lysotracker cannot be used for long term imaging due to the inherent toxicity of dextran towards lysosomal functions *[39]*. Among these fluorophores, some of them have short wavelength excitation leading to cellular auto-fluorescence resulting in photodamage and photobleaching.

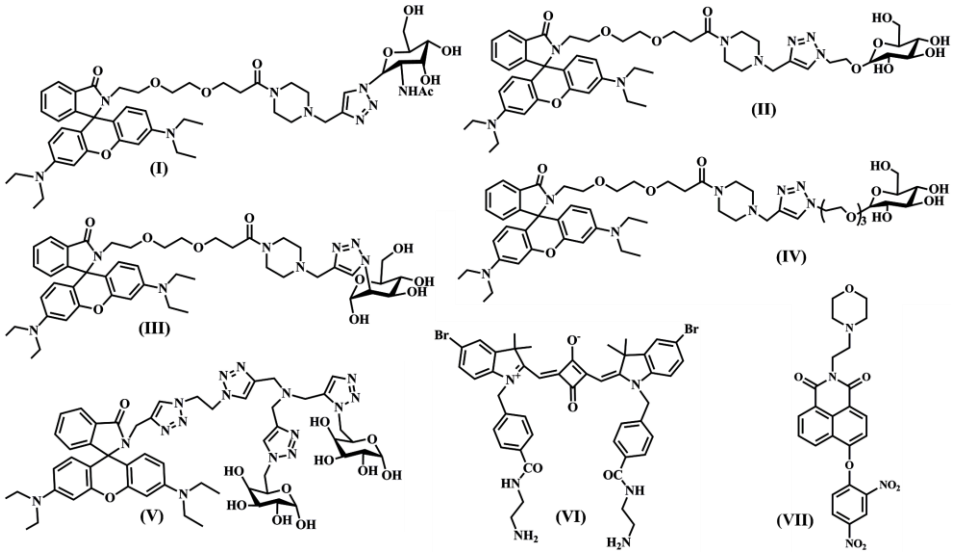

Chart 2.1. Some reported multi-step organic fluorophores for lysosome imaging.

To overcome the above limitations, we need small water soluble organic probes having two-photon (TP) fluorescence properties. Owing to the low background interference, minimal photodamage of cells or tissues, penetration depth (4500 μm) and near-infrared light (700–1100 nm) excitation wavelengths *[40]*, two-photon microscopy (TPM) is an essential tool for bio-imaging within intact tissue and live cells.

In this chapter, a new water soluble fluorescent Schiff-base ligand (**L-lyso**) was designed and synthesized, which containing two hydroxyl groups. The morphological alteration of lysosomes is a powerful indicator of various pathological disorders. In this regard, **L-lyso** was synthesized

which exhibits excellent two-photon properties with tracking of lysosomes in live cells as well as in 3D tumor spheroids. Furthermore, it can label lysosomes for more than 3 days. Thus, **L-lyso** has an edge over the commercially available expensive LysoTracker probes and also over other reported probes in terms of its long-term imaging, water solubility and facile synthesis.

2.2. Results and discussion

2.2.1. Synthesis and characterization:

A one-step Schiff base organic probe, **L-lyso** designed and synthesized in a facile manner by condensation of 4-(diethylamino)-2-hydroxy-benzaldehyde and 3-amino-2-hydroxynaphthalene **(Scheme 2.1)**. The **L-lyso** was characterized by standard spectroscopic methods viz FTIR, ^{1}H & ^{13}C NMR spectroscopy, and ESI-MS and further authenticated by a single crystal X-ray diffraction study.

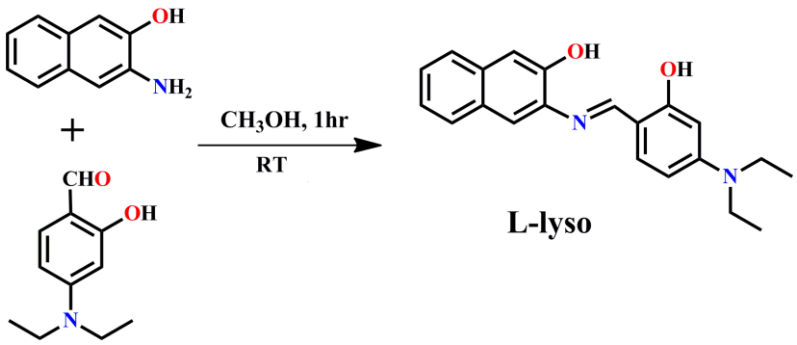

Scheme 2.1. Schematic representation of the synthesis of **L-lyso**.

2.2.2. Structural aspects of L-lyso:

The single crystal of **L-lyso**, was grown in methanol/ chloroform solution by slow evaporation at 25°C and crystallized in orthorhombic crystal system with non-centrosymmetry *P*na2_1 space group **(Figure 2.1 and Tables A1 and A2).**

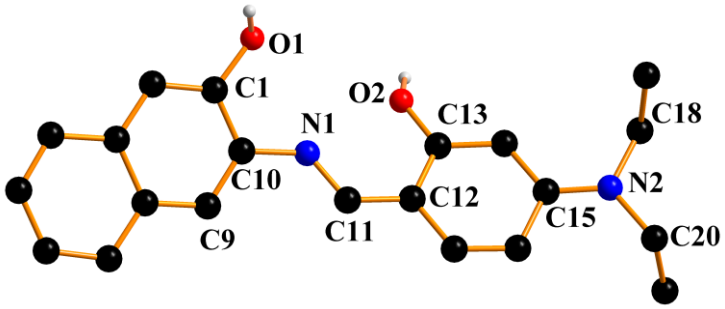

Figure 2.1. Molecular Structure of **L-lyso**

L-lyso is non-planar due to presence of naphthyl and phenyl ring in two different planes attached from imine (>C=N–) unit, with torsion angle 25.86°. The packing features of **L-lyso** reveal the presence of intra and inter molecular H-bonding interactions *[41]* as depicted in **Figure 2.2**. The intra-molecular H-bonding interaction O(2)–H(1)···N(1), bond length 1.924 Å, was observed between the hydroxyl group of the phenolic moiety and nitrogen atom of the imine group (>C=N–). In the intra-molecular H-bonding O(2)–H(1)···N(1) interactions, O(2)–H(1) is donor and N(1) is acceptor. While intermolecular H-bonding interaction results between phenolic moiety of one molecule and naphthyl ring of neighbouring unit, O(1)–H(1)···O(2), 1.764 Å where O(1)–H(1) is donor and O(2) is acceptor leads to the formation of 2D-network **(Figure 2.2)**. Moreover, the π–π interaction *[42]* 4.060Å, between phenyl and naphthyl rings, facilitates the charge transfer from electron rich phenyl to electron deficient naphthyl ring **(Figure 2.3)**.

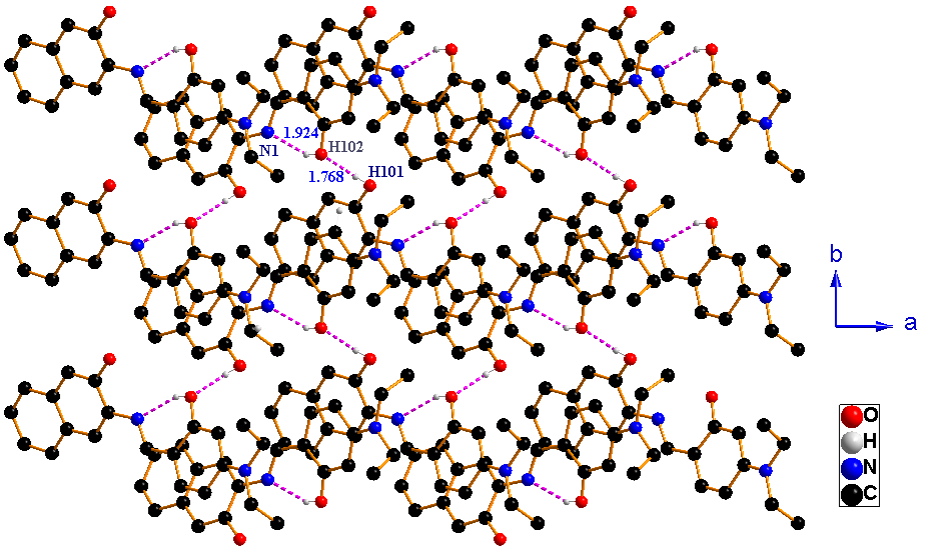

Figure 2.2. 2D network chain of **L-lyso** along *c*-axis due to inter and intra molecular H-bonding (Pink dots represent H-bonds).

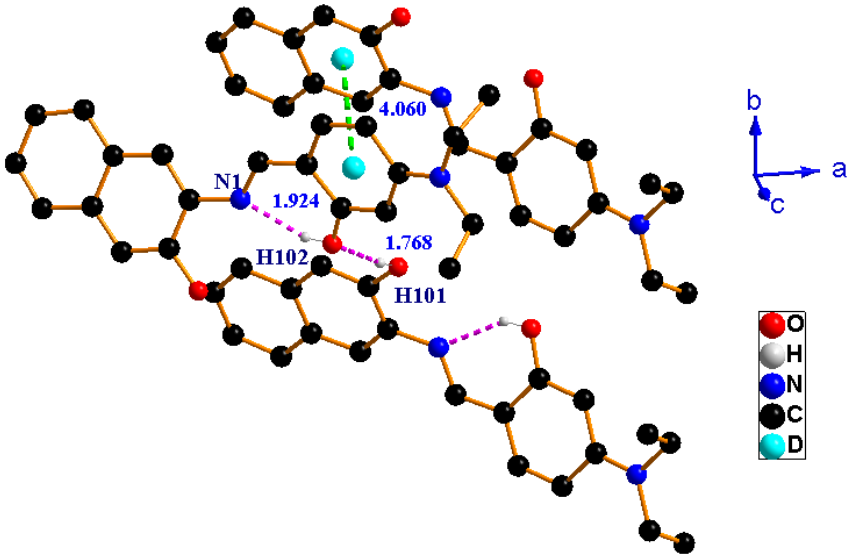

Figure 2.3. Ball and stick model of **L-lyso** showing π–π interaction between phenyl and naphthyl rings, where D is the dummy atom (Fragmented green line represented as π–π interaction and pink dots depicted as H- bond).

2.2.3. Photophysical properties:

L-lyso is found to be an excellent candidate for two-photon (TP) excitation that have ability to label lysosome in live cells as well as tumor spheroids. TP fluorescent probe for lysosomes imaging are rare *[24, 43]*.

Moreover, most of them emit two-photon excited fluorescence near 500 nm, which is very close to the emission spectrum of the existing TP probes for other targets *[44-45]*. Therefore, TP **L-lyso** was designed, that emits fluorescence in the short wavelength (λ_{em} = 415-470 nm).

The lysosome pH is between 4.5−5.5 *[26]*. Therefore, the photo-physical properties of **L-lyso** were studied in a disodium hydrogen phosphate / citric acid buffer at pH 5.5. The absorption bands of **L-lyso** was at 235, 349, 429 nm which attributed to the spin-allowed ligand-centred (LC) π→π* and 452 nm for n→π* transitions. The emission spectrum of **L-lyso** at excitation 280 nm exhibited the highest intensity at 383 nm **(Figure 2.4)**.

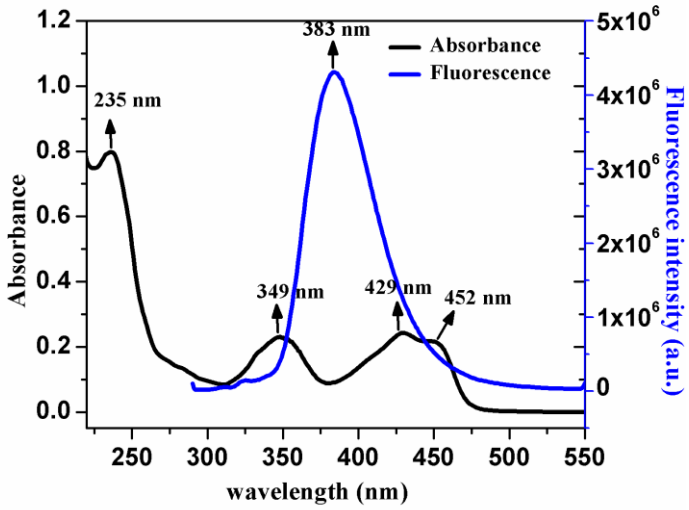

Figure 2.4. UV-vis (in methanol) and fluorescence spectrum of **L-lyso** (10 µM) in buffer solution.

The fluorescent intensity of **L-lyso** was quite stable upto pH 8.3 **(Figure 2.5)**. The fluorescence intensity of **L-lyso** quenching slightly at high pH, may be due to the formation of electron donor phenoxide ion, through photo-induced electron transfer (PET) under basic conditions. Moreover, the highly elevated Stokes shift of 148 nm for **L-lyso** has added advantages over the commercially available LysoTrackers such as LysoTracker Green DND-26 (LTG) having Stokes shift = 7 nm and

LysoTracker Red DND-99 (LTR) having Stokes shift = 13 nm *[46]*. Thus, higher stroke shift in **L-lyso** will restrict cross-talk between absorption and emission spectrum and will allow distinguished peak separation with high signal to noise ratio in cellular imaging.

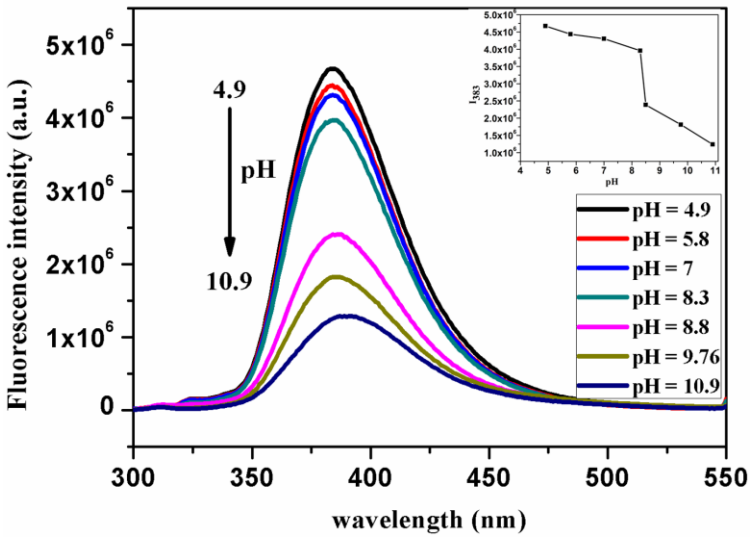

Figure 2.5. pH-sensitive emission spectrum of **L-lyso** (10 μM buffer solution). Inset: a plot of emission intensity of **L-lyso** at 383 nm versus various pH values. Buffer solution: disodium hydrogen phosphate/citric acid.

The two-photon emission intensity was compared at varying excitation wavelength in range 700-830 nm and found maximum at λ_{ex} = 790 nm **(Figure 2.6)**. A log–log linear relationship between the emission intensity and the incident power of **L-lyso** was measured at 790 nm by using femtosecond laser pulse and the resulting slope of 2.22, confirm the two-photon process **(Figure 2.7)**. The retaining of **L-lyso** inside lysosomes may be probably explained by the low pKa values of 3.27 for amine and 3.55 for imine present in **L-lyso**. The amine and imine group present in **L-lyso** prefer the most acidic lysosomes compared to other subcellular organelles and get protonated inside lysosomes which increases the hydrophilicity. Thus, the protonated amine and imine group of **L-lyso** restrict its movement in acidic lysosomes.

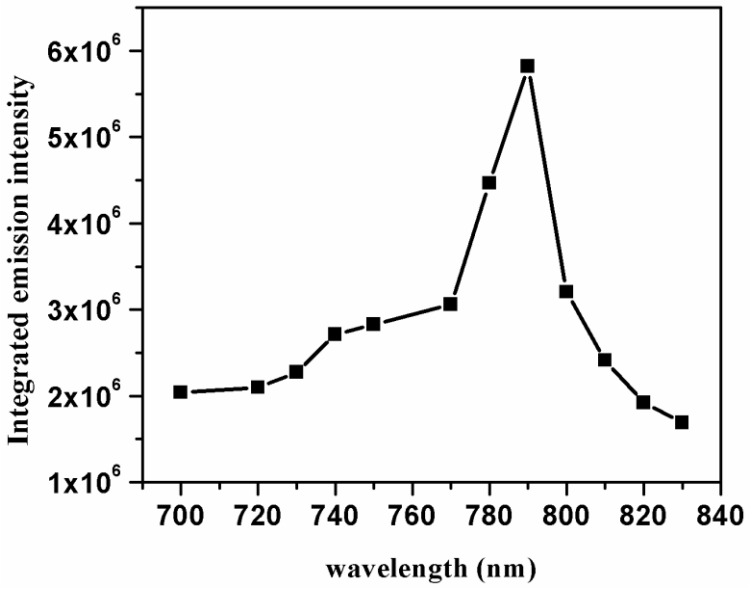

Figure 2.6. Two-photon integrated fluorescence emission intensity of **L-lyso** at excitation wavelengths 700–830 nm in live HeLa cells.

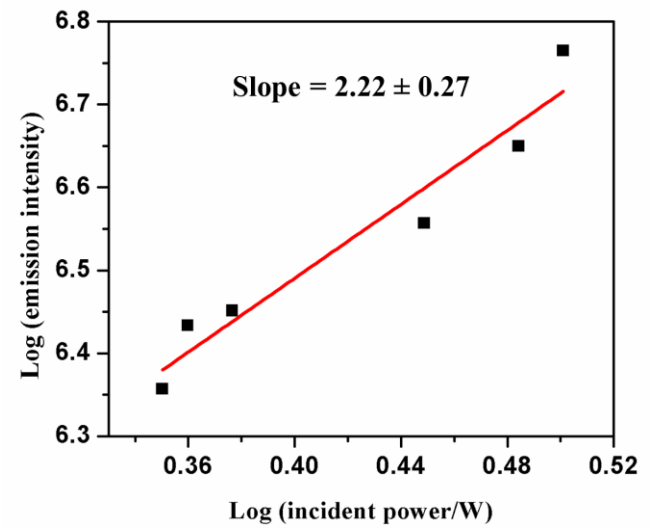

Figure 2.7. A representative logarithmic plot of integrated emission intensity as a function of laser power (**L-lyso).** The solid red line represents the best fit line to the data. Slope is 2.22 ± 0.27.

2.2.4. Cell viability assay of L-lyso:

High cellular viability is necessary for long term imaging of lysosomes. The MTT assay result demonstrates that the **L-lyso** probe is highly biocompatible for cellular and physiological studies within the concentration range 10–80 μM **(Figure 2.8)** for 24 h incubation and

further increasing the incubation time to up to 34 h still shows a high IC50 value of 600 ±2.783 μM **(Figure 2.9)**.

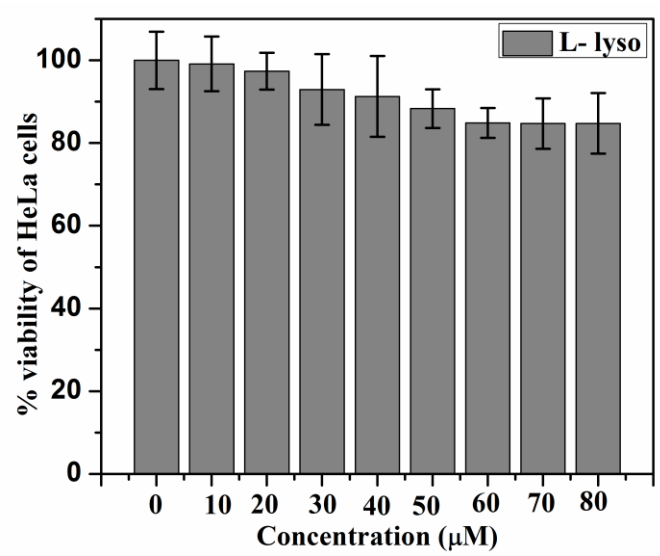

Figure 2.8. Cell viability study of **L-lyso** by the MTT assay, after 24 h (treatment). The results shown are mean ± SD of four independent measurements.

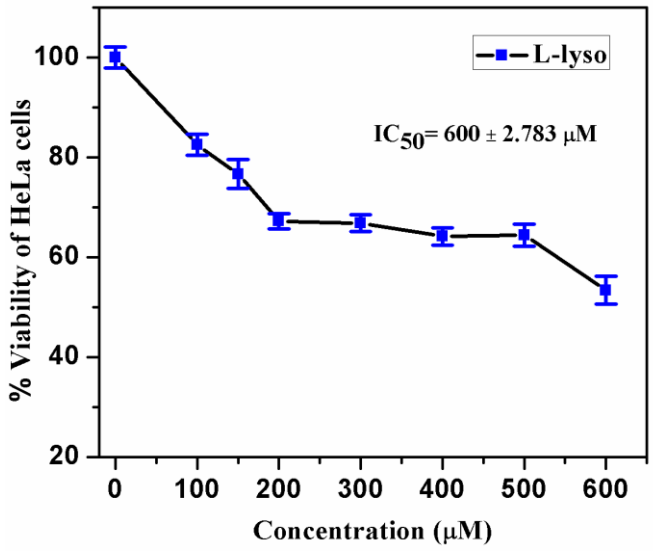

Figure 2.9. Cell viability study of **L-lyso** by the MTT assay after 34 h treatment at 37°C. The results shown are mean ± SD of four separate measurements. IC_{50} = 600 ± 2.783 μM.

2.2.5. Flow cytometry studies of L-lyso:

Flow cytometry was used to acquire high quality fluorescence signals with high spatial resolution from significant populations of cells in flow *[47]*. Hence, concentration dependent analysis was done by both flow cytometry and by confocal microscopic imaging. The fluorescence emitted by the cells (60 µM **L-lyso**) was more intense; hence, both the scatter plot and the histogram shifted more toward right (**Figures 2.10a and 2.10b**). Furthermore, cells treated with 0 µM (control), 30 µM and 60 µM **L-lyso** exhibits mean fluorescence intensities of 75, 953 and 1804, respectively. This indicates that **L-lyso** can uniformly label lysosomes over a large population of cells, which was detected in live suspension cells by flow cytometry and live adhered cells by microscopy **(Figure 2.10c)**.

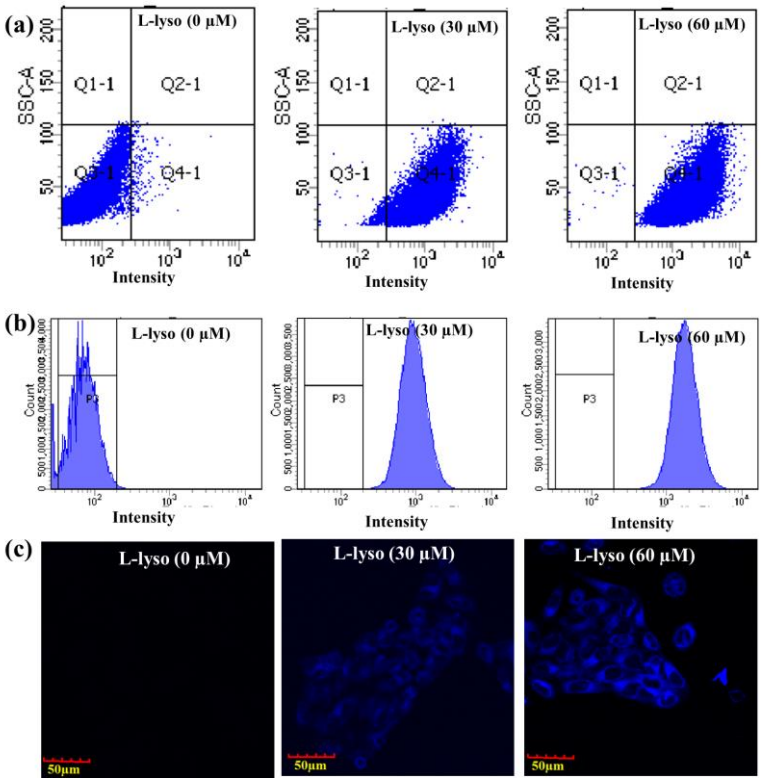

Figure 2.10. Concentration dependent analysis of **L-lyso** in live HeLa cells. **(a)** Flow cytometric analysis, scatter plot. **(b)** Flow cytometric analysis, histogram. c) Confocal image; after incubation with **L-lyso** (30 µM and 60 µM) for 10 min. **L-lyso:** λ_{ex} = 405 nm; λ_{em} = 415-470 nm.

3.2.6. Organelles' selectivity of L-lyso:

In order to investigate the binding of **L-lyso** to lysosomes, we examined the co-staining of MCF-7 cells with two organelle trackers LysoTracker Red DND-99 (LTR) for lysosomes and MitoTracker Red CMXRos for mitochondria separately **(Figure 2.11)**. The pink staining in the overlay images was generated by superimposition of blue **L-lyso** and red organelle trackers, which shows that **L-lyso** have immense correlation with LysoTracker Red **(Figure 2.11a)** and is compatible for counter staining with MitoTracker Red **(Figure 2.11b)**.

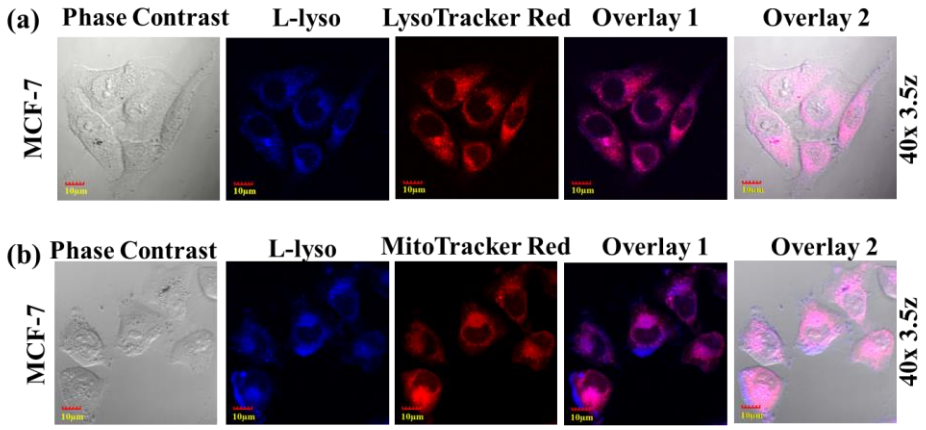

Figure 2.11. The subcellular fluorescence imaging of **L-lyso** in MCF-7 cells. Cells were co-incubate with **L-lyso** (60 μM, 10 min) and two different organelle trackers. **(a)** LysoTracker Red DND-99 (80 nM, 10 min) for lysosomes, **(b)** MitoTracker Red CMXRos (80 nM for 10 min) for mitochondria. The images from left to right shows phase contrast (column 1), **L-lyso** (column 2), organelle trackers (column 3) and Overlay 1: overlay of the 2nd and 3rd columns. Overlay 2: overlay of the 1st, 2nd and 3rd columns. Scale bar: 10 μm.

2.2.7. Universal staining ability L-lyso in various cell lines:

Furthermore, the universal lysosomal selective staining ability of **L-lyso** was evaluated in four different cell lines i.e., HeLa (Cervical cancer), MCF-7 (breast cancer), A375 (skin melanoma) and DU145 (prostate cancer) cells **(Figure 2.12)**. An excellent lysosome labeling pattern was achieved in all examined live cells. Moreover, the co-localization effect of **L-lyso** and LTR was evaluated by Pearson's co-

localisation coefficient (R_r) **(Figure 2.13)**. The overlapping fluorescence signals showed high Pearson's coefficients of 0.84, 0.83, 0.85 and 0.87 for HeLa, MCF-7, A375 and DU145 cells respectively, which were found to be the best among the reported lysosome probes *[48-49]*. Furthermore, Manders' coefficients were calculated indicating very good colocalization of the blue (**L-lyso**) and red (LTR) channels with each other on a per-pixel level **(Table 2.1)**.

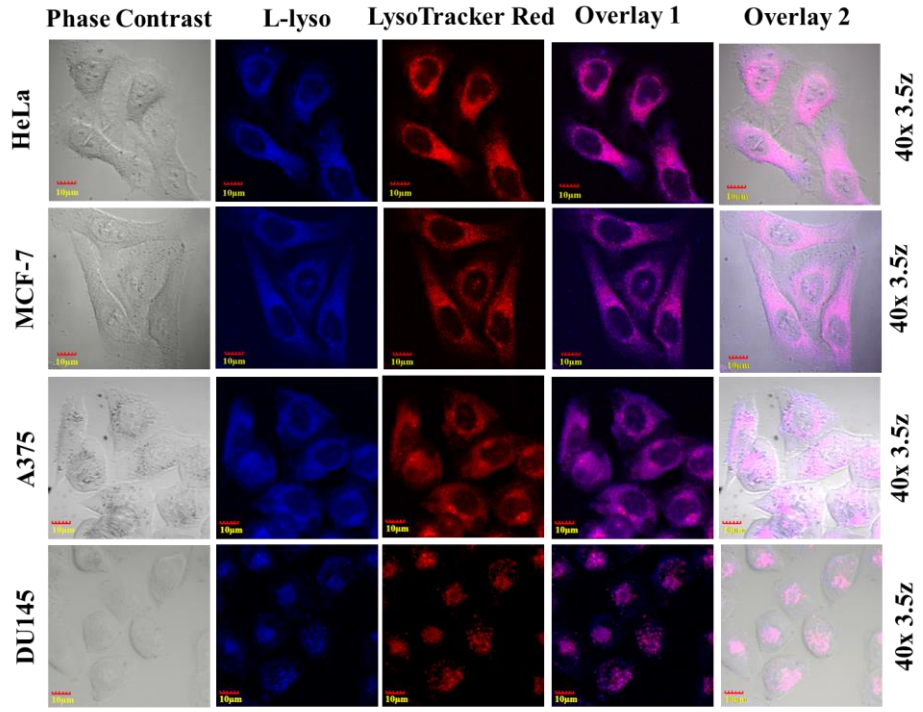

Figure 2.12. Lysosome specific live cell imaging of **L-lyso** in HeLa, MCF-7, A375 and DU145 cells. All cells were co-stained with **L-lyso** (60 μM, 10 min) and LysoTracker Red DND-99 (80 nM, 10 min). **L-lyso**: λ_{ex} = 405 nm; λ_{em} = 415-470 nm; LysoTracker Red λ_{ex} = 559 nm; λ_{em} = 580-700 nm. Overlay 1: overlay of the 2nd and 3rd columns. Overlay 2: overlay of the 1st, 2nd and 3rd columns. Scale bar: 10 μm.

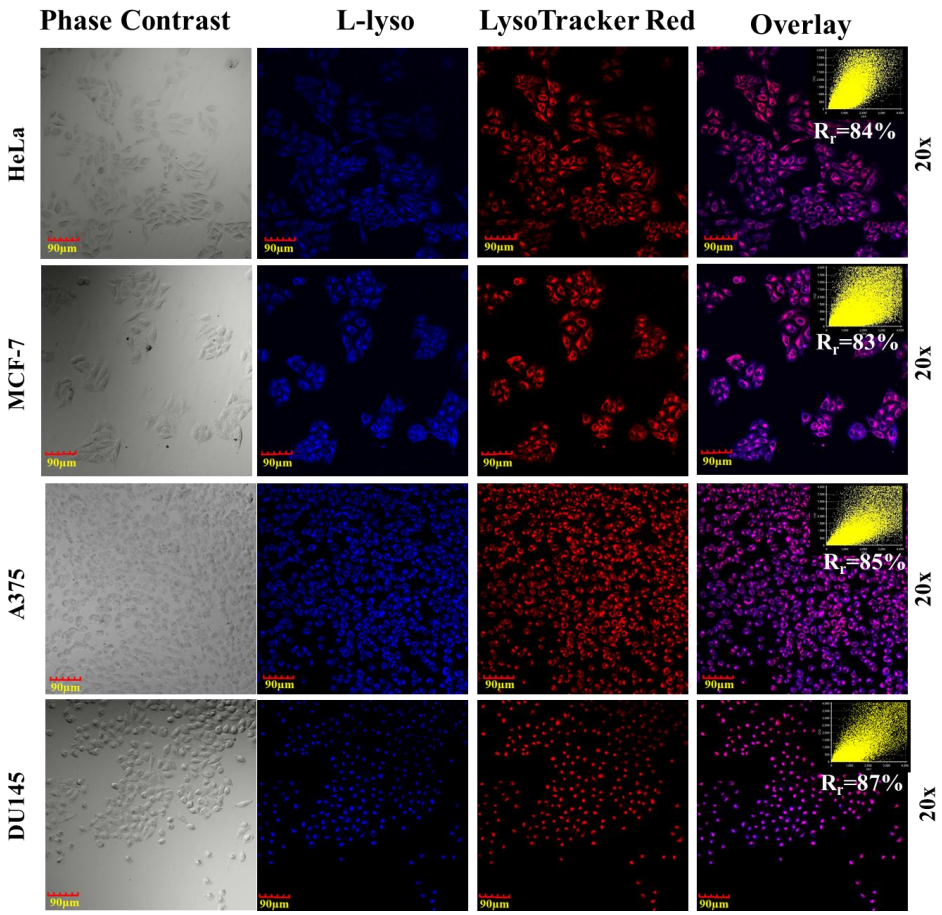

Figure 2.13. Lysosome specific live cell imaging by **L-lyso** in HeLa (cervical cancer), MCF-7 (breast cancer) A375 (skin melanoma) and DU145 (prostate cancer) cells and corresponding insets depict the Pearson's colocalisation coefficient (R_r) on different cell line. All cells were co-stained with **L-lyso** (60 µM, 10 min) and LysoTracker Red DND-99 (80 nM, 10 min). **L-lyso** λ_{ex} = 405 nm; λ_{em} = 415–470 nm; LysoTracker Red λ_{ex} = 559 nm; λ_{em} = 580–700 nm.

Table 2.1. Per-pixel spatial colocalization analysis of **L-lyso** with LysoTracker Red

Cell lines	Manders' M1	Manders' M2	Pearson's R value
Hela	0.925	0.986	0.83
MCF-7	0.911	0.972	0.84
A375	0.999	0.972	0.85
DU145	0.983	0.929	0.87

2.2.8. The probable mechanistic pathway of L-lyso:

Confocal microscopy was further used to explore the probable mechanistic pathways of cellular uptake of ligand **L-lyso**. HeLa cells were treated with **L-lyso** in two confocal dishes; one dish was incubated at 37 °C and the other at 4 °C to identify whether the uptake by the cells was via an energy-dependent (endocytosis) or an energy-independent transport pathway. The uptake of **L-lyso** by the cells at 4°C as well as 37°C suggested that it was taken up via an energy-independent pathway **(Figure 2.14)**.

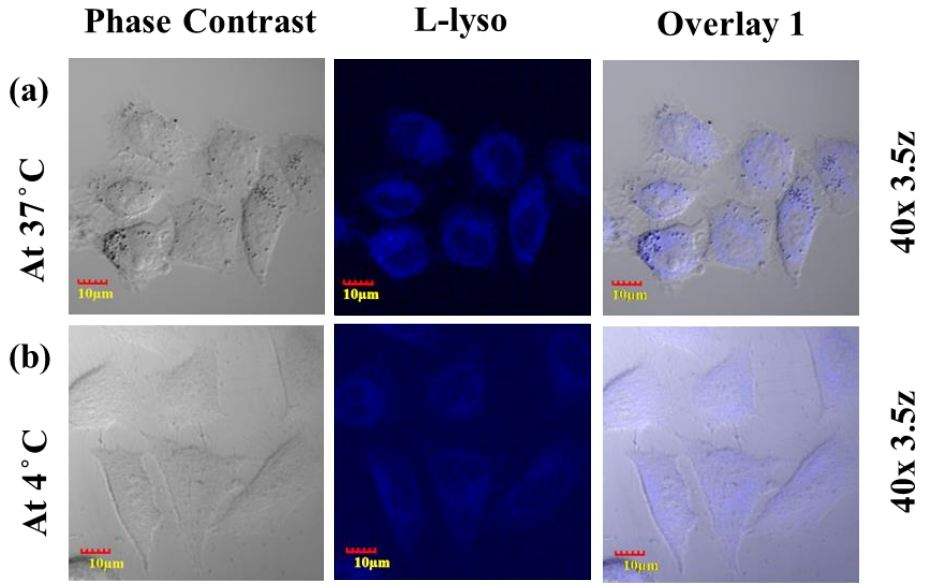

Figure 2.14. Live cells (HeLa) imaging under different conditions **(a)** The cells were incubated with **L-lyso** (60 µM) at 37°C for 1h. **(b)** The cells were incubated with **L-lyso** (60 µM) at 4°C for 1 h.

2.2.9. The photostability of L-lyso:

The photostability of the lysosome tracking probe is an essential parameter for long term imaging during physiological and morphological alterations *[24]*. To examine the photostability of **L-lyso**, photo-bleaching experiments for both **L-lyso** and LysoTracker Red DND-99 in HeLa cells were performed and the results were compared. After 1800 scans the fluorescence intensity of LysoTracker Red was reduced to 2%, however

the one-photon and two photon fluorescence intensity of **L-lyso** was 36% and 60% respectively **(Figure 2.15)**. These results showed that **L-lyso** exhibits better photostability compared to commercial LysoTracker Red and is suitable for long term lysosomal bio-imaging.

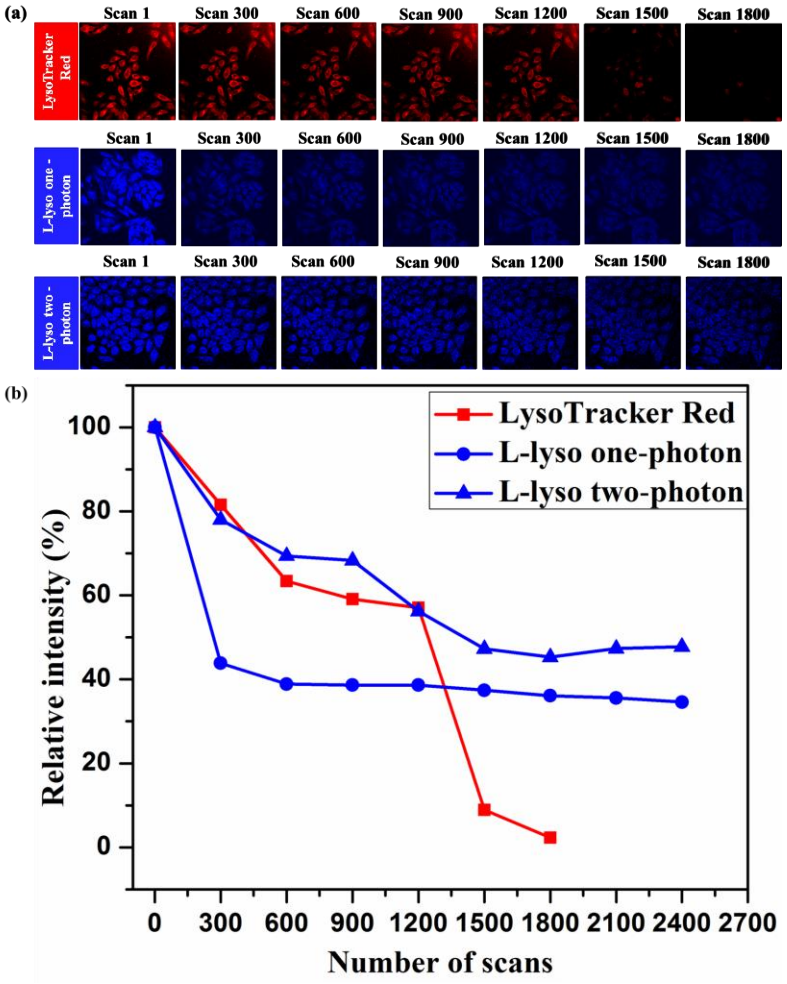

Figure 2.15. Comparisons of the *in vitro* photostability of LysoTracker Red and **L-lyso** in HeLa cell lines. **(a)** Confocal images of **L-lyso** (60 μM, One-photon microscopy: λ_{ex} = 405nm, TPM: λ_{ex} = 790 nm, λ_{em} = 415–470 nm) and LysoTracker Red (80 nM, λ_{ex} = 559 nm, λ_{em} = 580–700 nm) for photobleaching in HeLa cells. **(b)** Graph showing photobleaching result of LysoTracker Red and **L-lyso.**

2.2.10. Two-photon microscopy (TPM) study of L-lyso:

Two photon imaging is superior to one photon microscopy imaging in terms of low phototoxicity, low background signal, high photostability and more imaging depth (>500 μm) *[50]*. Thus, we

performed both one and two-photon co-localization imaging of **L-lyso** with LysoTracker Red which demonstrated a strong overlap in both cases **(Figure 2.16)**.

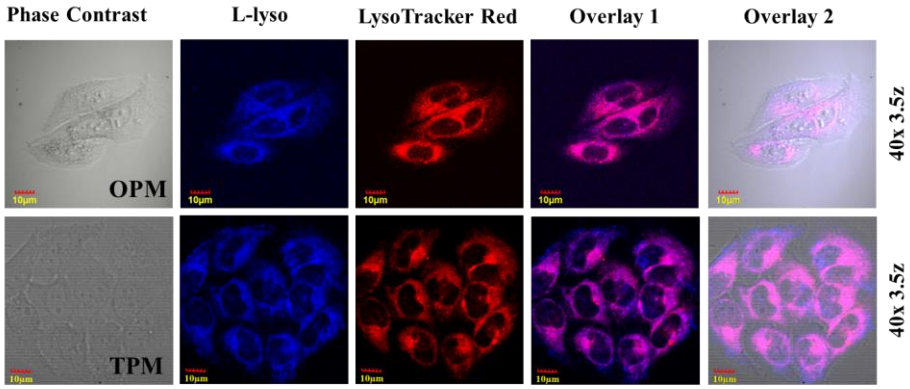

Figure 2.16. One-photon microscopy (OPM) and two-photon microscopy (TPM) images of **L-lyso** in live HeLa cells. **L-lyso** co-stained with **L-lyso** (60 μM, 10 min) and LysoTracker Red DND-99 (80 nM, 10 min). **L-lyso**: λ_{ex} = 405 nm (OPM) or 790 nm (TPM). LysoTracker Red DND-99, λ_{ex} = 559 nm (OPM). Scale bar: 10 μm.

2.2.11. Cell apoptosis study of L-lyso:

Lysosomes involve in cell apoptosis and cell death which leads to lysosomal membrane permeabilization. Therefore, to focus on tracking of lysosomes during apoptosis, we performed further studies. Carbonyl cyanide m-chloro-phenylhydrazone (CCCP) leads to dysfunction of ATP synthase by reducing mitochondrial membrane potential, resulting inadequate ATP supply to the cells *[51-52]*. CCCP, an uncoupler of oxidative phosphorylation was used to monitor apoptosis. MitoTraker Red, target mitochondria by utilizing its membrane potential *[53-54]*. After addition of 20 μM CCCP, red color stain of MitoTracker Red disappeared after 10 min **(Figure 2.17)**. This implies that the mitochondrial membrane potential starts abolishing and apoptosis is initiated. After 2 h, the cell morphology changes and apoptotic bodies begins to appear and after 3 h and 10 min, various apoptotic bodies were found. Simultaneously, the pH increases as a result of lysosomal membrane permeabilization, which causes a slight decrease in the

intensity of blue fluorescence in most of the cells, further validating the pH based quenching of **L-lyso**, indicating lysosomal physiological conditions.

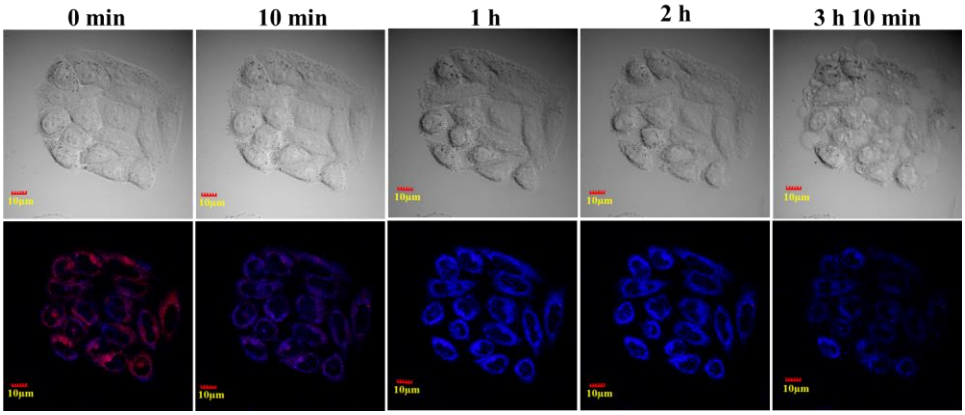

Figure 2.17. Tracking lysosome during cell apoptosis. Live HeLa cells stained with **L-lyso** (60 μM, 10 min) and MitoTracker Red CMXRos (80 nm, 10 min) and then CCCP (20 μM). (here only the merged images are depicted for clarity)

2.2.12. 3D tumor spheroids imaging by L-lyso:

In order to simulate an in vivo environment, 3D tumor spheroids, which consist of cells in different phases i.e. proliferating, hypoxic, apoptotic and necrotic cells, were used. In 3D multicellular tumor spheroids, the cell–cell interactions as well as cell–extracellular matrix interactions prominently simulate the natural pattern of the body environment *[55]*.

The imaging of tumor spheroid depth layers through microscopy study still has many technical challenges *[56]*. Two spheroids of different sizes were labelled by **L-lyso** and the fluorescence images were taken after every 2 μm section cutting along the Z-axis. The TP fluorescence images of spheroid showed deeper and uniform tissue penetration in the deeper cell layer as compared to one-photon fluorescence microscopy, where the fluorescence intensity was observed up to ~46 μm **(Figure 2.18 and Figure 2.19).** The results concluded that the two-photon excitation

light has a deeper penetrating power. Thus **L-lyso** may be further utilized in the imaging of lysosomes in tissue.

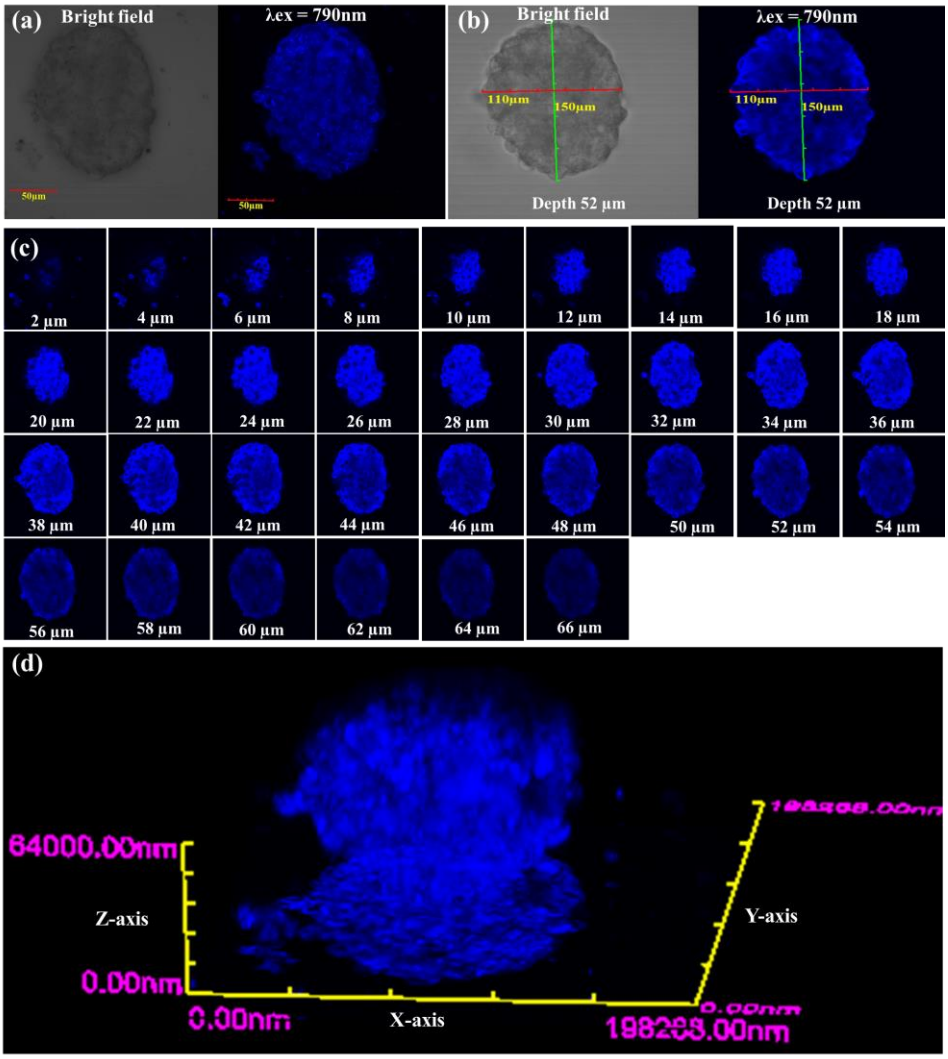

Figure 2.18. (a) Two-photon fluorescence images of 3D intact tumor spheroid after incubation of **L-lyso** (60 µM) for 1 h). **(b)** Image of at depth of 52 µm **(c)** The two-photon Z-stack images was captured after every 2 µm section from the top to bottom of tumor spheroid. **(d)** The two-photon Z-stack 3D images of intact spheroid. The images were captured under a 40× objective λ_{ex} = 790 nm; λ_{em} = 415–470 nm.

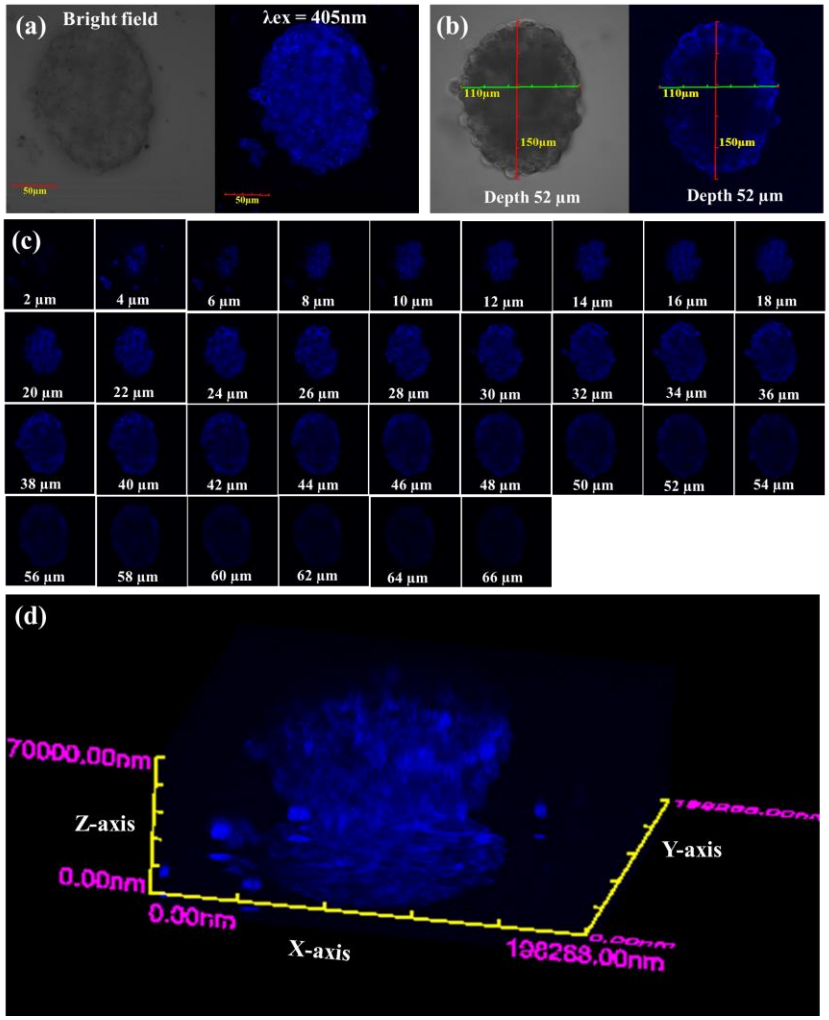

Figure 2.19. (a) One-photon fluorescence images of 3D HeLa tumor spheroid was incubated with **L-lyso (**60 µM for 1 h), **(b)** Image of at depth of 52 µm, **(c)** One-photon fluorescence Z-stack images were captured after every 2 µm section from top to bottom. **(d)** The one-photon 3D Z-stack picture of an intact HeLa spheroid. The images were captured under a 40× objective. λ_{ex} = 405 nm; λ_{em} = 415–470 nm.

2.2.11. Long-term tracking of lysosomes:

Lysosome tracking probes should possess the ability to stay in the lysosomes for a long period of time. Imaging of **L-lyso** was compared with LysoTracker Red. After 2nd passage (48 h), the fluorescence signal of LysoTracker Red diminished completely, whereas the **L-lyso** fluorescence signal was still clearly visible even after 72 h. This justified that **L-lyso** could track lysosomes in live cells for at least 3 days **(Figure**

2.20 and Figure 2.21). This confirmed the stable imaging of most of the physiological activities of the lysosomes in living cells.

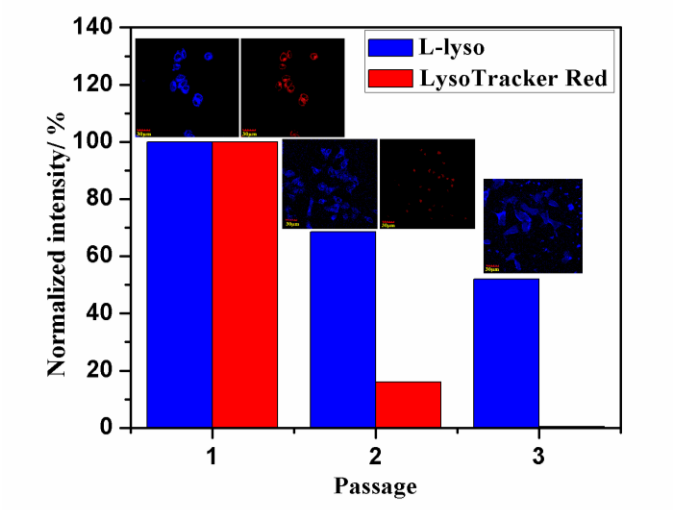

Figure 2.20. Normalized fluorescent intensities and images of live HeLa cells, which was stained with 60 μM of **L-lyso** and 60 μM of LysoTracker Red at different passages. Scale bar: 30 μm.

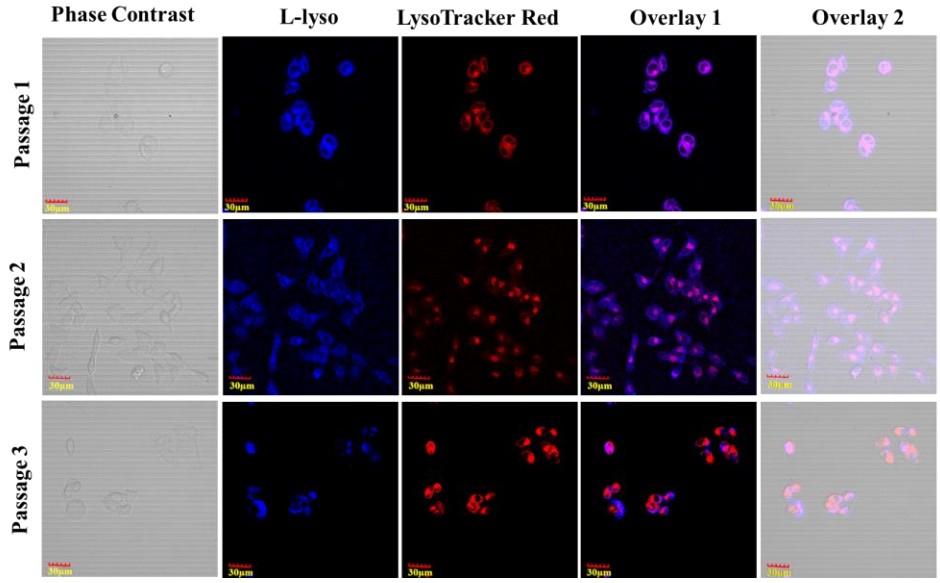

Figure 2.21. Two-photon fluorescence images of HeLa cells, passage 1 (after 24 h), passage 2 (after 48 h), and passage 3 (after 72 h) respectively. HeLa cells treated with **L-lyso** (60 μM, 10 min) and then incubated for 24 h. Lysosomes labeling with LysoTracker Red (80 nM, 10 min) was done just 15 min before cell imaging in 2nd and 3rd passage. **L-lyso** λ_{ex} = 790 nm; λ_{em} = 415–470 nm; LysoTracker Red λ_{ex} = 790 nm; λ_{em} = 580–700 nm. Overlay 1: overlay of the 2nd and 3rd columns. Overlay 2: overlay of the 1st, 2nd and 3rd columns. Scale bar: 30 μm.

2.3. Conclusions

In short, we have designed and synthesized a water soluble and non-cytotoxic organic probe **L-lyso**, in a facile manner with high yield. Furthermore, **L-lyso** was confirmed to be an effective two-photon fluorescent probe for long-term tracking of lysosomes. The excellent two-photon properties of **L-lyso** were further explored using in vivo replica by employing in 3D multicellular tumor spheroids. **L-lyso** also enabled tracking of the lysosomes during cell apoptosis, and a mechanistic pathway for cell uptake has also been discussed. More importantly, **L-lyso** has a large Stokes shift (148 nm) and higher photostability compared to the commercially available Lyso-Tracker Red DND-99.

2.4. Experimental Section

2.4.1. Materials:

4-(Diethylamino) salicylaldehyde, 3-amino-2-naththol purchased from TCI Chemicals (India) Pvt. Ltd., LysoTracker Red DND-99 and MitoTracker Red CMXRos were purchased from Invitrogen. MTT and carbonyl cyanide m-chlorophenylhydrazone (CCCP) from Sigma Aldrich Chemical Co., USA. Fetal bovine serum (FBS) and Dulbecco's modified eagle medium (DMEM) were purchased from Gibco. Minimum Essential Medium (MEM) received from Himedia. HeLa cells (cervical cancer cell line), MCF-7 (breast cancer) and A375 (skin melanoma), DU145 (prostate cancer) cells was obtained from National Centre for Cell Science, Pune. All other chemical reagents and solvents were obtained from Merck and S.D Fine Chem. Ltd. Ultrapure water obtained from arium® pro ultrapure water systems (Sartorius) and used throughout the experiments. All commercially available materials were used without further purification.

^{1}H NMR (400 MHz) and ^{13}C NMR (100 MHz) spectra were measured by Bruker Avance (III) instrument by using DMSO-d_6. FTIR spectrum was recorded by using Bio-Rad FTS 3000MX instrument on KBr pellets. The mass spectrum was recorded by Brucker-Daltonics, micrOTOF-QII mass spectrometer. Spectrophotometric measurements were performed by UV-vis spectrophotometer (Varian Cary 100) using a quartz cuvette with a path length of 1cm. FluoroMax-4 Spectrophotometer (HORIBA Scientific) was used for Fluorescence measurement. The excitation and emission slits were 5/5 nm for the emission measurements. pH-meter (LABMAN Scientific Instrument PVT. LTD) was used for pH measurements. The absorbance for MTT analysis was recorded by microplate reader (Synergy H1 BioTek microplate reader) at 570 nm. Fluorescence imaging experiments were performed by Olympus laser-scanning microscope, Mai Tai eHP Spectra physics femtosecond (fs) laser having power peak >450 KW, pulse width

≤ 70 fs, tuning range 690-1040 nm, average power >2.5 W, repetition rate 80 MHz ± 1 MHz was used to acquire the two photon fluorescence imaging and BD LSRFortessa TM Flow cytometry analysis. Image processing was done with the help of Olympus software (FV10-ASW 4.2). For bioimaging purpose (better cell permeability), **L-lyso** stock solution was prepared in 0.1M NaOH solution in water. Flow cytometry data were analyzed by DB FACSDiva software. pKa of amine and imine present in **L-lyso** is 3.27 and 3.55 respectively calculated by ACD software.

2.4.2. Synthesis of lysosome targeted probe (L-lyso):

4-(Diethylamino) salicylaldehyde (386 mg, 2 mmol), 3-amino-2-naththol (318 mg, 2 mmol) was taken in 25 mL of methanol and then added NaOH (80 mg, 2 mmol) was added. The reaction was continuously stirred at room temperature for 2 h. Reaction was monitored by TLC. After completion of the reaction, solvent was evaporated from rotator evaporator. Solid product was washed with acidic chilled water and then chilled water only for several times. Solid yellow precipitate was formed, which was filtered and dried in desiccator. Yield 90%, ^{1}H NMR (400 MHz,DMSO-d_6): δ 14.10 (s, 1H), 9.99 (s, 1H), 8.74 (s, 1H, -CH=N), 7.76 (d, 2H), 7.66 (d, 1H), 7.32 (dd, 2H), 7.26 (t, 1H), 7.22 (s, 1H), 6.30 (d, 1H), 5.99 (s, 1H), 3.40 (q, 4H), 1.12 (t, 6H) as shown in **Figure 2.22**. ^{13}C NMR (100 MHz, DMSO-d_6): δ166.45, 159.80, 152.35, 150.00, 137.67, 134.59, 132.71, 128.62, 127.57, 126.02, 125.61, 123.65, 115.70, 110.02, 109.61, 104.44, 97.57, 44.33, 13.02 depicted in **Figure 2.23**. IR (KBr, cm-1): 3415 (br), 3067 (s), 2957 (vs), 1707 (vs), 1611 (s), 1513 (s), 1465 (s), 1383 (s), 1252 (vs), 1180 (w), 1142 (s), 1110 (w), 1033 (s), 830 (s), 798 (s), 542 (s) as shown in **Figure 2.24)**. LCMS (m/z): $[M+1]^+$ 335.2 represented in **Figure 2.25**.

2.4.3. X-ray crystallography:

The crystal data of **L-lyso** was collected at 150(2) K by the means of graphite-monochromated Mo Kα (λα = 0.71073 Å). The procedure for

the data collection was evaluated by the support of CrysAlisPro CCD software. The data were collected by the standard phi-omega scan techniques and were scaled and reduced by using CrysAlisPro RED software. The structures were solved by the direct methods by using SHELXS-97 and refined by full matrix least squares with SHELXL-97, refining on F2 *[57-58]*. By direct methods the positions of all the atoms were obtained and all non-hydrogen atoms were refined anisotropically. All the remaining hydrogen atoms were placed in geometrically constrained positions and the data refined with isotropic temperature factors, generally 1.2 × Ueq of their parent atoms. The Hydrogen bonding interactions, mean plane analysis, and molecular drawings were obtained using the program Mercury (ver 3.1) and Diamond (ver 3.1d). The crystal and refinement data are summarized in **Table A1** and the selected bond distances and bond angles are shown in **Table A2**. All the Hydrogen atoms have been omitted for clarity in the molecular structure of **L-lyso**.

2.4.4. Two photon intensity measurement:

Mai Tai eHP Spectra physics femtosecond laser having power peak >450 KW, pulse width ≤ 70 fs, tuning range 690–1040 nm, average power >2.5 W, repetition rate 80 MHz ± 1 MHz was used to acquire the two photon fluorescence imaging. The two-photon fluorescence intensity was measured at 700–830 nm. Cervical cancer cells (HeLa), were seeded in confocal dishes and incubated for 22 hours. Live cells were stained with **L-lyso** (60 µM) in cell culture medium for 10 min then washed thrice with PBS. Images were captured at different wavelength. Maximum integrated intensity was observed at wavelength 790 nm. Autofluorescence of cells and spheroid was done without applying probe (control) using same setting of confocal and two photon Laser microscopes.

2.4.5. MTT cell viability assay:

In order to determine the cytotoxicity of **L-lyso** on living systems, we performed cell viability assay. 7000 HeLa cells $well^{-1}$ were seeded in 96-well plate in 100 µL media (Minimum essential medium, 10% (v/v) FBS and 1% antibiotics Penicillin-Streptomycin10,000 U/mL) and cultured for 24 hours for cell adhesion. **L-lyso** were dissolved in water (stock solution) and 20 µL added to each well in order to give final concentration ranging from 10-80 µM. Another MTT assay was done using concentration 100-600 µM. 20µL water was used as control. Experiment was done in quadruplet. Cells exposed to drug for 24 h and 34 h respectively. After that cells were washed with PBS (PBS, pH 7.4) and 100 µL MTT (0.5 mg/mL in phenol red free media) was added in each well. Cells incubated for next 4 hours at 37℃ and 5% CO_2 atmosphere. Then media was carefully removed and subsequently 100 µL DMSO was added in order to dissolve purple formazan crystals. After 20 minutes incubation, absorbance at 570 nm was measured using Synergy H1 Biotek microplate reader. The % cell viability was calculated as: % cell viability = [Mean O.D. of the drug treated cell/Mean O.D. of the control well] × 100

2.4.6. Flow cytometry:

HeLa cells were cultured in six-well tissue culture plates. When cells became 70% confluent then one well treated with 30 µM **L-lyso** and another well with 60 µM **L-lyso** for 10 min and control well left without any treatments. After that the cells were washed with PBS three times. Then harvested by trypsin and re-suspended in PBS. The samples were analyzed by BD LSRFortessa ^{TM} Flow cytometry with excitation at 405 nm and emission 415-470 nm. Data were analyzed by DB FACSDiva software. Total one lakh events were acquired for each sample.

2.4.7. Lysosome staining and co-localization studies in various cell lines: Cervical cancer (HeLa), Breast cancer (MCF-7), skin melanoma

(A375) and prostate cancer (DU145) cell lines were seeded in confocal dishes and incubated for 24 hours. For lysosome imaging, live cells were stained with **L-lyso** (60 μM) in cell culture medium for 10 min then washed thrice with PBS (pH = 7.4) and co-stain with LysoTracker Red (80 nM, 10 min) and incubated at 37°C and 5% CO_2. For mitochondria imaging, cells were stain with MitoTracker Red (80 nM) for 10 min. An Olympus laser scanning microscope was used for confocal imaging. Cells ware visualized at an excitation of λ_{ex} = 405 nm for **L-lyso** and λ_{ex} = 559 nm for LysoTracker Red as well as MitoTracker Red for one photon. **L-lyso** λ_{ex} = 790 nm for two photon imaging.

2.4.8. Per-pixel spatial colocalization analysis:

A significance test was performed for the images in blue (**L-lyso**) and red (LysoTracker red) channels using Costes' method *[59]* and the P-value was found to be 1.00, which indicates that a randomized image set does not produce better correlation/colocalization than the real image. Furthermore, Manders' coefficients were calculated based on the formulae presented by Manders et al *[60]* and the results are shown in **Table 2.1** indicating very good colocalization of the blue (**L-lyso**) and red (LysoTracker red) channels with each other on per-pixel level.

2.4.9. Cell uptake pathway studies:

In order to study probable mechanistic pathway of cellular uptake of **L-lyso**, HeLa cells were seeded in two confocal dishes and incubated at 37°C for 24 h. The cells in dishes were exposed with 60 μM **L-lyso** at 37°C or 4°C for 1 h. After that cells were washed with PBS three times and images captured by confocal microscope at excitation 405 nm and emission signal collected at 415-470 nm.

2.4.10 *In vitro* photostability study:

Cervical cancer cell line HeLa was seeded in two confocal dishes. Dishes were incubated with **L-lyso** (60 μM, 10 min) and LysoTracker Red DND-99 (80 nM, 10 min) separately. The cells were imaged using

confocal microscope and Mai Tai eHP Spectra physics femtosecond laser used for two photon imaging with no delay scan mode. Videos were recorded up to 1800 and scan 2650 scans for LysoTracker Red and **L-lyso** respectively. LysoTracker Red and **L-lyso** ware excited at 559 nm and 405 nm respectively for one photon. **L-lyso** ware excited at 790 nm for two photon imaging. Maximum intense signal of first scan was considered 100% for measuring relative decrease in intensity. Images at every 300 scans were obtained from video. The relative intensity decay spectrum upto 2650 scans.

2.4.11. Generation of multicellular 3D spheroids:

Multicellular tumor spheroids (MCTSs) were produced using the liquid overlay method *[61-62]*. When HeLa cells became 60% confluent in T-25 flack, they were harvested by trypsin/EDTA solution and resuspended in MEM complete media. Flat-bottom 96 well plates were coated with 60µL of a sterile 1.5% (wt/vol) agarose solution in complete MEM to make a non-adherent surface. 4000 cells were seeded in each agarose-coated well in 200µl complete MEM. The plates were incubated at 37°C and 5% CO_2 until spheroids formed. For compound treatment and imaging, spheroid were transfers in confocal disc followed by spheroids treatment by 60 µM **L-lyso** for 30 min, then image were captured by two photon as well as one photon confocal laser scanning microscopy.

2.4.12. Long-term imaging of lysosomes:

HeLa cells were seeded in 20 mm^2 Petri dish (ThermoFisher) and incubated at 37°C for 24 h. Then the cells were treated with 60 µM **L-lyso** (or 80 nM LysoTracker Red) for 10 min at 37°C. After that, cells were washed three times with PBS to remove the unbound probe. Then the cells were harvested and divided into two new sterile dishes and kept for further incubation for 24 h at 37°C. After 24 h incubation (passage 1), one dish was used for imaging and cells of another dish was harvested and 30% cells was transferred to the third dish and incubated at 37°C and

rest reseed in the same dish. Image was taken after 24 h (passage 2).Cells in the second dish was again transferred into forth dish and image captured after 24 h (passage 3).

NMR and mass spectrum of L-lyso

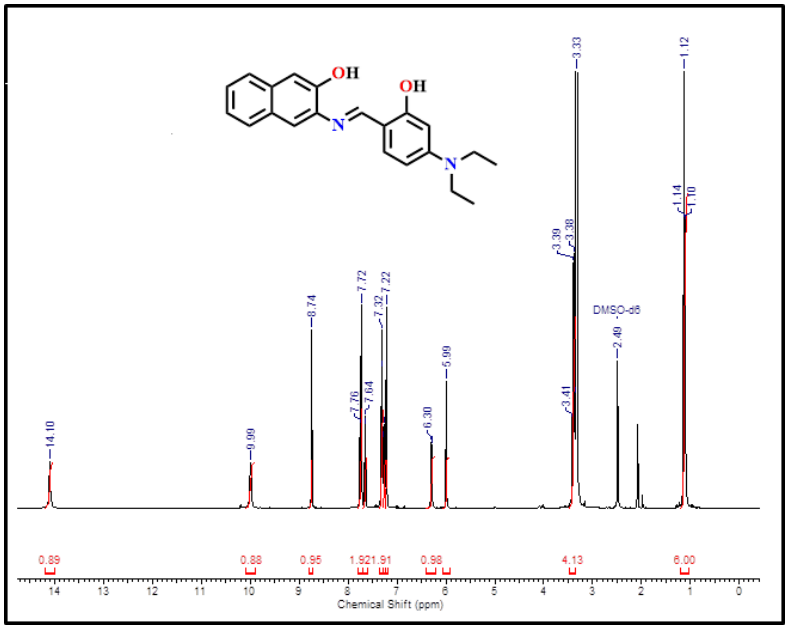

Figure 2.22. ^{1}H NMR spectrum of **L-lyso.**

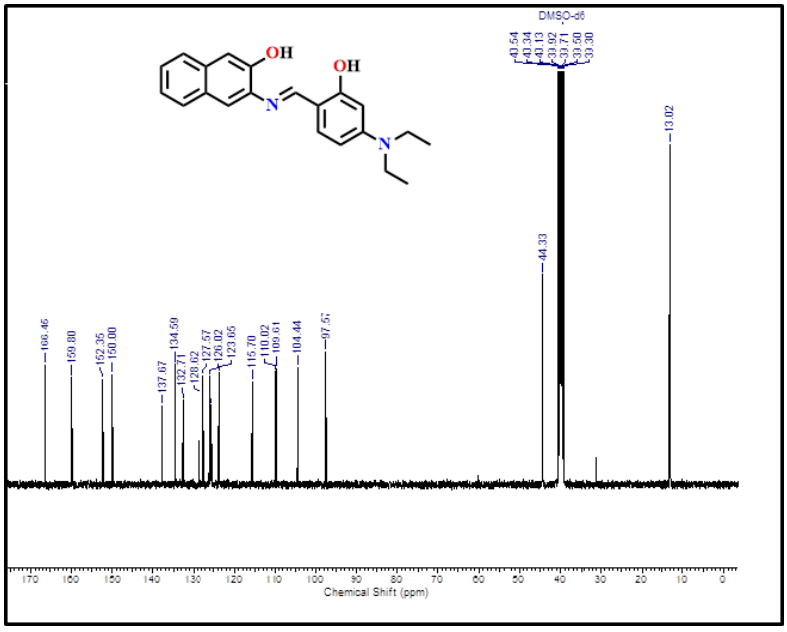

Figure 2.23. ^{13}C NMR spectrum of **L-lyso**

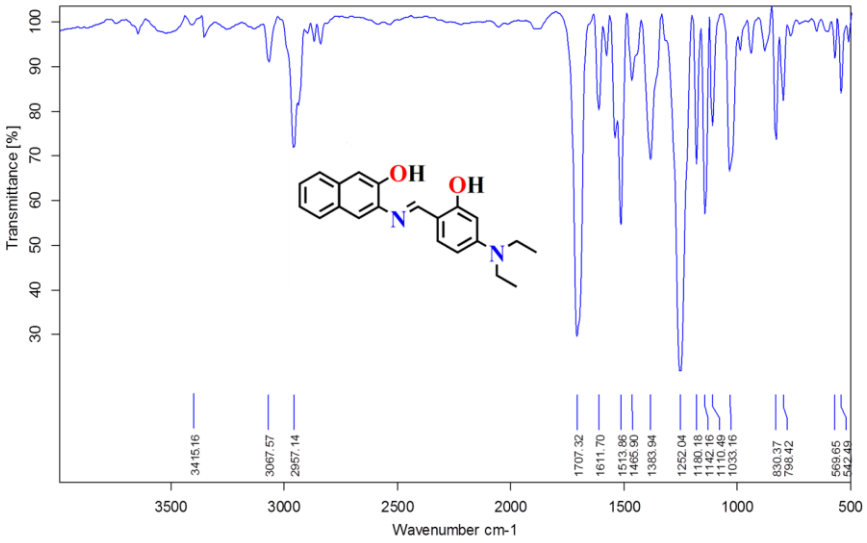

Figure 2.24. IR spectrum of **L-lyso**

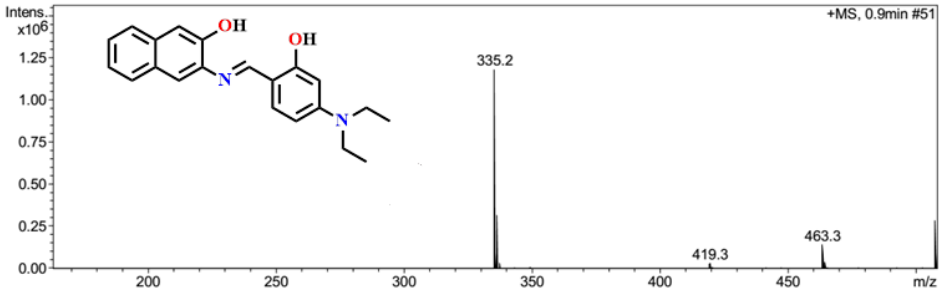

Figure 2.25. ESI-MS spectrum of **L-lyso**

2.5. References

[1]. Aizawa, S., Contu, V. R., Fujiwara, Y., Hase, K., Kikuchi, H., Kabuta, C., Wada, K., Kabuta, T. (2017), Lysosomal membrane protein SIDT2 mediates the direct uptake of DNA by lysosomes, Autophagy, 13, 218-222 (DOI: 10.1080/15548627.2016.1248019).

[2]. Li, Y., Chen, B., Zou, W., Wang, X., Wu, Y., Zhao, D., Sun, Y., Liu, Y., Chen, L., Miao, L., Yang, C., Wang, X. (2016), The lysosomal membrane protein SCAV-3 maintains lysosome integrity and adult longevity, J. Cell Biol., 215, 167-185 (DOI: 10.1083/jcb.201602090).

[3]. Jiang, P., Mizushima, N. (2014), Autophagy and human diseases, Cell Res., 24, 69-79 (DOI: 10.1038/cr.2013.161).

[4]. Kim, S. E., Overholtzer, M. (2013), Autophagy proteins regulate cell engulfment mechanisms that participate in cancer, *Semin. Cancer Biol.*, 23, 329-336 (DOI:10.1016/j.semcancer.2013.05.004).

[5]. Maes, H., Agostinis, P. (2014), Autophagy and mitophagy interplay in melanoma progression, Mitochondrion, 19 Pt A, 58-68 (DOI: 10.1016/j.mito.2014.07.003).

[6]. Raben, N., Puertollano, R. (2016), TFEB and TFE3: Linking Lysosomes to Cellular Adaptation to Stress, Annu. Rev. Cell Dev. Biol., 32, 255-278 (DOI: 10.1146/annurev-cellbio-111315-125407).

[7]. Platt, F. M. (2014), Sphingolipid lysosomal storage disorders, Nature, 510, 68-75 (DOI: 10.1038/nature13476).

[8]. Luzio, J. P., Hackmann, Y., Dieckmann, N. M., Griffiths, G. M. (2014), The biogenesis of lysosomes and lysosome-related organelles, Cold Spring Harb. Perspect. Biol., 6, a016840 (DOI: 10.1101/cshperspect.a016840).

[9]. Zhu, X., Sun, Y., Chen, D., Li, J., Dong, X., Wang, J., Chen, H., Wang, Y., Zhang, F., Dai, J., Pirraco, R. P., Guo, S., Marques, A. P., Reis, R. L., Li, W. (2017), Mastocarcinoma therapy synergistically promoted by lysosome dependent apoptosis

specifically evoked by 5-Fu@nanogel system with passive targeting and pH activatable dual function, J. Control Release, 254, 107-118 (DOI: 10.1016/j.jconrel.2017.03.038).

[10]. Hamasaki, M., Furuta, N., Matsuda, A., Nezu, A., Yamamoto, A., Fujita, N., Oomori, H., Noda, T., Haraguchi, T., Hiraoka, Y., Amano, A., Yoshimori, T. (2013), Autophagosomes form at ER-mitochondria contact sites, Nature, 495, 389-393 (DOI: 10.1038/nature11910).

[11]. Venkatesan, R., Park, Y. U., Ji, E., Yeo, E. J., Kim, S. Y. (2017), Malathion increases apoptotic cell death by inducing lysosomal membrane permeabilization in N2a neuroblastoma cells: a model for neurodegeneration in Alzheimer's disease, Cell Death Discov., 3, 17007 (DOI: 10.1038/cddiscovery.2017.7).

[12]. Ohmae, S., Noma, N., Toyomoto, M., Shinohara, M., Takeiri, M., Fuji, H., Takemoto, K., Iwaisako, K., Fujita, T., Takeda, N., Kawatani, M., Aoyama, M., Hagiwara, M., Ishihama, Y., Asagiri, M. (2017), Actin-binding protein coronin 1A controls osteoclastic bone resorption by regulating lysosomal secretion of cathepsin K, Sci. Rep., 7, 41710 (DOI: 10.1038/srep41710).

[13]. Dersh, D., Iwamoto, Y., Argon, Y. (2016), Tay-Sachs disease mutations in HEXA target the alpha chain of hexosaminidase A to endoplasmic reticulum-associated degradation, Mol. Biol. Cell, 27, 3813-3827 (DOI: 10.1091/mbc.E16-01-0012).

[14]. Saftig, P., Sandhoff, K. (2013), Cancer: Killing from the inside, Nature, 502, 312-313 (DOI: 10.1038/nature12692).

[15]. Zhang, F., Zhu, X., Gong, J., Sun, Y., Chen, D., Wang, J., Wang, Y., Guo, M., Li, W. (2016), Lysosome-mitochondria-mediated apoptosis specifically evoked in cancer cells induced by gold nanorods, Nanomedicine, 11, 1993-2006 (DOI: 10.2217/nnm-2016-0139).

[16]. Moors, T., Paciotti, S., Chiasserini, D., Calabresi, P., Parnetti, L., Beccari, T., van de Berg, W. D. (2016), Lysosomal Dysfunction and alpha-Synuclein Aggregation in Parkinson's Disease: Diagnostic Links, Mov. Disord., 31, 791-801 (DOI: 10.1002/mds.26562).

[17]. Yamamoto, T., Takabatake, Y., Takahashi, A., Kimura, T., Namba, T., Matsuda, J., Minami, S., Kaimori, J. Y., Matsui, I., Matsusaka, T., Niimura, F., Yanagita, M., Isaka, Y. (2017), High-Fat Diet-Induced Lysosomal Dysfunction and Impaired Autophagic Flux Contribute to Lipotoxicity in the Kidney, J. Am. Soc. Nephrol., 28, 1534-1551 (DOI: 10.1681/asn.2016070731).

[18]. Awad, O., Sarkar, C., Panicker, L. M., Miller, D., Zeng, X., Sgambato, J. A., Lipinski, M. M., Feldman, R. A. (2015), Altered TFEB-mediated lysosomal biogenesis in Gaucher disease iPSC-derived neuronal cells, Hum. Mol. Genet., 24, 5775-5788 (DOI: 10.1093/hmg/ddv297).

[19]. Pierzynska-Mach, A., Janowski, P. A., Dobrucki, J. W. (2014), Evaluation of acridine orange, LysoTracker Red, and quinacrine as fluorescent probes for long-term tracking of acidic vesicles, Cytometry A., 85, 729-737 (DOI: 10.1002/cyto.a.22495).

[20]. Myochin, T., Kiyose, K., Hanaoka, K., Kojima, H., Terai, T., Nagano, T. (2011), Rational design of ratiometric near-infrared fluorescent pH probes with various pKa values, based on aminocyanine, J. Am. Chem. Soc., 133, 3401-3409 (DOI: 10.1021/ja1063058).

[21]. Smith, D. G., McMahon, B. K., Pal, R., Parker, D. (2012), Live cell imaging of lysosomal pH changes with pH responsive ratiometric lanthanide probes, Chem. Commun., 48, 8520-8522 (DOI: 10.1039/c2cc34267g).

[22]. Li, G., Zhu, D., Xue, L., Jiang, H. (2013), Quinoline-based fluorescent probe for ratiometric detection of lysosomal pH, Org. Lett., 15, 5020-5023 (DOI: 10.1021/ol4023547).

[23]. Kim, H. J., Heo, C. H., Kim, H. M. (2013), Benzimidazole-based ratiometric two-photon fluorescent probes for acidic pH in live cells and tissues, J. Am. Chem. Soc., 135, 17969-17977 (DOI: 10.1021/ja409971k).

[24]. Wang, X., Nguyen, D. M., Yanez, C. O., Rodriguez, L., Ahn, H. Y., Bondar, M. V., Belfield, K. D. (2010), High-fidelity hydrophilic probe for two-photon fluorescence lysosomal imaging, J. Am. Chem. Soc., 132, 12237-12239 (DOI: 10.1021/ja1057423).

[25]. He, L., Li, Y., Tan, C. P., Ye, R. R., Chen, M. H., Cao, J. J., Ji, L. N., Mao, Z. W. (2015), Cyclometalated iridium(iii) complexes as lysosome-targeted photodynamic anticancer and real-time tracking agents, Chem. Sci., 6, 5409-5418 (DOI: 10.1039/c5sc01955a).

[26]. He, L., Tan, C. P., Ye, R. R., Zhao, Y. Z., Liu, Y. H., Zhao, Q., Ji, L. N., Mao, Z. W. (2014), Theranostic iridium(III) complexes as one- and two-photon phosphorescent trackers to monitor autophagic lysosomes, Angew. Chem. Int. Ed. Engl., 53, 12137-12141 (DOI: 10.1002/anie.201407468).

[27]. Zhang, D. Y., Zheng, Y., Tan, C. P., Sun, J. H., Zhang, W., Ji, L. N., Mao, Z. W. (2017), Graphene Oxide Decorated with Ru(II)-Polyethylene Glycol Complex for Lysosome-Targeted Imaging and Photodynamic/Photothermal Therapy, ACS Appl. Mater. Interfaces, 9, 6761-6771 (DOI: 10.1021/acsami.6b13808).

[28]. Zhang, J., Yang, M., Mazi, W., Adhikari, K., Fang, M., Xie, F., Valenzano, L., Tiwari, A., Luo, F. T., Liu, H. (2016), Unusual Fluorescent Responses of Morpholine-functionalized Fluorescent Probes to pH via Manipulation of BODIPY's HOMO and LUMO Energy Orbitals for Intracellular pH Detection, ACS Sens., 1, 158-165 (DOI: 10.1021/acssensors.5b00065).

[29]. Wang, H., Wu, Y., Shi, Y., Tao, P., Fan, X., Su, X., Kuang, G. C. (2015), BODIPY-based fluorescent thermometer as a lysosome-targetable probe: how the oligo(ethylene glycols) compete photoinduced electron transfer, Chemistry, 21, 3219-3223 (DOI: 10.1002/chem.201405853).

[30]. Ji, C., Zheng, Y., Li, J., Shen, J., Yang, W., Yin, M. (2015), An amphiphilic squarylium indocyanine dye for long-term tracking of lysosomes, J. Mater. Chem., 3, 7494-7498 (DOI: 10.1039/C5TB01738F).

[31]. Chen, X., Bi, Y., Wang, T., Li, P., Yan, X., Hou, S., Bammert, C. E., Ju, J., Gibson, K. M., Pavan, W. J., Bi, L. (2015), Lysosomal targeting with stable and sensitive fluorescent probes (Superior LysoProbes): applications for lysosome labeling and tracking during apoptosis, Sci. Rep., 5, 9004 (DOI: 10.1038/srep09004).

[32]. Yapici, N. B., Bi, Y., Li, P., Chen, X., Yan, X., Mandalapu, S. R., Faucett, M., Jockusch, S., Ju, J., Gibson, K. M., Pavan, W. J., Bi, L. (2015), Highly stable and sensitive fluorescent probes (LysoProbes) for lysosomal labeling and tracking, Sci. Rep., 5, 8576 (DOI: 10.1038/srep08576).

[33]. Liu, T., Xu, Z., Spring, D. R., Cui, J. (2013), A lysosome-targetable fluorescent probe for imaging hydrogen sulfide in living cells, Org. Lett., 15, 2310-2313 (DOI: 10.1021/ol400973v).

[34]. Wan, Q., Chen, S., Shi, W., Li, L., Ma, H. (2014), Lysosomal pH rise during heat shock monitored by a lysosome-targeting near-infrared ratiometric fluorescent probe, Angew. Chem. Int. Ed. Engl., 53, 10916-10920 (DOI: 10.1002/anie.201405742).

[35]. Shi, H., He, X., Yuan, Y., Wang, K., Liu, D. (2010), Nanoparticle-based biocompatible and long-life marker for lysosome labeling and tracking, Anal. Chem., 82, 2213-2220 (DOI: 10.1021/ac902417s).

[36]. Ho, Y. P., Leong, K. W. (2010), Quantum dot-based theranostics, Nanoscale, 2, 60-68 (DOI: 10.1039/b9nr00178f).

[37]. Li, Z., Song, Y., Yang, Y., Yang, L., Huang, X., Han, J., Han, S. (2012), Rhodamine-deoxylactam functionalized poly[styrene-alter-(maleic acid)]s as lysosome activatable probes for intraoperative detection of tumors, Chem. Sci., 3, 2941-2948 (DOI: 10.1039/C2SC20733H).

[38]. Farcal, L. R., Uboldi, C., Mehn, D., Giudetti, G., Nativo, P., Ponti, J., Gilliland, D., Rossi, F., Bal-Price, A. (2013), Mechanisms of toxicity induced by SiO2 nanoparticles of in vitro human alveolar barrier: effects on cytokine production, oxidative stress induction, surfactant proteins A mRNA expression and nanoparticles uptake, Nanotoxicology, 7, 1095-1110 (DOI: 10.3109/17435390.2012.710658).

[39]. Ohno, N., Hashimoto, T., Adachi, Y., Yadomae, T. (1996), Conformation dependency of nitric oxide synthesis of murine peritoneal macrophages by beta-glucans in vitro, Immunol. Lett., 52, 1-7 (DOI: 10.1016/S0165-2478(96)02639-9).

[40]. Zhu, L., Lv, W., Liu, S., Yan, H., Zhao, Q., Huang, W. (2013), Carborane enhanced two-photon absorption of tribranched fluorophores for fluorescence microscopy imaging, Chem. Commun., 49, 10638-10640 (DOI: 10.1039/c3cc46276e).

[41]. Saini, A. K., Natarajan, K., Mobin, S. M. (2017), A new multitalented azine ligand: elastic bending, single-crystal-to-single-crystal transformation and a fluorescence turn-on Al(iii) sensor, Chem. Commun., 53, 9870-9873 (DOI: 10.1039/c7cc04392a).

[42]. Chang, Y. C., Chen, Y. D., Chen, C. H., Wen, Y. S., Lin, J. T., Chen, H. Y., Kuo, M. Y., Chao, I. (2008), Crystal engineering for pi-pi stacking via interaction between electron-rich and electron-deficient heteroaromatics, J. Org. Chem., 73, 4608-4614 (DOI: 10.1021/jo800546j).

[43]. Yao, S., Ahn, H. Y., Wang, X., Fu, J., Van Stryland, E. W., Hagan, D. J., Belfield, K. D. (2010), Donor-acceptor-donor fluorene derivatives for two-photon fluorescence lysosomal imaging, J. Org. Chem., 75, 3965-3974 (DOI: 10.1021/jo100554j).

[44]. Son, J. H., Lim, C. S., Han, J. H., Danish, I. A., Kim, H. M., Cho, B. R. (2011), Two-photon Lysotrackers for in vivo imaging, *J. Org. Chem.*, 76, 8113-8116 (DOI: 10.1021/jo201504h).

[45]. Sumalekshmy, S., Fahrni, C. J. (2011), Metal Ion-Responsive Fluorescent Probes for Two-Photon Excitation Microscopy, Chem. Mater., 23, 483-500 (DOI: 10.1021/cm1021905).

[46]. Qiu, K., Huang, H., Liu, B., Liu, Y., Huang, Z., Chen, Y., Ji, L., Chao, H. (2016), Long-Term Lysosomes Tracking with a Water-Soluble Two-Photon Phosphorescent Iridium(III) Complex, *ACS* Appl. Mater. Interfaces, 8, 12702-12710 (DOI: 10.1021/acsami.6b03422).

[47]. Godfrey, W. L., Hill, D. M., Kilgore, J. A., Buller, G. M., Bradford, J. A., Gray, D. R., Clements, I., Oakleaf, K., Salisbury, J. J., Ignatius, M. J., Janes, M. S. (2005), Complementarity of Flow Cytometry and Fluorescence Microscopy, Microsc. Microanal., 11, 246-247 (DOI: 10.1017/S1431927605510316).

[48]. Dong, B., Song, X., Wang, C., Kong, X., Tang, Y., Lin, W. (2016), Dual Site-Controlled and Lysosome-Targeted Intramolecular Charge Transfer-Photoinduced Electron Transfer-Fluorescence Resonance Energy Transfer Fluorescent Probe for Monitoring pH Changes in Living Cells, Anal. Chem., 88, 4085-4091 (DOI: 10.1021/acs.analchem.6b00422).

[49]. Fan, F., Nie, S., Yang, D., Luo, M., Shi, H., Zhang, Y. H. (2012), Labeling lysosomes and tracking lysosome-dependent apoptosis with a cell-permeable activity-based probe, Bioconjug. Chem., 23, 1309-1317 (DOI: 10.1021/bc300143p).

[50]. Xu, Q., Heo, C. H., Kim, G., Lee, H. W., Kim, H. M., Yoon, J. (2015), Development of imidazoline-2-thiones based two-photon fluorescence probes for imaging hypochlorite generation in a co-culture system, Angew. Chem. Int. Ed. Engl., 54, 4890-4894 (DOI: 10.1002/anie.201500537).

[51]. Park, J. S., Kang, D. H., Bae, S. H. (2015), p62 prevents carbonyl cyanide m-chlorophenyl hydrazine (CCCP)-induced apoptotic cell death by activating Nrf2, Biochem Biophys Res Commun, 464, 1139-1144 (DOI: 10.1016/j.bbrc.2015.07.093).

[52]. Itami, N., Shiratsuki, S., Shirasuna, K., Kuwayama, T., Iwata, H. (2015), Mitochondrial biogenesis and degradation are induced by CCCP treatment of porcine oocytes, Reproduction, 150, 97-104 (DOI: 10.1530/rep-15-0037).

[53]. Chen, Y., Qiao, L., Ji, L., Chao, H. (2014), Phosphorescent iridium(III) complexes as multicolor probes for specific mitochondrial imaging and tracking, Biomaterials, 35, 2-13 (DOI: 10.1016/j.biomaterials.2013.09.051).

[54]. Huang, S., Han, R., Zhuang, Q., Du, L., Jia, H., Liu, Y., Liu, Y. (2015), New photostable naphthalimide-based fluorescent probe for mitochondrial imaging and tracking, Biosens. Bioelectron., 71, 313-321 (DOI: 10.1016/j.bios.2015.04.056).

[55]. Patra, B., Peng, C. C., Liao, W. H., Lee, C. H., Tung, Y. C. (2016), Drug testing and flow cytometry analysis on a large number of uniform sized tumor spheroids using a microfluidic device, Sci. Rep., 6, 21061 (DOI: 10.1038/srep21061).

[56]. Zhang, P., Huang, H., Chen, Y., Wang, J., Ji, L., Chao, H. (2015), Ruthenium(II) anthraquinone complexes as two-photon luminescent probes for cycling hypoxia imaging in vivo, Biomaterials, 53, 522-531 (DOI: 10.1016/j.biomaterials.2015.02.126).

[57]. Sheldrick, G. M. (2015), Crystal structure refinement with SHELXL, Acta Crystallogr. C Struct. Chem., 71, 3-8 (DOI: 10.1107/s2053229614024218).

[58]. Sheldrick, G. M. (2015), SHELXT - integrated space-group and crystal-structure determination, Acta Crystallogr. A Found. Adv., 71, 3-8 (DOI: 10.1107/s2053273314026370).

[59]. Costes, S. V., Daelemans, D., Cho, E. H., Dobbin, Z., Pavlakis, G., Lockett, S. (2004), Automatic and quantitative measurement of protein-protein colocalization in live cells, Biophys. J., 86, 3993-4003 (DOI: 10.1529/biophysj.103.038422).

[60]. Manders, E. M. M., Verbeek, F. J., Aten, J. A. (1993), Measurement of co-localization of objects in dual-colour confocal images, J. Microsc., 169, 375-382 (DOI: 10.1111/j.1365-2818.1993.tb03313.x).

[61]. Friedrich, J., Seidel, C., Ebner, R., Kunz-Schughart, L. A. (2009), Spheroid-based drug screen: considerations and practical approach, Nat. Protoc., 4, 309-324 (DOI: 10.1038/nprot.2008.226).

[62]. Boo, L., Ho, W. Y., Ali, N. M., Yeap, S. K., Ky, H., Chan, K. G., Yin, W. F., Satharasinghe, D. A., Liew, W. C., Tan, S. W., Ong, H. K., Cheong, S. K. (2016), MiRNA Transcriptome Profiling of Spheroid-Enriched Cells with Cancer Stem Cell Properties in Human Breast MCF-7 Cell Line, Int. J. Biol. Sci., 12, 427-445 (DOI: 10.7150/ijbs.12777).

MCHAPTER 3

Fluorescent Organic Probe Selectively Label an Endoplasmic Reticulum; Monitoring ER Stress and Vesicular Transport to Lysosomes

3.1. Introduction

The Endoplasmic reticulum (ER) plays an important role in various biological processes such as synthesis, proper folding, modification of proteins and their trafficking to other organelles. It also regulates intracellular calcium ions and lipid metabolism *[1-3]*. With the help of vesicles, intracellular movement of constituents is carried out between different cell organelles *[4]*. Transport of materials to specific organelles depends on the target motifs of the transported proteins, conformational variation and chemical modifications *[5]*. Various human diseases are caused by the improper function of the vesicle transport process, including Alzheimer's disease *[6]*, and several associated genetic disorders such as Niemann–Pick disease type C *[7]*, Lafora disease *[8]*, and Tay–Sachs disease *[9]*.

The ER is extremely sensitive to stress, which causes aggregation and accumulation of unfolded proteins *[10]*. Since protein aggregation is harmful to cells, ER stress leads to various pathological conditions, which include stroke, heart disease, neurodegenerative diseases, ischaemia, diabetes, and cancer *[11-13]*. For imaging of the ER, various fluorescent probes have been developed, such as DiOC5(3), DiOC6(3) and hexyl rhodamine B *[14-15]*. Nevertheless, these probes have some limitations like low selectivity, poor photo-stability, non-specific localization to other organelles and broad emission spectrum insensitivity *[16-18]*. The green fluorescent protein (GFP) fusion technology, which is commonly used for monitoring vesicle transport, is restricted to living organisms *[19]* due to

the fact that artificial fusion gene transfection requires hostile conditions *[20]*, which can alter the organisms' cellular metabolism *[21]*. Cells expressing GFP undergo oxidative stress *[22]* and apoptosis *[21]*. Thus, a consistent fluorescent ER targeting probe that monitors vesicular transport should exhibit ER selective localization, a narrow emission spectrum, photostability, high cell viability and display two-photon excited fluorescence. Two-photon microscopy (TPM) is an attractive instrument for live cell and tissue imaging where the fluorophore gets excited by two near-infrared photons (>700 nm). This technique has numerous advantages over one-photon microscopies such as low phototoxicity to cells, negligible background interference, limited photobleaching and a deep penetration depth (>500 μm) *[23]*. Therefore, TPM is a significant device for bio-imaging within living tissue or cells and is rarely explored in small molecules *[24]*.

The probes reported so far for endoplasmic reticulum imaging are generally based on one-photon microscopy based on rhodol analogs, complex organic fluorophores and metal-complexes **(Chart 3.1)**, which involves multi-step tedious synthetic routes *[1, 17-18, 25-27]*.

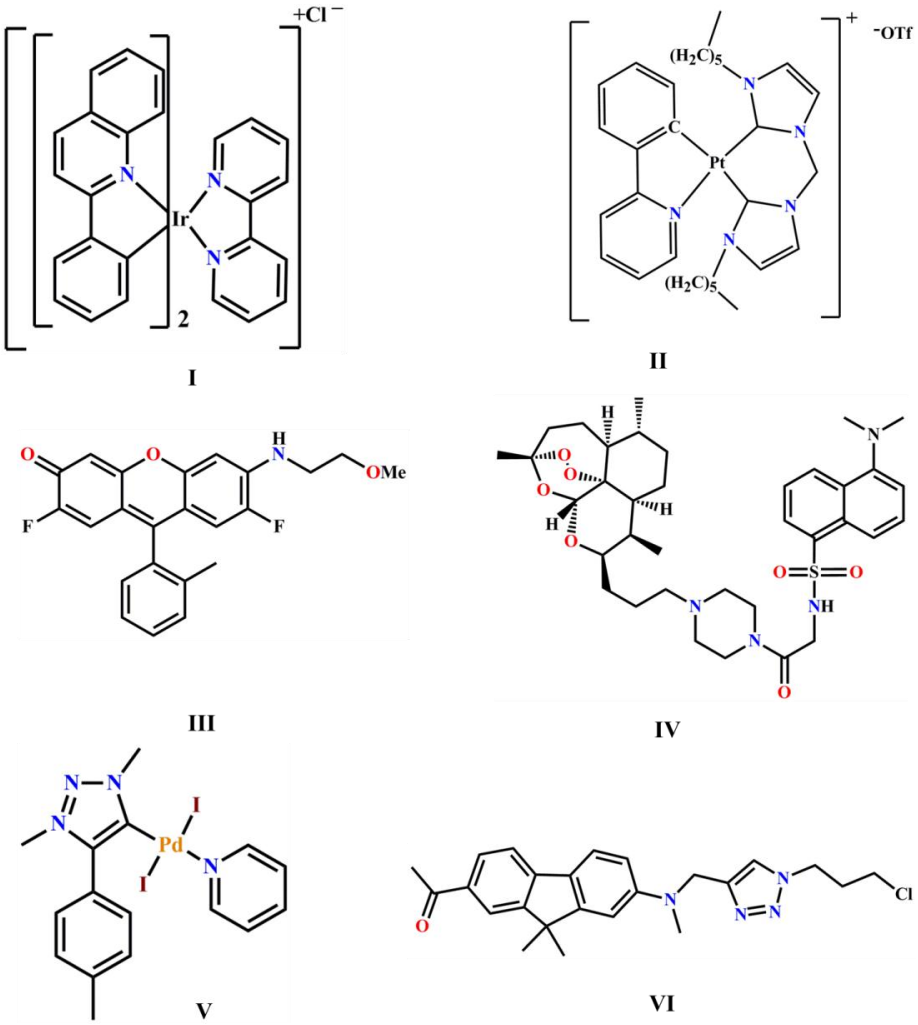

Chart 3.1. ER targeting multistep reported compounds.

In this chapter, we report the design and facile synthesis of a Schiff base **ERLp** with sharp fluorescence emission and high photostability. The morphological divergence of the Endoplasmic Reticulum (ER) during stress is a powerful indicator of several diseases. A new two-photon, non-cytotoxic, fluorescent probe (**ERLp**) was designed and synthesized in a facile manner for selective tracking of Endoplasmic Reticulum (ER) with high Pearson's co-localization coefficient 0.91, in live cells and tumor spheroids. Further, ER stress during cell apoptosis and vesicular transport from the ER to the lysosomal compartment were also explored by employing **ERLp**. Therefore, **ERLp** can be used as a potent tool for examining vesicle transport or ER stress associated diseases in real time.

3.2. Results and discussion

3.2.1. Synthesis and characterization:

We have designed and synthesized a one-step Schiff base organic probe **ERLp** by the simple condensation reaction of 2-hydroxy-1 naphthaldehyde with 4-(aminomethyl)-2-methoxyphenol hydrochloride in methanol at room temperature, resulting in a light brown solid in 92% yield **(Scheme 3.1)**. **ERLp** was well characterized by ^{1}H, ^{13}C NMR, FTIR and mass spectroscopy and for chemical stability in solution; the ^{1}H NMR spectrum of **ERLp** was recorded after 2 days in DMSO-d_6 solution at 25 °C and found to be stable.

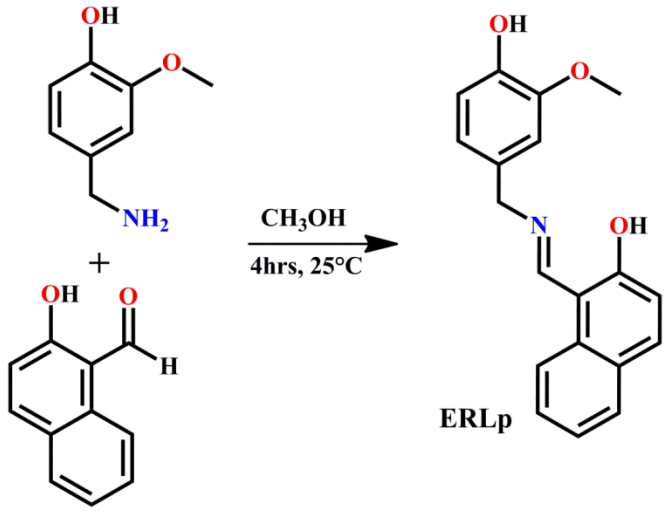

Scheme 3.1. Schematic representation of synthesis of **ERLp**.

3.2.2. Molecular Structure of ERLp:

It was further authenticated by single crystal X-ray diffraction study. The single crystal of **ERLp** was grown by slow evaporation of methanol solution at 25°C and crystallized in monoclinic crystal system with centrosymmetry $P2_1/n$ space group *[28]* depicted in **Tables A3 and A4 and Figure 3.1**. The non-planar crystal structure of **ERLp** is due to the presence of naphthyl and methoxy phenolic ring in two different planes *via* the imine (>C=N–) unit, with a torsion angle of 70.62°.

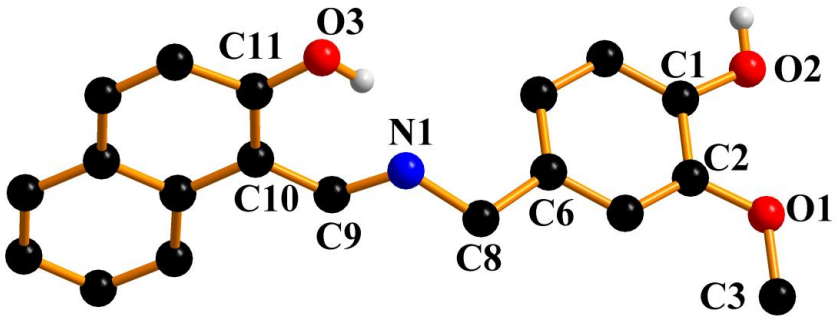

Figure 3.1. Crystal structure of **ERLp.**

The packing features of **ERLp** reveal the presence of intra molecular H-bonding interaction O(3)–H(3)···N(1) = 1.885(0) Å and inter molecular H-bonding interactions O(3)–H(2)···O(2) = 1.835(0) Å, O(3)–H(3)···O(3) = 2.561(1) Å resulting in a 1D-chain along *c*-axis **(Figure 3.2)**. This 1D-chains are further interconnected to each other by H-bonding interactions through C(18)– H(18)···O(2) = 2.606(1) Å forming supra-molecular 2D-network along *a*-axis, where C(18)–H(18) is donor and O(2) is acceptor **(Figure 3.3)**. It is to be noted that the presence of four kinds of donor-acceptor interactions O(3)–H(2)···O(2) = 1.835(0) Å, C(9)–H(9)···O(2) = 2.661(0) Å, C(9)– H(9)···O(1) = 2.561(0) Å and C(18)–H(18)···O(2) = 2.606(1) Å which provide an opportunity to extend the dimensionality to supra-molecular 3D-architecture along *b*-axis **(Figure 3.4)**. Further, the 3D supra-molecular network is stabilized by π···π stacking interactions (3.931 Å) between the two phenyl rings of the different moieties in a *tail-to-tail* arrangement **(Figure 3.5).**

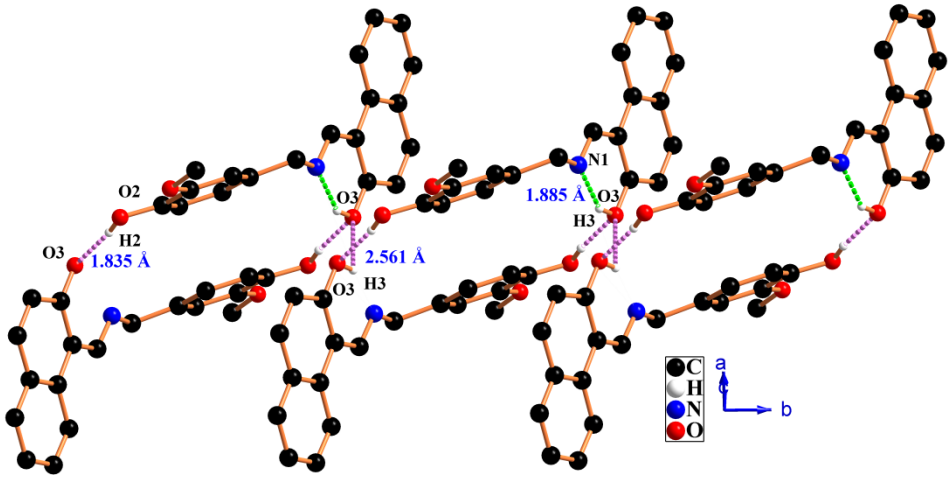

Figure 3.2. 1D chain along *c*-axis in **ERLp** in the presence of inter and intra molecular H-bonding (Purple and green dots represent inter and intra H-bond respectively).

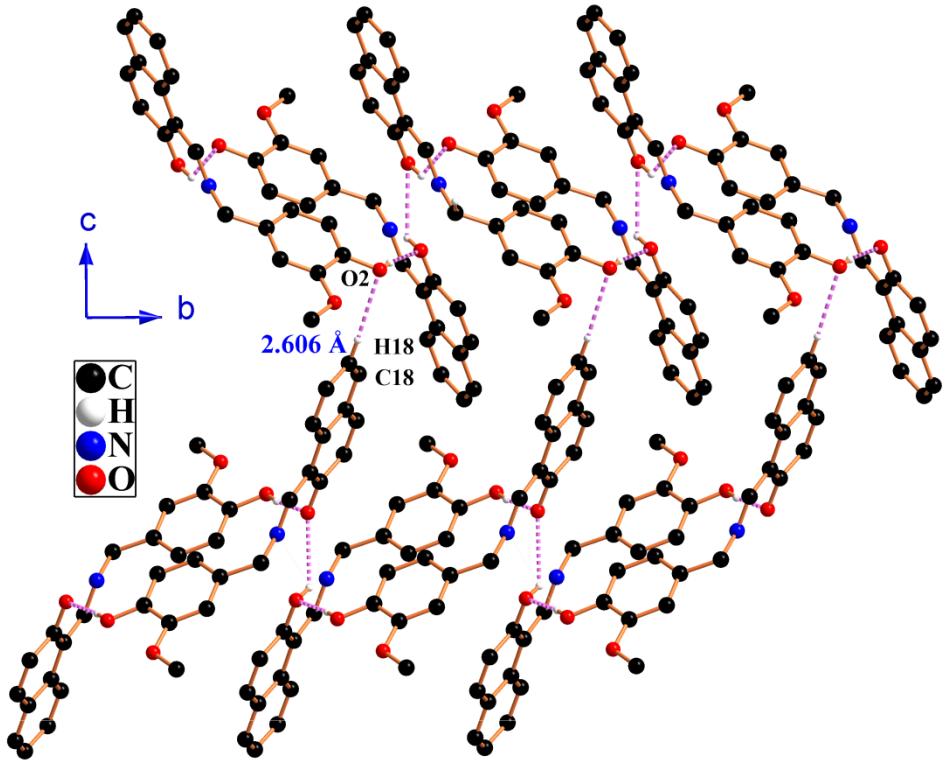

Figure 3.3. 2D network chain of **ERLp** along *a*-axis in the presence of inter molecular H-bonding (Purple dot represent H-bond).

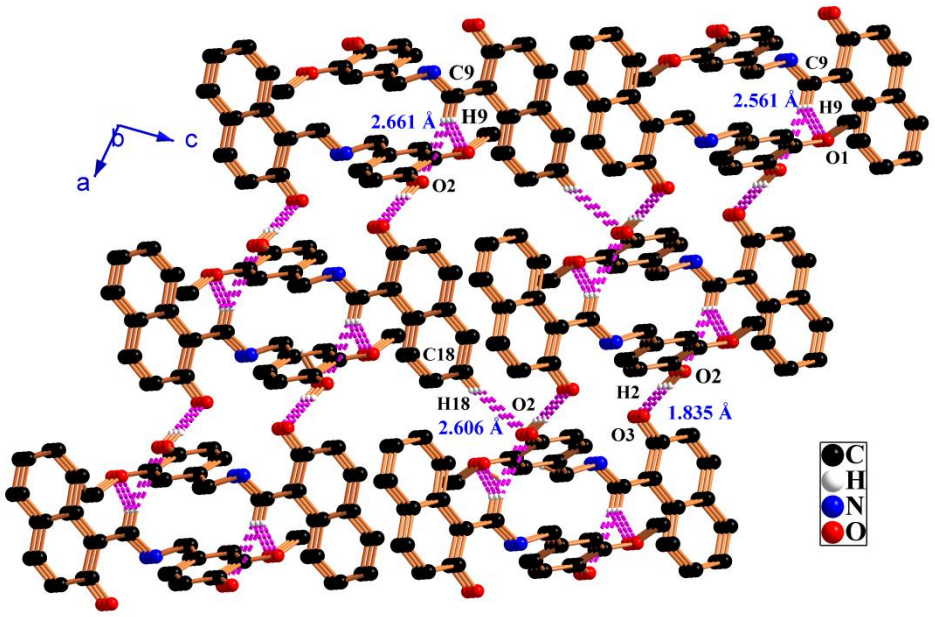

Figure 3.4. 3D network of **ERLp** along *b*-axis in the presence of inter molecular H-bonding (Purple dot represent H-bond).

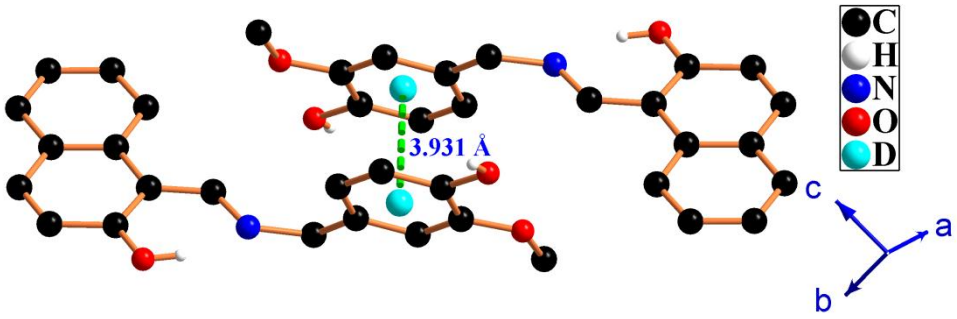

Figure 3.5. Ball and stick model of **ERLp** showing the π···π interaction between two phenyl rings of a different molecule. (fragmented green line represented as π···π interaction).

3.2.3. photophysical properties of ERLp:

To examine the photo-physical behavior of ERLp, absorption and emission spectrum were recorded in acetonitrile solution **(Figure 3.6)**. The ERLp exhibits absorption band at 230 nm that corresponds to π→π* which indicates the presence of aromatic moiety whereas the bands at 306, 400 and 419 nm are due to n→π* because of the presence of hetero-atom. Further, a strong and sharp emission band at 423 nm was observed in the

fluorescence spectra of **ERLp** in acetonitrile solution **(Figure 3.6)** but in PBS (Phosphate Buffer Saline) it shows slightly hypochromic-shift as compared to the acetonitrile solution this may be due to the presence of hydrophobic methoxy group in the **ERLp (Figure 3.7)**. Moreover, the fluorescence intensity of **ERLp** was measured at different pH (pH 9.45-4.14) which shows that the fluorescence signal is almost stable **(Figure 3.8)**. The two-photon fluorescence intensity was confirmed at 740nm **(Figure 3.9 and Figure 3.10)**.

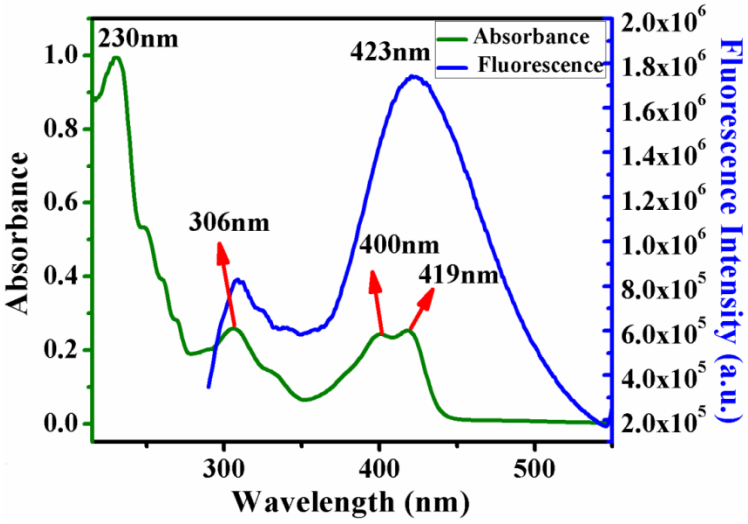

Figure 3.6. Absorption and emission spectra of ERLp (10 μM) in acetonitrile solution.

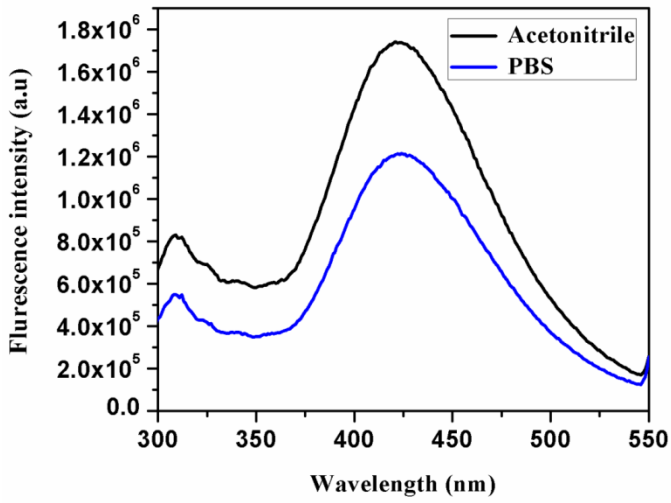

Figure 3.7. Emission spectra of **ERLp** (10μM) in acetonitrile and PBS.

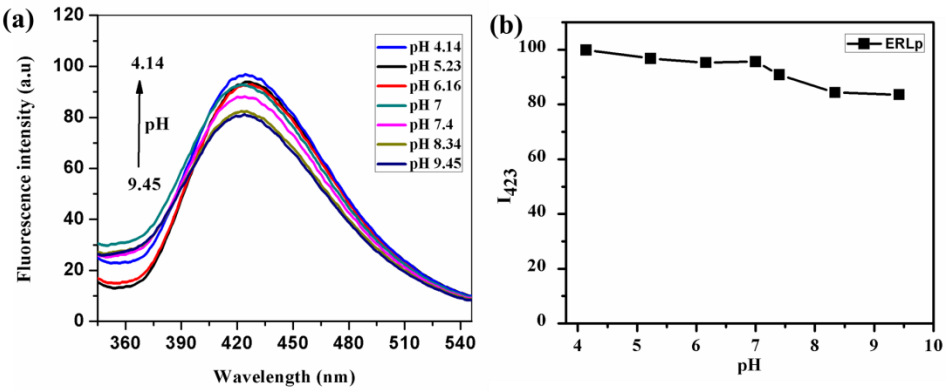

Figure 3.8. (a) pH-sensitive emission spectra of **ERLp** (10 μM) in PBS buffer. (b) The plot of the emission intensity of **ERLp** at 423 nm versus various pH values.

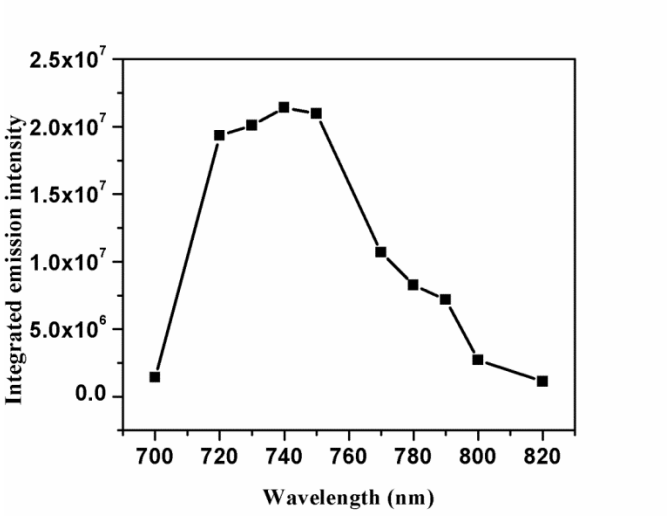

Figure 3.9. Two-photon integrated fluorescence emission intensity of **ERLp** at excitation wavelengths 700–820 nm in live HeLa cells.

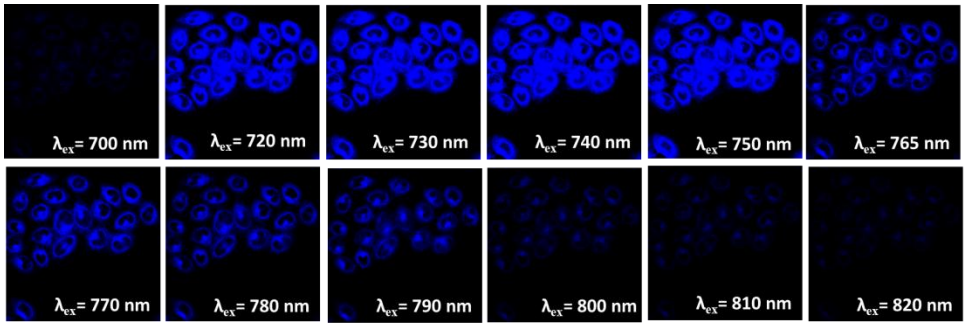

Figure 3.10. Two-photon microscopy (TPM) images of HeLa cells labeled with **ERLp**. The excitation wavelength was 700 to 820 nm. Maximum fluorescence intensity was obtained at λ_{ex} = 740 nm

3.2.4. Cell viability assay of ERLp:

The excellent photo-physical properties and highly fluorescent nature of **ERLp** prompted us to explore the cell activities by employing **ERLp** probe. The probe **ERLp** was found to be biocompatible as it does not interfere in the cells proliferation up to tested concentration of 140μM for 24h as confirmed by MTT assay **(Figure 3.11)**.

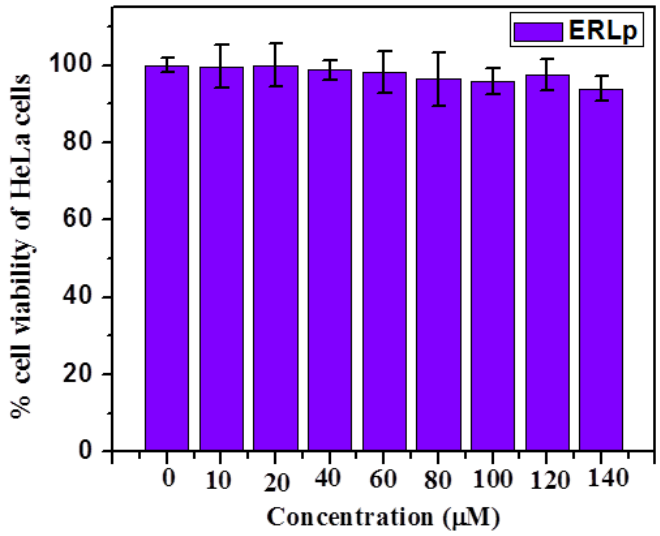

Figure 3.11. Cell viability assay of **ERLp** was determined by the MTT assay after 24 h incubation at 37°C and the results shown in mean ± SD of three separate measurements.

3.2.5. Flow cytometry studies of ERLp:

For profound cell activities, flow cytometry and fluorescence microscopy techniques were introduced, which provide data of single-cell analysis. Flow cytometry provides high-quality fluorescence signals from large populations of cells in flow (suspension cells), whereas fluorescence microscopy provides detailed evidence of the target morphology in small sample sizes *[29]*. Hence, fluorescence imaging analysis was done by flow cytometry. The mean fluorescence intensity of control cells (unstained cells) corresponds to 70 and those of **ERLp** treated cells with 40 μM and 80 μM were found to be 1141 and 1772, respectively, which leads to the movement of a huge population of cells towards the right with respect to

the control **(Figure 3.12)**. This reveals that **ERLp** can uniformly label a huge population of cells.

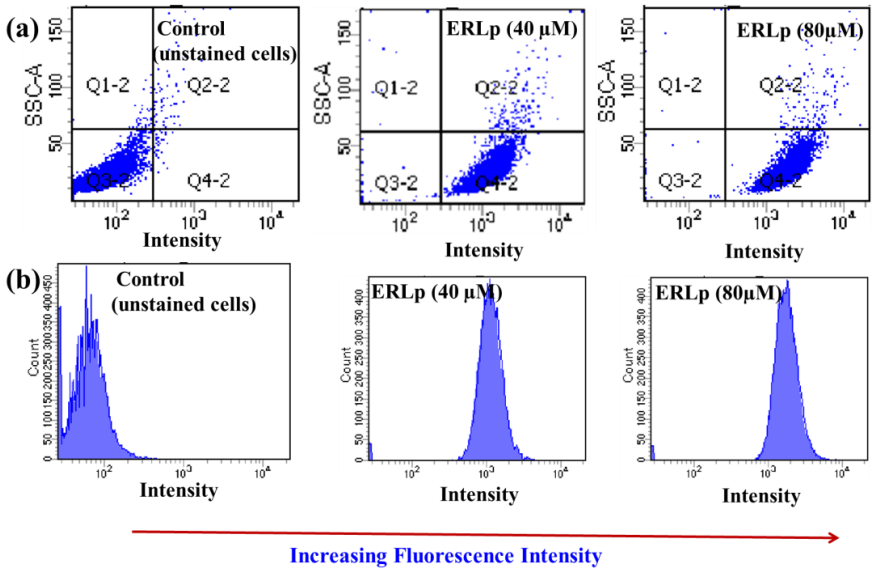

Figure 3.12. Concentration-dependent flow cytometry analysis of **ERLp** in live HeLa cells. (a) Scatter plot. (b) Histogram. **ERLp**: λ_{ex} = 405 nm; λ_{em} = 415–470 nm.

3.2.6. Concentration dependent study of ERLp:

Concentration dependent live cell staining was performed with **ERLp**. As the time of incubation is increased from 10 min to 2 h, staining is possible even at low concentrations up to 5 µM **(Figure 3.13 and Figure 3.14)**. The **ERLp** concentration used for the cellular experiment is higher than that of the standard ER tracker due to the lower quantum yield of **ERLp** (12%) than the commercial ER Tracker Red as shown in **Table 3.1** *[30]*.

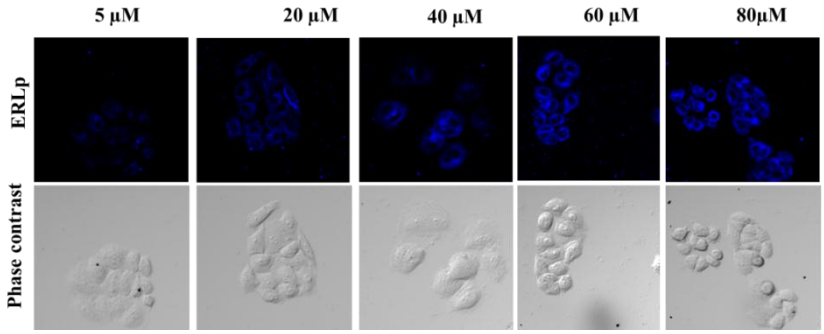

Figure 3.13. Concentration-dependent staing of live cells using **ERLp** for 10 min incubation time (λex = 405 nm; λem = 415-470 nm).

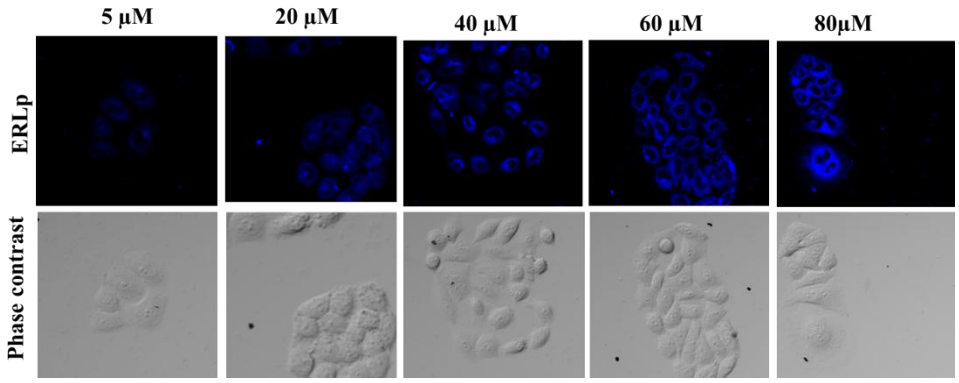

Figure 3.14. Concentration-dependent staining of live cells using **ERLp** for 2h incubation time (λ_{ex} = 405 nm; λ_{em} = 415-470 nm).

Table 3.1. The quantum yield of **ERLp** and ER tracker red

Sensor	Solvent	Excitation	Emission	Quantum yield(ΦF)
Trptophan (standard)	H_2O	280 nm	300-380 nm	0.14
ERLp	H_2O	280 nm	360-494 nm	0.12
Quinine Sulfate (standard)	0.1 M H_2SO_4	350 nm	400-600 nm	0.54
ER traker red	H_2O	587 nm	598-650 nm	0.35

3.2.7. The photostability of ERLp:

The photostability of the ER tracking marker is an important parameter for long-term bio-imaging during morphological and physiological changes or ER stress study. Thus, an **ERLp** photobleaching experiment was performed both in solution and in live cells. An aqueous solution of **ERLp** was continuously UV illuminated (254 nm) at 25 °C, and no drastic change in the fluorescence intensity of **ERLp** was observed up to 80 min **(Figure 3.15)**. Further **ERLp** and ER Tracker Red were

explored for the photobleaching experiment using HeLa cells. The result indicates that the two-photon fluorescence intensity of **ERLp** after 1800 scans is retained at an impressive 64%, whereas the fluorescence intensity of ER Tracker Red after 1800 scans diminished to 28% **(Figure 3.16)**. Photostability was high in the cells due to the visible light range wavelength used in confocal microscopy, whereas the infrared light region is used in two photon microscopy. Thus, **ERLp** shows high photo-stability for long-term live cell imaging.

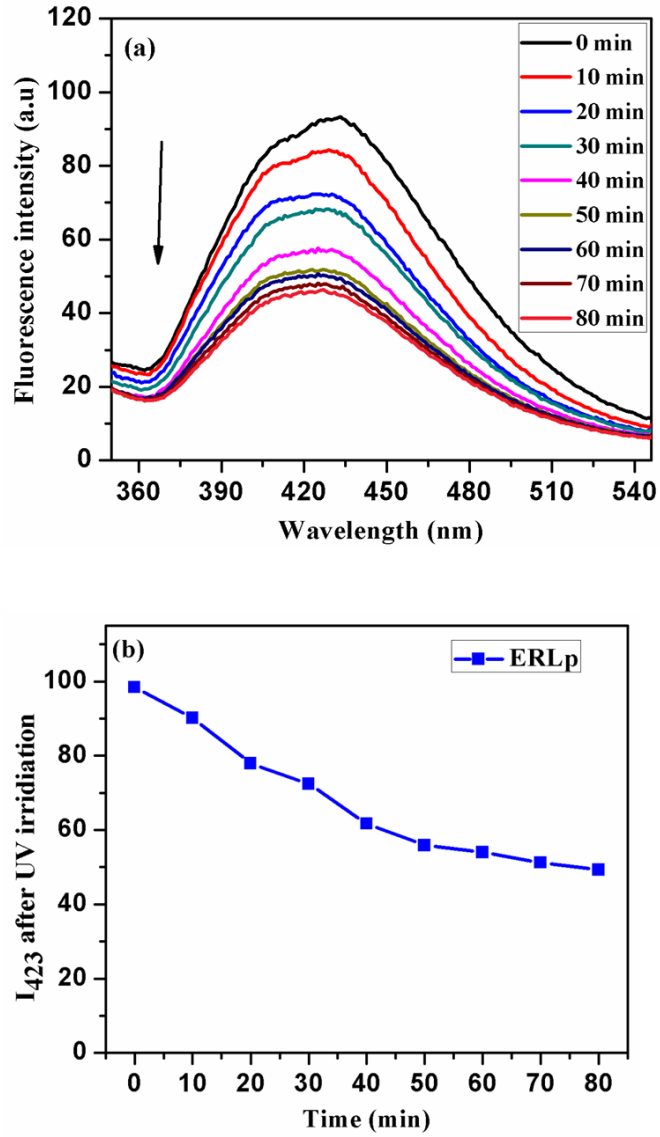

Figure 3.15. Photobleaching study of **ERLp** (10 μM) in water under UV illumination (254 nm). (a) Fluorescence intensity measure after different time interval. (b) The plot of the emission intensity of **ERLp** at 423 nm versus exposure time (min) of UV rays.

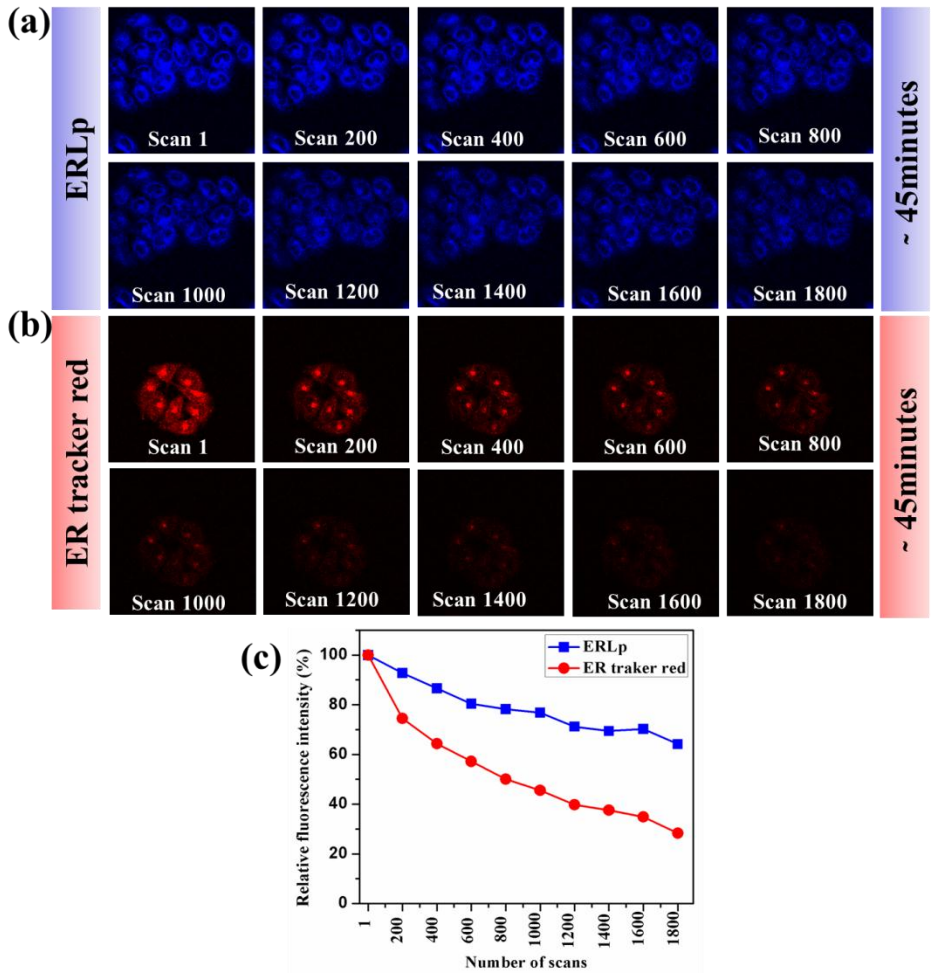

Figure 3.16. Comparisons of the *in vitro* photostability of ER-Tracker Red and **ERLp** in HeLa cell lines. (a) **ERLp** (80 μM): λ_{ex} = 740 nm, λ_{em} = 415–470 nm) photobleaching HeLa cells. (a) ER tracker red (1μM): λ_{ex} = 559 nm, λ_{em} = 580–700 nm) photobleaching study in HeLa cells. (b) Graph showing photobleaching result of **ERLp** and ER tracker red**.**

3.2.8. Organelles' selectivity of ERLp:

In order to confirm the intracellular specific localization of **ERLp**, co-localization experiments were conducted with **ERLp** and various commercially available organelle trackers such ER, lysosome and mitochondria trackers **(Figure 3.17)**. The Pearson colocalization coefficient of **ERLp** with an ER tracker was found to be 0.86, whereas the colocalization coefficients for **ERLp** with lyso and mito trackers were

0.69 and 0.46, respectively **(Figure 3.17)**, thus indicating that **ERLp** specifically localized in the endoplasmic reticulum with a high Pearson coefficient.

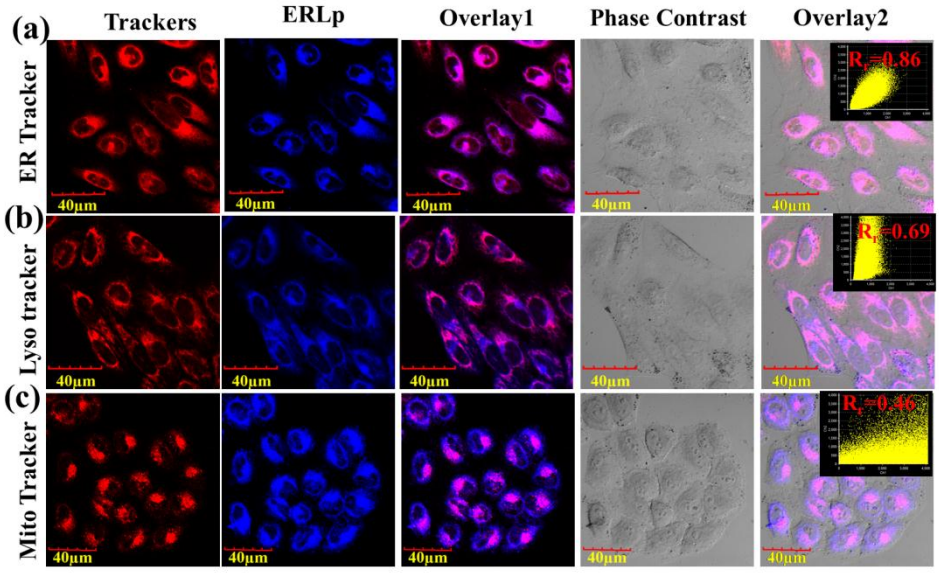

Figure 3.17. Co-localization experiment of probe **ERLp** (80 µM, 10 min) with different organelles specific trackers in live Hela cells. (a) ER tracker Red (1µM, 30 min) label endoplasmic reticulum. (b) LysoTracker Red DND-99 (80 nM, 30 min) label lysosomes. (c) MitoTracker Red CMXRos (90 nM for 15 min) label mitochondria. The images from left to right depict organelle trackers (column 1), **ERLp** (column 2), Overlay 1: overlay of the 1st and 2nd columns. Phase contrast (column 4) and Overlay 2: overlay of 1st, 2nd and 4th columns. **ERLp** λ_{ex} = 405 nm; λ_{em} = 415–470 nm; ER tracker Red λ_{ex} = 559 nm; λ_{em} = 570–700 nm.

3.2.9. ER selective staining ability of ERLp in various cell lines:

Further, the selective staining capability of **ERLp** towards the universal Endoplasmic Reticulum (ER) was evaluated on various cell lines such as cervical cancer (HeLa), prostate cancer (DU145), skin melanoma (A375) and breast cancer (MCF-7) cells **(Figure 3.18)**. **ERLp** shows an excellent ER labeling pattern in all the studied cell lines. Additionally, the co-localization result of **ERLp** and ER-Tracker Red was calculated using the Pearson colocalisation coefficient (R_r) **(Figure 3.19)**. To our surprise, the super-imposed fluorescent pink signals (blue and red) exhibited high

Pearson coefficients of 0.87, 0.88, 0.85 and 0.84 for HeLa, DU145, A375 and MCF-7 cells, respectively.

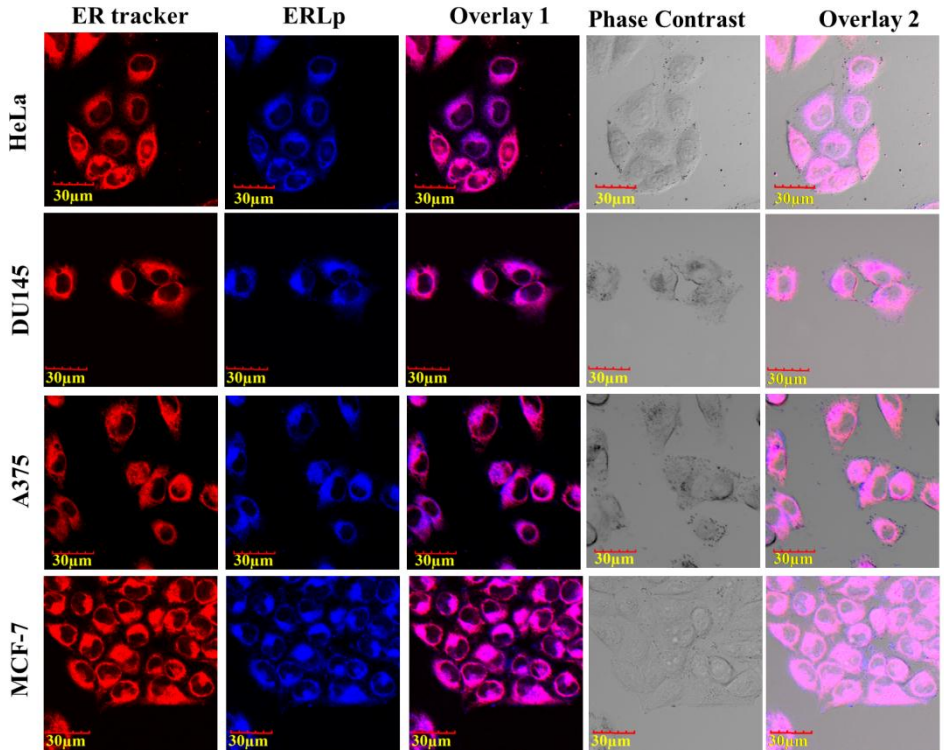

Figure 3.18. Endoplasmic Reticulum selective staining of **ERLp** in HeLa, DU145, A375 and MCF-7 cells. All cells were co-treated with **ERLp** (80 µM, 10 min) and ER tracker red (1µM, 30 min). **ERLp**: λ_{ex} = 405 nm; λ_{em} = 415-470 nm; ER tracker red λ_{ex} = 559 nm; λ_{em} = 580-700 nm. Overlay 1: overlay of the 1st and 2nd column. Overlay 2: overlay of the 1st, 2nd and 4th columns. Scale bar: 30 µm.

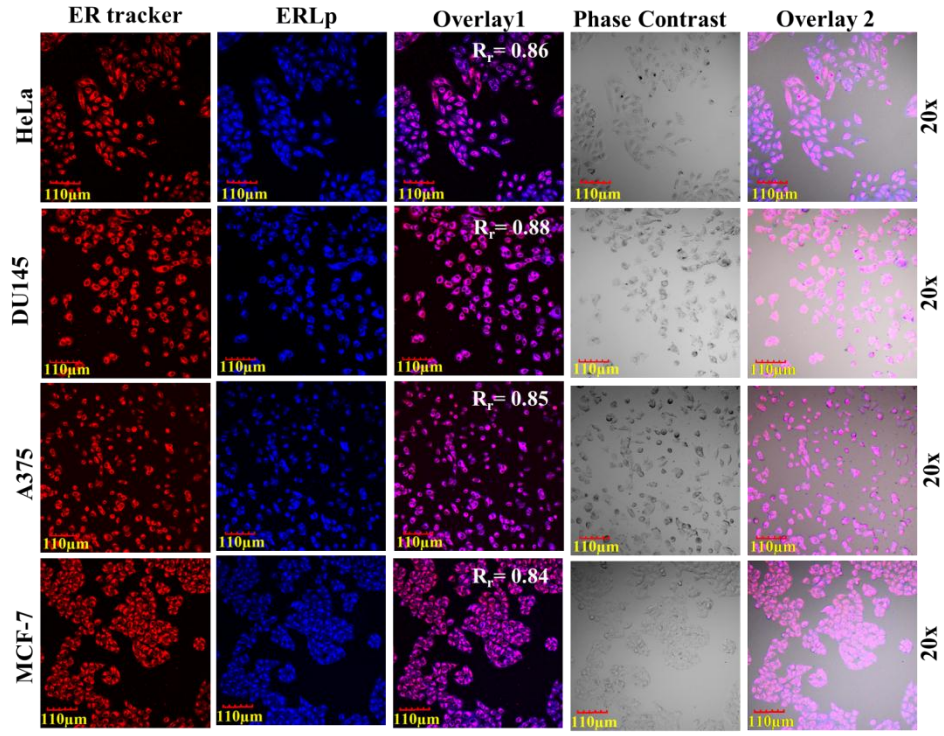

Figure 3.19. Endoplasmic reticulum selective live cell imaging of **ERLp** in HeLa, DU145, A375 and MCF-7 cell lines with respective Pearson co-localization coefficient. All cells were co-stained with **ERLp** (80 µM, 10 min) and ER-tracker red (1µM, 30 min). R_r = Pearson's co-localization of **ERLp** with ER-tracker red on all four cell lines. **ERLp**: λ_{ex} = 405 nm; λ_{em} = 415–470 nm; ER tracker red λ_{ex} = 559 nm; λ_{em} = 580-700 nm. Overlay 1: overlay of the 1st and 2nd. Overlay 2: overlay of the 1st, 2nd and 4th columns. Scale bar: 110 µm.

3.2.10. Two-photon microscopy (TPM) study of ERLp:

TPM live cell imaging is a superior technology to one photon imaging in terms of its low background signal, low photo damage, and large depth imaging (>500 mm) *[31]*. However, to compare both one and two-photon microscopies, co-localization imaging was performed for **ERLp** with ER Tracker Red, which validates excellent superimposition in both cases with a very high Pearson colocalization coefficient of 0.91 **(Figure 3.20)**. To the best of our knowledge, this is the best among the so far reported ER probes *[27, 32-34]*.

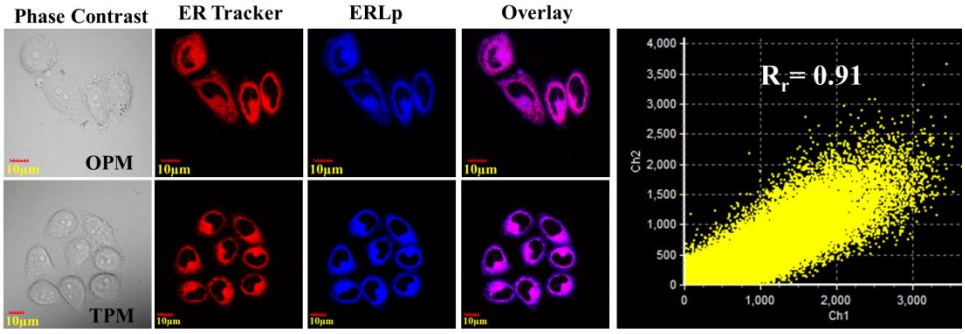

Figure 3.20. One-photon microscopy (OPM) and two-photon microscopy (TPM) images of **ERLp** in live HeLa cells. Cells were co-stained with **ERLp** (80 μM, 10 min) and ER tracker red (1μM, 30 min). **ERLp**: λ_{ex} = 405 nm (OPM) or 740 nm (TPM). ER tracker red, λ_{ex} = 559 nm (OPM). The images were taken under 60×2z oil immersion objective, scale bar 10μm.

3.2.11. ER stress monitored by ERLp:

ER stress is triggered by various conditions that interrupt the proper folding of proteins in the ER *[35-36]*. After confirming the role of **ERLp** as an ER tracker, we decided to further explore the possibility whether **ERLp** is capable of monitoring ER stress. Thus, to emphasize tracking of ER stress during apoptosis, cells were treated with tunicamycin, which blocks N-linked glycosylation of newly synthesized proteins, or Dithiothreitol (DTT, a strong reducing agent), which blocks disulfide-bond formation in proteins, and consequently induces ER stress causing various misfolded proteins in the ER. After addition of Tunicamycin (40 mg ml^{-1}) or DTT (200 μM), the red color stain of ER Tracker Red starts disappearing after 1 h; this implies that the ER is under stress and apoptosis is initiated. Subsequently, the cell morphology starts changing. The fluorescence intensity of ER Tracker Red diminishes as cells undergo stress, but **ERLp** remains fluorescent and tracks ER stress during apoptosis **(Figure 3.21 and Figure 3.22)**. Thus, it can be concluded that **ERLp** is capable of monitoring dynamic changes in the ER membrane during stress conditions. Possibly, **ERLp** may provide a useful tool for examining ER dynamics.

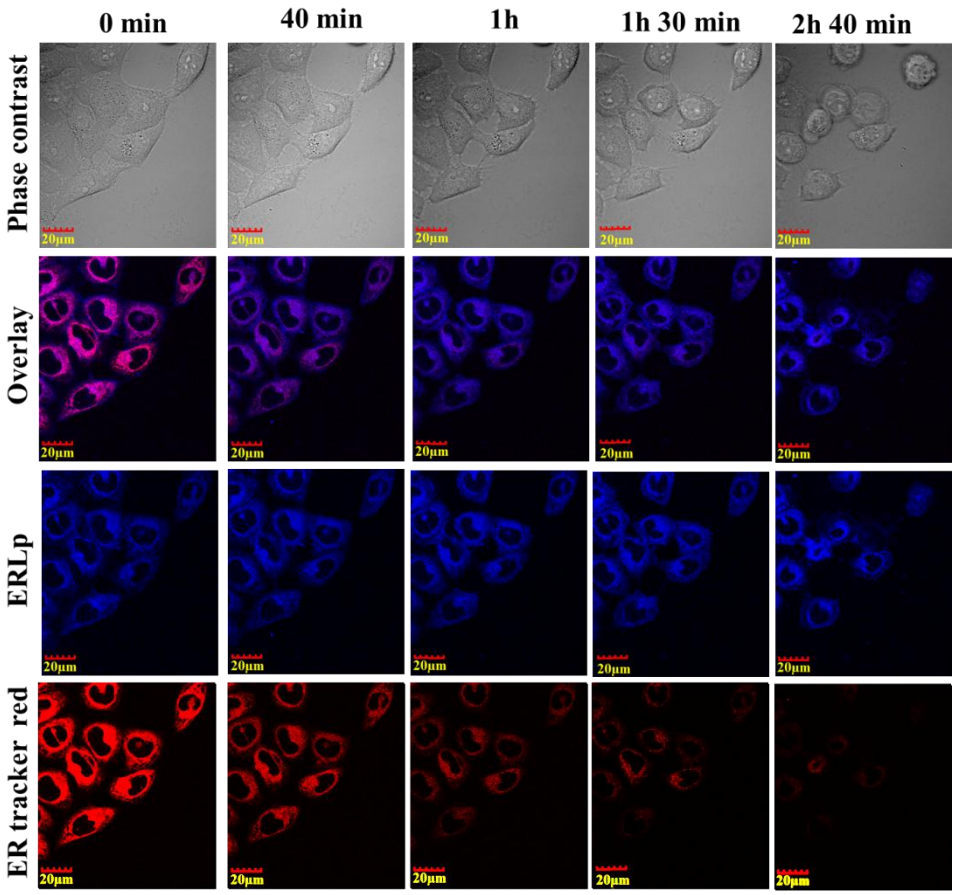

Figure 3.21. Endoplasmic Reticulum stress by tunicamycin leads to cell apoptosis monitored by **ERLp.** Here HeLa cells labeled with **ERLp** (80 μM, 10 min) and co-stained with ER tracker red (1μM, 30 min), then tunicamycin (40 μg/ml) added and the image captured after a different time interval.

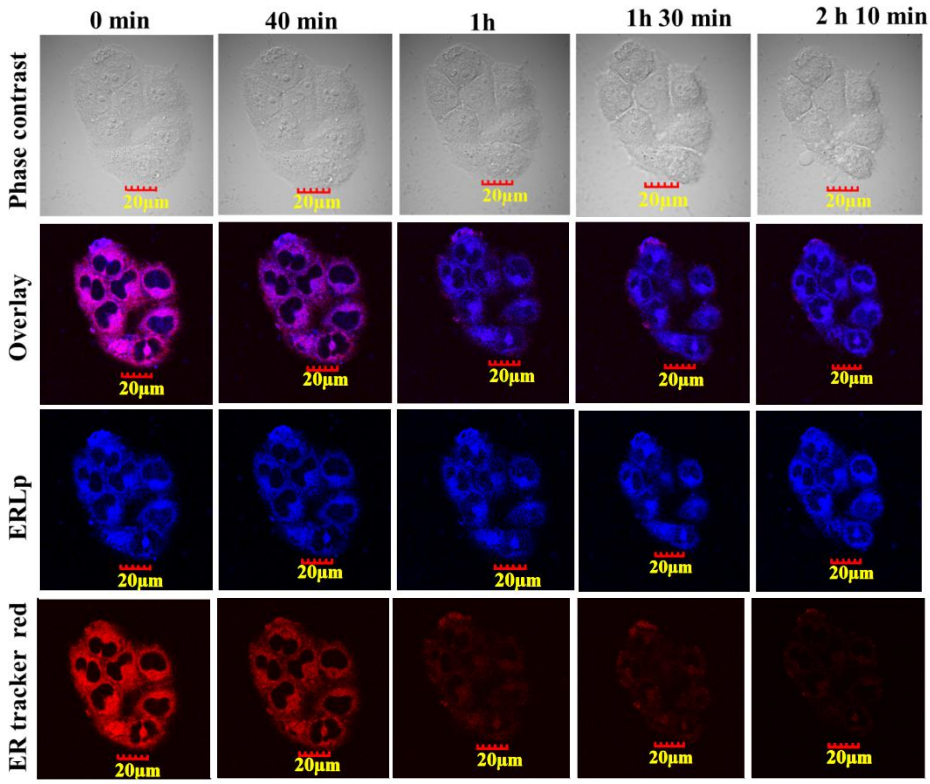

Figure 3.22. Endoplasmic Reticulum stress by Dithiothreitol leads to cell apoptosis monitored by **ERLp**. Here HeLa cells labeled with **ERLp** (40 µM, 10 min) and co-stained with ER tracker red (1µM, 30 min), then 200 µM Dithiothreitol (DTT) added in media and the image captured after a different time interval.

3.2.12. Trafficking of ERLp from ER to lysosome:

ERLp gradually shifted from the ER to a granular shape within 90 minutes as shown in time course TPM images **(Figure 3.23a)**. Therefore, the time dependent Pearson colocalization (Rr) values were monitored from the colocalization experiments of **ERLp** with ER Tracker Red and lysosome tracker red **(Figure 3.23b, c)**. The R_r (co-localization) value of **ERLp** towards the ER tracker gradually decreases from 0.91 to 0.72, whereas the R_r value towards lysosome tracker slowly increases from 0.74 to 0.81. These results demonstrate the dual nature of **ERLp**, initially restricted to the ER and then slowly transported from the ER to lysosomes. This may be associated with the ER to the lysosome vesicle transport system.

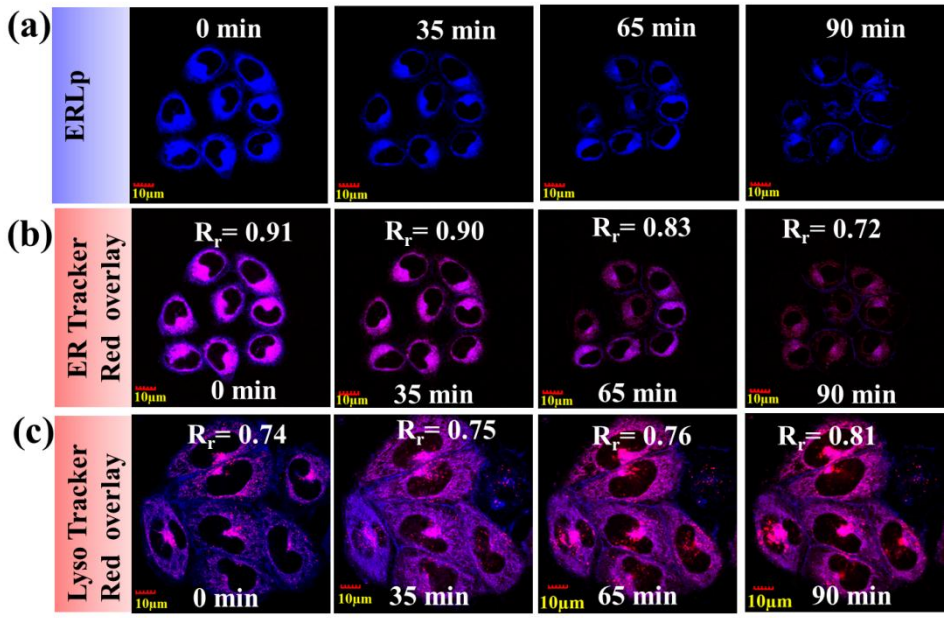

Figure 3.23. (a) Time-dependent TPM images of live HeLa cells stained with **ERLp**. (b) HeLa cells stained with **ERLp** and co-labeled with ER tracker red (c) HeLa cells stained with **ERLp** and co-labeled with Lyso tracker red DND-99. (In case of b and c only the overlay images are displayed for clarity), Scale bars = 10µm.

3.2.11. 3D tumor spheroids imaging by ERLp:

In comparison with 2D cell monolayer culture, 3D tumor spheroids mimic numerous in vivo features of solid tumors, such as cell–cell interactions, spatial architecture, hypoxia, physiological responses, gene expression patterns and drug penetration mechanisms. Thus, the cell morphology closely resembles its natural pattern in the human physiological system *[29]*.

The imaging of deeper layers of tumor spheroids through a confocal microscope still has so many technical challenges. To address this issue, one spheroid was incubated with **ERLp** for imaging. The images were captured after every 2 µm section cutting along the Z-axis. The two-photon excitation showed much deeper and uniform penetration of **ERLp** up to ~ 94 µm as compared to one-photon excitation, where the

penetration was up to ~ 42 µm **(Figure 3.24 and Figure 3.25)**. The results concluded that the spheroids exhibited stronger fluorescence in deeper layers, signifying the enhanced penetrating power of two-photon excitation light. Thus, **ERLp** may be further exploited for its application in in vivo endoplasmic reticulum imaging in living organs or tissue.

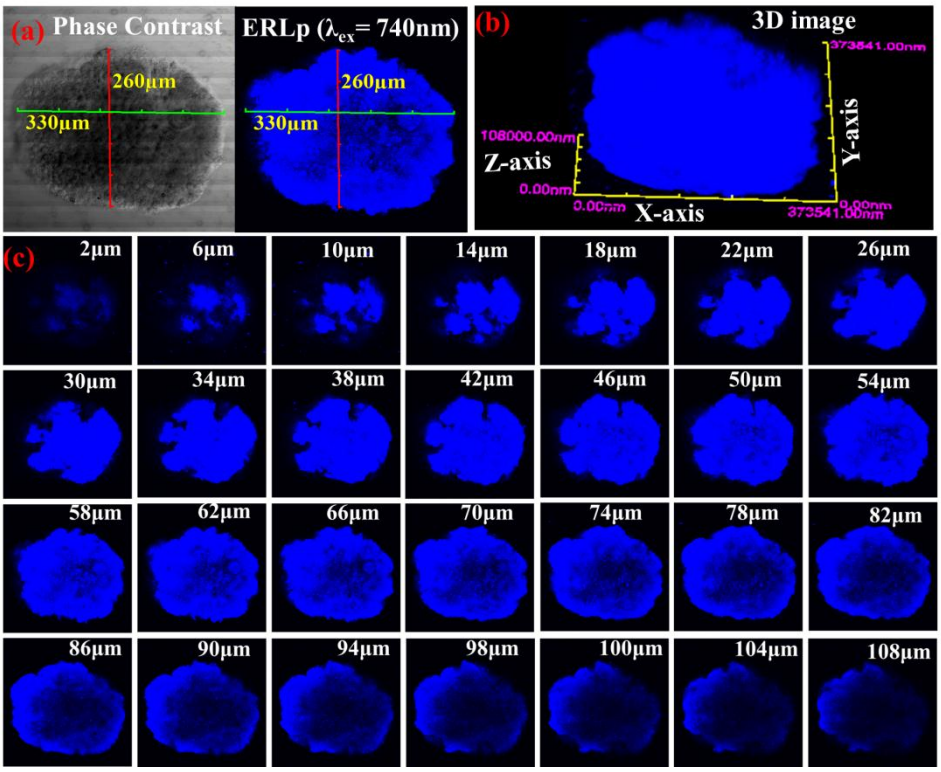

Figure 3.24. (a) Two-photon fluorescence images of multicellular tumor spheroid after **ERLp** treatment (80 µM, for 1 h). (b) The Z-stack 3D images of the tumor spheroid. (c) Z-stack images were taken from the top to bottom of a spheroid, after every 2 µm section cutting. The images were taken under a 20×1.7z objective λ_{ex} = 740 nm; λ_{em} = 415–470 nm.

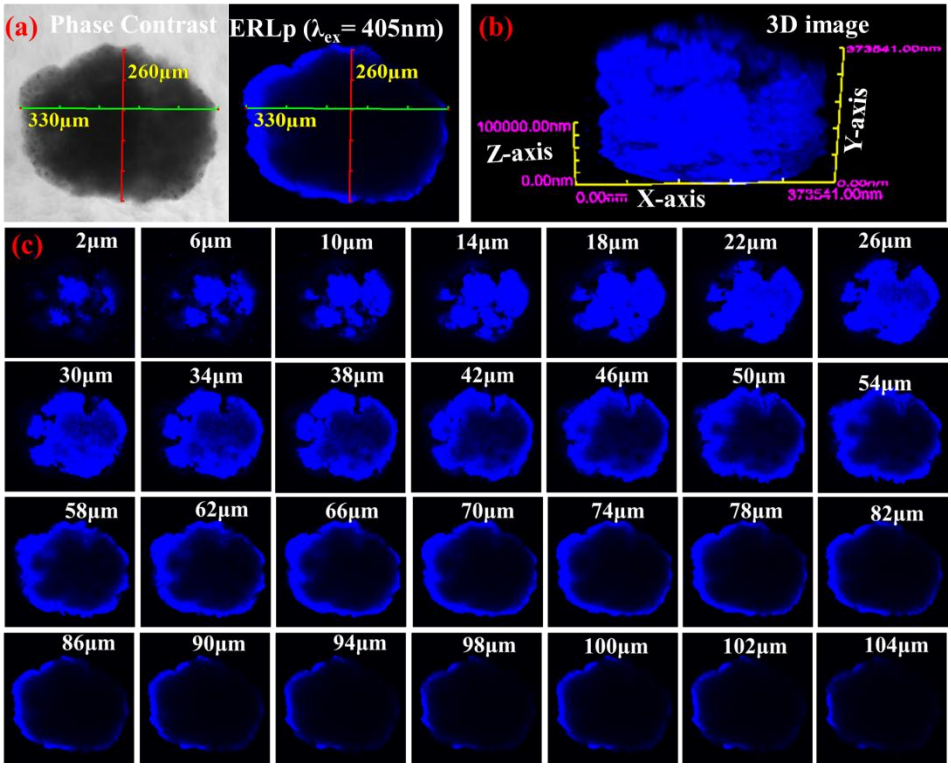

Figure 3.25. (a) One-photon fluorescence images of 3D intact tumor spheroid after **ERLp** (80 µM, for 1 h) treatment. (b) The Z-stack 3D images of the intact spheroid. (c) The two-photon Z-stack images were taken after every 2 µm section from the top to bottom spheroid. The images were captured under a 20×1.7z objective λ_{ex} = 405 nm; λ_{em} = 415–470 nm.

3.2.12. The probable mechanistic pathway of ERLp:

The cellular uptake pathway ERLp was determined by confocal microscopy. For this purpose, HeLa cells were treated with **ERLp** in two separate dishes; one of them incubated at 4 °C and the other at 37 °C, in order to diagnose ligand uptake by the cells via an energy-independent or an energy-dependent pathway. The **ERLp** uptake by live cells at 4 °C as well as 37 °C demonstrates that the uptake is through an energy-independent pathway **(Figure 3.26)**.

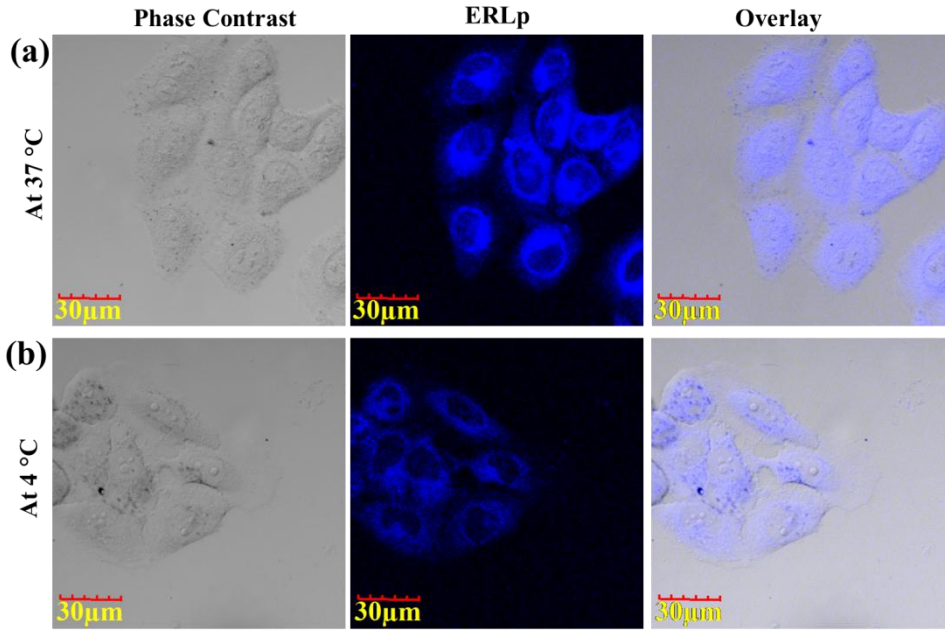

Figure 3.26. Live cells imaging under different conditions (a) The HeLa cells were incubated with **ERLp** (80 µM) at 37°C for 50 min. (b) The cells were incubated with **ERLp** (80 µM) at 4°C for 50 min.

To explain the dual role of **ERLp** probe as ER tracker and subsequently with time as lysosome tracker, a two-photon excitable probe was designed by introducing (i) an imine group at position 1 of the β-hydroxy naphthalene, and (ii) ortho methoxy phenol unconjugated unit which leads to a push–pull of the **ERLp** from ER to lysosomes. The pKa value plays a decisive role in controlling the movement of the probe inside the cell *[37]*.

The remote phenolic hydroxyl group of the **ERLp** is responsible for the ER tracking this may be due to the hydrophobic nature of this group having the pKa value of 9.9 **(Figure 3.27)**. On the other hand, the presence of the imine having low pKa values of 3.9 and naphthyl hydroxyl group of **ERLp** in a conjugated manner with hydrophilic nature, presence of strong intra-molecular hydrogen bonding interactions drives **ERLp** to leave ER and travel to the lysosome. Thus, the protonated conjugated imine group of **ERLp** restricts its movement in the acidic lysosomes.

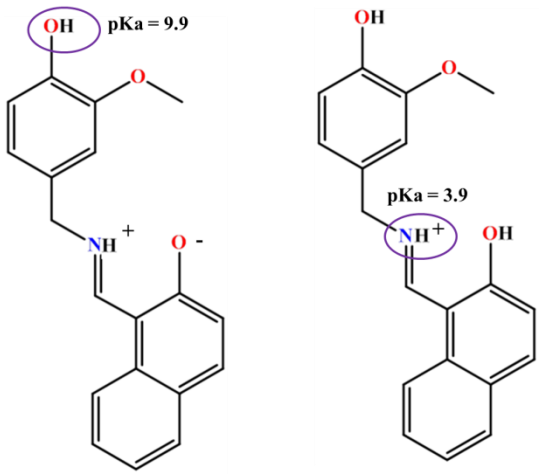

Figure 3.27. The ionization state of imine and remote phenolic hydroxyl group of **ERLp.**

3.3. Conclusions

In summary, a two-photon fluorescent organic probe (**ERLp**) was designed and synthesized in a facile manner. **ERLp** is noncytotoxic and photostable. It can selectively label the Endoplasmic Reticulum (ER) with a very high Pearson colocalization coefficient of 0.91. **ERLp** can monitor ER dynamic changes during ER stress and cell apoptosis. The probe uptake by the cells' mechanistic pathway was discussed. Further, **ERLp** was confirmed to be exhibiting excellent two-photon fluorescence properties (excitation 740 nm) for studying intracellular vesicle transport from the ER to the lysosome in living cells. More importantly, the two-photon ability of **ERLp** was further explored by employing 3D multicellular tumor spheroids similar to in vivo tumors. Thus, **ERLp** may serve as a potential tool for monitoring ER stress or vesicle trafficking associated with pathological disorders.

3.4. Experimental Section

3.4.1. Materials:

2-hydroxy-1-naphthaldehyde and 4-(Aminoethyl)-2-methoxyphenol hydrochloride purchased from TCI Chemicals (India) Pvt. Ltd., LysoTracker Red DND-99 and MitoTracker Red CMXRos, ER-Tracker Red (BODIPY TR Glibenclamide) were purchased from Invitrogen. 3-(4,5-dimethylthiazol-2-yl)-2,5-diphenyltetrazolium bromide (MTT), Tunicamycin and Dithiothreitol (DTT) purchase from Sigma Aldrich Chemical Co., USA. Fetal bovine serum (FBS) and Dulbecco's modified Eagle medium (DMEM) were purchased from Gibco. HeLa cells (cervical cancer cell line), A375 (skin melanoma), MCF-7 (breast cancer) and DU145 (prostate cancer) cells were obtained from National Centre for Cell Science, Pune. All other chemical reagents and solvents were obtained from Merck and S.D Fine Chem.Ltd. Ultrapure water obtains from arium® pro ultrapure water systems (Sartorius) was used throughout the experiment. All commercially available materials were used without further purification.

3.4.2. Physical Measurements:

^{1}H NMR (400 MHz) and ^{13}C NMR (100 MHz) spectra were measured by Bruker Avance (III) instrument by using DMSO-*d6*. Mass spectrum was recorded by Brucker-Daltonics, micrOTOF-QII mass spectrometer. FTIR spectrum was recorded by using Bio-Rad FTS 3000MX instrument on KBr pellets. Spectrophotometric measurements were performed by UV-vis spectrophotometer (Varian Cary 100) using a quartz cuvette with a path length of 1 cm. FluoroMax-4 Spectrophotometer (HORIBA Scientific) was used for Fluorescence measurement. The excitation and emission slits were 5/5 nm for the emission measurements. pH-meter (LABMAN Scientific Instrument PVT. LTD) was used for pH measurements. The absorbance for MTT analysis

was recorded by a microplate reader (Synergy H1 BioTek microplate reader) at 570 nm. Fluorescence imaging experiments were performed by Olympus laser-scanning microscope, Mai Tai eHP Spectra physics femtosecond (fs) laser having power peak >450 KW, pulse width ≤ 70 fs, tuning range 690-1040 nm, average power >2.5 W, repetition rate 80 MHz ± 1 MHz was used to acquire the two-photon fluorescence imaging and BD LSRFortessa TM Flow cytometry analysis. Image processing was done with the help of Olympus software (FV10-ASW 4.2). For bioimaging purpose (better cell permeability), **ERLp** stock solution was prepared in 0.1M NaOH solution in water and 0.05% acetonitrile. Flow cytometry data were analyzed by DB FACSDiva software. pK_a of imine group and the remote phenolic hydroxyl group of **ERLp** is 3.9 and 9.9 respectively, calculated by ACD software.

3.4.3. X-ray Crystallographic data collection and structure determination of ERLp: The crystal data of **ERLp** was collected at 298 K using graphite-monochromated Mo Kα (λα = 1.54184 Å). The strategy for the data collection was evaluated with the help of CrysAlisPro CCD software. The data were collected by the standard phi-omega scan techniques and were scaled and reduced using CrysAlisPro RED software. The structures were solved by the direct methods by using SHELXS-2014 and refined by full matrix least squares with SHELXL-2014, refining on F^2 *[38-39]*. By direct methods the positions of all the atoms were obtained and all non-hydrogen atoms were refined anisotropically. All the remaining hydrogen atoms were placed in geometrically constrained positions and refined with isotropic temperature factors, generally 1.2 × Ueq of their parent atoms. The Hydrogen bonding interactions, mean plane analysis, and molecular drawings were obtained using the program Mercury (ver 3.1) and Diamond (ver 3.1d). The crystal and refinement data are summarized in **Table A3** and the selected bond distances and

bond angles are shown in **Table A4**. All the Hydrogen atoms have been omitted for clarity in the molecular structure of **ERLp**.

3.4.4. Synthesis of ERLp ($C_{19}H_{17}NO_3$):

Condensation reaction was performed from 2-hydroxy-1-naphthaldehyde (172.18 mg, 1 mmol) and 4-(Aminomethyl)-2-methoxyphenol hydrochloride (189.64 mg, 1 mmol) in 20 mL of methanol at 25°C with continuously stirring for 3h in single neck 100 ml RBF (To get the primary amine group free of 4-(Aminomethyl)-2-methoxyphenol hydrochloride, we have treated it with aqueous potassium carbonate). Reaction was monitored by TLC. After completion of the reaction, the solvent was evaporated from rotatory evaporator. The solid product was washed with acidic chilled water and then chilled water only, for several times. The solid orange precipitate was formed, which was filtered and dried in a desiccator. Yield 92%, ^{1}H NMR (400 MHz,DMSO-d_6): δ 14.26 (s, 1H), 9.24 (s, 1H) (d, 1H, -CH=N), 9.01 (s, 1H), 8.09 -8.07 (d, 1H, *ph*), 7.72-7.70 (d, 1H, *ph*), 7.63-7.62 (d, 1H, *ph*), 7.43 (t, 1H, *ph*), 7.19 (t, 1H, *ph*), 7.01 (s, 1H, *ph)*, 6.81- 6.78 (dd, 2H, *ph*), 6.71- 6.68 (d, 1H, *ph*), 4.73(s, 2H), 3.76 (s, 3H) **(Figure 3.28)**. ^{13}C NMR (100 MHz, DMSO-d_6): δ176.65, 158.31, 147.28, 145.80, 136.62, 133.84, 128.44, 127.89, 127.45, 124.93, 124.80, 121.76, 120.05, 118.07, 115.16, 111.87, 105.35, 55.21, 54.00 **(Figure 3.29)**. FTIR (KBr, cm-1): 3465 (br), 3052 (s), 3006 (s), 2966 (s), 1636 (vs), 1614 (s), 1543 (s), 1453 (s), 1351 (s), 1250 (vs), 1148 (s), 1120 (s), 1065 (vs), 886 (s), 806 (vs), 763 (vs), 647 (s), 587 (s) **(Figure 3.30)**. LCMS (m/z): $[M+H]^+$ 308.1 **(Figure 3.31)**.

^{1}H NMR spectrum of the **ERLp** after 2 days in DMSO-d_6 solution at 25°C. ^{1}H NMR (400 MHz,DMSO-d_6): δ 14.25 (s, 1H), 9.24 (s, 1H) (d, 1H, -CH=N), 9.01 (s, 1H), 8.09 -8.07 (d, 1H, *ph*), 7.72-7.70 (d, 1H, *ph*), 7.63-7.62 (d, 1H, *ph*), 7.43 (t, 1H, *ph*), 7.19 (t, 1H, *ph*), 7.01 (s, 1H, *ph)*, 6.81- 6.78 (dd, 2H, *ph*), 6.71- 6.68 (d, 1H, *ph*), 4.73(s, 2H), 3.76 (s, 3H) **(Figure 3.32).**

3.4.5. Two-photon intensity measurement:

Mai Tai eHP Spectra physics femtosecond laser having power peak >450 KW, average power >2.5 W, tuning range 690–1040 nm, pulse width ≤ 70 fs, repetition rate 80 MHz ± 1 MHz was used to capture the two-photon fluorescence imaging. The two-photon fluorescence intensity was measured at 700–820 nm. Cervical cancer (HeLa) cells were seeded in confocal dishes and incubated for 24 hours. Live cells were stained with **ERLp** (80 µM) in cell culture medium for 10 min then washed thrice with PBS. Images were captured at a different wavelength. Maximum integrated fluorescence intensity was observed at wavelength 740 nm.

3.4.6. Quantum yield calculation:

The fluorescence quantum yield (ΦF) of **ERLp** was calculated using equation (1) by the steady-state comparative method using tryptophan as the standard having Φ_{st} = 0.14 *[40]*, since excitation wavelength of tryptophan and **ERLp** is similar.

$$\Phi_x = \Phi_{st} \times S_x/S_{st} \times A_{st}/A_x \times \eta^2_x /\eta^2_{st} \quad \text{equation (1)}$$

where St and X denote standard and unknown respectively. Φ_x is the fluorescence quantum yield of the unknoun sample (test sample), Φ_{st} is the fluorescence quantum yield of the standard sample, S_x and S_{st} are the integrated emission band areas of the unknown sample and the standard respectively. A_{st} and A_x represent the absorbance of the standard and the unknown sample at the excitation wavelength, respectively. η^2_x and η^2_{st} are the refractive index of the solvent of test sample and the standard sample. Here both standard sample tryptophan and **ERLp** dissolve in water. Therefore refractive index of solvent is same in both case. The

fluorescence quantum yield (ΦF) of ER traker red was calculated using above equation (1). In this case quinine sulfate used as the standard having Φst = 0.54 *[41]*.

3.4.7. Cell viability assay (MTT assay):

Cell viability assay of **ERLp** was performed on Hela cells, 6000 HeLa cells well^{-1} were seeded in 96-well plate in 200 µL media (Dulbecco's Modified Eagle Medium, 10% (v/v) FBS and 1% Penicillin-Streptomycin antibiotics 10,000 U/mL) and incubated for one day for cell adhesion. Next day media was removed and fresh media 100 µL added in each well. A stock solution of **ERLp** was prepared in 0.05% acetonitrile and rest water. 20 µL added to each well in order to give final concentration ranging from 10-140 µM. 20 µL water having 0.05% acetonitrile was used as a control. The experiment was done in triplicate. Cells exposed to the drug for 24 hours followed by washing with PBS (pH 7.4) and 100 µL MTT (1 mg/mL in phenol red free media) was added in each well. Cells incubated for next 4 hours at 37 °C and 5% CO_2 atmosphere. After that media was carefully removed and 100 µL DMSO was added in order to dissolve purple formazan crystals. After 15 minutes incubation, absorbance at 570 nm was measured using Synergy H1 Biotek microplate reader. The % cell viability was calculated as: % cell viability = [Mean O.D. of the drug-treated cell/Mean O.D. of the control well] × 100.

3.4.8. **Flow cytometry:**

HeLa cells were cultured in six-well tissue culture plates. When cells became 80% confluent then one well treated with 40 µM probe **ERLp** and another well with 80 µM **ERLp** for 10 min and control well left without any treatments. After that, the cells were washed with PBS three times. Then harvested by trypsin and re-suspended in PBS. The samples were analyzed by BD LSRFortessa TM Flow cytometry with excitation at 405 nm and emission 415–470 nm. Data were analyzed by

DB FACSDiva software. Total ten thousand events were acquired for each sample.

3.4.9. Concentration dependent confocal imaging of ERLp:

HeLa cells were seeded in confocal dishes. Cells in each dishes treated with diffrent concentration of **ERLp** (5µM, 20 µM, 40 µM, 60 µM, 80 µM) for 10 min followed by washing with PBS. In other case incubation time of **ERLp** increased to 2 h by keeping concentration constant (5µM, 20 µM, 40 µM, 60 µM, 80 µM). After 2 h washed with PBS and images captured by confocal microscope.

3.4.10. **Endoplasmic reticulum (ER) staining and co-localization studies in various cell lines:** Cervical cancer (HeLa), skin melanoma (A375), prostate cancer (DU145) and Breast cancer (MCF-7) cell lines were seeded in confocal dishes and incubated for 24 hours for cell attachment with the bottom surface of dishes. For ER imaging, live cells were stained with **ERLp** (80 µM) in cell culture medium for 10 min then washed thrice with PBS (pH = 7.4) and co-stain with ER tracker Red (1µM, 30 min), LysoTracker Red DND 99 (80nM, 30 min), MitoTracker Red (90 nM,15 min) for ER, lysosomes and mitochondria respectively in separate dishes. Cells incubated at 37°C in 5% CO_2 atmosphere. An Olympus laser scanning microscope was used for confocal imaging. Cells ware visualized at an excitation of λ_{ex} = 405 nm for **ERLp** in case of one photon excitation and λ_{ex} = 740 for two-photon excitation, λ_{ex} = 559 nm for ER tracker red, Lyso tracker red as well as Mito tracker red.

3.4.11. Cell uptake pathway studies:

In order to study the probable mechanistic pathway of cellular uptake of **ERLp**, HeLa cells were seeded in two confocal dishes and incubated at 37°C for 24h. The cells seeded in two separate dishes were exposed with **ERLp** (80 µM) at 37°C or 4°C for 1 h. After that cells were

washed with PBS three times and images captured by a confocal microscope at excitation 405 nm and emission signal collected at 415-470 nm.

3.4.12. Photostability study of ERLp:

Photostability is an important factor that play significant role in fluorescent imaging purpose. Photobleaching experiment was performed, both in solution as well as on live cells to check the photostability of **ERLp**. Solution of **ERLp** in water was continuously UV illuminated (254 nm) at 25 °C for upto 80 min, fluorescence intensity of **ERLp** measure after every 10 min upto 80 min by FluoroMax-4 Spectrophotometer.

To further evaluate whether **ERLp** is also photostable for Endoplasmic Reticulum imaging in living cell. HeLa cells were seeded in confocal dishes and incubated overnight for cell attachment. Dishes were incubated with **ERLp** (80 μM, 10 min). After 10 min incubation, washed thrice with PBS to remove unbounded probe in media. The cells were imaged using Mai Tai eHP Spectra physics femtosecond laser used for two-photon imaging with no delay scan mode. Videos and images were recorded up to 1800 scans. **ERLp** were excited at 740 nm for two-photon imaging. The maximum intense signal of the first scan was considered 100% for measuring the relative decrease in intensity. Images at every 200 scans were obtained from the video. The relative percent intensity calculated as F/F_0*100.

3.4.13. Prolong ER stress leads to cells apoptosis:

HeLa cells in confocal dishes were treated with **ERLp** (80 μM) and incubated for 10 min followed by washing with PBS. The cells were co-stained with ER tracker red (1μM, 30 min) and again washed with PBS. Tunicamycin 40μg/ml (Tunicamycin 1mg/ml stock solution in DMSO) added in 1ml media in the confocal dish. Immediately images were captured after a different time interval to monitor morphological

changes in cells due to excess ER stress in real time. Further to explore more ER stress study, Dithiothreitol (DTT) which known as strong reducing agent and blocks protein disulfide- bond formation. So in another experiment cells were treated with **ERLp** and co-treated with ER tracker red followed by washing with PBS buffer. Then 200 μM DTT (solublized in Milli-Q water) added in 1 ml DMEM media and images captured after different time intervals.

3.4.14. ER to lysosome vesicles transports study:

In order to study vesicles transport from ER to lysosomes, HeLa cells were seeded in two separate dishes. In both dishes, cells were treated with **ERLp** (80μM, 10 min) and unbonded probe washed with PBS. One dish co-stained with ER tracker red and another dish co-stained with Lyso tracker red followed by washing with PBS. Then images were captured in a different time interval to monitor **ERLp** transported from ER to lysosome. As Pearson's colocalization coefficient decreases in the case of ER tracker red and increases in case of Lyso tracker red.

3.4.15. Generation of multicellular 3D spheroids:

Multicellular tumor spheroids (MCTSs) were produced using the liquid overlay method *[42-43]*. Flat-bottom 96 well plates were coated with 50μL of a sterile 1.5% (wt/vol) warm agarose solution in complete DMEM media to make a non-adherent surface. After that HeLa cells (~70% confluent in T-25 flack) were harvested by 0.25% trypsin/EDTA solution and re-suspended in DMEM media. Approx 3000 cells were seeded in each agarose coated well in 200μl complete DMEM media. The plates were incubated at 37°C and 5% CO_2 until spheroids formed. For compound treatment and imaging, spheroids were gently transfers in confocal disc with the help of 1ml pipette. Spheroids were treated with 80 μM **ERLp** and incubated for 1h, then washed gently with PBS three to four times and images were captured by two-photon microscopy as well as one photon confocal laser scanning microscopy.

NMR FTIR and Mass spectra of ERLp:

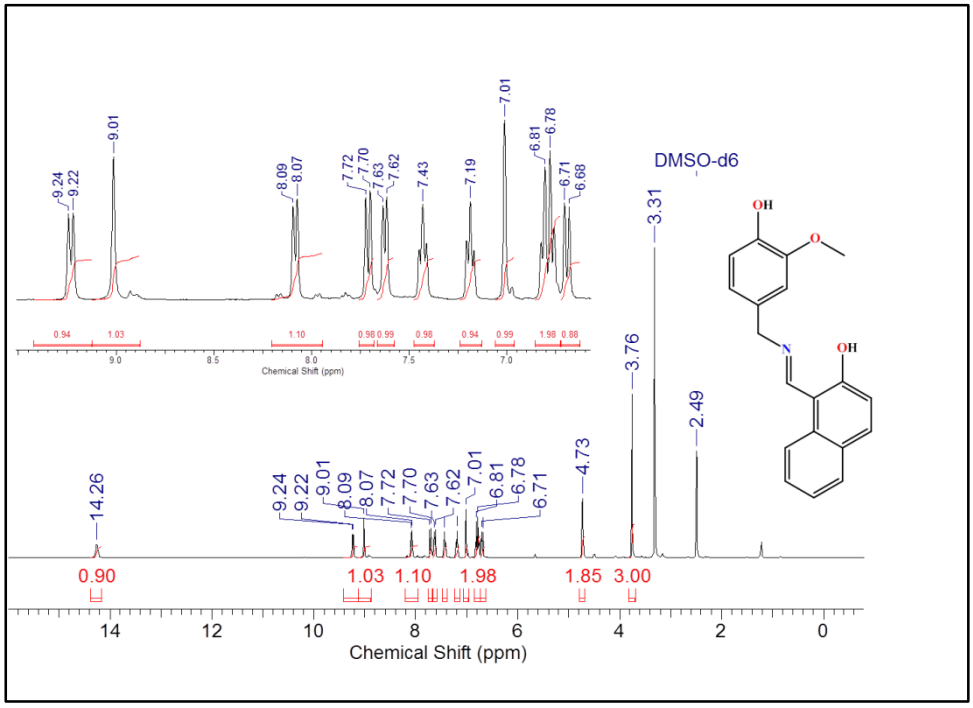

Figure 3.28. ^{1}H NMR spectrum of **ERLp**.

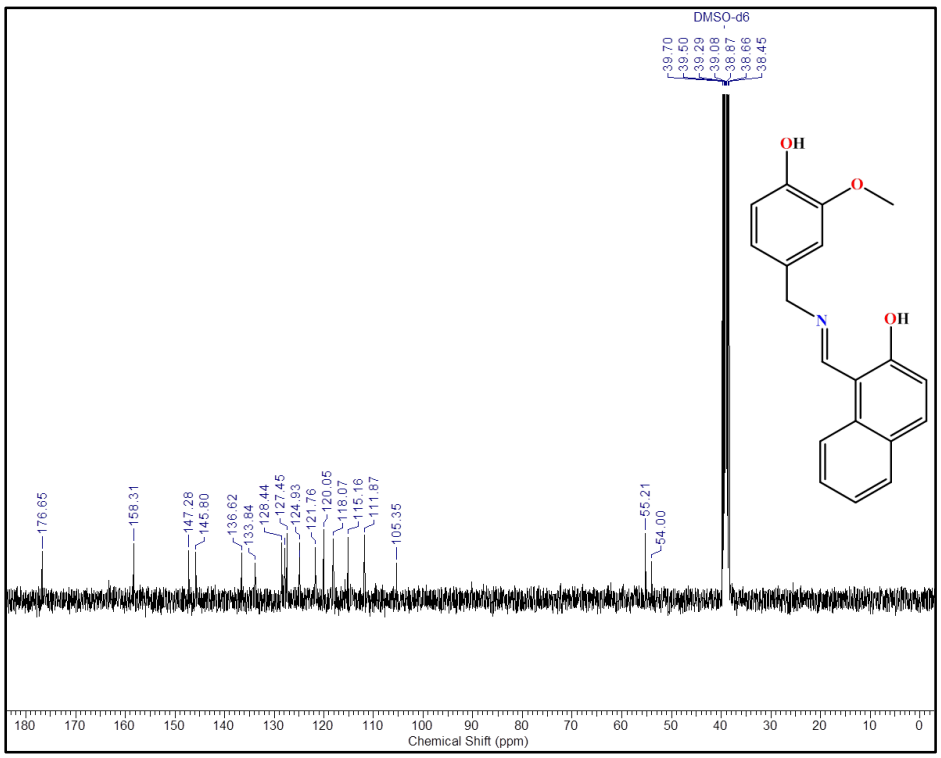

Figure 3.29. ^{13}C NMR spectrum of **ERLp**.

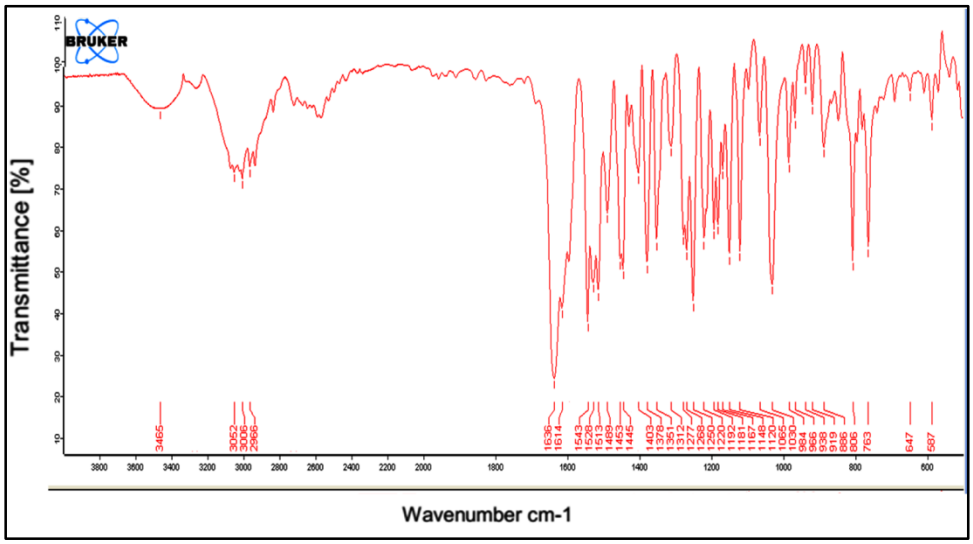

Figure 3.30. FTIR spectrum of **ERLp**.

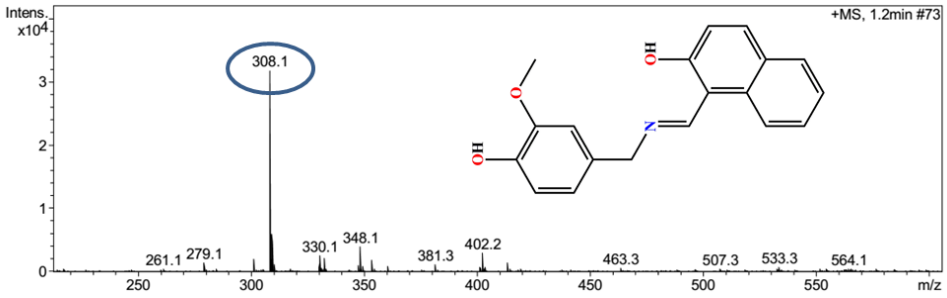

Figure 3.31. LCMS spectrum of **ERLp**

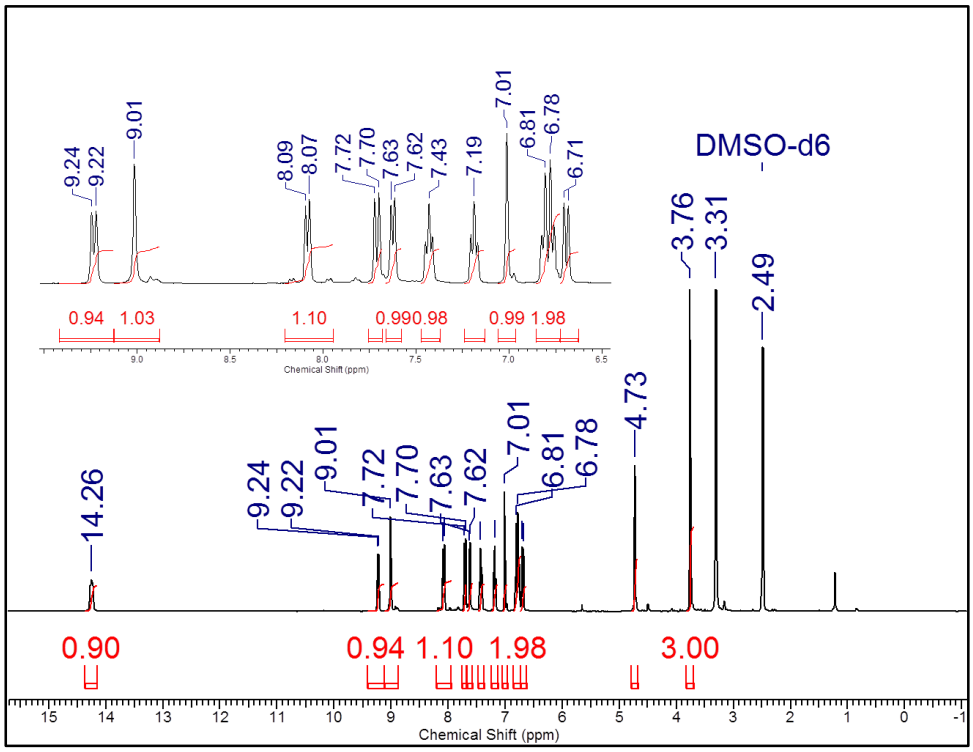

Figure 3.32. Chemical stability of **ERLp** was quantified by ^{1}H NMR spectrum**. ERLp** solution in DMSO-d_6, kept at 25 °C for 2 days then ^{1}H NMR spectrum measured.

3.5. References

[1]. Meinig, J. M., Fu, L., Peterson, B. R. (2015), Synthesis of Fluorophores that Target Small Molecules to the Endoplasmic Reticulum of Living Mammalian Cells, Angew. Chem. Int. Ed. *Engl.*, 54, 9696-9699 (DOI: 10.1002/anie.201504156).

[2]. Dawidowicz, E. A. (1987), Dynamics of membrane lipid metabolism and turnover, Annu. Rev. Biochem., 56, 43-61 (DOI: 10.1146/annurev.bi.56.070187.000355).

[3]. Meldolesi, J., Pozzan, T. (1998), The endoplasmic reticulum Ca2+ store: a view from the lumen, Trends Biochem. Sci., 23, 10-14 (DOI: 10.1016/S0968-0004(97)01143-2)

[4]. English, A. R., Voeltz, G. K. (2013), Endoplasmic reticulum structure and interconnections with other organelles, *Cold Spring* Harb. Perspect. Biol., 5, a013227 (DOI: 10.1101/cshperspect.a013227).

[5]. Kim, D. H., Hwang, I. (2013), Direct targeting of proteins from the cytosol to organelles: the ER versus endosymbiotic organelles, Traffic, 14, 613-621 (DOI: 10.1111/tra.12043).

[6]. Hetz, C., Mollereau, B. (2014), Disturbance of endoplasmic reticulum proteostasis in neurodegenerative diseases, Nat. Rev. Neurosci., 15, 233-249 (DOI: 10.1038/nrn3689).

[7]. Kulkarni, A., Caporali, P., Dolas, A., Johny, S., Goyal, S., Dragotto, J., Macone, A., Jayaraman, R., Fiorenza, M. T. (2018), Linear Cyclodextrin Polymer Prodrugs as Novel Therapeutics for Niemann-Pick Type C1 Disorder, Sci. Rep., 8, 9547 (DOI: 10.1038/s41598-018-27926-9).

[8]. Araya, N., Takahashi, Y., Shimono, M., Fukuda, T., Kato, M., Nakashima, M., Matsumoto, N., Saitsu, H. (2018), A recurrent homozygous NHLRC1 variant in siblings with Lafora disease, Hum. Genome. Var., 5, 16 (DOI: 10.1038/s41439-018-0015-9).

[9]. Chen, Y., Jian, J., Hettinghouse, A., Zhao, X., Setchell, K. D. R., Sun, Y., Liu, C. J. (2018), Progranulin associates with hexosaminidase A and ameliorates GM2 ganglioside accumulation and lysosomal storage in Tay-Sachs disease, J. Mol. Med., 96, 1359-1373 (DOI: 10.1007/s00109-018-1703-0).

[10]. Halbleib, K., Pesek, K., Covino, R., Hofbauer, H. F., Wunnicke, D., Hanelt, I., Hummer, G., Ernst, R. (2017), Activation of the Unfolded Protein Response by Lipid Bilayer Stress, Mol. Cell, 67, 673-684.e678 (DOI: 10.1016/j.molcel.2017.06.012).

[11]. Lin, W., Popko, B. (2009), Endoplasmic reticulum stress in disorders of myelinating cells, Nat. Neurosci., 12, 379-385 (DOI: 10.1038/nn.2273).

[12]. Kim, I., Xu, W., Reed, J. C. (2008), Cell death and endoplasmic reticulum stress: disease relevance and therapeutic opportunities, Nat. Rev. Drug Discov., 7, 1013-1030 (DOI: 10.1038/nrd2755).

[13]. Martin-Jimenez, C. A., Garcia-Vega, A., Cabezas, R., Aliev, G., Echeverria, V., Gonzalez, J., Barreto, G. E. (2017), Astrocytes and endoplasmic reticulum stress: A bridge between obesity and neurodegenerative diseases, Prog. Neurobiol., 158, 45-68 (DOI: 10.1016/j.pneurobio.2017.08.001).

[14]. Colston, J., Horobin, R. W., Rashid-Doubell, F., Pediani, J., Johal, K. K. (2003), Why fluorescent probes for endoplasmic reticulum are selective: an experimental and QSAR-modelling study, *Biotech.* Histochem., 78, 323-332 (DOI: 10.1080/10520290310001646659).

[15]. (a) Cole, L., Davies, D., Hyde, G. J., Ashford, A. E. (2000), ER-Tracker dye and BODIPY-brefeldin A differentiate the endoplasmic reticulum and golgi bodies from the tubular-vacuole system in living hyphae of Pisolithus tinctorius, *J. Microsc.*, 197, 239-249 (10.1046/j.1365-2818.2000.00664.x). (b) Terasaki, M. (1993), Probes for endoplasmic reticulum, in Fluorescent and Luminescent Probes for Biological Activity, ed. W. T. Mason, Academic Press,

London, pp. 120–123; (c) Terasaki, M., (1998), Labeling of the endoplasmic reticulum with DiOC6(3), in Cell Biology, A Laboratory Handbook, ed. Celis, J. E., Academic Press, San Diego, 2nd edn, pp. 501–506.

[16]. Terasaki, M., Reese, T. S. (1992), Characterization of endoplasmic reticulum by co-localization of BiP and dicarbocyanine dyes, J. Cell Sci., 101 (Pt 2), 315-322 (PMID: 1378452).

[17]. Zou, T., Lok, C. N., Fung, Y. M., Che, C. M. (2013), Luminescent organoplatinum(II) complexes containing bis(N-heterocyclic carbene) ligands selectively target the endoplasmic reticulum and induce potent photo-toxicity, Chem. Commun., 49, 5423-5425 (DOI: 10.1039/c3cc40953h).

[18]. Nam, J. S., Kang, M. G., Kang, J., Park, S. Y., Lee, S. J., Kim, H. T., Seo, J. K., Kwon, O. H., Lim, M. H., Rhee, H. W., Kwon, T. H. (2016), Endoplasmic Reticulum-Localized Iridium(III) Complexes as Efficient Photodynamic Therapy Agents via Protein Modifications, J. Am. Chem. Soc., 138, 10968-10977 (DOI: 10.1021/jacs.6b05302).

[19]. Chalfie, M., Tu, Y., Euskirchen, G., Ward, W. W., Prasher, D. C. (1994), Green fluorescent protein as a marker for gene expression, Science, 263, 802-805 (DOI: 10.1126/science.8303295).

[20]. Liu, H. S., Jan, M. S., Chou, C. K., Chen, P. H., Ke, N. J. (1999), Is green fluorescent protein toxic to the living cells?, Biochem. Biophys. Res. Commun., 260, 712-717 (DOI: 10.1006/bbrc.1999.0954).

[21]. Hoogenkamp, M. A., Crielaard, W., Krom, B. P. (2015), Uses and limitations of green fluorescent protein as a viability marker in Enterococcus faecalis: An observational investigation, J. Microbiol. Methods, 115, 57-63 (DOI: 10.1016/j.mimet.2015.05.020).

[22]. Kalyanaraman, B., Zielonka, J. (2017), Green fluorescent proteins induce oxidative stress in cells: A worrisome new wrinkle in the

application of the GFP reporter system to biological systems?, Redox Biol., 12, 755-757 (DOI: 10.1016/j.redox.2017.03.019).

[23]. He, L., Tan, C. P., Ye, R. R., Zhao, Y. Z., Liu, Y. H., Zhao, Q., Ji, L. N., Mao, Z. W. (2014), Theranostic iridium(III) complexes as one- and two-photon phosphorescent trackers to monitor autophagic lysosomes, Angew. Chem. Int. Ed. Engl., 53, 12137-12141 (DOI: 10.1002/anie.201407468).

[24]. Lee, H. W., Cho, M. K., Kim, H. R., Lim, C. S., Kang, C., Kim, H. M. (2017), Visualization of vesicular transport from the endoplasmic reticulum to lysosome using an amidine derived two-photon probe, Chem. Commun., 53, 6097-6100 (DOI: 10.1039/c7cc01518f).

[25]. Zhang, H., Fan, J., Dong, H., Zhang, S., Xu, W., Wang, J., Gao, P., Peng, X. (2013), Fluorene-derived two-photon fluorescent probes for specific and simultaneous bioimaging of endoplasmic reticulum and lysosomes: group-effect and localization, J. Mater. Chem., 1, 5450-5455 (DOI: 10.1039/C3TB20646G).

[26]. Liu, Y., Lok, C. N., Ko, B. C., Shum, T. Y., Wong, M. K., Che, C. M. (2010), Subcellular localization of a fluorescent artemisinin derivative to endoplasmic reticulum, Org. Lett., 12, 1420-1423 (DOI: 10.1021/ol902890j).

[27]. Verma, S. K., Kumari, P., Ansari, S. N., Ansari, M. O., Deori, D., Mobin, S. M. (2018), A novel mesoionic carbene based highly fluorescent Pd(ii) complex as an endoplasmic reticulum tracker in live cells, Dalton. Trans., 47, 15646-15650 (DOI: 10.1039/c8dt02778a).

[28]. Sheldrick, G. M. (2015), Crystal structure refinement with SHELXL, Acta. Crystallogr. C Struct. Chem., 71, 3-8 (DOI: 10.1107/s2053229614024218).

[29]. Kumari, P., Verma, S. K., Mobin, S. M. (2018), Water soluble two-photon fluorescent organic probes for long-term imaging of

lysosomes in live cells and tumor spheroids, Chem. Commun., 54, 539-542 (DOI: 10.1039/c7cc07812a).

[30]. Huang, S., Han, R., Zhuang, Q., Du, L., Jia, H., Liu, Y., Liu, Y. (2015), New photostable naphthalimide-based fluorescent probe for mitochondrial imaging and tracking, Biosens. Bioelectron., 71, 313-321 (DOI: 10.1016/j.bios.2015.04.056).

[31]. Zhu, L., Lv, W., Liu, S., Yan, H., Zhao, Q., Huang, W. (2013), Carborane enhanced two-photon absorption of tribranched fluorophores for fluorescence microscopy imaging, Chem. Commun., 49, 10638-10640 (DOI: 10.1039/c3cc46276e).

[32]. Lin, W., Buccella, D., Lippard, S. J. (2013), Visualization of peroxynitrite-induced changes of labile Zn2+ in the endoplasmic reticulum with benzoresorufin-based fluorescent probes, J. Am. Chem. Soc., 135, 13512-13520 (DOI: 10.1021/ja4059487).

[33]. Kim, H. R., Kumar, R., Kim, W., Lee, J. H., Suh, M., Sharma, A., Kim, C. H., Kang, C., Seung Kim, J. (2016), A far-red, photo- and bio-stable fluorescent marker selective to the endoplasmic reticulum and its application to tunicamycin-treated HeLa cells, Chem. Commun., 52, 7134-7137 (DOI: 10.1039/c6cc02330d).

[34]. Kong, L., Yang, L., Zhang, G.-b., Chen, Q.-y., Wang, H., Gan, X.-p., Li, H., Zhou, H.-p., Yang, J.-x., Tian, Y.-p. (2018), High fluorescence of carbazole derivatives for bioimaging of endoplasmic reticulum and lysosome: the influence of molecular structure on optical properties and cell uptake, J. Mater. Sci., 53, 921-936 (DOI: 10.1007/s10853-017-1570-z).

[35]. Szegezdi, E., Logue, S. E., Gorman, A. M., Samali, A. (2006), Mediators of endoplasmic reticulum stress-induced apoptosis, EMBO Rep., 7, 880-885 (DOI: 10.1038/sj.embor.7400779).

[36]. Oslowski, C. M., Urano, F. (2011), Measuring ER stress and the unfolded protein response using mammalian tissue culture system,

Methods Enzymol., 490, 71-92 (DOI: 10.1016/b978-0-12-385114-7.00004-0).

[37]. Herce, H. D., Garcia, A. E., Cardoso, M. C. (2014), Fundamental molecular mechanism for the cellular uptake of guanidinium-rich molecules, J. Am. Chem. Soc., 136, 17459-17467 (DOI: 10.1021/ja507790z).

[38]. Sheldrick, G. M. (2015), SHELXT - integrated space-group and crystal-structure determination, Acta Crystallogr. A Found. Adv., 71, 3-8 (DOI: 10.1107/s2053273314026370).

[39]. Linden, A. (2015), Chemistry and structure in Acta Crystallographica Section C, Acta Crystallogr. C Struct. Chem., 71, 1-2 (DOI: 10.1107/s2053229614026540).

[40]. Heller, A., Williams, D. L. (1970), Intramolecular proton transfer reactions in excited fluorescent compounds, J. Phys. Chem., 74, 4473-4480 (DOI: 10.1021/j100720a003).

[41]. Melhuish, W. H. (1961), Quantum efficiencies of fluorescence of organic susbstances: effect of solvent and concentration of the fluorescent solute, J. Phys. Chem., 65, 229-235 (DOI: 10.1021/j100820a009).

[42]. Friedrich, J., Seidel, C., Ebner, R., Kunz-Schughart, L. A. (2009), Spheroid-based drug screen: considerations and practical approach, Nat. Protoc., 4, 309-324 (DOI: 10.1038/nprot.2008.226).

[43]. Kessel, S., Cribbes, S., Bonasu, S., Rice, W., Qiu, J., Chan, L. L. (2017), Real-time viability and apoptosis kinetic detection method of 3D multicellular tumor spheroids using the Celigo Image Cytometer, Cytometry A., 91, 883-892 (DOI: 10.1002/cyto.a.23143).

CHAPTER 4

Mesoionic Carbene Based Fluorescent Palladium (II) Complex Selectively Label Endoplasmic Reticulum of Live Cells

4.1. Introduction

Owing to the advancement in bio-imaging techniques, the in vivo subcellular organelle targets and biochemical processes have gained much attention towards basic biomedical research and the development of novel clinical diagnostics *[1-3]*. In this regard, some organic ligand and metal complex based probes have been explored *[4-6]*. Among the sub-cellular organelles, the endoplasmic reticulum (ER) plays an important role in eukaryotic cells *[7]* in the synthesis and processing of proteins, and calcium storage *[8-9]*. Improper protein folding may interfere with ER functions. A recent development suggests that ER dysfunction is directly linked to many metabolic diseases, such as diabetes, obesity, insulin resistance, critical neurotrauma and advanced tauopathy *[10-12]*.

The design and synthesis of an appropriate chemical probe as the tool for the diagnosis and monitoring of diseases as well as biomarkers are the current area of focus. Understanding the complex molecular interactions in the human physiological system had posed a challenge to both chemists and biologists. Therefore, fluorescent probes have become popular because of their low cost, sensitive nature and ease of operation and use in bioactive molecules in living systems for both in vitro and in vivo studies. To understand the desired selectivity towards selective organelles, the recognition site of a fluorescent probe is designed in such a way that it maximizes the binding interactions *[13-18]*. Furthermore, fluorescence recovery after photobleaching (FRAP) is widely used as a powerful tool for monitoring the molecular dynamics of fluorescent-

tagged molecules within living cells by employing confocal microscopes (CSLMs) *[19]*.

There exist few reports on ER tracking by employing some metal complexes *[20]*, oxovanadium(IV) vitamin-B6 Schiff base complex *[21]*, and tunicamycin-treated and organoplatinum(II) complexes containing bis(N-heterocyclic carbene) *[7]* but all of these lack FRAP.

So far, reports on Pd complexes being engaged in anti-bacterial, anti-fungal, anti-viral and, more recently, anti-cancer activities with a focus on tumor cell lines like breast and prostate cancer by using different ligands such as triazole, dithiocarbamate *[22]*, triphenylphosphines *[23]*, hydrazine *[24]* and even curcumin, which is a well-known plant-based compound with apoptosis-inducing activity on cancer cells, are well documented. Furthermore, better lipophilicity or solubility results in enhanced cytostatic activity of Pd(II) complexes. Only one report is available on Pt(II) complex based ER tracking, but to the best of our knowledge this is the first report on a MIC based Pd(II) complex as an efficient ER tracker *[23-28]*.

In this chapter, we report the synthesis of a phenylene based MIC ligand forming a Pd(II) complex and its biological evaluation which has been ignored to date. A recent study advocates that endoplasmic reticulum (ER) dysfunction may be linked to critical neurotrauma and advanced tauopathy. In this regard, targeting the ER warrants urgent attention towards the therapeutic treatment of neurotrauma related neuro-degeneration. Herein, we report the synthesis of a new N-heterocyclic mesoionic carbene based highly fluorescent square-planar Pd(II) complex **1**, with a high quantum yield (0.737). Furthermore, the cytotoxicity associated with metal complexes is a key factor for their *in vivo* applicability; hence the cytotoxicity of Pd(II) complex **1** was also evaluated against HeLa and HEK 293 cell lines. Their localization in particular organelles of live cells was confirmed by co-localization with commercial organelle-targeting organic dyes.

4.2. Results and discussion

4.2.1. Synthesis and characterization:

Pd(II) complex **1** was synthesized by the Cu(I) catalyzed click reaction of 4-ethynyl toluene and sodium azide in the presence of sodium ascorbate and copper sulfate in a tert-butanol and water mixture; then the resulting product was converted into its triazolium iodide salt. This triazolium salt upon reaction with $PdCl_2$ in the presence of a base resulted in the formation of complex **1 (Scheme 4.1)**. The Pd(II) complex **1** is highly soluble in dichloromethane and ethyl acetate. **1** was characterized by ^{1}H, ^{13}C NMR, FTIR and mass spectroscopy and further authenticated by single crystal X-ray studies.

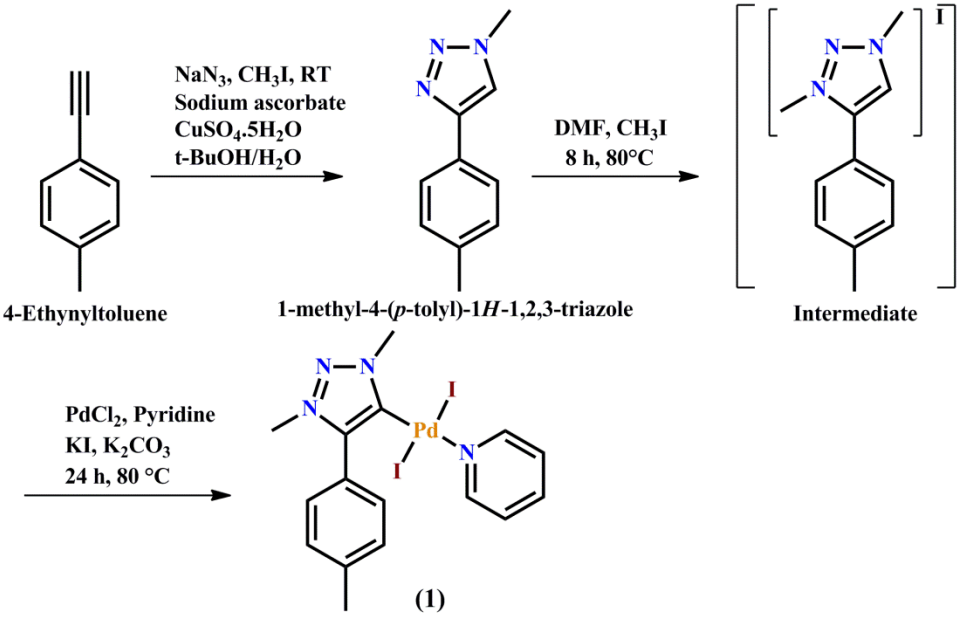

Scheme 4.1. Schematic representation of the synthesis of Pd(II) complex **1**.

The FTIR spectroscopy of **1** reveals the band at ~3100-3000 cm^{-1} which correspond to the presence of aromatic (C-H) stretching vibrations *[29]*. The ^{1}H NMR spectrum showed the absence of triazolium signal substituted with palladium. The ^{1}H NMR spectra of the **1** show the absence of azolium C–H proton which was observed at δ = 8.43 ppm for its parent 1-methyl-4-(p-tolyl)-1H-1,2,3-triazole compound. The

resonance for the aryl C–H protons (δ = 7.37 ppm) is significantly downfield shifted compared to their corresponding resonance (δ = 7.21 ppm) in complex **1**. The resonance for the C–H protons of pyridine ring were detected as multiplet at δ = 8.93, 7.78–7.80 and 7.66 ppm. Upon complex formation (**1**) the resonance for α-hydrogen atom of the pyridine ring (δ = 8.93) was more downfield shifted compared to their corresponding resonance in free pyridine (δ = 8.62) *[30]*. The resonance for the characteristic carbene carbon atom was observed at δ = 137.1 ppm in the ^{13}C NMR spectra of complex **1** which is quite similar to corresponding compound (δ = 137.6 ppm) *[31]*. The resonance for the α-carbon atom of the pyridine ring appeared downfield shifted: δ = 154.5 ppm, compared to their corresponding resonances in free pyridine. The LC-MS spectrum of Pd(II) complex **1** having peak 697.7 corresponds to $[M+ 2Cl]^+$ which supports the formation of the Pd(II) complex **1**.

4.2.2. Structural aspects of Pd(II) complex 1:

A single crystal suitable for X-ray diffraction study was obtained by slow evaporation of the dichloromethane–hexane solution of **1** at room temperature. Complex **1** that crystallizes in the monoclinic *P*21/n space group reveals the formation of the mononuclear **1 (Table A5)**. The Pd(II) atom in **1** is coordinated by a C-donor from the MIC ligand and a N-donor from pyridine, in a trans-fashion, and the remaining coordination sites are occupied by two iodide donors **(Figure 4.1)** forming a square planar geometry around the Pd atom. The C9–Pd1–N4 bond angle is almost linear at 177.77(5)° and the Pd1–C9 (1.967(8) Å) and Pd1–N4 (2.100(6) Å) bond lengths are in the range previously described for Pd(II) MIC complexes *[32-33]*. The dihedral angle between the NHC plane {N1 N2 N3 C8 C9} and the phenyl ring plane {C2 C3 C4 C5 C6 C7} is found to be 43.09° **(Figure 4.2).** The Pd–Py and triazole carbon–Pd moieties are twisted in the opposite direction, thus featuring the antigeometry of the complex **1**.

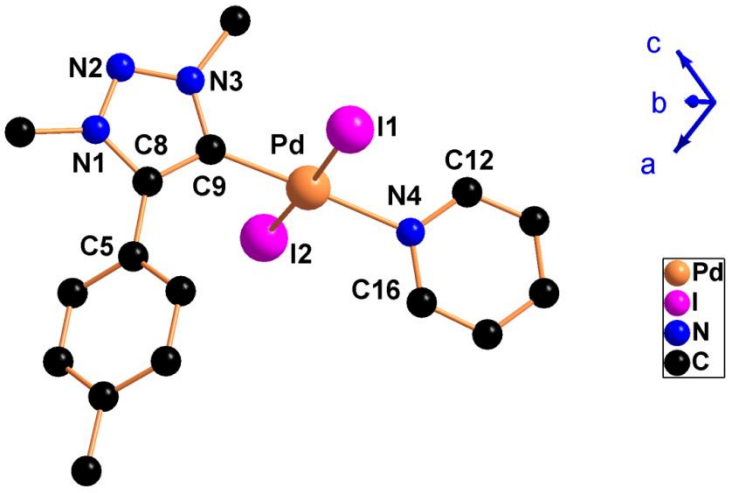

Figure 4.1. Perspective view of **1**

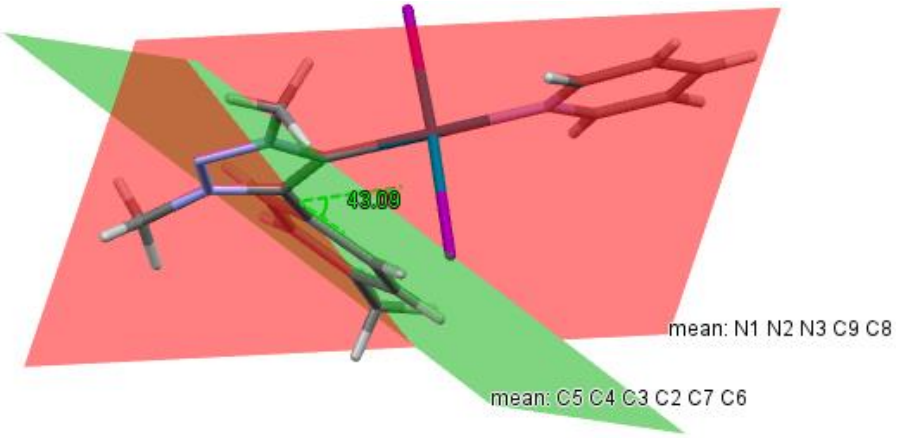

Figure 4.2. Dihedral angle between the NHC plane {N1 N2 N3 C8 C9} and the phenyl ring plane {C2 C3 C4 C5 C6 C7} is measured to be 43.09°.

The packing diagram of **1** reveals the presence of the C–H···I interaction. The intermolecular C(4)–H(4)···I(2) interactions, 3.092 Å, involve the donor carbon atom of the phenyl group and the acceptor I (2) atom of the other molecule leading to the formation of 1D polymeric chains **(Figure 4.3)** resembling the single-stranded helical structure of **1** via the I2···H4–C4 interaction along the *b*-axis **(Figure 4.4)**.

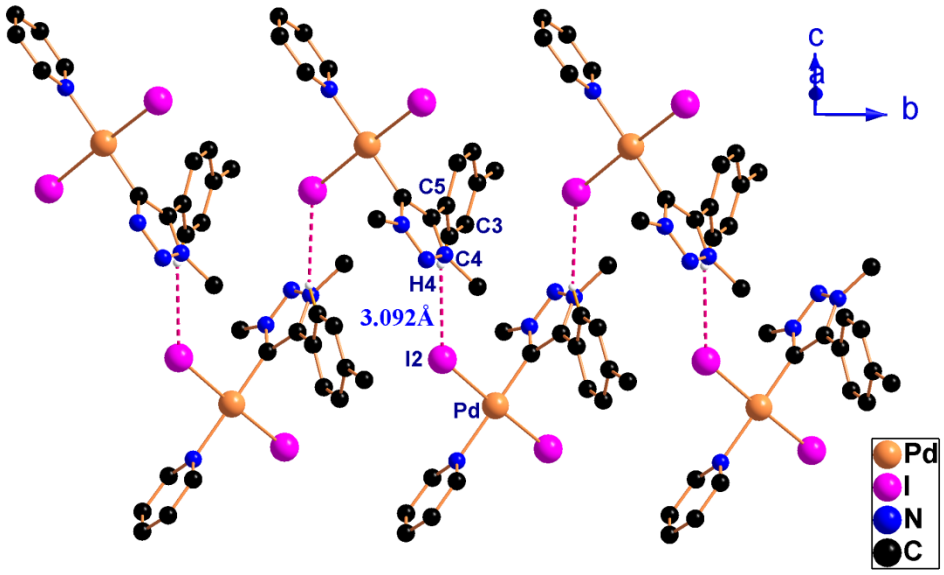

Figure 4.3. Supramolecular architecture of **1** via I2...H4−C4 interaction along *b*-axis.

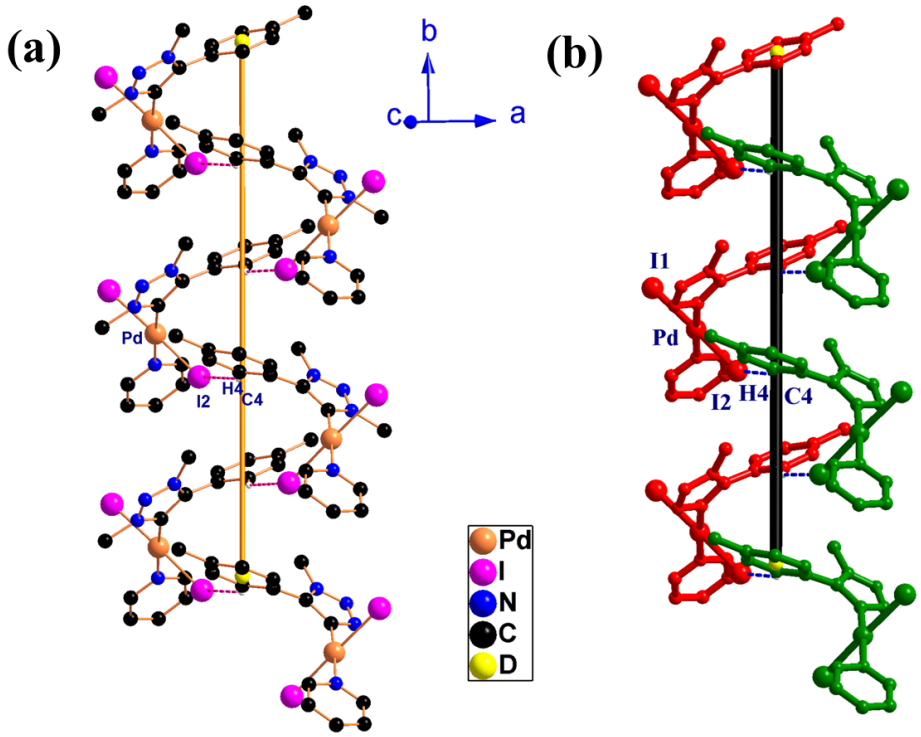

Figure 4.4. (a) Formation of single stranded helical structure of **1** via I2...H4−C4 along *b*-axis. **(b)** Helical view of **1**.

4.2.3. Photophysical properties of Pd(II) complex 1:

The electronic absorption and emission spectra of **1** were recorded in a tetrahydrofuran solution. The absorption bands of **1** at 233, 282 and

371 nm are attributed to the π → π* (aromatic moiety) and n → π* (triazole and pyridine) transitions respectively, for the ligand moiety, occurring due to the heteroaromatic moiety **(Figure 4.5).** The fluorescence emission data of **1** were obtained in a tetrahydrofuran solution upon excitation at λ_{ex} = 371 nm. The emission spectrum of **1** exhibited the highest intensity band at 405 and 430 nm via vibrionic splitting **(Figure 4.5).** Moreover, the Stokes shifts of Pd(II) complex **1** were found to be 34 and 59 nm. The quantum yield of **1** was found to be very high, 0.737 **(Figure 4.5).**

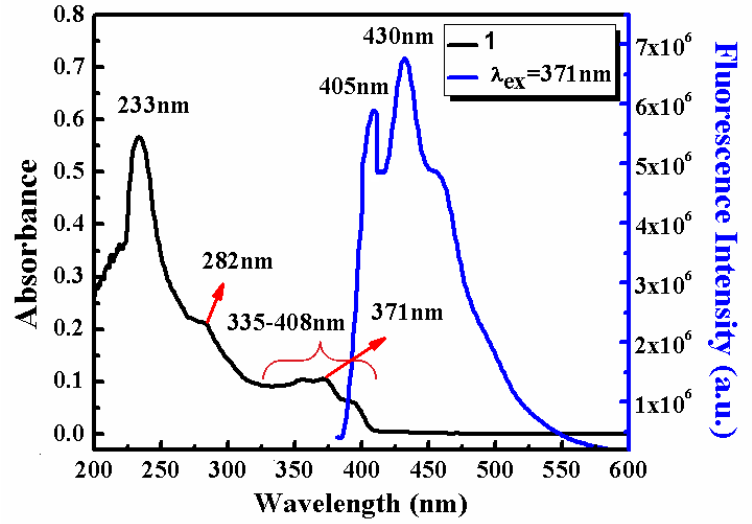

Figure 4.5. UV-visible (black) and fluorescence spectrum (blue) of the complex **1** at room temperature in 10^{-4} M tetrahydrofuran solution.

We recorded the emission spectra of Pd(II) complex **1** in 1% DMSO with various solvents (acetonitrile/THF/methanol/water) and found that the emission band splits into two partially resolved bands except in water **(Figure 4.6)**. This may be due to the strong hydrogen bonding between complex **1** and H_2O which locks the molecule for vibronic coupling. The fluorescence intensity of **1** was found to be trivial quenching at high pH (phosphate buffer saline containing 1% DMSO at various pH values); this may be due to the formation of the electron donor 1,2,3-triazole/iodine, through photo-induced electron transfer (PET) under basic conditions. **1** showed a slight red shift with a decrease in pH up to

3.1 and was quite stable up to pH 7.4 **(Figure 4.7A).** The fluorescence emission of **1** was also investigated in the micelles of positively charged cetyl-trimethyl-ammonium bromide (CTAB) and negatively charged sodium dodecyl sulfate (SDS) at 5.0 mM and 2.0 mM concentration respectively for mimicking the probe in the cell membranes **(Figure 4.7B and C)**. In addition, the fluorescence behaviors of **1** were unaffected at the studied pH range, indicating that the binding of the probe to the micelles efficiently shields the probe from the aqueous environment. These results imply that **1** can be localized in the membrane phases rather than in the aqueous phase in the cells.

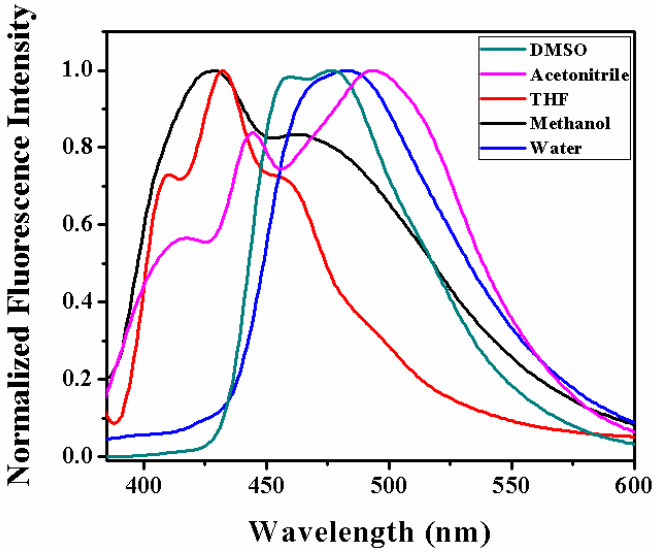

Figure 4.6. Emission spectrum of Pd(II) complex **1** in 1.0% DMSO and some other solvents (DMSO/Acetonitrile/THF/Methanol/Water) upon excitation at 371 nm.

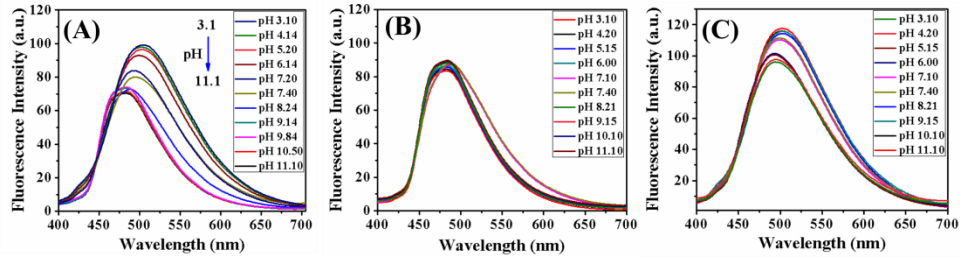

Figure 4.7. **(a)** Fluorescence spectra of Pd(II) complex **1** (10 μM) in different pH solutions 1% DMSO in PBS (phosphate-buffered saline) upon excitation at 371 nm. **(b)** In the presence of 5.0 mM CTAB (positively charged micelles). **(c)** In the presence of 2.0 mM SDS (negatively charged micelles).

The Pd(II) complexes are known for their extraordinary photo-luminescence due to the σ-donating property of the anionic carbons, which effectively raises the energy of the d–d states, diminishing their deactivating effect *[32-33]*. Furthermore, the photoluminescence spectra of **1** show two separate electronic transitions at 370 and 392 nm attributed to π* → π and π* → n transitions for the ligand moiety **(Figure 4.8)** upon excitation at 25 °C (λex = 282 nm) as expected in such Pd(II)/Pt(II) complexes *[34-36]*.

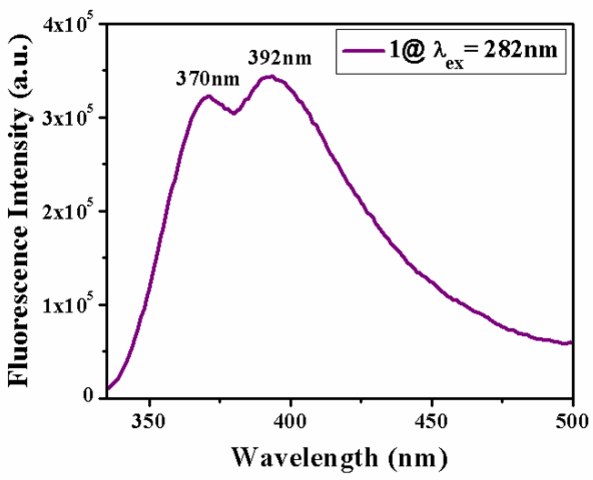

Figure 4.8. Photoluminescence spectrum of the complex **1** at room temperature in solid state.

4.2.4. Cytotoxicity studies:

The highly fluorescent nature of **1** prompted us to explore the role of **1** in live cells as a potential candidate for cellular organelle marker. To initiate biological activities, probe **1** was checked for cytotoxicity on both cancerous and normal cells, i.e. HeLa (cervical cancer cells) and HEK 293 (human embryonic kidney cells 293) cells, and was found to be nontoxic at a concentration up to 180 μM for 24 h as proved by the cell viability assay using MTT **(Figure 4.9)**.

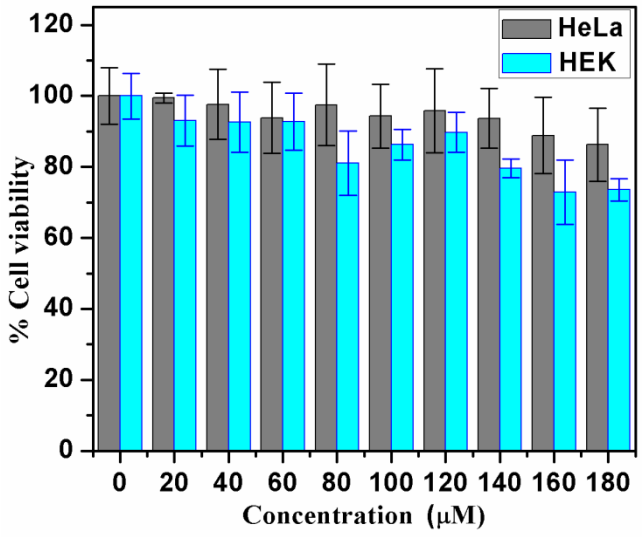

Figure 4.9. Cell viability study of probe **1** on HeLa (cervical cancer cells) and HEK 293 (Human embryonic kidney cells 293) normal cells by the MTT assay after 24 h incubation at 37°C and the results shown in mean ± SD of three separate measurements.

4.2.5. Flow cytometry studies:

Furthermore, flow cytometry acquires superior quality fluorescence signals with an elevated spatial resolution from a significant population of cells in flow *[37-39]*. Probe **1** labeled HeLa cells were estimated by flow cytometry **(Figure 4.10)**. The mean fluorescence intensity of a huge number of cells shifted from quadrant Q3–2 (control) to Q4–3 (treated) **(Figure 4.10a)** and a subsequent shift in the histogram towards higher intensity was also observed **(Figure 4.10b)**. Moreover, the mean fluorescence intensity of the untreated cells was as low as 62 as compared to the treated cells having a higher mean fluorescence intensity of 2759. This indicates that **1** can uniformly label an enormous population of cells, which was detected in live cell suspensions by flow cytometry. The rapid population-based fluorescence statistical data of flow cytometry are further supported by the pictorial images obtained from confocal laser scanning microscopy.

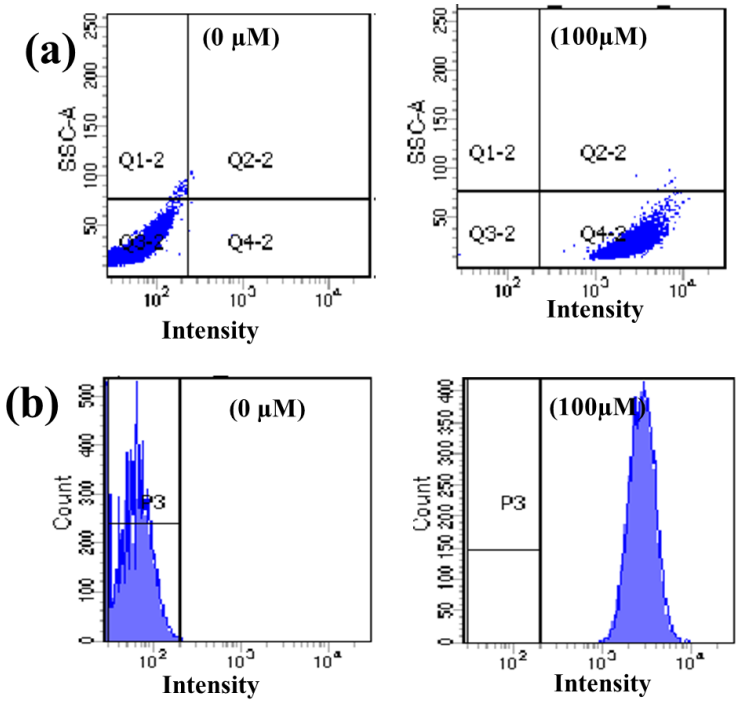

Figure 4.10. Flow cytometric analysis of probe **1** label large population of Living HeLa cells in suspension: **(a)** Scatter plot. **(b)** Histogram. **1**, λex = 405 nm; λem = 415-470 nm.

4.2.6. Organelles selectivity study by confocal imaging:

To confirm the initial cellular location of probe **1**, HeLa cells were treated with probe **1**, and the images were captured in both blue and red channels. The probe is fluorescent in the blue channel and non-fluorescent in the red channel; hence probe **1** was excited by 405 nm not by 599 nm **(Figure 4.11)**.

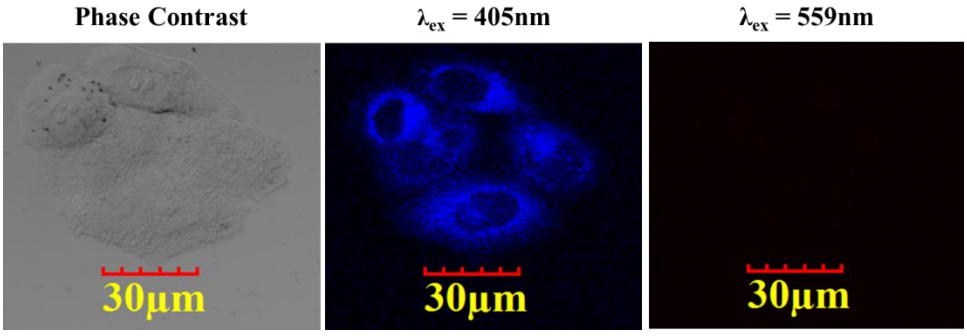

Figure 4.11. HeLa cells were treated with probe **1** and image where captured in blue and red channels. λ_{ex} =405nm; λ_{em} = 415-470 nm; λ_{ex} = 559 nm; λ_{em} = 580-700 nm.

Therefore we performed co-localization experiments with three commercially available red fluorescent organelle trackers (ER-Tracker Red for the endoplasmic reticulum, MitoTracker Red CMXRos for mitochondria and LysoTracker Red DND99 for lysosomes). The fluorescent co-localization images (pink) of **1** with these organelle trackers **(Figure 4.12)** indicated that **1** overlapped well with ER-Tracker Red with a high Pearson's colocalization coefficient R_r = 0.75 **(Figure 4.12a and Figure 4.13)**. However, the poor colocalization effect were observed for mitochondria (R_r value = 0.44) and lysosomes (R_r value = 0.49) **(Figure 4.12b and 4.12c)**. Moreover, Manders' coefficients were calculated with Manders' M1 = 0.901 and Manders' M2 = 0.679 signifying good colocalization of probe **1** (blue) and ER-Tracker Red (red) on a per-pixel level. This demonstrates that the probe **1** is highly selective towards localization in the endoplasmic reticulum and also compatible for counter-staining with LysoTracker Red and MitoTracker Red.

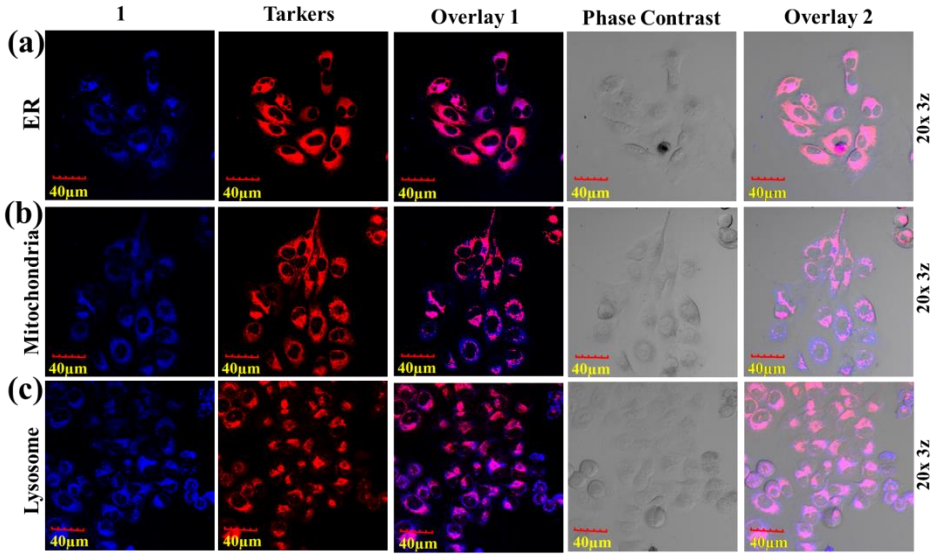

Figure 4.12. HeLa cells co-labeled with **1** (100 µM) and organelle markers. **(a)** ER-Tracker Red for the endoplasmic reticulum (1 µM); **(b)** MitoTracker Red CMXRos (80 nM) for mitochondria; **(c)** LysoTracker Red DND-99 (100 nM) for lysosomes. The images from left to right show probe **1** (column 1), organelle trackers (column 2), phase contrast (column 4), Overlay 1: overlay of the 1st and 2nd columns, and Overlay 2: overlay of the 1st, 2nd and 4th columns. Scale bar: 40 µm.

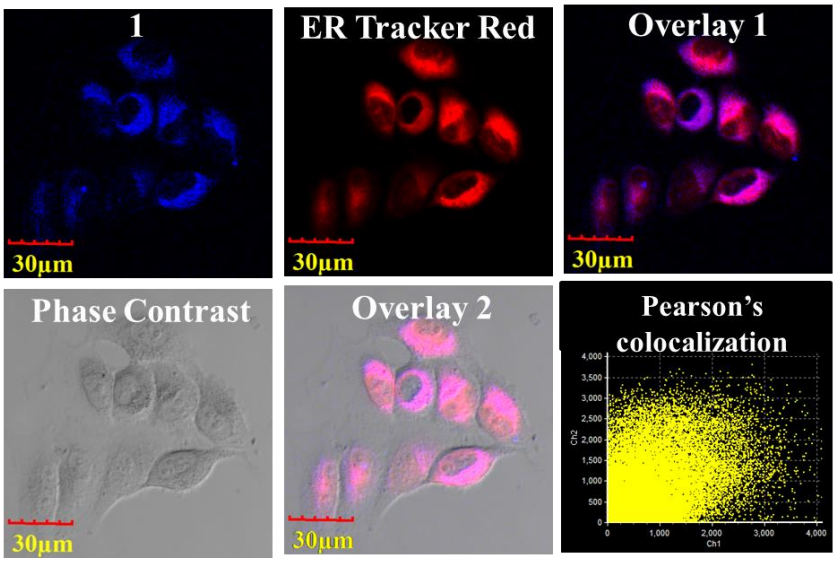

Figure 4.13. ER selective imaging of living HeLa cells treated with **1**. Live HeLa cells treated with **1** (100 µM) and ER-Tracker Red (1 µM). The fluorescence emission of **1** (blue). The ER-Tracker Red (red) colocalization of these two fluorophores is overlay 1 and 2 (pink). Pearson's colocalization graph (yellow). Probe 1: λ_{ex} = 405 nm, λ_{em} = 415–470 nm; ER-Tracker Red: λ_{ex} = 559 nm, λ_{em} = 580–700 nm.

4.2.7. *In vitro* photostability study of 1:

Photostability plays an important role for any marker in the cell to observe long-term imaging during physiological and morphological alterations within a stipulated time. In this regard, the photostability of **1** was studied in live HeLa cells and was compared with commercially available ER-Tracker Red. The fluorescence intensity initially decreases and after 200 scans it reaches 70% due to photobleaching but gradually recovers again up to 98% after 1800 scans **(Figure 4.14).**

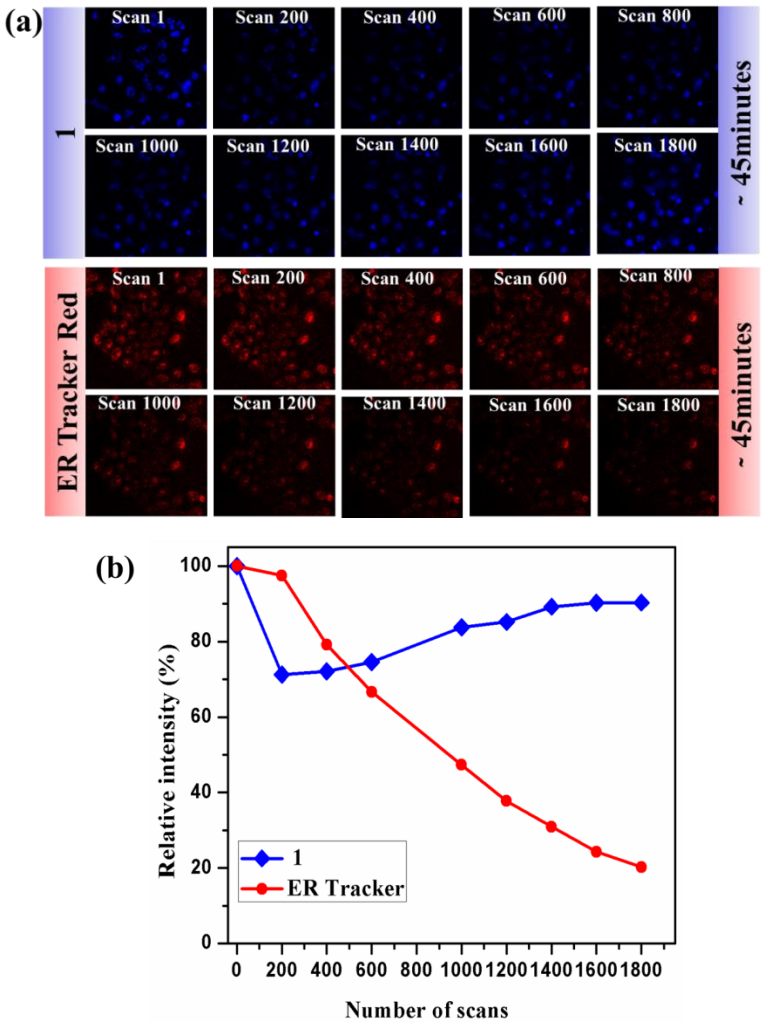

Figure 4.14. Comparisons of the photostability of probe **1** and ER-Tracker Red in HeLa cell lines. **(a)** Confocal images of **1** (100 μM, λ_{ex} = 405 nm, λ_{em} = 415–470 nm) and ER-Tracker Red (1 μM, λ_{ex} = 559 nm, λ_{em} =580–700 nm) for photobleaching in HeLa cells. **(b)** Comparative photostability graph of ER-Tracker Red and **1**.

This result indicate fluorescence recovery after photobleaching (FRAP) in the case of **1**. This may be due to any of the following reasons: (i) diffusion of soluble fluorescent probe **1** in the ER membrane and (ii) the movement of **1** between organelles. In contrast, the ER-Tracker Red shows very poor photostability with the intensity being reduced to 20% of the initial intensity after 1800 scans, and could not recover during laser scanning.

4.2.8. 3D Tumor spheroid imaging:

3D tumor spheroids possess numerous features that mimic in vivo tumors such as cell–cell interaction, hypoxia cells at the center and a well-oxygenated outer layer of the cells. In order to explore **1** towards 3D tumor spheroids, the fluorescence images were captured every 2 μm along the Z-axis. **1** penetrates to a depth of ~48 μm whereas the ER tracker penetrates up to ~24 μm depth **(Figure 4.15 and Figure 4.16)**. This suggests that the compound **1** exhibited more fluorescence in the deep layer cells of spheroids as compared to the standard dye.

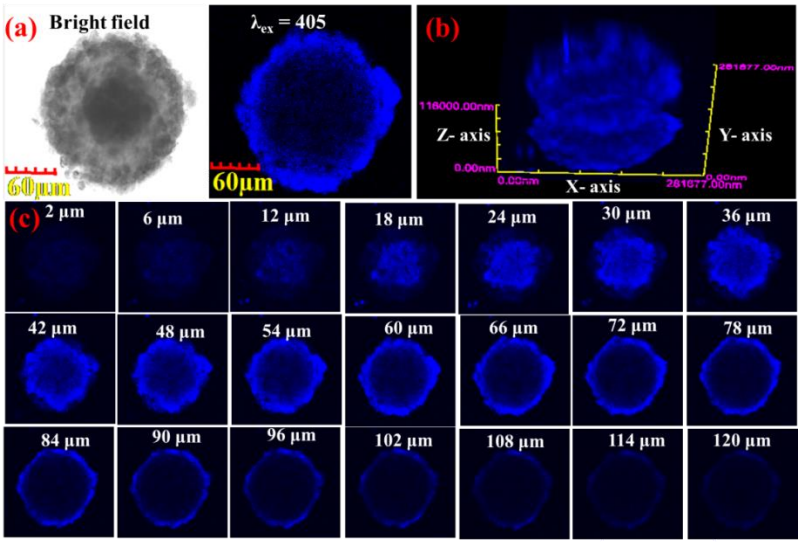

Figure 4.15. (a) Fluorescence images of 3D intact HeLa tumor spheroid after incubation of **1** (100 μM for 8 h) by confocal laser scanning microscope. **(b)** The Z-stack 3D images of intact spheroid. **(c)** The Z-stack images were captured after every 2 μm section from the top to bottom of tumor spheroid. The images were taken under a 10× objective λ_{ex} = 405 nm; λ_{em} = 415–470 nm.

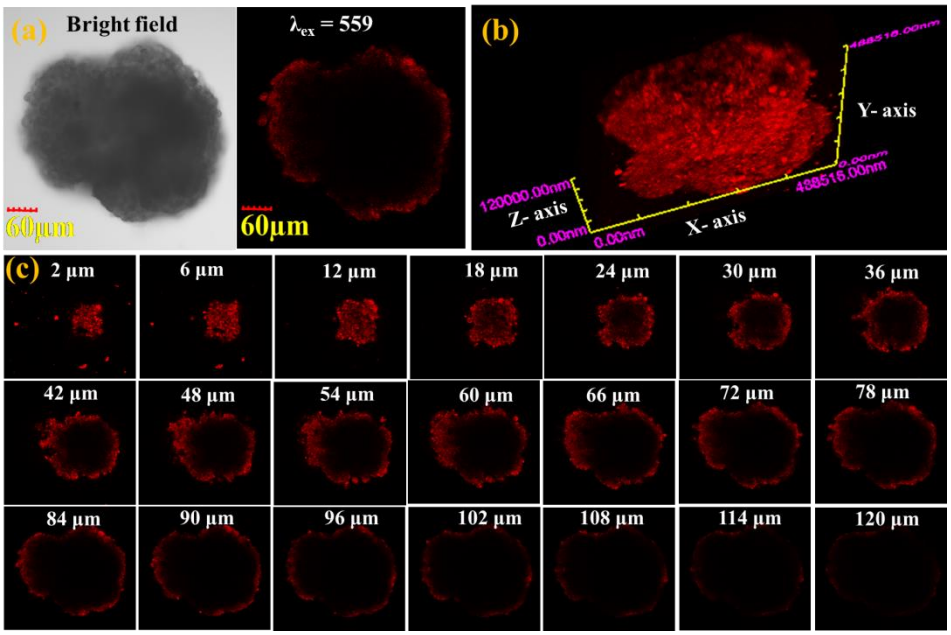

Figure 4.16. (a) Fluorescence images of 3D intact HeLa tumor spheroid after incubation of ER tracker (1.0 µM) for 8 h) by confocal laser scanning microscope. **(b)** The Z-stack 3D images of intact spheroid. **(c)** The Z-stack images were captured after every 2 µm section from the top to bottom of tumor spheroid. The images were taken under a 20× objective λ_{ex} = 559 nm; λ_{em} = 569–600 nm.

4.3. Conclusions

In conclusion, we report a rare example of the synthesis of new organometallic MIC based mononuclear Pd(II) complex **1**. The higher quantum yield and non-toxic nature of **1** make it a potential candidate for inter-cellular uptake. The fluorescence behavior of **1** was unaffected at a broad pH range, indicating that the binding of the probe to the micelles efficiently shields the probe from the aqueous environment. Thus, **1** selectively targets the ER of live cells and plays an important role in the movement of particles between organelles due to the fluorescence recovery after photobleaching (FRAP) property. **1** shows a rare FRAP property as compared to the so-far reported Pd/Pt complexes as well as commercially available ER-Tracker Red.

4.4. Experimental Section

4.4.1. Materials and physical measurements:

All reactions were carried out under nitrogen atmosphere using Schlenk techniques. Glassware was oven dried at 100 °C. Solvents were distilled by standard procedures prior to use. ^{1}H NMR (400 MHz), and ^{13}C NMR (400 MHz) spectra were collected on the Bruker Avance (III) instrument by using $CDCl_3$ and DMSO-d_6. ^{1}H NMR chemical shifts are reported in parts per million (ppm) in relation to the solvent residual peak ($CDCl_3$, 7.25 ppm; DMSO-d_6, 2.49 ppm). Chemical shifts of ^{13}C NMR are presented relative to the solvent residual peak ($CDCl_3$, 77.00 ppm; DMSO-d_6, 39.50 ppm). The FTIR spectra [400−4000 cm^{-1}] were obtained with a Bio-Rad FTS 3000MX instrument on KBr pellets. Melting points (mp) are recorded by means of open capillaries methods in degree centigrade. UV-Visible analysis were performed on a Varian UV-vis spectrophotometer (model: Cary 100) using a quartz cuvette with a path length of 1 cm. GC-MS spectra were recorded on a Bruker-Daltonics micro TOF-QII mass spectrometer.

4.4.2. X–ray Crystallography:

The crystal data of **1** was collected at 293 K by the means of graphite-monochromated Mo Kα (λα = 0.71073 Å). The strategy for the data collection was evaluated by the help of CrysAlisPro CCD software. The data were collected by the standard phi-omega scan techniques and were scaled and reduced using CrysAlisPro RED software. The structures were solved by the direct methods by using SHELXS-2014 and refined by full matrix least squares with SHELXL-2014, refining on F^2 *[40-41]* by direct methods the positions of all the atoms were obtained and all nonhydrogen atoms were refined anisotropically. All the remaining hydrogen atoms were placed in geometrically constrained positions and refined with isotropic temperature factors, generally 1.2 × Ueq of their

parent atoms. The hydrogen bonding interactions, molecular drawings and mean-plane analysis were obtained using the Diamond (ver. 3.1d). The crystal and refinement data are summarized in **Table A5** and the selected bond distances and bond angles are shown in **Table A6.**

4.4.3. Synthesis of 1-methyl-4-(p-tolyl)-1H-1,2,3-triazole:

4-Ethynyltoluene (97%), (252.0 mg, 2.0 mmol) and sodium azide (130 mg, 2.0 mmol) were suspended in a 1:1 mixture of water and *tert*-butyl alcohol (10 mL). After 30 minutes CH_3I (excess) was added. Further sodium ascorbate (5.0 mol %) was added, followed by copper (II) sulfate pentahydrate (1.0 mol %). The heterogeneous mixture was stirred for 10-12 hour; progress of the reaction was continuously monitored by TLC which indicates complete consumption of the reactants. The reaction mixture was diluted with water (10 mL), cooled in ice, and the white precipitate was collected by filtration. Precipitate was washed with cold water (2×10 mL) and dried under vacuum and further purified by column chromatography by elution of 10% ethyl acetate and hexane mixture. Yield: 320 mg (1.85 mmol, 92.4 %). ^{1}H NMR (400 MHz, DMSO-d_6) ppm δ: 8.4318 (s, 1H, Ctrz−H), 7.7136−7.6935 (d, J_{HH} = 8.04 Hz, 2H, HAr), 7.2476−7.2275 (d, J_{HH} = 8.04 Hz, 2H, HAr), 4.0637 (s, 3H, N−CH_3), 2.3131 (s, 3H, C−CH_3) ppm **(Figure 4.17)**. ^{13}C NMR (100 MHz, DMSO-d_6) ppm δ: 146.43 (Ctrz−Ar), 137.03 (Ctrz−H), 129.40 (*C*Ar−Ctrz), 128.04 (*C*Ar−CH_3), 125.01 (*C*Ar−Ctrz), 121.81 (*C*Ar−Ctrz), 36.33 (N−*C*H_3), 20.79 (C−*C*H_3) ppm **(Figure 4.18)**. DMF (3 mL) was added to the resulting compound (100 mg, 0.531 mmol) and CH_3I (excess). The solution was heated to 100 °C for 48 h. The reaction mixture was cooled to ambient temperature and to this was added diethyl ether (20 mL). The yellow colored solid was filtered and washed with excess amount of diethyl ether. We have taken this compound directly for the preparation of complex **1**. NMR spectra of 1-methyl-4-(p-tolyl)-1H-1,2,3-triazole are depicted in **Figure 4.17−4.18**.

4.4.4. Synthesis of Pd(II) complex 1:

To a mixture of 1,3-dimethyl-4-(4'-methylbenzene-1,2,3-triazolium Iodide salt (157 mg, 0.5 mmol), K_2CO_3 (138 mg, 1.0 mmol), $PdCl_2$ (88 mg, 0.5 mmol) and KI (excess) was added pyridine (5 mL). The resulting suspension was stirred for 24 h at 80 °C. The pyridine was removed in *vacuo* and the crude mixture was extracted with dichloromethane (15 mL). The solvent was removed and the yellow residue was loaded onto a silica gel column. Elution with a hexane:ethyl acetate (6:4, v:v) mixture gave compound **1** as a yellow solid. Yield: 187 mg (0.298 mmol, 60 %). ^{1}H NMR (400 MHz, $CDCl_3$) ppm δ: 8.9272 (d, 2H, HPy), 7.8001−7.7825 (d, J_{HH} = 7.04 Hz, 2H, HPy), 7.6633 (m, 1H, HPy), 7.3717−7.3541 (d, J_{HH} = 7.04 Hz, 2H, HAr), 7.2500 (d, 2H, HAr), 4.4162 (s, 3H, N−CH_3), 3.9244 (s, 3H, N−CH_3), 2.4460 (s, 3H, C−CH_3) ppm **(Figure 4.19).** ^{13}C NMR (100 MHz, $CDCl_3$) ppm δ: 153.81 (CPy), 144.13 (Ctrz−Ar), 140.01 (CPy), 137.31 (Ctrz−Pd), 133.50 (CAr−H), 130.19 (CAr−H), 129.46 (*C*Ar−Ctrz), 124.26 (CPy), 42.97 (N−CH_3), 37.21 (N−CH_3), 21.53 (C−*C*H_3) ppm **(Figure 4.20).** The LC-MS spectrum shows peak at 697.7 which corresponds to $[M + 2Cl]^+$ **(Figure 4.21).**NMR and ESI-MS spectra of complex **1** are depicted in **Figure 4.19−4.21**

4.4.5. Quantum yield calculation:

The fluorescence quantum yield (Φ_F) of **1** was calculated using eqn (1) by the steady-state comparative method using quinine sulfate as the standard having quantum yield Φ_{st} = 0.54 *[6]*.

$$\Phi_F = \Phi_{st} \times S_u/S_{st} \times A_{st}/A_u \times \eta^2_{Du}/\eta^2_{Dst} \qquad (1)$$

where Φ_F is the emission quantum yield of the sample, Φ_{st} is the emission quantum yield of the standard, S_u and S_{st} are the integrated emission band areas of the sample and the standard, respectively, while A_{st} and A_u represent the absorbance of the standard and the sample at the excitation

wavelength, respectively, and n_{Du} and n_{Dst} are the solvent refractive index of the sample and the standard, and u and st refer to the unknown and the standard, respectively.

4.4.6. Cytotoxicity studies:

Approx. 7000 HeLa (cervical cancer) cells and HEK 293 (Human embryonic kidney cells 293) normal cell line were seeded in in 96-well plate in 100 µL complete DMEM (DMEM, 10% (v/v) FBS and 1% antibiotics, Penicillin Streptomycin10,000 U/mL). Compound **1** was serial diluted in DMSO and added to media (0.1% DMSO in each well). The original media from each removed and 200 µL new media including compound (concentration ranging from 20 µM- 180 µM) added in each well. Each concentration experiment was performed in triplicate. Further cells were incubated for 24 h at 37 ℃ and 5% CO2 atmosphere followed by washing with phosphate buffered saline (PBS pH 7.4). 100 µL MTT *[42]* (1 mg/mL in phenol red free media) was added in each well and further incubated 4 hours at 37℃. Media rinsed and 100 µL DMSO added in order to dissolve purple formazan crystals. After 15 minutes shaking, absorbance at 570 nm was measured using Synergy H1 Biotek microplate reader. The % cell viability was calculated as: % cell viability = [Mean O.D. of the drug treated cell/Mean O.D. of the control well] × 100

4.4.7. Per-pixel spatial colocalization analysis:

A significance test was performed for the images in blue (probe **1**) and red (ER Tracker red) channels using Costes' method *[43]* and the P-value was found to be 1.00, which indicates that a randomized image set does not produce better correlation/colocalization than the real image. Furthermore, Manders' coefficients were calculated based on the formulae presented by Manders et al *[44]*.

4.4.8. *In vitro* photostability study:

Cervical cancer cell line HeLa was seeded in two confocal dishes. Dishes were incubated with **1** (100 μM for 8 h) and ER Tracker Red (1 μM, 30 min) separately. The cells were imaged using confocal microscope with no delay scan mode. Videos were recorded up to 1800 for ER Tracker Red and **1** respectively. ER Tracker Red and **1** ware excited at 559 nm and 405 nm respectively. Maximum intense signal of first scan was considered 100% for measuring relative decrease in intensity. Images at every 200 scans were obtained from video.

4.4.9. Flow cytometry:

HeLa cells were cultured in six-well tissue culture plates. When cells became 80% confluent then one well left without treatment with probe as control and another well treated with **1** (100μM) for 8 h. followed by washing with PBS three times. Cells were harvested by trypsin/EDTA and re-suspended in PBS. The samples were analyzed by BD LSRFortessa TM Flow cytometry with excitation at 405 nm and emission 415-470 nm. Data were analyzed by DB FACSDiva software. Total 10,000 events were acquired for each sample.

4.4.10. Cell imaging:

HeLa cells were grown overnight on a confocal microscope dish with a cover slip and 100 μM **1** was added to cells for 8 h. After washing twice with PBS, the live cells were stained with 500nM ER-Tracke Red for 30 min and washed with PBS three times. Subcellular localization analysis of **1** and ER-Tracke Red was imaged by confocal microscope. **1** was excited 405 nm and emission collected at 415–470 nm**;** ER-Tracker Red was excited at 559 nm and fluorescence was collected at 580–700 nm.

4.4.11. The selectivity of subcellular organelle:

Cervical cancer (HeLa) cell line was seeded in three confocal dishes and incubated for 24 h at 37°C and 5% CO_2 atmosphere. Then 100 µM **1** was added in each disc for 8 h followed by washing twice with PBS. The live cells were co-stain with ER-Tracke Red (1µM) for ER imaging, LysoTracker Red (100 nM) for lysosome imaging and MitoTracker Red (80 nM,) for mitochondria imaging. After incubation for 30 min, the live cells were washed with PBS four times. Subcellular localization analysis of complex **1** and ER-Tracke Red were imaged by confocal microscope. An Olympus laser scanning microscope was used for confocal imaging. Complex **1** was excited 405 nm and emission collected at 415–470 nm**;** ER-Tracke Red, LysoTracker Red DND99 as well as MitoTracker Red CMXRos were excited at 559 nm and fluorescence was collected at 580–700 nm.

4.4.12. Generation of multicellular 3D spheroids:

Multicellular tumor spheroids (MCTSs) were produced using the liquid overlay method *[45]*. When HeLa cells became 60% confluent in T-25 flack, they were harvested by trypsin/EDTA solution and re-suspended in Dulbecco's Modified Eagle's Medium (DMEM) complete media. Flat-bottom 96 well plates were coated with 80µL of a sterile 1.5% (wt/vol) agarose solution in complete DMEM to make a non-adherent surface. 600 cells were seeded in each agarose coated well in 150µl complete DMEM. The plates were incubated at 37°C and 5% CO2 until spheroids formed. Spheroid were transfers in confocal disc followed by spheroids treatment by 100µM **1** for 8 h, then image captured by confocal laser scanning microscopy.

NMR and mass spectra of 1-methyl-4-(p-tolyl)-1H-1,2,3-triazole and complex 1

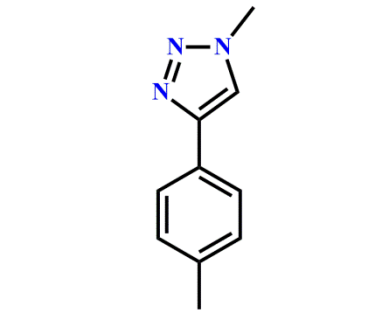

1-methyl-4-(*p*-tolyl)-1*H*-1,2,3-triazole

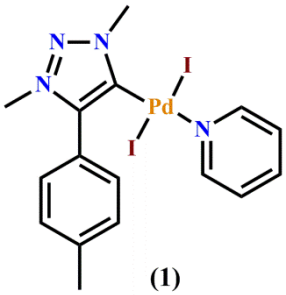

(1)

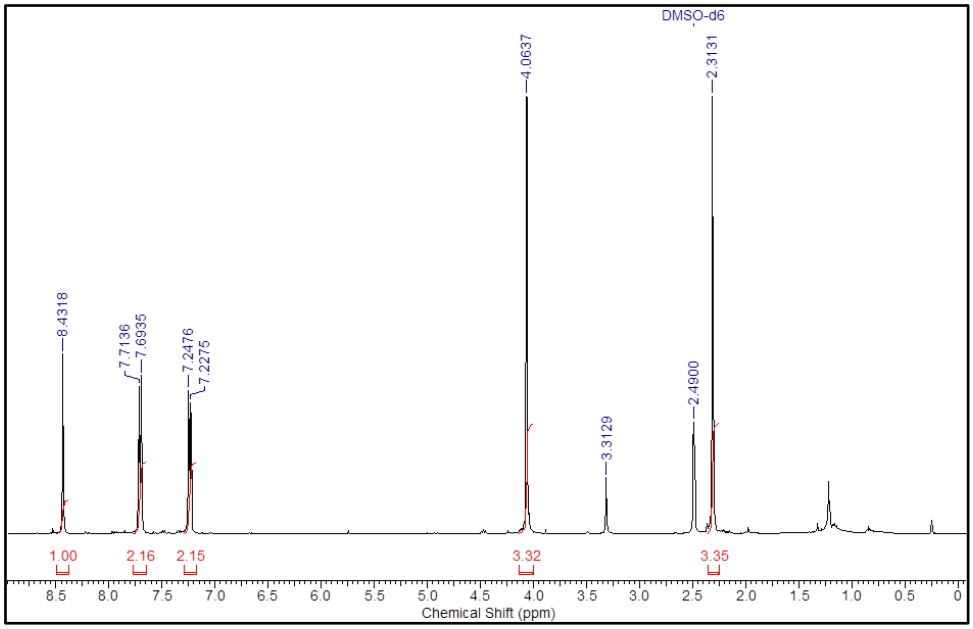

Figure 4.17. ^{1}H NMR Spectrum of 1-methyl-4-(p-tolyl)-1H-1,2,3-triazole in (DMSO-d_6).

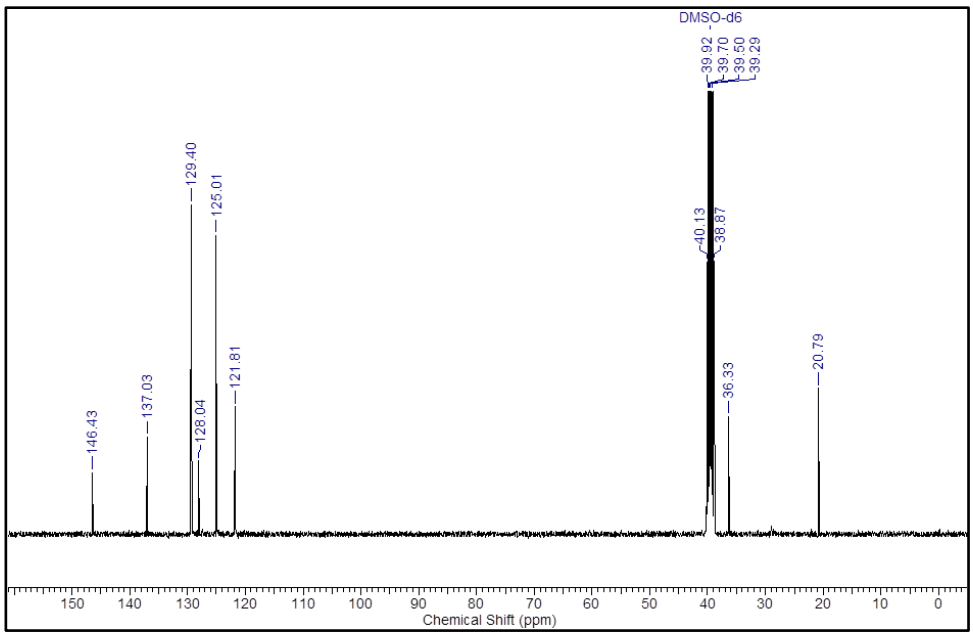

Figure 4.18. ^{13}C NMR Spectrum of 1-methyl-4-(p-tolyl)-1H-1,2,3-triazole (DMSO-d_6).

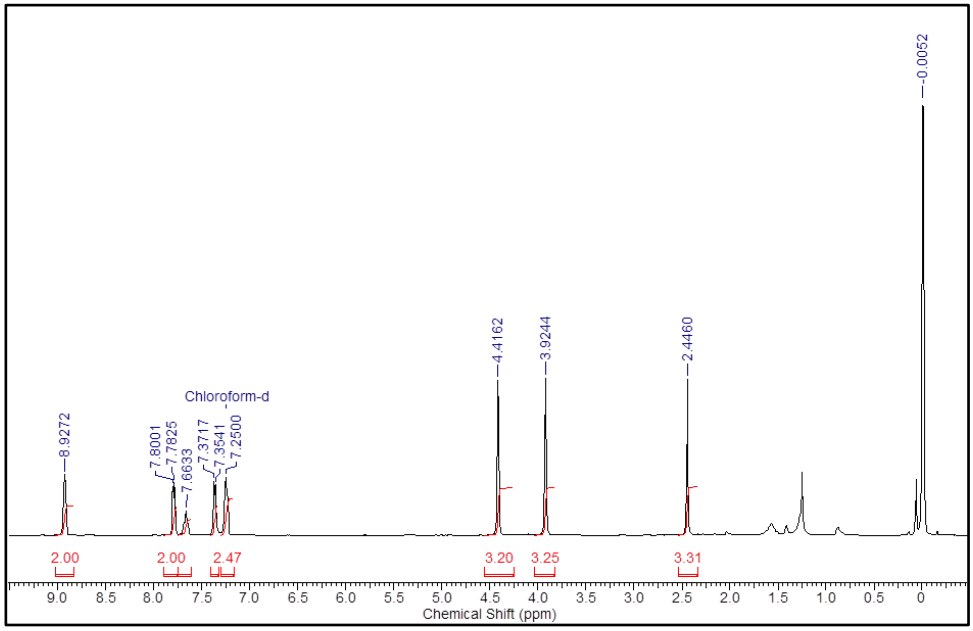

Figure 4.19. ^{1}H NMR Spectrum of **1.**

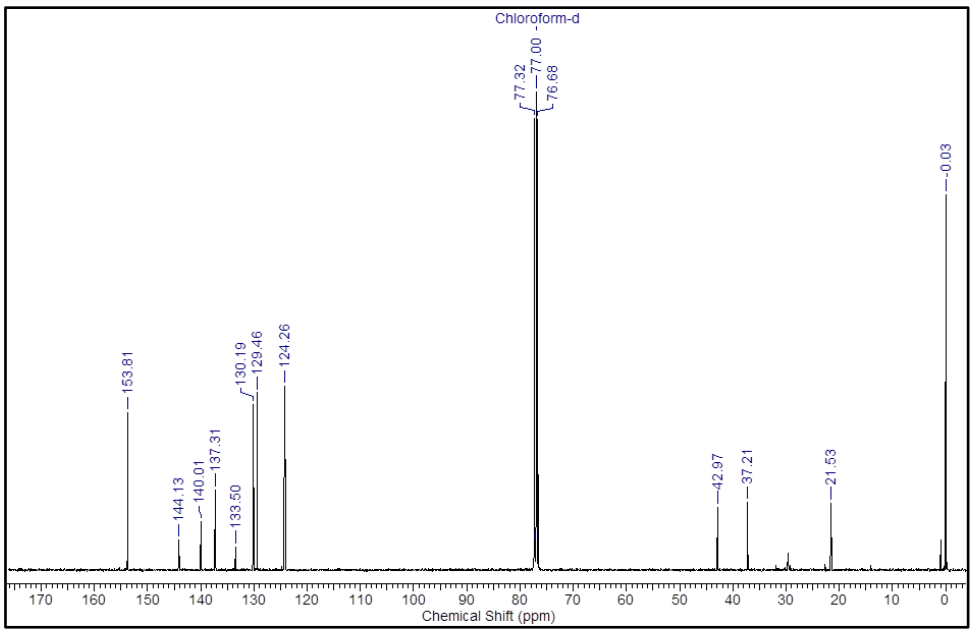

Figure 4.20. ^{13}C NMR Spectrum of **1.**

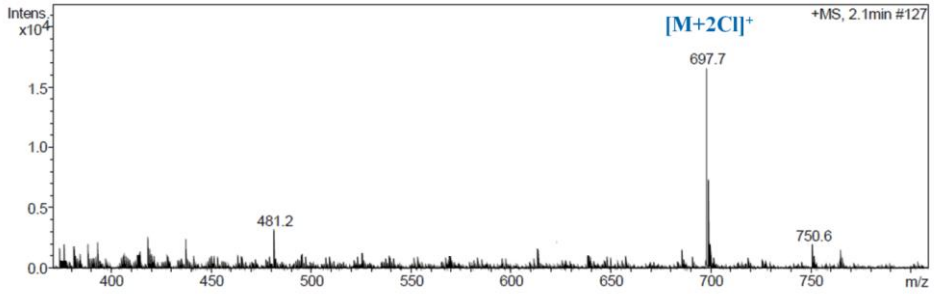

Figure 4.21. LC-MS spectrum of the complex **1.**

4.5. References

[1]. Walter, P., Ron, D. (2011), The unfolded protein response: from stress pathway to homeostatic regulation, Science, 334, 1081-1086 (DOI: 10.1126/science.1209038).

[2]. Kim, I., Xu, W., Reed, J. C. (2008), Cell death and endoplasmic reticulum stress: disease relevance and therapeutic opportunities, Nat. Rev. Drug. Discov., 7, 1013-1030 (DOI: 10.1038/nrd2755).

[3]. McDonald, L., Liu, B., Taraboletti, A., Whiddon, K., Shriver, L. P., Konopka, M., Liu, Q., Pang, Y. (2016), Fluorescent flavonoids for endoplasmic reticulum cell imaging, J. Mater. Chem. B, 4, 7902-7908 (DOI: 10.1039/c6tb02456d).

[4]. Huang, S., Han, R., Zhuang, Q., Du, L., Jia, H., Liu, Y., Liu, Y. (2015), New photostable naphthalimide-based fluorescent probe for mitochondrial imaging and tracking, Biosens. Bioelectron., 71, 313-321 (DOI: 10.1016/j.bios.2015.04.056).

[5]. Kumari, P., Verma, S. K., Mobin, S. M. (2018), Water soluble two-photon fluorescent organic probes for long-term imaging of lysosomes in live cells and tumor spheroids, Chem. Commun., 54, 539-542 (DOI: 10.1039/c7cc07812a).

[6]. Saini, A. K., Sharma, V., Mathur, P., Shaikh, M. M. (2016), The development of fluorescence turn-on probe for Al(III) sensing and live cell nucleus-nucleoli staining, Sci. Rep., 6, 34807 (DOI: 10.1038/srep34807).

[7]. Zou, T., Lok, C. N., Fung, Y. M., Che, C. M. (2013), Luminescent organoplatinum(II) complexes containing bis(N-heterocyclic carbene) ligands selectively target the endoplasmic reticulum and induce potent photo-toxicity, Chem. Commun., 49, 5423-5425 (DOI: 10.1039/c3cc40953h).

[8]. Harding, H. P., Zhang, Y., Ron, D. (1999), Protein translation and folding are coupled by an endoplasmic-reticulum-resident kinase, Nature, 397, 271-274 (DOI: 10.1038/16729).

[9]. Stevenson, J., Huang, E. Y., Olzmann, J. A. (2016), Endoplasmic Reticulum-Associated Degradation and Lipid Homeostasis, Annu. Rev. Nutr., 36, 511-542 (DOI: 10.1146/annurev-nutr-071715-051030).

[10]. Meinig, J. M., Fu, L., Peterson, B. R. (2015), Synthesis of Fluorophores that Target Small Molecules to the Endoplasmic Reticulum of Living Mammalian Cells, Angew. Chem. Int. Ed., 54, 9696-9699 (DOI: 10.1002/anie.201504156).

[11]. Deshaies, R. J. (2014), Proteotoxic crisis, the ubiquitin-proteasome system, and cancer therapy, BMC Biol., 12, 94 (DOI: 10.1186/s12915-014-0094-0).

[12]. Shore, G. C., Papa, F. R., Oakes, S. A. (2011), Signaling cell death from the endoplasmic reticulum stress response, Curr. Opin. Cell Biol., 23, 143-149 (DOI: 10.1016/j.ceb.2010.11.003).

[13]. Mejuto, C., Guisado-Barrios, G., Gusev, D., Peris, E. (2015), First homoleptic MIC and heteroleptic NHC–MIC coordination cages from 1,3,5-triphenylbenzene-bridged tris-MIC and tris-NHC ligands, Chem. Commun., 51, 13914-13917 (DOI: 10.1039/C5CC05114B).

[14]. Radloff, C., Hahn, F. E., Pape, T., Frohlich, R. (2009), Supramolecular structures from mono and dimetalated biscarbene ligands, Dalton Trans., 7215-7222 (DOI: 10.1039/b907896g).

[15]. Radloff, C., Weigand, J. J., Hahn, F. E. (2009), A tetranuclear molecular rectangle from four gold(I) atoms linked by dicarbene and diphosphine ligands, Dalton Trans., 9392-9394 (DOI: 10.1039/b916651c).

[16]. Han, Y., Lee, L. J., Huynh, H. V. (2010), Pyrazole-derived remote dicarbenes: versatile ligands for di- and tetranuclear complexes, Chemistry, 16, 771-773 (DOI: 10.1002/chem.200902737).

[17]. Rit, A., Pape, T., Hahn, F. E. (2010), Self-assembly of molecular cylinders from polycarbene ligands and Ag(I) or Au(I), J. Am. Chem. Soc., 132, 4572-4573 (DOI: 10.1021/ja101490d).

[18]. Maity, R., Rit, A., Schulte to Brinke, C., Daniliuc, C. G., Hahn, F. E. (2013), Metal center dependent coordination modes of a tricarbene ligand, Chem. Commun., 49, 1011-1013 (DOI: 10.1039/c2cc37446c).

[19]. Braga, J., Desterro, J. M., Carmo-Fonseca, M. (2004), Intracellular macromolecular mobility measured by fluorescence recovery after photobleaching with confocal laser scanning microscopes, Mol. Biol. Cell, 15, 4749-4760 (DOI: 10.1091/mbc.e04-06-0496).

[20]. Banerjee, S., Dixit, A., Shridharan, R. N., Karande, A. A., Chakravarty, A. R. (2014), Endoplasmic reticulum targeted chemotherapeutics: the remarkable photo-cytotoxicity of an oxovanadium(IV) vitamin-B6 complex in visible light, Chem. Commun., 50, 5590-5592 (DOI: 10.1039/c4cc02093f).

[21]. Kim, H. R., Kumar, R., Kim, W., Lee, J. H., Suh, M., Sharma, A., Kim, C. H., Kang, C., Seung Kim, J. (2016), A far-red, photo- and bio-stable fluorescent marker selective to the endoplasmic reticulum and its application to tunicamycin-treated HeLa cells, Chem. Commun., 52, 7134-7137 (DOI: 10.1039/c6cc02330d).

[22]. Moura, T. R. d., Cavalcanti, S. L., Godoy, P. R. D. A. V., Sakamoto-Hojo, E. T., Rocha, F. V., Almeida, E. T. d., Deflon, V. M., Mauro, A. E., Netto, A. V. d. G. (2017), Synthesis, characterization and antitumor activity of palladium(II) complexes of imidazolidine-2-thione, Transition Met. Chem., 42, 565-574 (DOI: 10.1007/s11243-017-0161-9).

[23]. Khan, H., Badshah, A., Murtaz, G., Said, M., Rehman, Z. U., Neuhausen, C., Todorova, M., Jean-Claude, B. J., Butler, I. S. (2011), Synthesis, characterization and anticancer studies of mixed

ligand dithiocarbamate palladium(II) complexes, Eur. J. Med. Chem., 46, 4071-4077 (DOI: 10.1016/j.ejmech.2011.06.007).

[24]. Mukherjee, S., Chowdhury, S., Chattapadhyay, A. P., Bhattacharya, A. (2011), Spectroscopic, cytotoxic and DFT studies of a luminescent palladium(II) complex of a hydrazone ligand that induces apoptosis in human prostate cancer cells, Inorg. Chim. Acta, 373, 40-46 (DOI: 10.1016/j.ica.2011.03.048).

[25]. Valentini, A., Conforti, F., Crispini, A., De Martino, A., Condello, R., Stellitano, C., Rotilio, G., Ghedini, M., Federici, G., Bernardini, S., Pucci, D. (2009), Synthesis, oxidant properties, and antitumoral effects of a heteroleptic palladium(II) complex of curcumin on human prostate cancer cells, J. Med. Chem., 52, 484-491 (DOI: 10.1021/jm801276a).

[26]. Divsalar, A., Saboury, A. A., Mansoori-Torshizi, H., Ahmad, F. (2010), Design, synthesis, and biological evaluation of a new palladium(II) complex: beta-lactoglobulin and K562 as targets, J. Phys. Chem. B, 114, 3639-3647 (DOI: 10.1021/jp909143b).

[27]. Eryazici, I., Moorefield, C. N., Newkome, G. R. (2008), Square-Planar Pd(II), Pt(II), and Au(III) Terpyridine Complexes: Their Syntheses, Physical Properties, Supramolecular Constructs, and Biomedical Activities, Chem. Rev., 108, 1834-1895 (DOI: 10.1021/cr0781059).

[28]. Ruiz, J., Villa, M. D., Cutillas, N., Lopez, G., de Haro, C., Bautista, D., Moreno, V., Valencia, L. (2008), Palladium(II) and platinum(II) organometallic complexes with 4,7-dihydro-5-methyl-7-oxo[1,2,4]triazolo[1,5-a]pyrimidine. Antitumor activity of the platinum compounds, Inorg. Chem., 47, 4490-4505 (DOI: 10.1021/ic701873b).

[29]. Tavassoli, M., Landarani-Isfahani, A., Moghadam, M., Tangestaninejad, S., Mirkhani, V., Mohammadpoor-Baltork, I. (2016), Copper Dithiol Complex Supported on Silica Nanoparticles:

A Sustainable, Efficient, and Eco-friendly Catalyst for Multicomponent Click Reaction, ACS Sustainable Chem. Eng., 4, 1454-1462 (DOI: 10.1021/acssuschemeng.5b01432).

[30]. Babij, N. R., McCusker, E. O., Whiteker, G. T., Canturk, B., Choy, N., Creemer, L. C., Amicis, C. V. D., Hewlett, N. M., Johnson, P. L., Knobelsdorf, J. A., Li, F., Lorsbach, B. A., Nugent, B. M., Ryan, S. J., Smith, M. R., Yang, Q. (2016), NMR Chemical Shifts of Trace Impurities: Industrially Preferred Solvents Used in Process and Green Chemistry, Org. Process Res. Dev., 20, 661-667 (DOI: 10.1021/acs.oprd.5b00417).

[31]. Maity, R., van der Meer, M., Sarkar, B. (2015), Redox-active multinuclear Pd(ii) complexes with bis- and tris-mesoionic carbenes, Dalton Trans., 44, 46-49 (DOI: 10.1039/C4DT03239J).

[32]. Herrmann, W. A. (2002), N-heterocyclic carbenes: a new concept in organometallic catalysis, Angew. Chem. Int. Ed., 41, 1290-1309 (PMID: 19750753).

[33]. Hahn, F. E., Jahnke, M. C. (2008), Heterocyclic carbenes: synthesis and coordination chemistry, Angew. Chem. In.t Ed., 47, 3122-3172 (DOI: 10.1002/anie.200703883).

[34]. Pugh, D., Danopoulos, A. A. (2007), Metal complexes with ‘pincer’-type ligands incorporating N-heterocyclic carbene functionalities, Coord. Chem. Rev., 251, 610-641 (DOI: 10.1016/j.ccr.2006.08.001).

[35]. Adams, C. J., Fey, N., Parfitt, M., Pope, S. J., Weinstein, J. A. (2007), Synthesis, structures and properties of a new series of platinum-diimine-dithiolate complexes, Dalton Trans., 4446-4456 (DOI: 10.1039/b709252k).

[36]. Cummings, S. D., Eisenberg, R. (1996), Tuning the Excited-State Properties of Platinum(II) Diimine Dithiolate Complexes, J. Am. Chem. Soc., 118, 1949-1960 (DOI: 10.1021/ja951345y).

[37]. Zhang, D. Y., Zheng, Y., Tan, C. P., Sun, J. H., Zhang, W., Ji, L. N., Mao, Z. W. (2017), Graphene Oxide Decorated with Ru(II)-Polyethylene Glycol Complex for Lysosome-Targeted Imaging and Photodynamic/Photothermal Therapy, ACS Appl. Mater. Interfaces., 9, 6761-6771 (DOI: 10.1021/acsami.6b13808).

[38]. Godfrey, W. L., Hill, D. M., Kilgore, J. A., Buller, G. M., Bradford, J. A., Gray, D. R., Clements, I., Oakleaf, K., Salisbury, J. J., Ignatius, M. J., Janes, M. S. (2005), Complementarity of Flow Cytometry and Fluorescence Microscopy, Microsc. Microanal., 11, 246-247 (DOI: 10.1017/S1431927605510316).

[39]. Chen, X., Bi, Y., Wang, T., Li, P., Yan, X., Hou, S., Bammert, C. E., Ju, J., Gibson, K. M., Pavan, W. J., Bi, L. (2015), Lysosomal targeting with stable and sensitive fluorescent probes (Superior LysoProbes): applications for lysosome labeling and tracking during apoptosis, Sci. Rep., 5, 9004 (DOI: 10.1038/srep09004).

[40]. Sheldrick, G. M. (2015), SHELXT - integrated space-group and crystal-structure determination, Acta Crystallogr. A Found. Adv., 71, 3-8 (DOI: 10.1107/s2053273314026370).

[41]. Sheldrick, G. M. (2015), Crystal structure refinement with SHELXL, Acta Crystallogr. C Struct. Chem., 71, 3-8 (DOI: 10.1107/s2053229614024218).

[42]. Bernas, T., Dobrucki, J. (2002), Mitochondrial and nonmitochondrial reduction of MTT: interaction of MTT with TMRE, JC-1, and NAO mitochondrial fluorescent probes, Cytometry, 47, 236-242 (DOI: 10.1002/cyto.10080).

[43]. Costes, S. V., Daelemans, D., Cho, E. H., Dobbin, Z., Pavlakis, G., Lockett, S. (2004), Automatic and quantitative measurement of protein-protein colocalization in live cells, Biophys. J., 86, 3993-4003 (DOI: 10.1529/biophysj.103.038422).

[44]. Manders, E. M. M., Verbeek, F. J., Aten, J. A. (1993), Measurement of co-localization of objects in dual-colour confocal images, J.

Microsc., 169, 375-382 (DOI: 10.1111/j.1365-2818.1993.tb03313.x).

[45]. Friedrich, J., Seidel, C., Ebner, R., Kunz-Schughart, L. A. (2009), Spheroid-based drug screen: considerations and practical approach, Nat. Protoc., 4, 309-324 (DOI: 10.1038/nprot.2008.226).

CHAPTER 5

Design and Synthesis of a New Ligand with Dual Role: Mechanically Elastic Crystal and Selective Mitochondria Imaging

5.1. Introduction

The use of multi-talented materials has been of great interest to the researchers considering the vast array of potential applications and good economic viability *[1]*. Although, the properties of flexible organic materials in solid-state has been explored extensively but their solution state studies were unnoticed *[2]*. In the solid-state, crystalline organic materials are attractive because of their potential applications in phototransistors*[3]*, solar cells *[4]*, light-emitting diodes (LEDs) *[5]*, photonics *[6]*, flexible electronics *[7]*, bioelectronics *[8]*, integrated optical waveguides *etc [9-11]*. Nowadays, widespread attention has been attracted towards mechanically flexible materials due to their encouraging applications in pharmaceutical industries for artificial muscles *[12]*, molecular robotics *[13]*, and biomedical devices *[14-15]*. Organic crystals have various advantages over inorganic counterparts, such as light-weight, cheaper cost and intrinsic structure-function tunability, which makes them extremely attractive. But for their practical utilization on bendable substrates, the poor mechanical performance at single molecule level remains a significant drawback *[16-17]*.

In general, the single crystals of organic compounds are well-shaped and hard in macroscopic dimension but in rare cases it crystallizes in thin and flexible manner to resists the stress, this may be due to the arrangement of orientated layers of molecular assembly *[18-19]*. There exists some reports on dynamic single crystals that show photomechanical effect *[20-21]*, plastic or elastic flexibility *[2, 22-24]*, thermosalient effect *[25]*, or twisting *[26]* but often these discoveries are serendipitous. The

bendable organic crystals display plastic (irreversible) distortion under applied stress *[27]*. Elastic bending of organic single crystals is an unusual phenomenon, only recently described in few reports *[2, 13, 19-20, 22, 28-34]* Therefore, the single organic crystal which can withstand high mechanical flexibility similar to the soft material such as elastomers, thin film and polymers can be of prime importance for the design of future smart materials.

Mechanical bending properties of molecular crystals has been explored by various groups such as Reddy *[27–28]* Desiraju, *[33,35]* Naumov *[36–39]* Takamizawa *[40–41]* etc. The elasticity of single organic crystals usually governed by the applied mechanical stress, which is based on weak or strong interactions between crystal's lattice molecules. So far most of the reports on flexible organic ligands are based on thiophenyl and tetrafluoropyridyl based π-conjugated derivatives *[19, 32]*, halogenated N-benzylideneanilines based Schiff base *[33]* tri-substituted haloimidazoles *[34]*, terephthalamide *[39]*, fluorobenzoic acid derivative *[40]*, and benzonitrile derivative *[42]*, either involved substitution of halogens or tedious synthetic routes. However, to the best of our knowledge, so far only few reports are available on non-halogenated simple Schiff base ligand with elastic flexible crystals in solid-state *[2, 9]*.

On the other hand, rapid development has been observed recently in the field of bio-imaging in live cells, in particular tracking of the cellular organelles by employing small organic molecules *[43-45]*. Mitochondria are semiautonomous organelles, which found in most of the eukaryotic cells. They play a central role in adenosine triphosphate (ATP) production which is considered as energy currency for cells *[45-46]*. They also participate in amino acids metabolism, synthesis of a few important biological macromolecules, and also regulate ion homeostasis and respiration *[47]*. Mitochondrial dysfunction leads to various neurological glitches for example, Alzheimer's disease, Parkinson's disease, etc.

Improper function of mitochondria causes cancer and diabetes *[48]*. Therefore, tracking of mitochondria is significant in developing a profound understanding of their function and regulation mechanisms. Such studies also support the expansion of new strategies for the diagnosis and treatment of mitochondrial-related diseases. Commercially available fluorescent mitochondria imaging dyes are Mito trackers red FM, JC-1, Mito trackers green FM. However, rapid photobleaching and poor photostability of these conventional dyes restrict their application for long term live cell imaging *[47, 49-50]*. Due to excellent photostability and fluorescence properties of semiconductor quantum dots, they are extensively used for bio-imaging purposes. However, biological toxicity caused by the release of heavy metals limits their use in live cells *[51]*. Hence, there is a need to develop a fluorescent probe for live cell imaging which has high photostability and negligible cytotoxicity.

5.2. Results and discussion

5.2.1. Synthesis and characterization:

Herein, we designed and synthesized a ligand with multi-functional properties, we attempt to explore the solid-state crystalline properties which involve the mechanical elastic bending phenomenon of the crystals and the solution state properties which involve mitochondria imaging in live cells. A new multitasking Schiff base (E)-2-(((3-hydroxynaphthalen-2-yl)imino)methyl) naphthalen-1-ol (**H_2L**) was synthesized by the condensation reaction of 1-hydroxy-2-naphthaldehyde and 3-Amino-2-naphthol (1:1) in methanol at 25° C for 5h **(Scheme 5.1)**.

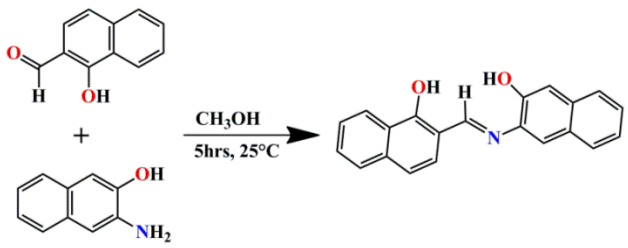

Scheme 5.1. Schematic representation of the synthesis of **H_2L**.

H_2L has been characterized by ^1H NMR, ^{13}C NMR, FTIR, ESI-MS, powder XRD and further authenticated by single crystal X-ray diffraction studies. **H_2L** crystallizes in the orthorhombic with $P2_12_12_1$ space group **(Figure 5.1 and Table A7 and A8).** Molecular crystals of **H_2L** were grown in polar protic solvents such as ethanol and methanol and were found to be lengthy and elastic in nature. In ethanol, crystal quality was quite good as compared to methanol and other solvents. The crystal structure of **H_2L** is found to be planar in nature.

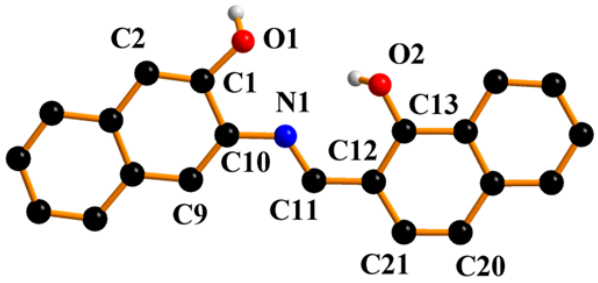

Figure 5.1. Perspective view of **H_2L**.

5.2.2. Structural aspects of H_2L:

Elastic bending behavior of the single crystals of **H_2L** was examined by applying mechanical stress using tweezers and a thin needle under a binocular microscope and to our excitement; it shows good elastic flexibility *viz* on releasing the stress, the crystal returns to its original position **(Figure 5.2)**. The various successive bending stages of **H_2L** are depicted in **(Figure 5.2)**. Furthermore, to confirm elasticity, **H_2L** crystal was mounted in bent position with greater difficulties by entangling the single crystal in a Y-shaped designed metal needle and X-ray diffraction patterns were recorded by SCXRD techniques. X-ray diffraction spots intensity slightly decrease in the crystal under bending stress in comparison to the original straight crystal, which is attributed to the modified absorption and reflection characteristics of the bent crystal **(Figure 5.3)**. During elastic bending of the single crystal, its effective thickness is altered at the critical bending points which lead to very weak

diffraction. The molecules retain their crystallinity even under bending stress. Additionally, after the relaxation of the bent crystal, it exhibits the original unit cell parameters. This serves as evidence of the remarkable elastic bending characteristics of the single crystal **(Figure 5.2)**.

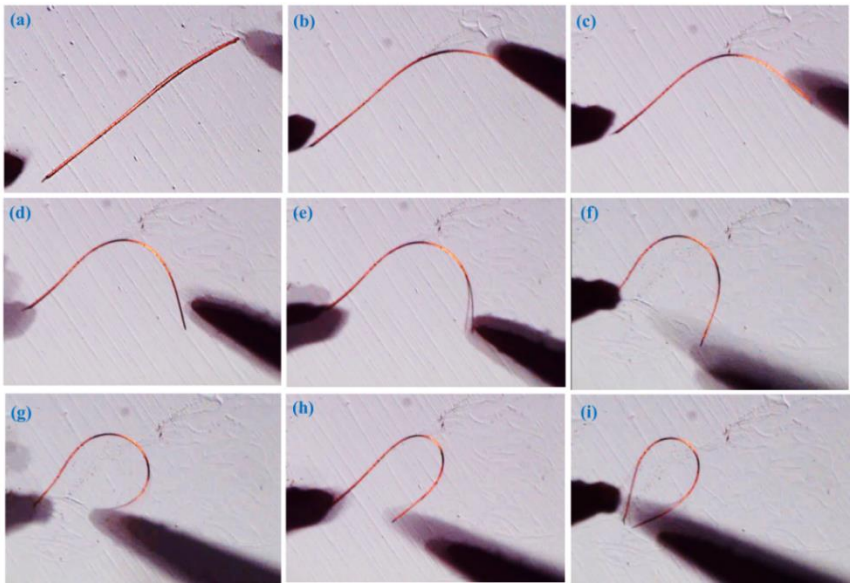

Figure 5.2. Various elastic stages **(a–i)** in the successive bending of **H_2L** crystal.

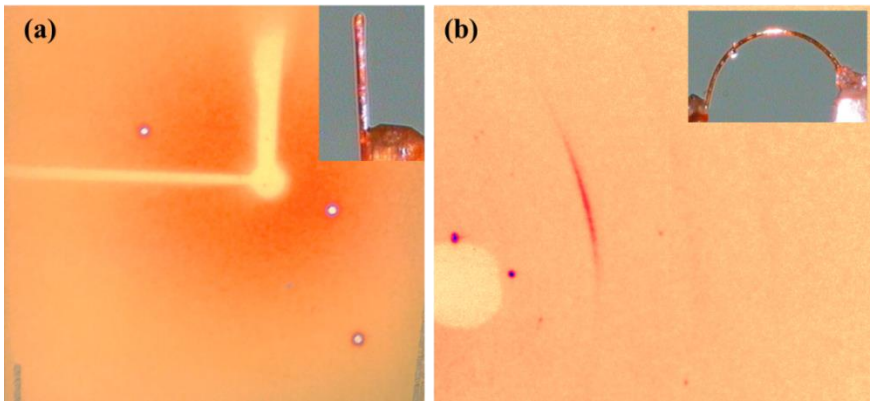

Figure 5.3. Diffraction images obtained from the mounted crystal and the inset shows the **(a)** original form and **(b)** bent form of **H_2L**.

Bending calculations were performed on the **H_2L** crystal in accordance with the methodology described earlier *[2, 52-53]*. Briefly, a model was adopted in which elastic bending introduces strain energy (E_s) due to compression and elongation of outer and inner arcs, respectively **(Figure 5.4)**. The strain energy is greater for a thicker crystal and lesser

for a thinner crystal as the magnitude of Δl is greater for the inner and outer arcs for a thicker crystal. Consequently, thinner crystals can be bent farther than thicker ones. The strain energy (E_s) increases with a decrease in critical radius r_c *[52-53]*. Simple calculations are presented in the supporting information to determine the values of Δl and critical radius r_c for the **H_2L** crystal.

The average change in translation along the 1D axis (Δl) is found to be 0.6248 Å/molecule for a crystal with length of 0.25 mm. The critical radius for breakage of the crystal is found to be 19.9 μm and the breaking strain is experienced by the crystal when the change in angle per molecule upon bending is 0.0004498847°/molecule. The difference between these calculations for the crystals before and after bending is negligible, indicating excellent elastic properties of the **H_2L** crystal.

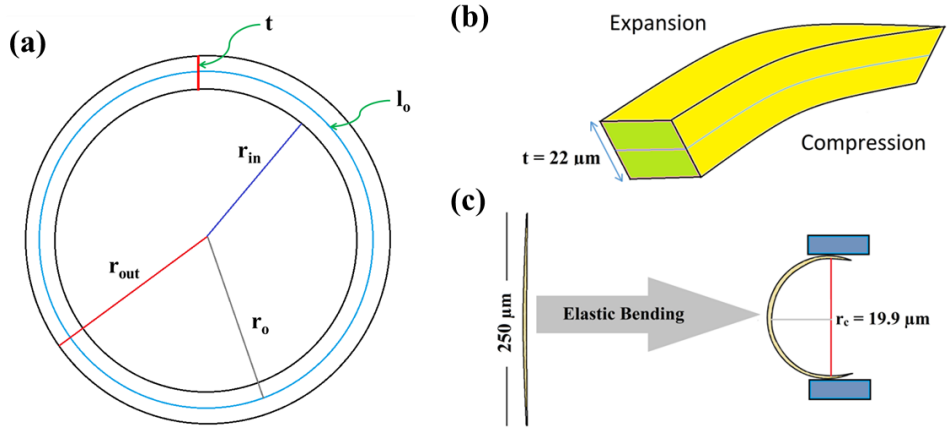

Figure 5.4. Illustrative diagrams: **(a)** full loop considered for calculation of changes in lengths and angles in an elastic crystal with thickness t and an initial length of l_o. **(b)** Forces acting on crystal during elastic bending and **(c)** Bending of crystal showing critical radius.

H_2L crystallizes as a planar molecular structure, where imine (>CH=N-) group is attached to two naphthyl moiety in its both arms. The packing feature of **H_2L** shows the presence of two O(1)–H(1)···O(2) type intermolecular hydrogen bonding interactions. Interestingly, **H_2L** shows two hydrogen bonds by connecting with two neighbouring molecules. **H_2L**

presents a dual role, where the electron-rich naphthyl moiety attached to an amine group (behaving as a donor) and naphthyl moiety attached to an aldehyde group (behaving as an acceptor). Such interactions O(1)–H(1)···O(2) (bond length 2.152(0) Å) between the donor, O(1)···H(1) of the naphthyl moiety attached with 3-Amino-2-naphthol and acceptor group O(2) of another naphthyl moiety of the 1-hydroxy-2-naphthaldehyde **(Figure 5.5)** is observed. These interactions lead to the formation of 1-D polymeric chains **(Figure 5.5)** which further extended through intermolecular C–H···π inter-actions, 3.445(1) Å forming a 2D-network **(Figure 5.6)**.

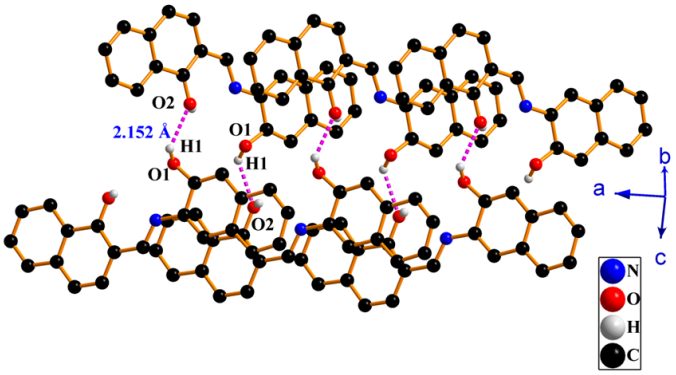

Figure 5.5. O–H···O type H-Bonding interactions, distance = 2.125(0) Å, forming 1D polymeric chain in **H_2L**.

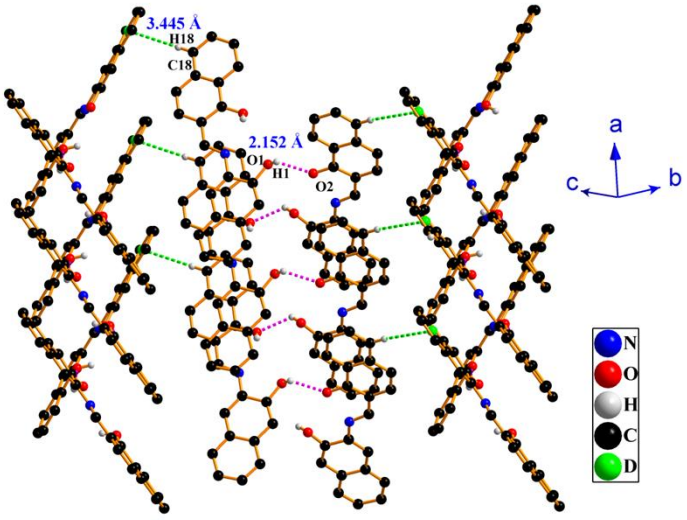

Figure 5.6. Packing diagram of **H_2L**, showing intermolecular C-H···π interactions, distance = 3.445(1) Å and O–H···O type H-Bonding interactions, distance = 2.152(0) Å, forming a 2D framework (D represent the dummy atom).

The molecular wires at the (100), (010) and (001) faces **(Figure 5.7)** through the self-assembly of planar (E)-2-(((3-hydroxynaphthalen-2-yl)imino) methyl)naphthalen-1-ol (**H_2L**) molecules shown in **Figure 5.7** *[19, 32]*.

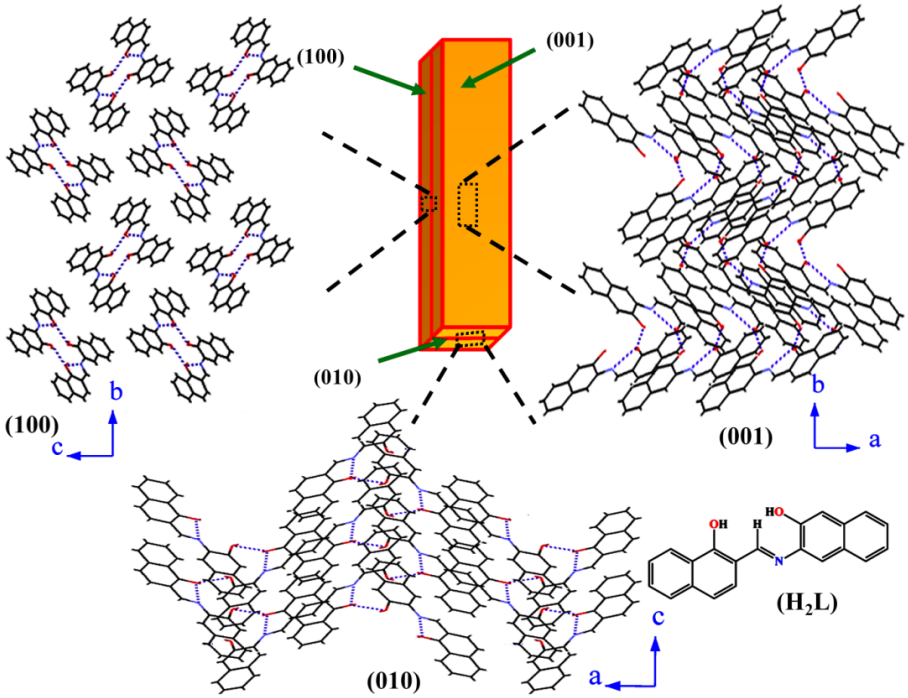

Figure 5.7. Molecular packing of **H_2L** in viewed into (100), (010) and (001) faces.

The wire shape elastic crystals of H2L were formed due to the formation of cross-linking of molecules which are sliding over each other as shown above in the packing of H2L (Figure 4). This may be generated through intermolecular hydrogen bonding (O(1)–H(1)···O(2)) and C–H···π interactions in the three domains, outer, inner, and central arcs shown in Figure 6 *[31]*. These observations are in line with previous reports stating that intermolecular hydrogen bonding and C–H···π interactions are highly beneficial in stabilizing the crystal structure and imparting compressive and tensile strength facilitating high elasticity *[24,31,54-56]*.

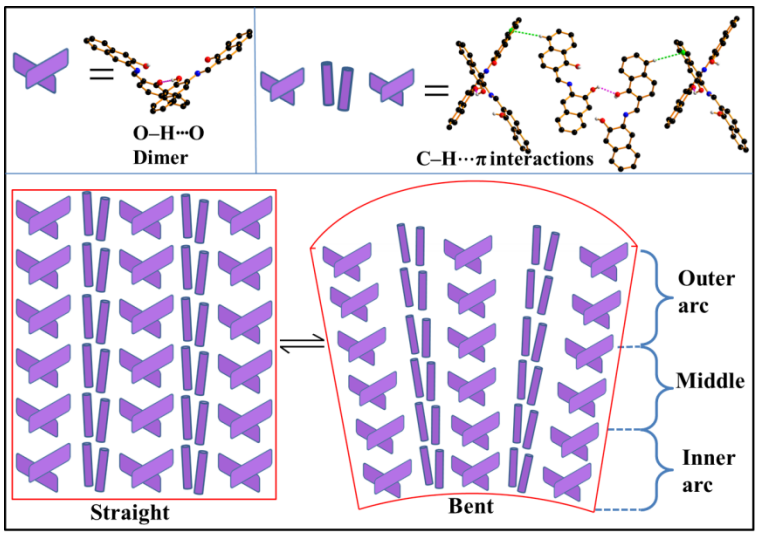

Figure 5.8. Schematic illustration of the probable molecular rearrangement of **H_2L** during straight and bending state.

Raman Spectra of the straight crystal when compared to those taken of the crystal bent from outer and inner arcs **(Figure 5.9)** show only negligible differences, indicative a low impact of stress/strain and high elasticity *[56-57]*. The Raman results suggest that the chemical bonding between the atoms in **H_2L** is well-retained even upon bending, and that the chemical bonds are not affected by the bending phenomena.

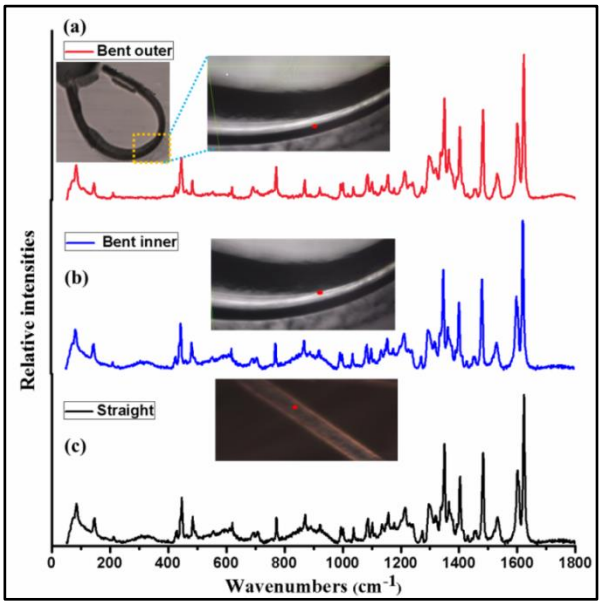

Figure 5.9. Raman spectra corresponding to the bent **(a)** outer part **(b)** inner part and **(c)** straight crystals of **H_2L**.

The Powder XRD spectrum of **H_2L** in it's straight, bent and relaxed form is given in **Figure 5.10**. It is found that the crystal exhibits several planes *via* unique diffraction peaks. It is observed that all of these planes are retained after relaxation post-bending, indicating a very high elastic property and almost complete retention of long-range order. However, the peaks are slightly shifted when comparing the straight, bent and relaxed crystals. We believe that these changes are caused due to the introduction of elastic stress during bending *[57]* and the slight peak shifting of the relaxed crystal XRD spectrum relative to the original, straight crystal is likely due to the effect of residual strain arising from the bending event *[58-59]*.

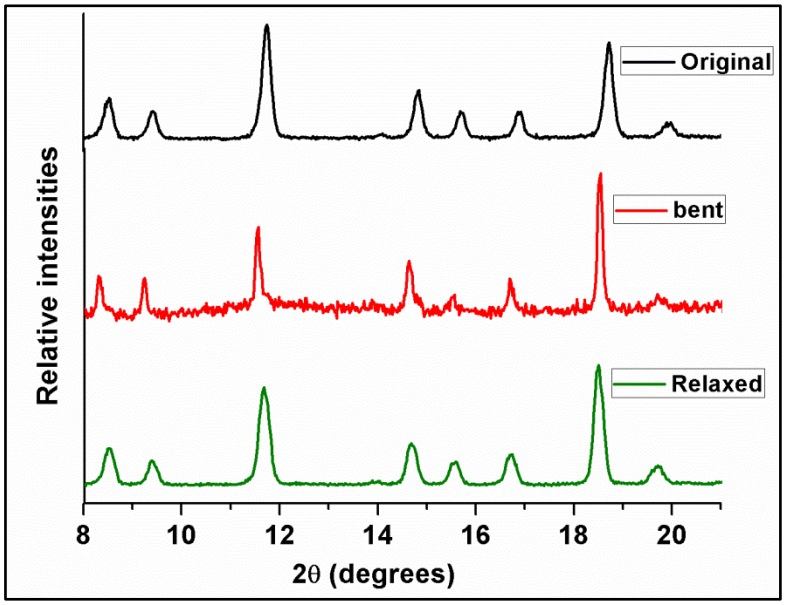

Figure 5.10. Powder X-ray diffraction spectra of **H_2L** straight, bent and relaxed crystals.

Further, the optimized structure of **H_2L** shown in **Figure 5.11a** (DFT B3LYP/6–31G, Gaussian09 Program) illuminating a highly planar conformation. The electron density of HOMO and LUMO of **H_2L** is distributed throughout the molecule **(Figure 5.11b)**. The low observed band gap of 0.43 eV is favorable for applications in microelectronic and photovoltaic devices *[60]*.

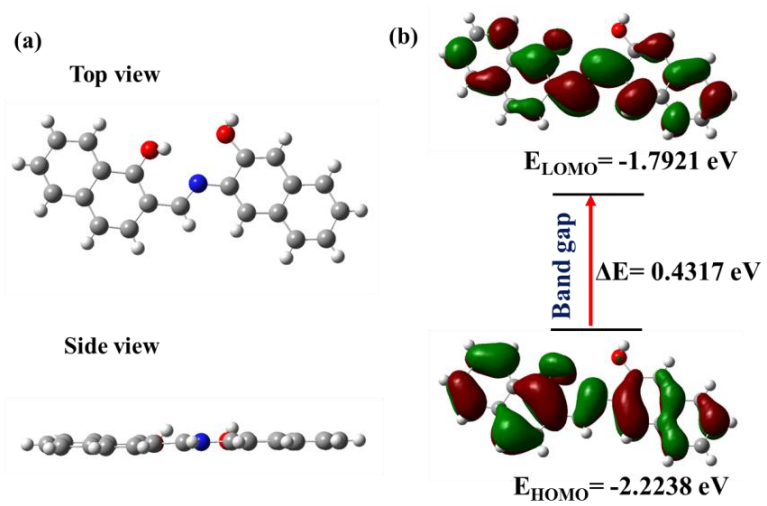

Figure 5.11. (a) Optimized structure of **H_2L** by DFT B3LYP/6–31G, Gaussian 09 Program. **(b)** Depicting electron cloud distributions of HOMO and LUMO and band gap between them.

5.2.3. photophysical properties of H_2L:

After exploring the excellent solid-state crystalline properties of **H_2L**, we further decided to examine its solution state properties. To examine its photo-physical properties, absorption, and emission spectra were recorded in DMSO/water (3:7 v/v). Absorption bands of **H_2L** at 219 nm, 280 nm and 325 nm are attributed to π–π* transitions, whereas bands at 461 nm and 490 nm correspond to n–π* transitions due to the presence of aromatic and phenolic as well as imine moieties respectively **(Figure 5.12)**. Further, upon excitation at 280 nm, a sharp and strong emission band was observed at 373 nm due to the presence of π*–π transition and another broad band at 502nm attributed to π*–n transition was observed in DMSO/water (3:7 v/v), respectively **(Figure 5.12)**. Additionally, **H_2L** fluorescence intensity was recorded at physiological pH range (pH 9.26–4.31) in phosphate buffer saline (PBS). The fluorescence signals are almost stable at various pHs **(Figure 5.13)**. The two-photon fluorescence intensity was con-firmed at 720 nm **(Figure 5.14 and 5.15)**.

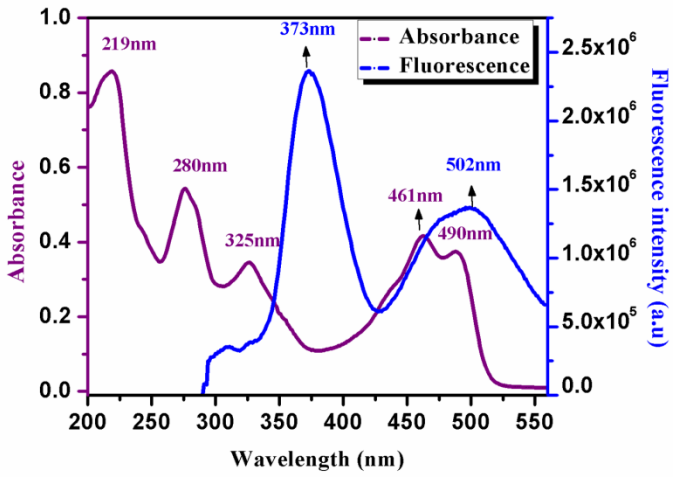

Figure 5.12. UV-vis and fluorescence spectrum of **H_2L** (10μM) in methanol.

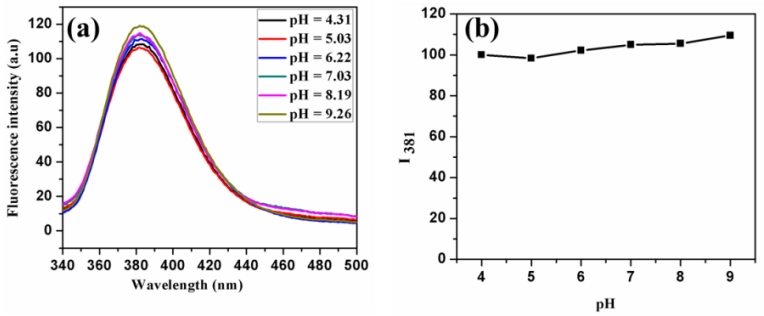

Figure 5.13. (a) pH sensitive emission spectra of **H_2L** (10 μM) in PBS buffer solution. **(b)** a plot of emission intensity of **H_2L** at 381 nm versus various pH values. Buffer solution: Phosphate saline solution.

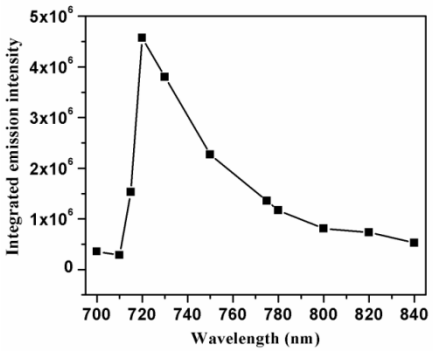

Figure 5.14. Two-photon integrated fluorescence emission intensity of **H_2L** at excitation wavelengths 700–840 nm in live HeLa cells. Maximum fluorescence intensity was obtained at λ_{ex} = 720 nm.

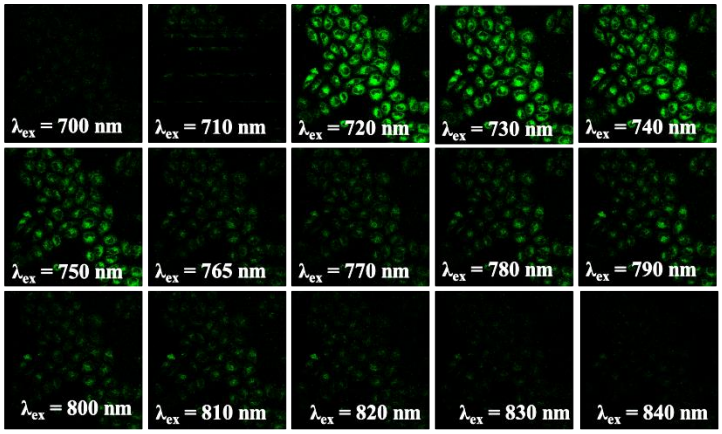

Figure 5.15. Two-photon microscopy (TPM) images of HeLa cells stained with **H_2L**. The excitation wavelength was 700 to 840 nm. Maximum fluorescence intensity was obtained at λ_{ex} = 720 nm.

5.2.4. Cell viability assay of H_2L:

The fluorescent nature and excellent photophysical properties of **H_2L** encouraged us to explore its application on live cells. The MTT assay *[61]* result reveals that the probe **H_2L** is biocompatible and not interferes with cell proliferation within the concentration range 5-45 µM for 12h **(Figure 5.16)**.

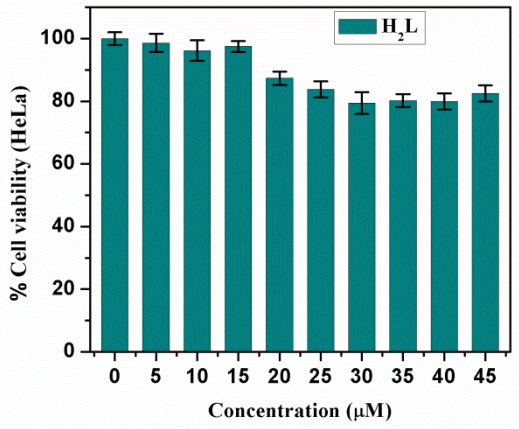

Figure 5.16. Cell viability assay of **H_2L** was determined by the MTT assay after 12 h incubation at 37°C and the results depicted of mean ± SD of three separate measurements.

5.2.5. Flow cytometry and bio-imaging of H_2L:

In this study, we used both flow cytometry and confocal microscopic techniques for live cell imaging. Flow cytometry technique was used to acquire high-quality fluorescence signals from huge populations of cells in suspension; while confocal microscopy provides good-quality visual detail of target morphology in a small population of adherent cells *[62-63]*. **H_2L** is excited by lasers at excitation wavelengths of 405 nm as well as 488 nm and give respective emission in blue and green region **(Figure 5.17)**. Almost all HeLa cells were able to uptake **H_2L** since approximately 100% of stained cells fluorescence intensity increased with respect to the control (unstained) sample **(Figure 5.17a)**. **H_2L** can uniformly label large population of live cells, which was detected by both flow cytometry as well as confocal microscopy techniques **(Figure 5.17)**.

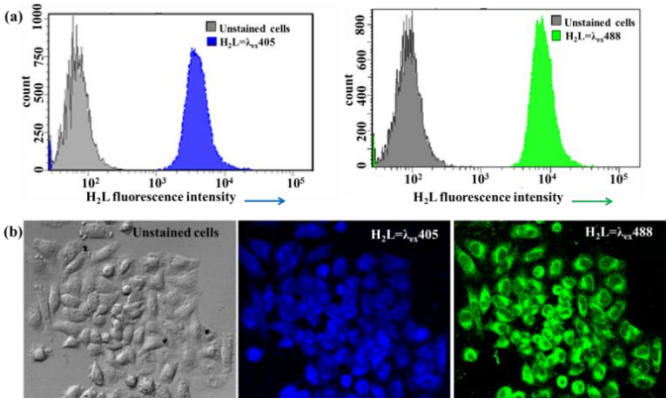

Figure 5.17. Flow cytometry and confocal live cells (HeLa) imaging of **H_2L** (40 μM, 1h). **(a)** Flow cytometric analysis, **(b)** confocal imaging: λ_{ex} = 405nm, λ_{ex} = 488nm.

5.2.6. The photostability of H_2L:

The photostability of fluorescent probe is a significant factor for long-term imaging of any physiological changes in live cells. Here photobleaching experiments of **H_2L** were performed by both one photon as well as two-photon microscopy. After 1850 scans, one-photon and two-photon fluorescence intensity remains 73% and 89% respectively **(Figure**

5.18) which is better than mitotraker green FM *[49]* and can be used for long term imaging.

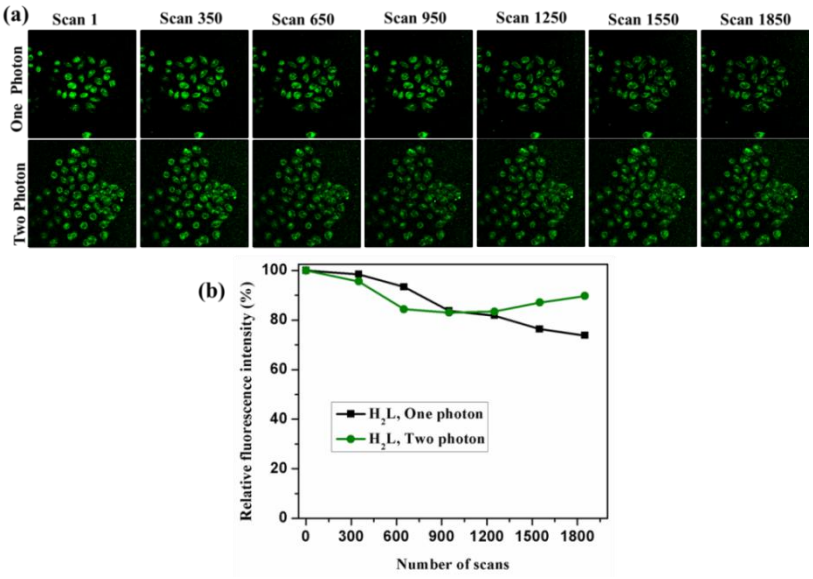

Figure 5.18. **(a)** In vitro photostability of **H_2L** in HeLa cell lines by both one and two photon microscopy. **(b)** Graph showing photobleaching result of **H_2L**. **H_2L** (40 μM): λ_{ex} = 488nm for one photon and λ_{ex} = 720 nm for two photon, λ_{em} = 500–560 nm.

5.2.7. Organelles' selectivity of H_2L:

In order to investigate intracellular selective localization of **H_2L**, co-localization studies were performed with **H_2L** and various standard organelles trackers such mitochondria trackers, ER, lysosome and, nucleus tracker (Hoechst 33342). The Pearson co-localization coefficient of **H_2L** with mitochondria trackers red was found to be 0.85; whereas with ER tracker red, lysotracker red and Hoechst 33342, Pearson co-localization coefficients were found to be 0.71 and 0.48, 0.10 respectively **(Figure 5.19)**. These results confirm that **H_2L** is predominantly localized in the mitochondria with a high Pearson coefficient.

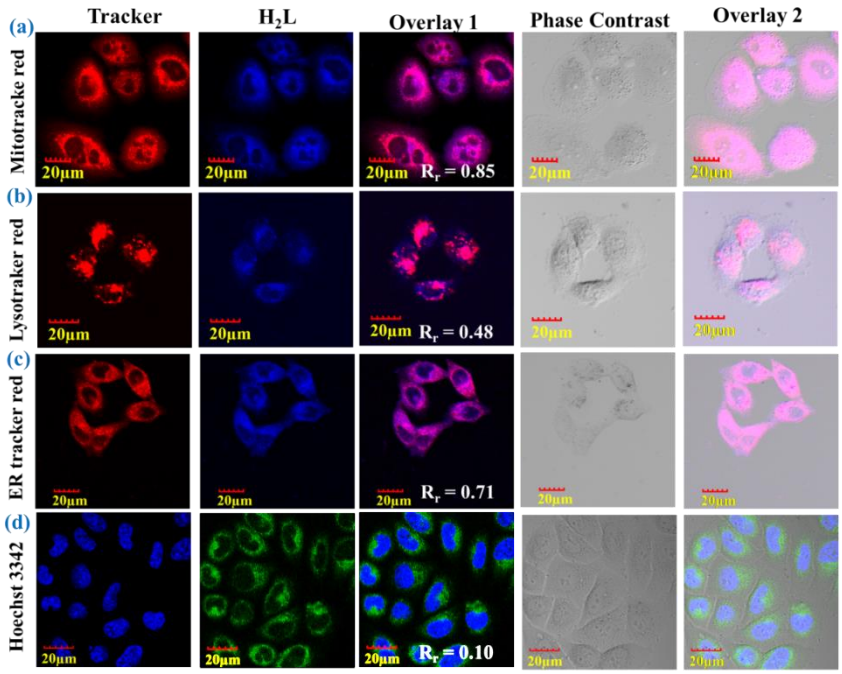

Figure 5.19. Co-localization experiment of probe **H_2L** (40 µM, 1h) with different organelles specific trackers in live Hela cells. **(a)** MitoTracker Red CMXRos (90 nM for 30 min) label mitochondria **(b)** LysoTracker Red DND-99 (90 nM, 30 min) label lysosomes **(c)** ER tracker Red (1µM, 30 min) label endoplasmic reticulum **(d)** Hoechst3342 (5µM, 30 min) for nucleus. The images from left to right depict organelle trackers (column 1), **H_2L** (column 2), Overlay 1: overlay of the 1st and 2nd columns. Phase contrast (column 4) and Overlay 2: overlay of 1st, 2nd and 4th columns. **H_2L** λ_{ex} = 405 nm; λ_{em} = 420–470 nm; **H_2L** λ_{ex} = 488nm, λ_{em} =500–560 n; ER, Lyso and Mitotraker Red λ_{ex} = 559 nm; λ_{em} = 570–700 nm.

5.2.8. Mitochondria selective staining ability of H_2L in various cell lines:

Moreover, the universal mitochondria selective staining prop-erty of **H_2L** was evaluated on numerous cell lines i.e., breast cancer (MCF-7), cervical cancer (HeLa), human lung carcinoma (A549) and prostate cancer (DU145) cells **(Figure 5.20)**. An excellent mitochondria labeling pattern was seen in all examined live cell lines with high Pearson co-localization coefficients 0.81, 0.87, 0.82 and 0.85 on MCF-7, HeLa, A549, and DU145 cell lines respectively.

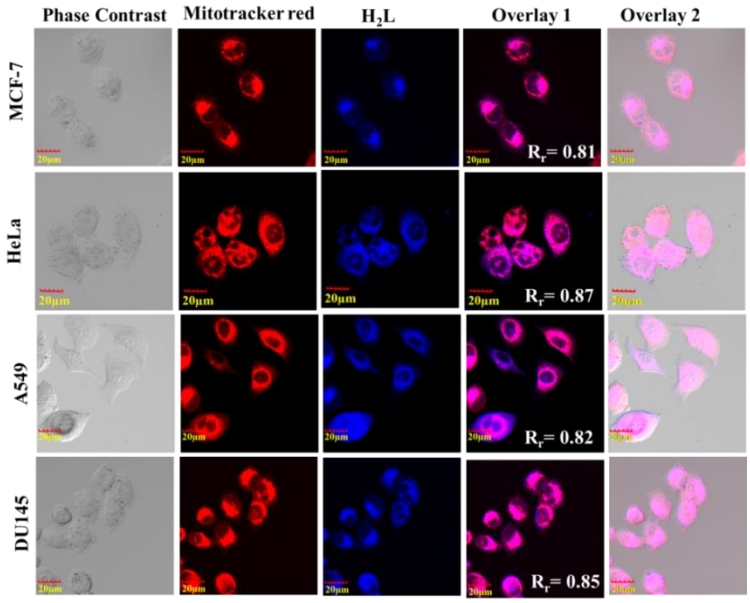

Figure 5.20. Mitochondria selective live cell imaging by using **H_2L** in MCF-7, HeLa, A549 and DU145 cells. All cell lines were co-stained with **H_2L** (40 μM, 1h) and Mitotracker Red (90 nM, 30 min). **H_2L**: λ_{ex} = 405 nm; λ_{em} = 420-470 nm; mitotracker Red λ_{ex} = 559 nm; λ_{em} = 580-700 nm. Overlay 1: overlay of the 2nd and 3rd columns. Overlay 2: overlay of the 1st, 2nd and 3rd columns. Scale bar: 20 μm.

5.2.9. 3D tumor spheroids imaging using H_2L:

After performing experiments on 2D cell culture models, 3D spheroid was employed for imaging since it mimics various in vivo features of solid tumors such as their gene expression patterns, physiological responses, spatial architecture, drug resistance mechanism, *etc.* Spheroids are considered as a valid intermediate between in vitro monolayer cells and in vivo tissue *[64]*. With in-creasing depth, confocal microscopic imaging of live tumor spheroids still has various technical challenges. Two-photon micro-scopes have high penetration power (~500 μm) as compare to the one-photon microscope. Therefore, a spheroid was used to study the penetration depth of **H_2L**. Hela cells spheroid was stained with **H_2L** and images were taken after 2 μm section cutting along Z-axis. Two-photon excitation exhibited much stronger fluorescence in deeper layer upto 56 μm **(Figure 5.21)**, compared to the depth of 26 μm achieved with one-photon microscopy **(Figure 5.22)**. This result

establishes the high penetration power of the two-photon excitation process. Based on this encouraging result, we believe that **H_2L** can be further exploited for potential applications in *in-vivo* tissue imaging.

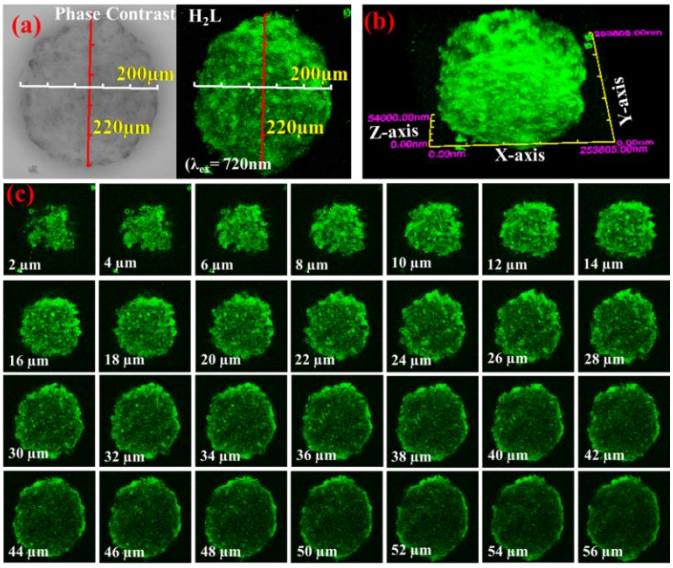

Figure 5.21. (a) Two-photon fluorescence images of 3D intact tumor spheroid stained with **H2L** (40 µM, for 2 h). (b) The Z-stack 3D images of the intact spheroid. (c) The two-photon Z stack images were taken after every 2 µm section cutting from the top to bottom spheroid. The images were taken under a 20× objective. λ_{ex} = 720 nm; λ_{em} = 500–560 nm.

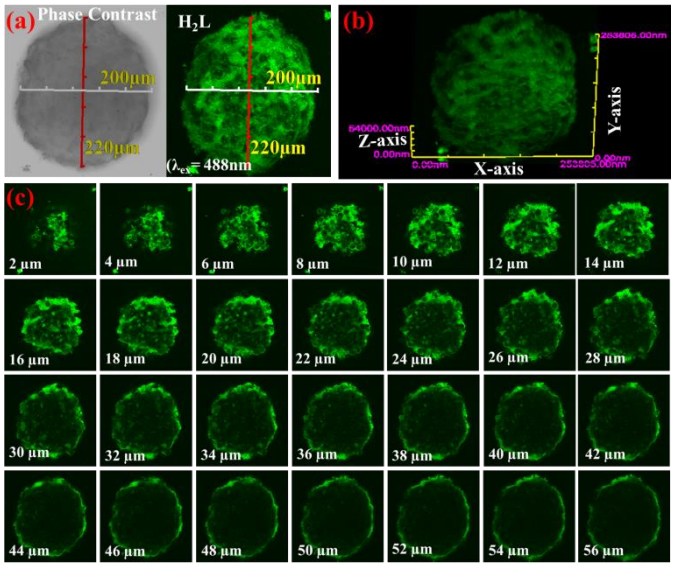

Figure 5.22. (a) One-photon fluorescence images of 3D intact tumor spheroid after **H_2L** (40 µM, for 2 h) treatment. **(b)** The Z-stack 3D images of the intact spheroid. **(c)** The two-photon Z stack images were taken after every 2 µm section from the top to bottom spheroid.

Generally, proton pumping during oxidative phosphorylation and the use of ions channel pumps results in strong negative membrane potential (108−158 mV) across the lipid bilayer *[65]*. Consequently, the electrostatic-driven force of the mitochondrial membrane may be used to direct cationic lipophilic probes by using the negative membrane potential gradient of the mitochondria *[66]*. Even though lipophilic cationic dyes can stain mitochondria; an important disadvantage should be noted in that these trackers are membrane potential-dependent. Additionally, they alter the membrane potential, which may be a major problem depending on the requirements of the experiment *[66-67]*. Therefore recently there is more focus on developing neutral probes for mitochondrial imaging *[66-67]*. The probable mechanistic pathway of **H_2L** is based on a few factors such as lipophilicity and its neutral behavior. Owing to the presence of two hydroxyls and an amine group in the **H_2L** framework, intermolecular hydrogen bonding is formed which serves to increase its lipophilicity, by creating unavailability of the hydroxyl group to form extra hydrogen bond with the solvents.

5.3. Conclusions

In summary, a new elastic flexible crystal (**H_2L**) was synthesized in a facile manner with high yield. The powder XRD and Raman studies indicate a high retention of crystallinity and chemical bonds even under stress (bend) conditions which infer that the bending in **H_2L** is due to the intermolecular hydrogen bonding interactions viz. O(1)–H(1)···O(2) between the donor, O(1)···H(1) and acceptor group O(2). These interactions lead to the formation of 1-D polymeric chains which further extended through intermolecular C–H···π interactions forming a 2-D network to govern the flexibility of the crystal. **H_2L** is two-photon fluorescent organic probe, non-cytotoxic, photostable and selective to mitochondria of live cells. Two-photon excitation ability of **H_2L** was further utilized for imaging of deeper layer of tissue spheroids. Thus, due to its elastic nature, it can be used in mechanical actuators or in flexible electronics in solid state and in solution state it can monitor mitochondria in mitochondria-associated pathological disorders.

5.4. Experimental Section

5.4.1. Materials:

1-hydroxy-2-naphthaldehyde and 3-Amino-2-naphthol purchased from TCI Chemicals (India) Pvt. Ltd., MitoTracker Red CMXRos, ER tracker red (BODIPY TR Glibenclamide), LysoTracker Red DND-99 and were purchased from Invitrogen. Hoechst 3342, 3-(4,5-Dimethylthiazol-2-Yl)-2,5-Diphenyltetrazolium Bromide (MTT) purchased from Sigma-Aldrich Chemical Co., USA. Dulbecco's modified eagle medium (DMEM) and Fetal bovine serum (FBS) were purchased from Gibco. Breast cancer (MCF-7) cell lines, prostate cancer (DU145), human lung carcinoma (A459), cervical cancer (HeLa) cell lines were obtained from National Centre for Cell Science, Pune. All other chemical reagents and solvents were obtained from Merck and S.D Fine Chem. Ltd. and all chemicals used without further purifications. The solvents were dried and distilled following the standard literature procedures prior to their use.

5.4.2. Physical measurements:

Ultrapure (Milli Q) water from arium® pro ultrapure water systems (Sartorius) was used thoughout the experiments. Binocular Microscope of Leica Company (model EC3) used to capture bending images of crystal. ^{1}H NMR (400 MHz) and ^{13}C NMR (100 MHz) spectra were recorded by Bruker Avance (III) instrument by using DMSO-d_6. The mass spectrum was measured by Brucker-Daltonics, micrOTOF-QII mass spectrometer. FTIR spectrum was recorded on KBr pellets by using Bio-Rad FTS 3000MX instrument. Powder X-ray diffraction (PXRD) data was recorded on a Rigaku Smart Lab X-ray diffractometer using monochromated Cu-Kα radiation (1.5406 Å). Raman measurement was performed with a 785 nm laser source using a LabRAM HR (UV system). pH measurements were performed using pH-meter (LABMAN Scientific Instrument PVT. LTD). Spectrophotometric measurements were performed by UV-vis spectrophotometer (Varian Cary 100) using a quartz

cuvette having a path length of 1 cm. All the fluorescence measurement was performed using FluoroMax-4 Spectrophotometer (HORIBA Scientific) measurement. The excitation and emission slits were 5/5 nm for the emission measurements. The molecular structures were optimized by using DFT with the B3LYP functional and the 6-31G basis set using Gaussian 09 program. pH-meter (LABMAN Scientific Instrument PVT. LTD) was used for pH measurements. The absorbance for MTT analysis was measured by a microplate reader (Synergy H1 BioTek microplate reader) at 570 nm. Fluorescence imaging experiments were performed by BD LSRFortessa TM Flow cytometry analysis, Olympus laser-scanning microscope, Mai Tai eHP Spectra physics femtosecond (fs) laser having power peak >450 KW, pulse width ≤ 70 fs, tuning range 690-1040 nm, average power >2.5 W, repetition rate 80 MHz ± 1 MHz was used to acquire the two-photon fluorescence imaging. For bioimaging purpose, H2L stock solution was prepared in 0.1M NaOH solution in water/DMSO (7:3v/v). Image processing was done with the help of Olympus software (FV10-ASW 4.2) and ImageJ software. Flow cytometry data were analyzed by DB FACSDiva software.

5.4.3. X-ray Crystallography:

The crystal data of **H_2L** was collected at 293 K using graphite-monochromated Mo Kα (λα = 1.54184 Å). The strategy for the data collection was evaluated with the help of CrysAlisPro CCD software. The data were collected by the standard phi-omega scan techniques and were scaled and reduced using CrysAlisPro RED software. The structures were solved by the direct methods by using SHELXS-2014 and refined by full matrix least squares with SHELXL-2014, refining on F_2. By direct methods the positions of all the atoms were obtained and all non-hydrogen atoms were refined anisotropically. All the remaining hydrogen atoms were placed in geometrically constrained positions and refined with isotropic temperature factors, generally 1.2 × Ueq of their parent atoms. The Hydrogen bonding interactions, mean plane analysis, and molecular

drawings were obtained using the program Mercury (ver 3.1) and Diamond (ver 3.1d). The crystal and refinement data are summarized in **Table A7** and the selected bond distances and bond angles are shown in **Table A8**. All the Hydrogen atoms have been omitted for clarity in the molecular structure of **H_2L**. Despite several attempts we could not get better quality crystals of **H_2L**, this always given thin wire like crystals which makes it diffraction quality very weak.

5.4.4. Synthesis of probe (E)-2-(((3-hydroxynaphthalen-2-yl)imino) methyl)naphthalen-1-ol (H_2L):

Condensation reaction was performed from 1-hydroxy-2-naphthaldehyde (172.18 mg, 1 mmol) and 3-Amino-2-naphthol (159.19 mg, 1 mmol) in 15 mL of ethanol at 25°C with continuously stirring for 5h in single neck 100 ml RBF. The reaction was monitored by TLC. After completion of the reaction, the solid orange precipitate was formed, which was filtered and washed with chilled ethanol and then chilled water only, for several times and dried in a desiccator. Yield 88%, ^{1}H NMR (400 MHz,DMSO-d_6): δ 14.48 (d, 1H), 10.89 (s, 1H), 9.01 (d, 1H, -CH=N), 8.33 (d, 1H, ph), 8.20 (s, 1H, ph), 7.79 (d,1H, ph), 7.71(d, 1H, ph), 7.63 (m, 2H, ph), 7.32 (m, 4H, ph), 7.27-7.21 (d, 1H, ph), 6.83-6.81 (d, 1H, ph) **(Figure 5.23)**. ^{13}C NMR (100 MHz, DMSO-d6): δ179.75, 151.95, 147.00, 137.85, 132.16, 131.36, 130.34, 129.39, 129.25, 128.16, 127.57, 127.29, 126.14, 125.85, 125.63, 125.42, 124.13, 115.08, 113.36, 110.50, 109.86 **(Figure 5.24)**. FTIR (KBr, cm-1): 3446(br), 3057(br), 1638(vs), 1603(s), 1543(vs), 1480(w), 1453(s), 1402(s), 1348(w), 1335(w), 1297(s), 1266(w), 1240(w), 1199(s), 1138(vs), 1066(s), 1036(w), 987(s), 853(w), 808(w), 794(s),745(s), 689(w), 620(w) **(Figure 5.25)**. LCMS (m/z): $[M+H+K]^+$ 353.3 **(Figure 5.26)**.

5.4.5. Calculation of crystal elongation, translational motion and critical radius for the crystal undergoing bending

5.4.5.1. Change in length per molecule (elongation/contraction on bending)

To analyse the change in length Δl upon bending, we used a simple calculation (assuming elastic bending). In this model, the crystal is bent into a full loop as shown in **Figure 5.4**, with the perimeter along the neutral axis being represented by l_o.

The length l_o is related to the radius r_o by the following relation:

$$r_0 = \frac{l_0}{2\pi} \qquad \textbf{(Equation 1)}$$

Where l_0 is the measured length of the crystal as determined by physical measurement and viewing in microscope, and found to be 250 um.

The radius value for outer and inner arcs as shown in **figure 5.4** is given by:

$$r_{out} = r_0 + \frac{t}{2} \qquad \textbf{(Equation 2)}$$

$$r_{in} = r_0 - \frac{t}{2} \qquad \textbf{(Equation 3)}$$

where 't' is the thickness of the crystal (found to be 22 μm). From equations 1, 2 and 3, the values of r_{out} and r_{in} are calculated to be 50.81 μm and 28.81 μm respectively for the untouched crystal. These values are found to be unchanged after bending.

The change in length (or perimeter), i.e. crystal elongation upon bending, is given by the following set of equations:

$$\Delta l_{out} = 2\pi(r_{out} - r_o)$$
$$\Delta l_{in} = 2\pi(r_o - r_{in})$$
$$\Delta l_{in} = \Delta l_{out} = \pi t \qquad \textbf{(Equation 4, 5, 6)}$$

For a crystal with a thickness of 22 μm, the elongation is calculated to be 69.08 μm.

5.4.5.2. Translational movement per molecule for 0.25 mm long crystal: This is given by the below equation:

$$\frac{\Delta l}{n} = 0.314 \times \frac{6.2484}{10^7 \times 4 \times 0.25} = 0.6248 \frac{\text{Å}}{molecule} \qquad \textbf{(Equation 7)}$$

If the crystal length is halved, the translation movement will double. Thus, 0.3124 Å/molecule is the yield point for this crystal, i.e. translational movement beyond this value will induce breaking in the crystal if a full circle is attempted to be made by bending. The critical radius for this condition is given by the following equation:

$$r_c = \frac{0.125}{2\pi} = 0.0199\ mm = 19.9\ \mu m \qquad \textbf{(Equation 8)}$$

5.4.5.3. Change in angle per molecule upon bending:

For an orthorhombic crystal, the formula unit is 4 and lattice parameter (a) is 6.2484 Å, therefore 1 mm of crystal contains 10^7 x (4/6.2484) molecules. Therefore, for a crystal of length 0.25 mm, the value works out to be 1,600,409.705 molecules

For a crystal of length 0.25 mm, the change in angle per molecule upon bending is given by 360/(number of molecules). Substituting appropriate

values, the change in angle is found to be 0.00022494°/molecule. This quantity also doubles as the crystal sizes halves, meaning that the breaking strain is 0.0004498847°/molecule.

5.4.6. Two-photon intensity measurement:

Mai Tai eHP Spectra physics femtosecond laser having power peak >450 KW, tuning range 690–1040 nm, average power >2.5 W, pulse width ≤ 70 fs, repetition rate 80 MHz ± 1 MHz was used to capture the two-photon fluorescence imaging. The two-photon fluorescence intensity was measured at 700–840 nm. Cervical cancer (HeLa) cells were seeded in confocal dishes and incubated for 24 hours for cell adhesion. Live HeLa cells were labeled with **H_2L** (40 µM) in DMEM medium for 1 hour then washed twice with PBS (pH=7.4). Images were captured at a different wavelength excitation. Maximum integrated fluorescence intensity was observed at wavelength 720 nm.

5.4.7. MTT cell viability assay:

Cell viability assay of **H_2L** was performed on Hela cells, 7000 HeLa cells $well^{-1}$ were seeded in 96-well plate in 200 µL media (Dulbecco's Modified Eagle Medium, 10% (v/v) FBS and 1% Penicillin-Streptomycin antibiotics 10,000 U/mL) and incubated for one day for cell adhesion. Next day media was removed and fresh media 100 µL added in each well. All biological experiments were performed by using H2L crystals to maintain high purity. A stock solution of **H_2L** was prepared in 0.05% DMSO and 0.1M NaOH in water. 20 µL added to each well in order to give final concentration ranging from 10-45 µM. 20 µL water having 0.05% DMSO and 0.1M NaOH was used as a control. The experiment was done in triplicate. Cells exposed to the drug for 12 hours followed by washing with PBS (pH 7.4). Then 100 µL MTT (1 mg/mL in phenol red free media) was added in each well. Cells incubated at 37 ℃ and 5% CO2 atmosphere for next 4 hours. After that media was carefully removed and 100 µL DMSO was added in order to dissolve purple

formazan crystals. After 15 minutes incubation, absorbance at 570 nm was measured using Synergy H1 Biotek microplate reader. The % cell viability was calculated as: % cell viability = [Mean O.D. of the drug-treated cell/Mean O.D. of the control well] × 100

5.4.8. Flow cytometry study:

HeLa cells were seeded in six-well tissue culture plates. When cells became 90% confluent, then one well treated with 40 μM probe **H_2L** for 1 hour and control well left without any treatments (as control sample). After that, the cells were washed with PBS three to four times to remove excess probe in the media. Cells were harvested by 0.25% trypsin/EDTA, centrifuged and re-suspended pellet in PBS (pH=7.4). The samples were analyzed by BD LSRFortessa TM Flow cytometry with excitation at 405 nm and 488, emission 420–470 nm and 500–560 nm respectively. Data were analyzed by DB FACSDiva software. Total of ten thousand events were acquired for each sample.

5.4.9. Mitochondria selective staining and co-localization studies in various cell lines:

Breast cancer (MCF-7), cervical cancer (HeLa), human lung carcinoma (A549) and prostate cancer (DU145) cell lines were seeded in confocal dishes and incubated for 24 hours so that cells attached with the bottom of the surface of dishes. For mitochondria imaging, live cells were stained with **H_2L** (40 μM) in DMEM medium for 1 hour then washed twice with PBS (pH = 7.4) and co-stain with MitoTracker Red (90 nM, 15 min), LysoTracker Red DND 99 (80nM, 30 min), ER tracker Red (1μM, 30 min) and Hoechst 33342 (1μg/mL, 30 min) for mitochondria, lysosomes, ER and nucleus staining respectively in separate dishes. Cells were further incubated at 37℃ in 5% CO2 atmosphere for 30 min, Followed by washing twice with PBS. An Olympus laser scanning microscope was used for confocal imaging. Cells were visualized at an excitation of λ_{ex} = 405 nm as well λ_{ex} = 488nm for **H_2L** in case of one

photon excitation and λ_{ex} = 720nm for two-photon excitation, Mitotracker red, Lysotracker red and ER-tracker red excitation wavelength (λ_{ex}) = 559 whereas Hoechst 33342 excitation (λ_{ex}) = 405 nm.

5.4.10. In vitro photostability study:

HeLa cells were grown in T-25 flask. When cells get 60% confluent, trypsinized and reseeded in confocal dishes. When cells attached to the dishes treated with **H_2L** (40µM, 1 hr) and incubated at 37 °C and 5% CO2 atmosphere. After 1 hr incubation, cells washed twice with PBS to remove the unbounded probe. The one-photon photobleaching video was recorded using the confocal laser scanning microscope (CLSM) with no delay scan mode. Whereas two-photon photobleaching video was recorded using Mai Tai eHP Spectra physics femtosecond laser with no delay scan mode. In both case, video and images were recorded upto 1850 scans. **H_2L** excited by 488 nm for one-photon imaging and 720 nm for two-photon imaging. The integrated fluorescence intensity of first scans is considered as 100% for measuring the relative decrease in fluorescence intensity. Images at every 350 scans obtained from videos. The relative percent intensity calculated as F/F_0*100.

5.4.11. Generation of multicellular 3D tumor spheroids:

Tumor spheroids were prepared by using the liquid overlay method. To make a non-adherent bottom surface of 96 well plates (Flat-bottom), they were coated with 60µL of a sterile 1.5% (wt/vol) warm agarose solution in complete DMEM media. Then the HeLa cells (~80% confluent in T-25 flack) were harvested by 0.25% trypsin/EDTA solution and re-suspended in complete DMEM media. Approximately 4000 cells were seeded in each agarose coated well in 200µl complete DMEM media. The plates were incubated at 37°C and 5% CO_2 until spherical spheroids formed. Once spheroid formed in 96 well plates, then the spheroids were gently transfers in a confocal disc with the help of 1ml

pipette. Spheroids were treatment with 40 μM **H_2L** and incubated for 2h, then washed three to four times carefully with PBS (pH=7.4). The images were captured from 2μm section cutting from top to bottom along Z-axis. The video and images were recorded by two-photon microscopy as well as one photon confocal laser scanning microscopy.

NMR, FTIR, Mass and Powder XRD spectra of compounds H_2L

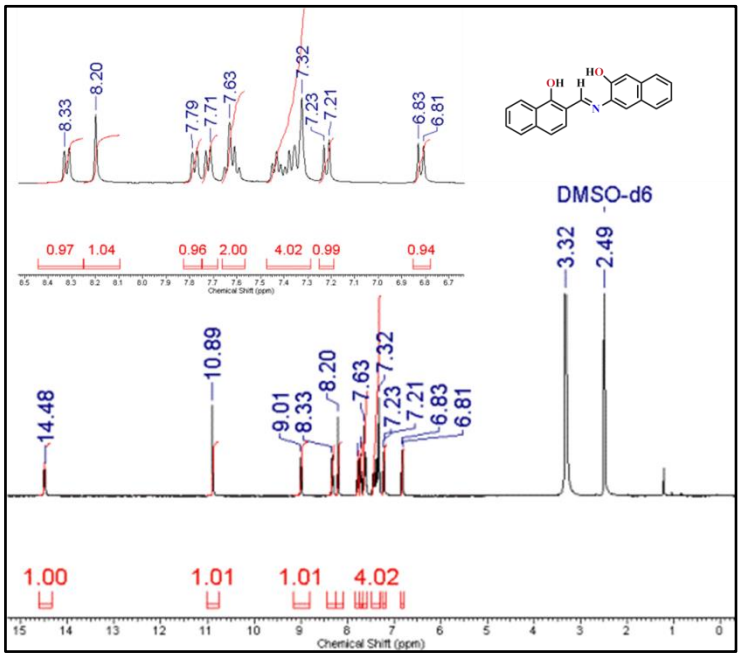

Figure 5.23. ^{1}H MNR spectrum of **H_2L.**

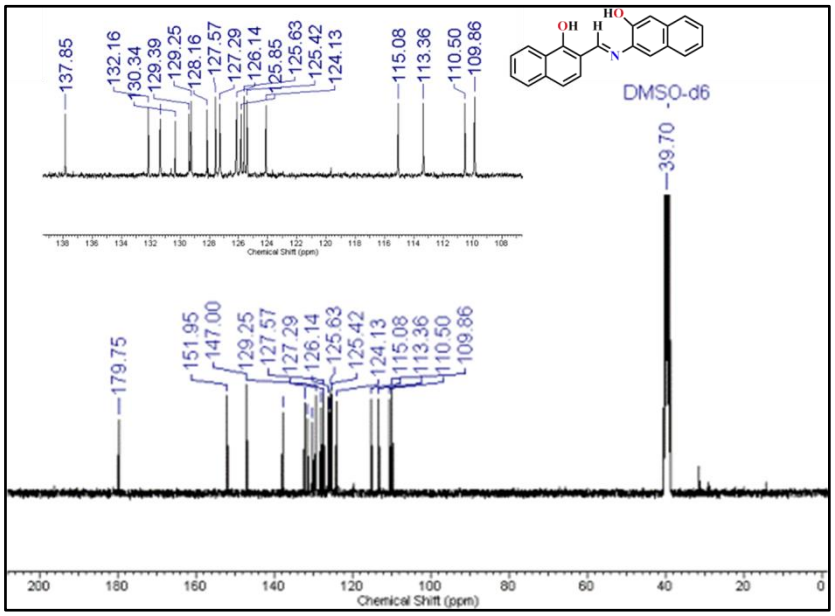

Figure 5.24. ^{13}C NMR spectrum of **H_2L**.

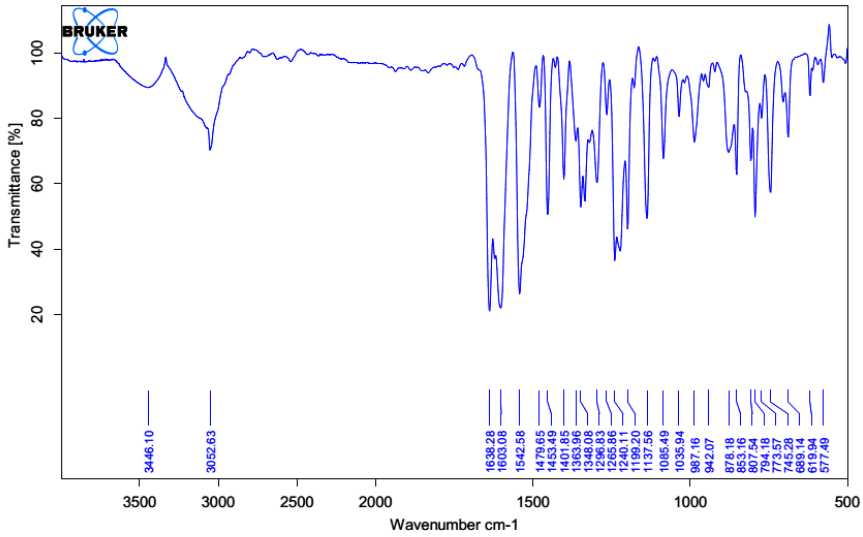

Figure 5.25. FTIR spectrum of **H_2L.**

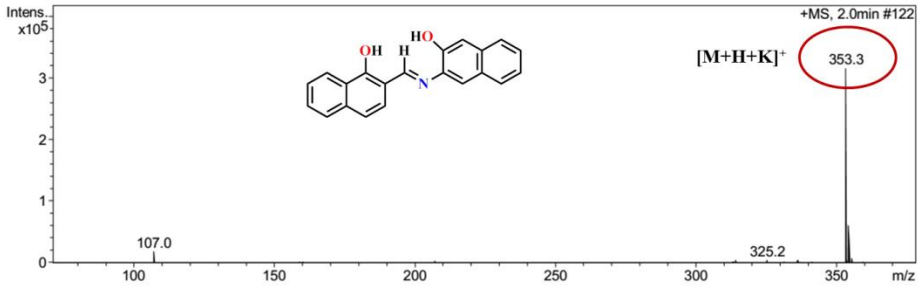

Figure 5.26. ESI-MS mass spectra of **H_2L**.

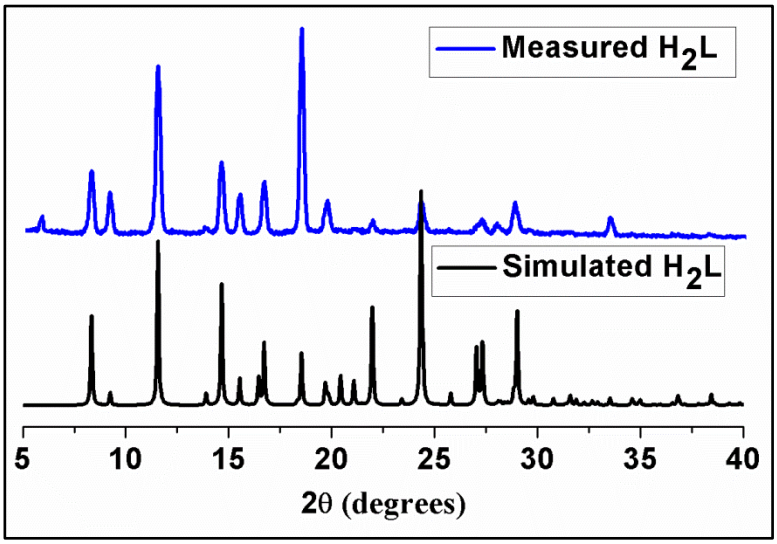

Figure 5.27. Powder X-ray diffraction spectra of **H_2L.**

5.5. References

[1]. Wei, Q., Achazi, K., Liebe, H., Schulz, A., Noeske, P. L., Grunwald, I., Haag, R. (2014), Mussel-inspired dendritic polymers as universal multifunctional coatings, Angew. Chem. Int. Ed., 53, 11650-11655 (DOI: 10.1002/anie.201407113).

[2]. Saini, A. K., Natarajan, K., Mobin, S. M. (2017), A new multitalented azine ligand: elastic bending, single-crystal-to-single-crystal transformation and a fluorescence turn-on Al(iii) sensor, Chem. Commun., 53, 9870-9873 (DOI: 10.1039/c7cc04392a).

[3]. Ji, D., Li, T., Liu, J., Amirjalayer, S., Zhong, M., Zhang, Z. Y., Huang, X., Wei, Z., Dong, H., Hu, W., Fuchs, H. (2019), Band-like transport in small-molecule thin films toward high mobility and ultrahigh detectivity phototransistor arrays, Nat. Commun., 10, 12 (DOI: 10.1038/s41467-018-07943-y).

[4]. Xie, H., Yin, X., Guo, Y., Liu, J., Que, W., Wang, G. (2019), Recent Progress of Flexible Perovskite Solar Cells, Phys. Status Solidi RRL, 13, 1800566 (DOI: 10.1002/pssr.201800566).

[5]. Choi, J., Park, C. H., Kwack, J. H., Lee, D. J., Kim, J. G., Choi, J., Bae, B. H., Park, S. J., Kim, E., Park, Y. W., Ju, B. K. (2019), Ag fiber/IZO Composite Electrodes: Improved Chemical and Thermal Stability and Uniform Light Emission in Flexible Organic Light-Emitting Diodes, Sci. Rep., 9, 738 (DOI: 10.1038/s41598-018-37105-5).

[6]. Qu, Y., Nguyen-Dang, T., Page, A. G., Yan, W., Das Gupta, T., Rotaru, G. M., Rossi, R. M., Favrod, V. D., Bartolomei, N., Sorin, F. (2018), Superelastic Multimaterial Electronic and Photonic Fibers and Devices via Thermal Drawing, Adv. Biomater., 30, 1707251 (DOI: 10.1002/adma.201707251).

[7]. Park, S., Loke, G., Fink, Y., Anikeeva, P. (2019), Flexible fiber-based optoelectronics for neural interfaces, Chem. Soc. Rev., 48, 1826-1852 (DOI: 10.1039/C8CS00710A).

[8]. Feron, K., Lim, R., Sherwood, C., Keynes, A., Brichta, A., Dastoor, P. C. (2018), Organic Bioelectronics: Materials and Biocompatibility, Int. J. Mol. Sci., 19, 2382 (DOI: 10.3390/ijms19082382).

[9]. Liu, H., Lu, Z., Zhang, Z., Wang, Y., Zhang, H. (2018), Highly Elastic Organic Crystals for Flexible Optical Waveguides, Angew. Chem., Int. Ed., 57, 8448-8452 (DOI: 10.1002/anie.201802020).

[10]. Liu, H., Bian, Z., Cheng, Q., Lan, L., Wang, Y., Zhang, H. (2019), Controllably realizing elastic/plastic bending based on a room-temperature phosphorescent waveguiding organic crystal, Chem. Sci., 10, 227-232 (DOI: 10.1039/c8sc03135e).

[11]. Huang, R., Wang, C., Wang, Y., Zhang, H. (2018), Elastic Self-Doping Organic Single Crystals Exhibiting Flexible Optical Waveguide and Amplified Spontaneous Emission, Adv. Biomater., 30, 1800814 (DOI: 10.1002/adma.201800814).

[12]. Lv, S., Dudek, D. M., Cao, Y., Balamurali, M. M., Gosline, J., Li, H. (2010), Designed biomaterials to mimic the mechanical properties of muscles, Nature, 465, 69-73 (DOI: 10.1038/nature09024).

[13]. Naumov, P., Chizhik, S., Panda, M. K., Nath, N. K., Boldyreva, E. (2015), Mechanically Responsive Molecular Crystals, Chem. Rev., 115, 12440-12490 (DOI: 10.1021/acs.chemrev.5b00398).

[14]. Bag, P. P., Chen, M., Sun, C. C., Reddy, C. M. (2012), Direct correlation among crystal structure, mechanical behaviour and tabletability in a trimorphic molecular compound, CrystEngComm, 14, 3865-3867 (DOI: 10.1039/C2CE25100K).

[15]. Saha, S., Desiraju, G. R. (2016), Using structural modularity in cocrystals to engineer properties: elasticity, Chem. Commun., 52, 7676-7679 (DOI: 10.1039/C6CC03226E).

[16]. Saha, S., Mishra, M. K., Reddy, C. M., Desiraju, G. R. (2018), From Molecules to Interactions to Crystal Engineering: Mechanical Properties of Organic Solids, Acc. Chem. Res., 51, 2957-2967 (DOI: 10.1021/acs.accounts.8b00425).

[17]. Varughese, S., Kiran, M. S., Ramamurty, U., Desiraju, G. R. (2013), Nanoindentation in crystal engineering: quantifying mechanical properties of molecular crystals, Angew. Chem. Int. Ed., 52, 2701-2712 (DOI: 10.1002/anie.201205002).

[18]. Chandrasekhar, N., Chandrasekar, R. (2012), Reversibly Shape-Shifting Organic Optical Waveguides: Formation of Organic Nanorings, Nanotubes, and Nanosheets, Angew. Chem., Int. Ed., 51, 3556-3561 (DOI: 10.1002/anie.201106652).

[19]. Hayashi, S., Koizumi, T. (2016), Elastic Organic Crystals of a Fluorescent π-Conjugated Molecule, Angew. Chem., Int. Ed., 55, 2701-2704 (DOI: 10.1002/anie.201509319).

[20]. Nath, N. K., Pejov, L., Nichols, S. M., Hu, C., Saleh, N. i., Kahr, B., Naumov, P. (2014), Model for Photoinduced Bending of Slender Molecular Crystals, J. Am. Chem. Soc., 136, 2757-2766 (DOI: 10.1021/ja4101497).

[21]. Kitagawa, D., Tanaka, R., Kobatake, S. (2015), Dependence of photoinduced bending behavior of diarylethene crystals on irradiation wavelength of ultraviolet light, Phys. Chem. Chem. Phys., 17, 27300-27305 (DOI: 10.1039/C5CP03073K).

[22]. Liu, B., Di, Q., Liu, W., Wang, C., Wang, Y., Zhang, H. (2019), Red-Emissive Organic Crystals of a Single-Benzene Molecule: Elastically Bendable and Flexible Optical Waveguide, J. Phys. Chem. Lett, 10, 1437-1442 (DOI: 10.1021/acs.jpclett.9b00196).

[23]. Alimi, L. O., Lama, P., Smith, V. J., Barbour, L. J. (2018), Hand-twistable plastically deformable crystals of a rigid small organic molecule, Chem. Commun., 54, 2994-2997 (DOI: 10.1039/C8CC00775F).

[24]. Ahmed, E., Karothu, D. P., Naumov, P. (2018), Crystal Adaptronics: Mechanically Reconfigurable Elastic and Superelastic Molecular Crystals, Angew. Chem., Int. Ed., 57, 8837-8846 (DOI: 10.1002/anie.201800137).

[25]. Sidelnikov, A. A., Chizhik, S. A., Zakharov, B. A., Chupakhin, A. P., Boldyreva, E. V. (2016), The effect of thermal expansion on

photoisomerisation in the crystals of $[Co(NH_3)_5NO_2]Cl(NO_3)$: different strain origins – different outcomes, CrystEngComm, 18, 7276-7283 (DOI: 10.1039/C6CE00840B).

[26]. Kim, T., Zhu, L., Mueller, L. J., Bardeen, C. J. (2014), Mechanism of photoinduced bending and twisting in crystalline microneedles and microribbons composed of 9-methylanthracene, J. Am. Chem. Soc., 136, 6617-6625 (DOI: 10.1021/ja412216z).

[27]. Krishna, G. R., Devarapalli, R., Lal, G., Reddy, C. M. (2016), Mechanically Flexible Organic Crystals Achieved by Introducing Weak Interactions in Structure: Supramolecular Shape Synthons, J. Am. Chem. Soc., 138, 13561-13567 (DOI: 10.1021/jacs.6b05118).

[28]. Ghosh, S., Reddy, C. M. (2012), Elastic and bendable caffeine cocrystals: implications for the design of flexible organic materials, Angew. Chem. Int. Ed., 51, 10319-10323 (DOI: 10.1002/anie.201204604).

[29]. Commins, P., Karothu, D. P., Naumov, P. (2019), Is a Bent Crystal Still a Single Crystal?, Angew. Chem., Int. Ed., 58, 2-11 (DOI: 10.1002/anie.201814387).

[30]. Ahmed, E., Karothu, D. P., Naumov, P. (2018), Kristall-Adaptronik: Mechanisch rekonfigurierbare elastische und superelastische molekulare Kristalle, Angew. Chem. Int. Ed., 130, 8974-8984 (DOI: 10.1002/ange.201800137).

[31]. Wang, K., Mishra, M. K., Sun, C. C. (2019), Exceptionally Elastic Single-Component Pharmaceutical Crystals, Chem. Mater., 31, 1794-1799 (DOI: 10.1021/acs.chemmater.9b00040).

[32]. Hayashi, S., Yamamoto, S.-y., Takeuchi, D., Ie, Y., Takagi, K. (2018), Creating Elastic Organic Crystals of π-Conjugated Molecules with Bending Mechanofluorochromism and Flexible Optical Waveguide, Angew. Chem. Int. Ed., 57, 17002-17008 (DOI: 10.1002/anie.201810422).

[33]. Ghosh, S., Mishra, M. K., Kadambi, S. B., Ramamurty, U., Desiraju, G. R. (2015), Designing elastic organic crystals: highly flexible polyhalogenated

N-benzylideneanilines, Angew. Chem. Int. Ed., 54, 2674-2678 (DOI: 10.1002/anie.201410730).

[34]. Owczarek, M., Hujsak, K. A., Ferris, D. P., Prokofjevs, A., Majerz, I., Szklarz, P., Zhang, H., Sarjeant, A. A., Stern, C. L., Jakubas, R., Hong, S., Dravid, V. P., Stoddart, J. F. (2016), Flexible ferroelectric organic crystals, Nat. Commun., 7, 13108 (DOI: 10.1038/ncomms13108)

[35]. Reddy, C. M., Gundakaram, R. C., Basavoju, S., Kirchner, M. T., Padmanabhan, K. A., Desiraju, G. R. (2005), Structural basis for bending of organic crystals, Chem. Commun., 3945-3947 (DOI: 10.1039/b505103g).

[36]. Pejov, L., Panda, M. K., Moriwaki, T., Naumov, P. (2017), Probing Structural Perturbation in a Bent Molecular Crystal with Synchrotron Infrared Microspectroscopy and Periodic Density Functional Theory Calculations, J. Am. Chem. Soc., 139, 2318-2328 (DOI: 10.1021/jacs.6b11212).

[37]. Panda, M. K., Ghosh, S., Yasuda, N., Moriwaki, T., Mukherjee, G. D., Reddy, C. M., Naumov, P. (2015), Spatially resolved analysis of short-range structure perturbations in a plastically bent molecular crystal, Nat. Chem., 7, 65-72 (DOI: 10.1038/nchem.2123).

[38]. Karothu, D. P., Weston, J., Desta, I. T., Naumov, P. (2016), Shape-Memory and Self-Healing Effects in Mechanosalient Molecular Crystals, J. Am. Chem. Soc., 138, 13298-13306 (DOI: 10.1021/jacs.6b07406).

[39]. Takamizawa, S., Miyamoto, Y. (2014), Superelastic Organic Crystals, Angew. Chem. Int. Ed., 126, 7090-7093 (DOI: 10.1002/ange.201311014).

[40]. Takamizawa, S., Takasaki, Y. (2015), Superelastic shape recovery of mechanically twinned 3,5-difluorobenzoic acid crystals, Angew. Chem. Int. Ed., 54, 4815-4817 (DOI: 10.1002/anie.201411447).

[41]. Commins, P., Desta, I. T., Karothu, D. P., Panda, M. K., Naumov, P. (2016), Crystals on the move: mechanical effects in dynamic solids, Chem. Commun., 52, 13941-13954 (DOI: 10.1039/C6CC06235K).

[42]. Alimi, L. O., van Heerden, D. P., Lama, P., Smith, V. J., Barbour, L. J. (2018), Reversible thermosalience of 4-aminobenzonitrile, Chem. Commun., 54, 6208-6211 (DOI: 10.1039/C8CC03636E).

[43]. Kitagawa, D., Nishi, H., Kobatake, S. (2013), Photoinduced twisting of a photochromic diarylethene crystal, Angew. Chem. Int. Ed., 52, 9320-9322 (DOI: 10.1002/anie.201304670).

[44]. Zhu, L., Al-Kaysi, R. O., Bardeen, C. J. (2011), Reversible photoinduced twisting of molecular crystal microribbons, J. Am. Chem. Soc., 133, 12569-12575 (DOI: 10.1021/ja201925p).

[45]. Das, M., Alzaid, F., Bayry, J. (2019), Regulatory T Cells under the Mercy of Mitochondria, Cell Metab., 29, 243-245 (DOI: 10.1016/j.cmet.2019.01.012).

[46]. Singh, H., Sreedharan, S., Tiwari, R., Walther, C., Smythe, C., Pramanik, S. K., Thomas, J. A., Das, A. (2018), A Fluorescent Chemodosimeter for Organelle-Specific Imaging of Nucleoside Polyphosphate Dynamics in Living Cells, Cryst. Growth Des., 18, 7199-7206 (DOI: 10.1021/acs.cgd.8b01409).

[47]. Huang, S., Han, R., Zhuang, Q., Du, L., Jia, H., Liu, Y., Liu, Y. (2015), New photostable naphthalimide-based fluorescent probe for mitochondrial imaging and tracking, Biosens Bioelectron, 71, 313-321 (DOI: 10.1016/j.bios.2015.04.056).

[48]. Lee, J., Kim, Y., Liu, T., Hwang, Y. J., Hyeon, S. J., Im, H., Lee, K., Alvarez, V. E., McKee, A. C., Um, S. J., Hur, M., Mook-Jung, I., Kowall, N. W., Ryu, H. (2018), SIRT3 deregulation is linked to mitochondrial dysfunction in Alzheimer's disease, Aging cell, 17, (DOI: 10.1111/acel.12679).

[49]. Chen, Y., Qiao, L., Ji, L., Chao, H. (2014), Phosphorescent iridium(III) complexes as multicolor probes for specific mitochondrial imaging and tracking, Biomaterials, 35, 2-13 (DOI: 10.1016/j.biomaterials.2013.09.051).

[50]. Gupta, G., Kumari, P., Ryu, J. Y., Lee, J., Mobin, S. M., Lee, C. Y. (2019), Mitochondrial Localization of Highly Fluorescent and Photostable BODIPY-Based Ruthenium(II), Rhodium(III), and Iridium(III) Metal Complexes, Inorg. Chem., (DOI: 10.1021/acs.inorgchem.9b00898).

[51]. Jin, Y. (2014), Multifunctional Compact Hybrid Au Nanoshells: A New Generation of Nanoplasmonic Probes for Biosensing, Imaging, and Controlled Release, Acc. Chem. Res., 47, 138-148 (DOI: 10.1021/ar400086e).

[52]. Balzani, V., Gómez-López, M., Stoddart, J. F. (1998), Molecular Machines, Acc. Chem. Res., 31, 405-414 (DOI: 10.1021/ar970340y).

[53]. Yakobson, B. I., Brabec, C. J., Berhnolc, J. (1996), Nanomechanics of carbon tubes: Instabilities beyond linear response, Phys. Rev. Lett., 76, 2511-2514 (DOI: 10.1103/PhysRevLett.76.2511).

[54]. Zhang, J., Wang, N., Liu, W., Zhao, X., Lu, W. (2013), Intermolecular hydrogen bonding strategy to fabricate mechanically strong hydrogels with high elasticity and fatigue resistance, Soft Matter, 9, 6331-6337 (DOI: 10.1039/C3SM50866H).

[55]. Knowles, T. P., Fitzpatrick, A. W., Meehan, S., Mott, H. R., Vendruscolo, M., Dobson, C. M., Welland, M. E. (2007), Role of intermolecular forces in defining material properties of protein nanofibrils, Science, 318, 1900-1903 (DOI: 10.1126/science.1150057).

[56]. Safarabadi, M., Shokrieh, M. M., 8 - Understanding residual stresses in polymer matrix composites. In Residual Stresses in Composite Materials, Shokrieh, M. M., Ed. Woodhead Publishing: 2014; pp 197-232 (DOI: 10.1533/9780857098597.2.197).

[57]. Lopez-Crespo, P., Mostafavi, M., Steuwer, A., Kelleher, J. F., Buslaps, T., Withers, P. J. (2016), Characterisation of overloads in fatigue by 2D strain mapping at the surface and in the bulk, Fatigue Fract. Eng. Mater. Struc., 39, 1040-1048 (DOI: 10.1111/ffe.12463).

[58]. Zhang, H., Sui, T., Salvati, E., Daisenberger, D., Lunt, A. J. G., Fong, K. S., Song, X., Korsunsky, A. M. (2018), Digital Image Correlation of 2D

X-ray Powder Diffraction Data for Lattice Strain Evaluation, Materials, 11, 427 (DOI: 10.3390/ma11030427)

[59]. Dunham, R. S., Gurtin, M. E. (1977), Surface stress and the equilibrium shape of an elastic crystal, Appl. Phys. Lett., 30, 255-256 (DOI: 10.1063/1.89371).

[60]. Jing, Y., Ma, Y., Li, Y., Heine, T. (2017), GeP3: A Small Indirect Band Gap 2D Crystal with High Carrier Mobility and Strong Interlayer Quantum Confinement, Nano. Lett., 17, 1833-1838 (DOI: 10.1021/acs.nanolett.6b05143).

[61]. Ansari, S. N., Saini, A. K., Kumari, P., Mobin, S. M. (2019), An imidazole derivative-based chemodosimeter for Zn2+ and Cu2+ ions through "ON–OFF–ON" switching with intracellular Zn2+ detection, Inorg. Chem. Front., 6, 736-745 (DOI: 10.1039/C8QI01127C).

[62]. Kumari, P., Verma, S. K., Mobin, S. M. (2018), Water soluble two-photon fluorescent organic probes for long-term imaging of lysosomes in live cells and tumor spheroids, Chem. Commun., 54, 539-542 (DOI: 10.1039/c7cc07812a).

[63]. Verma, S. K., Kumari, P., Ansari, S. N., Ansari, M. O., Deori, D., Mobin, S. M. (2018), A novel mesoionic carbene based highly fluorescent Pd(ii) complex as an endoplasmic reticulum tracker in live cells, Dalton Trans., 47, 15646-15650 (DOI: 10.1039/c8dt02778a).

[64]. Kumari, P., Verma, S. K., Mobin, S. M. (2019), A facile two-photon fluorescent probe: an endoplasmic reticulum tracker monitoring ER stress and vesicular transport to lysosomes, Chem. Commun., 55, 294-297 (DOI: 10.1039/C8CC07429A).

[65]. Gerencser, A. A., Chinopoulos, C., Birket, M. J., Jastroch, M., Vitelli, C., Nicholls, D. G., Brand, M. D. (2012), Quantitative measurement of mitochondrial membrane potential in cultured cells: calcium-induced de- and hyperpolarization of neuronal mitochondria, J. Physiol., 590, 2845-2871 (DOI: 10.1113/jphysiol.2012.228387).

[66]. Neto, B. A. D., Corrêa, J. R., Silva, R. G. (2013), Selective mitochondrial staining with small fluorescent probes: importance, design, synthesis, challenges and trends for new markers, RSC Adv., 3, 5291-5301 (DOI: 10.1039/C2RA21995F).

[67]. Gayathri, T., Karnewar, S., Kotamraju, S., Singh, S. P. (2018), High Affinity Neutral Bodipy Fluorophores for Mitochondrial Tracking, ACS Med. Chem. Lett., 9, 618-622 (DOI: 10.1021/acsmedchemlett.8b00022).

CHAPTER 6

Design and Synthesis of Bioactive Aroyl-Hydrazone Derivatives and Their Biological Studies

6.1. Introduction

Recently, there is a growing interest in developing new drugs which are based on the aroyl-hydrazone skeleton, Ar–CH=N–NH–C(=O)–Ar′ (Ar = aromatic ring) *[1]*. Basically, hydrazones are organic ligands consisting of –NH–N=CH– group. Addition donor site like C=O increase the flexibility and versatility of compound; enhance their biological properties for therapeutic application *[2]*. Aroyl-hydrazones inhibit metalloproteins, perturbation of intracellular homeostasis by interaction with DNA *[3]*. Hydrazones based molecules exhibit anti-inflammatory *[4]*, antimicrobial *[5]*, antiplatelet *[4]*, anticonvulsant *[6]*, antitubercular *[7]*, antitumor *[8]*, antifungal and antiviral activity with a potential to overcome multidrug resistance *[9-10]*.

Nowadays, there is a constantly emerging curiosity in computational protein binding with several ligands for medicinal applications. Avian influenza viruses are a widespread concern as it crosses the species barrier and become human transmissible strains which are highly pathogenic in nature. Recently, Influenza A virus RNA polymerase PB2 subunit is being explored for probing anti-influenza drugs *[11]*. Moreover, the efficiency of the currently accepted drugs (zanamivir and oseltamivir) *[12]* is limited due to the development of resistance viruses by changing various protein structure due to point mutation. Various highly pathogenic strains of influenza A virus are H1N1, H2N2, H3N2, H5N1, H7N9, H1N2 and many more. Thus, there is an urgent need for the development of new antiviral drugs *[13]*. RNA polymerase

PB2 is one of the promising drug target candidates to prevent the rapid spread of viral disease.

Another virus has significant global health associated problem is the hepatitis C virus (HCV). About 3% of the world population is suffered from the HCV *[14-15]*. Hepatitis C virus infection is one of the major causes of liver transplantation in the USA *[16]*. Therefore NS5B polymerase is responsible for viral RNA replication, is a crucial target for searching a better drug in order to prevent hepatitis C virus proliferation *[17]*. Both Influenza A virus polymerase PB2 subunit and Hepatitis C virus NS5B polymerase are RNA-dependent RNA polymerase which considers as a most important enzyme for the drug target because it has no functional role in mammalian cells *[18-21]*. Any novel drugs that have the ability to only target viruses are considered as supreme in terms of minimum or no side effect to human.

Like a deadly viral infection, cancer as well is a fearful disease recognized globally. It is the second leading cause of death worldwide *[22]*. Many drugs that target cancer cells have a high degree of toxicity due to poor selectivity leads to potential side effect on human health. Therefore, to design compounds that specifically target a particular enzyme (protein) that involve in the progression of cancer. Transforming growth factor-beta (TGF-β) *[23-24]* and cancer related EphA2 protein kinases *[25-27]* are involve in the proliferation of cancer, hence developing inhibitor against them are an attractive way to treat cancer.

Herein, we report four new aroyl-hydrazone derivatives $\mathbf{L_1}$–$\mathbf{L_4}$ which were designed and synthesized to explore their biological activities; molecular docking of $\mathbf{L_1}$–$\mathbf{L_4}$ carried out with various disease causing proteins (viral, bacteria or cancer causing proteins) and DNA, out of these $\mathbf{L_1}$ and $\mathbf{L_2}$ bind strongly with viral disease-causing protein whereas $\mathbf{L_3}$ and $\mathbf{L_4}$ revels best binding with protein which involves in the progression of cancer. Further to validate the docking results, Bovine serum albumin

(BSA) protein binding and calf thymus DNA (ct-DNA) binding was performed using spectroscopic techniques. These aroyl-hydrazone derivatives can be explore the pharmacological and biological significance for the development of new drug entities in the future.

6.2. Results and discussion

6.2.1 Synthesis and characterization

Aroyl-hydrazones derivatives (**L_1-L_4**) were synthesized by the condensation reaction of dipicolinic acid hydrazide *[28-29]* with different aldehydes (ratio 1:2) in methanol solvent as shown in **Scheme 6.1**. 4-phenylbenzaldehyde, 2,3,4-trihydroxybenzaldehyde, 4-(4-Pyridyl)-benzaldehyde and 3-cyanobenzaldehyde were used for the synthesis of bis[4-phenylbenzylidene]pyridine-2,6-dicarbohydrazide **(L_1)**, bis[2,3,4-trihydroxybenzylidene]pyridine-2,6-dicarbohydrazide **(L_2)**, bis[4-(4-pyridyl)benylidene]pyridine-2,6-dicarbohydrazide (**L_3**) and bis[3-cyanobenylidene] pyridine-2,6-dicarbohydrazide (**L_4**) respectively **(Scheme 6.1)**.

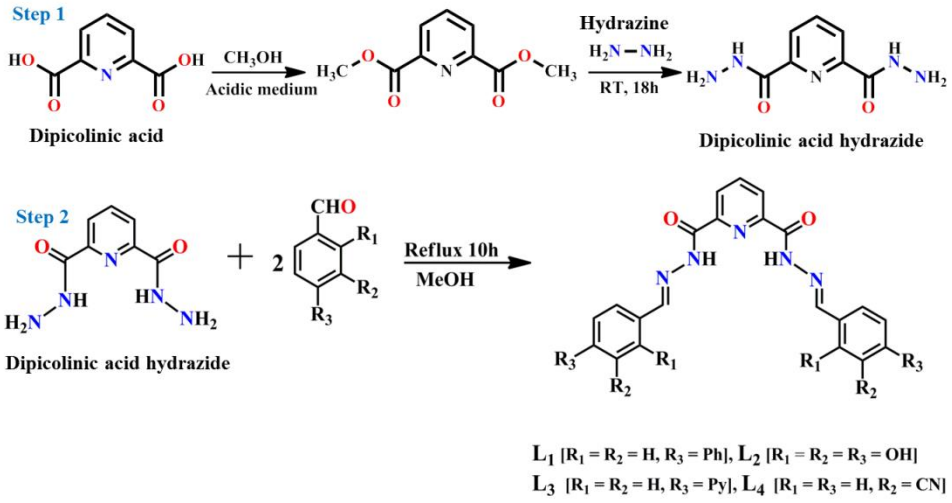

Scheme 6.1. Synthesis route of compounds **L_1–L_4**

L_1–L_4 are crystalline in nature and stable at room temperature. **L_1–L_4** have been well characterized by elemental analyses, ^{1}H, ^{13}C NMR, ESI-MS and FTIR spectroscopic techniques. Furthermore, the molecular

structures of ligands **L_1–L_4** were confirmed by single crystal X-ray diffraction studies.

In the electronic spectra of **L_1–L_4,** one absorption peak is found in the range of 300-338 nm wavelengths which is corresponding to the π –π* transitions *[30]* shown in **Figure 6.1 and Table 6.1**.

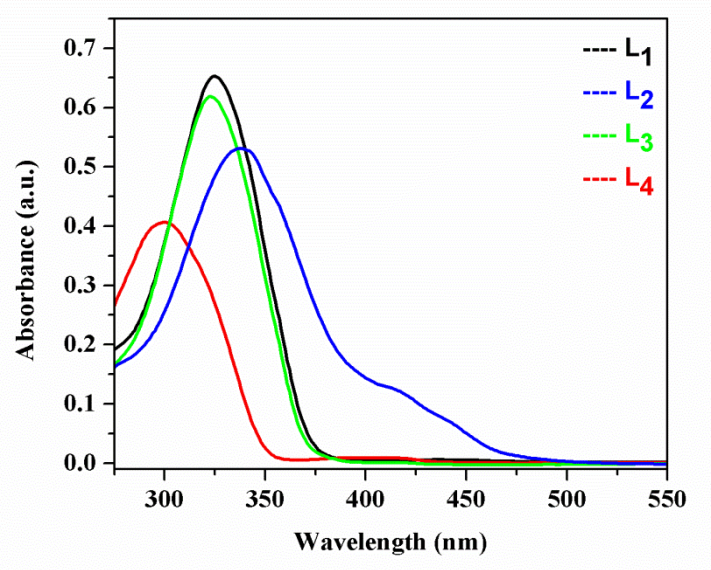

Figure 6.1. Absorption spectra of **L_1–L_4** in acetonitrile solvent ($con^c = 5.0\times10^{-5}$ M).

Table 6.1. Electronic properties of **L_1-L_4.**

Compounds	**$\lambda_{(S0\rightarrow S1)}$ (nm)**	**ε (M^{-1} cm^{-1})**
L_1	325	1.3×10^4
L_2	338	1.1×10^4
L_3	321	1.2×10^4
L_4	300	8.1×10^3

6.2.2. Molecular structures of L_1–L_4

The molecular structure of **L_1** and **L_4** were crystallized in the triclinic, ***P*-1** space group whereas, **L_2** and **L_3** was crystallized in monoclinic ***C* 2/*c*** and ***P* 2_1/*c*** space group, respectively **(Figure 6.2, Table A9**, and selected angles and bond lengths are listed in **Table A10-A13**).

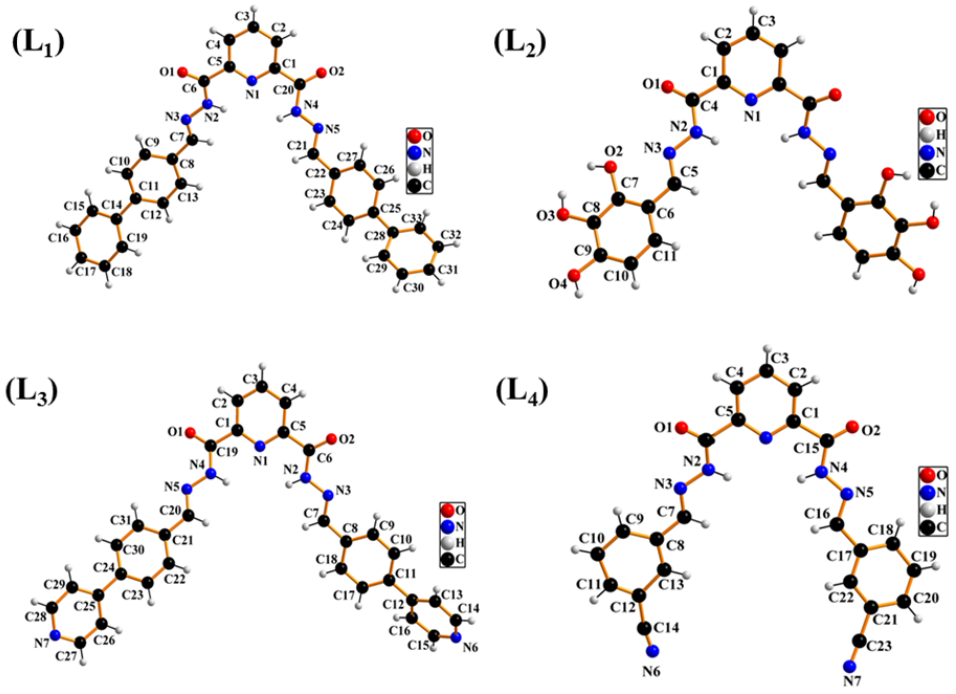

Figure 6.2. Molecular structures of **L_1, L_2, L_3** and **L_4**.

6.2.3. Molecular docking

To understand the binding affinity of aroyl-hydrazone derivatives **L_1–L_4** and its binding sites with protein, molecular docking was performed with twelve different proteins which involve in viral/ bacterial disease or cancer progressions. On the basis of inhibition constant, binding free energy, Electrostatic energy, van der Waal's interactions, Torsional free energy and intermolecular energy between protein and ligands **L_1–L_4** following observation derived: (i) **L_1** bind very strongly with Influenza A virus polymerase PB2 subunit surrounded by

interacting amino acid residues Leu599, Phe610, Asp611, Gln614, Ile615, Leu648, Val649, Arg650, Gly651, Asn652. The Arg650 form hydrogen bond, N–H···O1 with bond distance 1.912 Å **(Figure 6.3, Table 6.2 and Table A14)**. (ii) **L_2** reveals strong interaction with Hepatitis C Virus NS5B Polymerase via interacting residues Arg48, Ser218, Asp220, The221, Cys223, Phe224, Asp225, Asn291, Gly351, Asp352, and Pro354. **L_2** mostly surrounded by polar residues due to the presence of 2,3,4-trihydroxyphynyl group in **L_2** which form a hydrogen bond with polar amino acids. The hydrogen bonded residues Arg48 (N–H···O1, 2.13Å), Ser218 (O···H–O4, 2.069Å and O···H–O3, 1.915Å), The221(O···H–N2, 2.019 Å), Asp220(N–H···O2,1.975 Å and O···H–O2, 2.119 Å Phe224 (N–H···N3, 2.104 Å) Asp225(O···H–O3, 2.022 Å, and O···H–O4, 2.143 Å) as depicted in **Figure 6.3, Table 6.2 and Table A15**. (iii) **L_3** gives best binding with TGF-beta receptor 1 (Transforming growth factor β–R1) via interacting residues Ile211, Val219, Ala230, Lys232, Glu245, Tyr249, Leu260, Phe262, Leu278, Ser280, Tyr282, His283, Glu284, Gly286, Ser287, Phe289, Asp290, Lys337. Hydrogen-bonded protein residues are His283 (N–H···O, 2.117 Å) shown in **Figure 6.4, Table 6.2 and Table A16** (iii) **L_4** strongly with Cancer Related EphA2 Protein Kinases via interacting protein residues Glu623, Phe624, Gly625, Lys646, Thr647, Phe660, Glu663, Tyr735, His737, Arg743, Asp757, Phe758, Gly759, Lys778. Among these residues Glu623 (N–H···N, 1,916 Å) and Arg743 (N–H···O, 1.809 Å) forms a hydrogen bond with **L_4 (Figure 6.4, Table 6.2 and Table A17)**.

In the entire situation, the orientation of **L_1** was consistent with strong hydrophobic interaction may be due to the addition phenyl ring in **L_1**; whereas **L_2–L_4** was mostly interact with polar amino acids. Strangely, overall molecular docking results conclude that **L_1** reveals highest binding affinity than **L_2–L_4** with all the studied proteins. Strangely, **L_1** and **L_2** bind strongly with viral proteins out of twelve studied proteins. **L_1** strongly bind with Influenza A virus polymerase PB2 subunit with binding

energy11.42 Kcal/Mol and inhibition constant 4.23nM whereas **L_2** shows strong interaction with Hepatitis C Virus NS5B Polymerase with binding energy -10.47 Kcal/Mol and inhibition constant 21.06nM **(Figure 6.11 and Table 6.2, Table A14 and Table A15)**. **L_3** and **L_4** strongly bind with the proteins which involve in the proliferation of cancer. **L_3** shows the best binding with TGF-beta receptor 1 with binding energy and inhibition constant -10.61 Kcal/Mol 16.67nM respectively **(Figure 6.4, Table 6.2, and Table A16)**. **L_4** bind strongly with Cancer Related EphA2 Protein Kinases with binding energy and inhibition constant-10.02 Kcal/Mol, 45.41nM respectively **(Figure 6.4, Table 6.2 and Table A17).**

Table 6.2 Best binding of **L_1–L_4** with viral disease or cancers causing protein determine by molecular docking.

Ligands	Full name of protein	Binding free energy (Kcal/Mol)	Inhibition constant	Interacting residues	H- bonded residues
L_1	Influenza A virus polymerase PB2 subunit (2VY7)	-11.42	4.23nM	Leu599, Phe610, Asp611, Gln614, Ile615, Leu648, Val649, Arg650, Gly651, Asn652	Arg650
L_2	Hepatitis C Virus NS5B Polymerase (2WCX)	-10.47	21.06nM	Arg48, Ser218, Asp220, The221, Cys223, Phe224, Asp225, Asn291, Gly351, Asp352, Pro354	Arg48, Ser218, The221, Asp220, Phe224, Asp225
L_3	TGF-beta receptor 1 (3FAA)	-10.61	16.67nM	Ile211, Val219, Ala230, Lys232, Glu245, Tyr249, Leu260, Phe262, Leu278, Ser280, Tyr282, His283, Glu284, Gly286, Ser287, Phe289, Asp290, Lys337	His283
L_4	Cancer Related EphA2 Protein Kinases (1MQB)	-10.02	45.41nM	Glu623, Phe624, Gly625, Lys646, Thr647, Phe660, Glu663, Tyr735, His737, Arg743, Asp757, Phe758, Gly759, Lys778	Glu623, Arg743

Binding free energy $\Delta G_{binding} = \Delta G_{vdW+hb+desolv} + \Delta G_{total} + \Delta G_{elec} + \Delta G_{tor} - \Delta G_{unb}$).

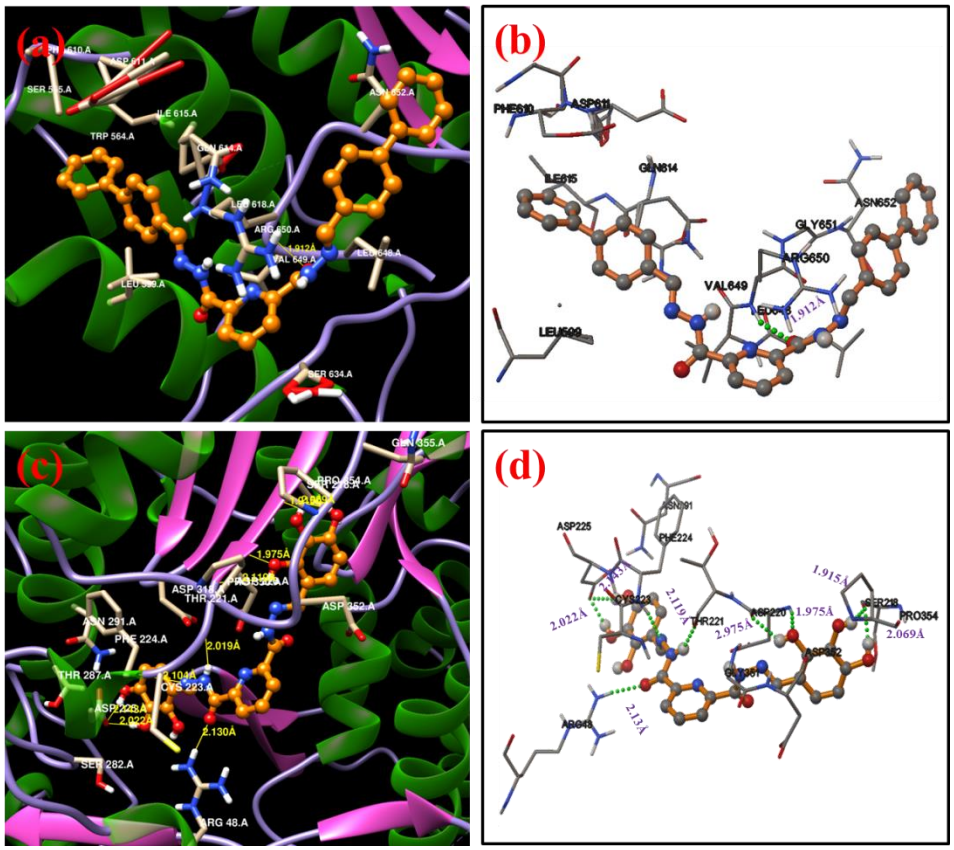

Figure 6.3. Molecular docking of $\mathbf{L_1}$ and $\mathbf{L_2}$ with viral proteins. The proteins are shown as ribbons (α-helix green, β-sheet purple and random coil violet). The interacting residue displayed as a stick, the ligand depicted as a ball-and-stick (orange). Hydrogen bonds are displayed as yellow line in (a) and (c) and green dots in (b) and (d). **(a)** Influenza A virus polymerase PB2 subunit (PDB: 2VY7), **(b)** interacting 2VY7 residues with ligand $\mathbf{L_1}$; **(c)** Hepatitis C virus NS5B polymerase (PDB: 2WCX), **(d)** interacting 2WCX residues with ligand $\mathbf{L_2}$.

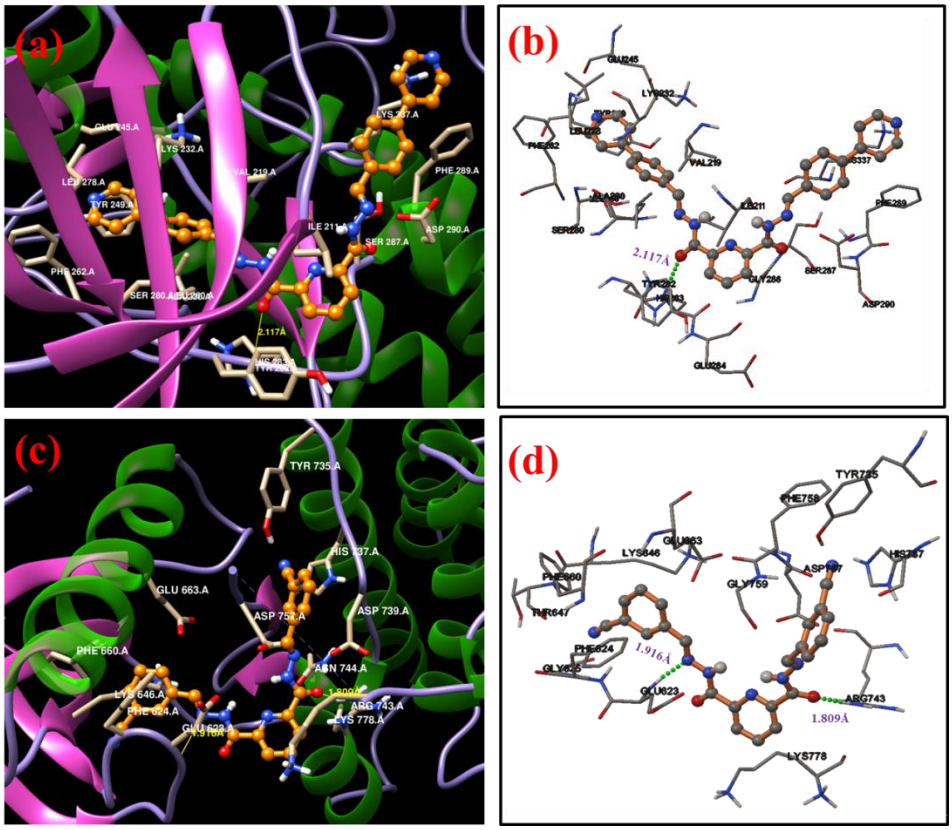

Figure 6.4. Molecular docking of $\mathbf{L_3}$ and $\mathbf{L_4}$ with cancer causing proteins. The proteins are shown as ribbons (α-helix green, β-sheet purple and random coil violet). The interacting residue displayed as a stick, the ligand depicted as a ball-and-stick (orange). Hydrogen bonds are displayed as yellow line in (a) and (c) and green dots in (b) and (d). **(a)** TGF-beta receptor 1 (PDB: 3FAA), **(b)** interacting 3FAA residues with ligand $\mathbf{L_3}$; **(c)** Cancer Related EphA2 Protein Kinases (PDB: 1MQB), **(d)** interacting 1MQB residues with ligand $\mathbf{L_4}$.

6.2.4. BSA binding by molecular docking

Proteins are essential biomolecules and serve as major targets for various types of drugs. Studies of the binding of aroyl hydrazones derivatives with proteins are significant for interpreting the transporting and metabolism processes. Bovine serum albumin (BSA) has structural homology with human serum albumin (HAS), unusual binding affinity with ligands, low cost, easy availability; hence BSA was selected as the model protein. Therefore, the BSA-binding affinities of aroyl hydrazones

derivatives **L_1–L_4** were studied theoretically by molecular docking and experimentally by tryptophan quenching.

Molecular docking studies of aroyl-hydrazones derivatives, **L_1–L_4** with BSA show that **L_1** has superior binding affinity than **L_2–L_4** in terms of both inhibitions constant (21.83nM) and binding energy (-10.45 Kcal/Mol). The interacting residues are Leu112, Lys114, Leu115, Pro117, Arg114, His145, Leu178, Glu182, Arg185, Ala193, Arg196, Asn457 and Arg458. **L_1** is surrounded by mostly hydrophobic residues **(Figure 6.5a, Figure 6.6a and Table 6.3).** **L_2** interact BSA via residues Leu197, Arg198, Ser201, Ala209, Leu210, Trp213, Leu346, Lys 350, Glu478 and Leu480. Out of these residues Ser201 (O–H···O2, 2.104 Å), Lys350 (N–H···O2, 2.118 Å), Leu480 (N–H···O1, 2.228 Å), Glu478 (O···H–O2, 2.159 Å and O···H–O3, 2.062 Å) are hydrogen bonded with ligand **(Figure 6.5b, Figure 6.6b and Table 6.3).** **L_3** surrounded by BSA protein residues Arg194, Leu197, Phe205, Arg208, Ala209, Trp213, Ser343, Leu346, Lys350, Asp450, Ser453, Thr477, Glu478 and Leu480. Leu480 is hydrogen bond with **L_3** oxygen atom (N–H···O, 1.679 Å) shown in **Figure 6.5c, Figure 6.6c and Table 6.3**. **L_4** bind BSA by interacting with mostly polar residues Pro110, Leu112, Pro113, Lys114, Leu115, Pro117, Arg144, His145, Tyr147, Arg185, Ser192, Arg196, and Arg458. Arg144 is hydrogen bond with an oxygen atom (N–H···O, 2.076 Å) depicted in **Figure 6.5d, Figure 6.6d and Table 6.3.** The binding affinity of aroyl-hydrazones derivatives with BSA in term of binding energy and inhibition constant are **L_1** (-10.45 Kcal/Mol, 21.83nM) > **L_4** (-10.19 Kcal/Mol, 20.5nM) > **L_3** (-9.23 Kcal/Mol, 171.34 nM) > **L_2** (-7.25 Kcal/Mol, 4.83µM).

Table 6.3 Molecular docking of **L_1, L_2, L_3, and L_4** with BSA (PDB: 4F5S)

Ligand	Binding energy (Kcal/Mol)	Inhibition constant	Interacting residues	H– bonded residues
L_1	–10.45	21.83nM	Leu112, Lys114, Leu115, Pro117, Arg114, His145, Leu178, Glu182, Arg185, Ala193, Arg196, Asn457, Arg458	
L_2	–7.25	4.83µM	Leu197, Arg198, Ser201, Ala209, Leu210, Trp213, Leu346, Lys 350, Glu478, Leu480	Ser201, Lys350, Leu480,Glu478
L_3	–9.23	171.34 nM	Arg194, Leu197, Phe205, Arg208, Ala209, Trp213, Ser343, Leu346, Lys350, Asp450, Ser453, Thr477, Glu478, Leu480	Leu480
L_4	–10.19	20.5nM	Pro110, Leu112, Pro113, Lys114, Leu115, Pro117, Arg144, His145, Tyr147, Arg185, Ser192, Arg196, Arg458	Arg144

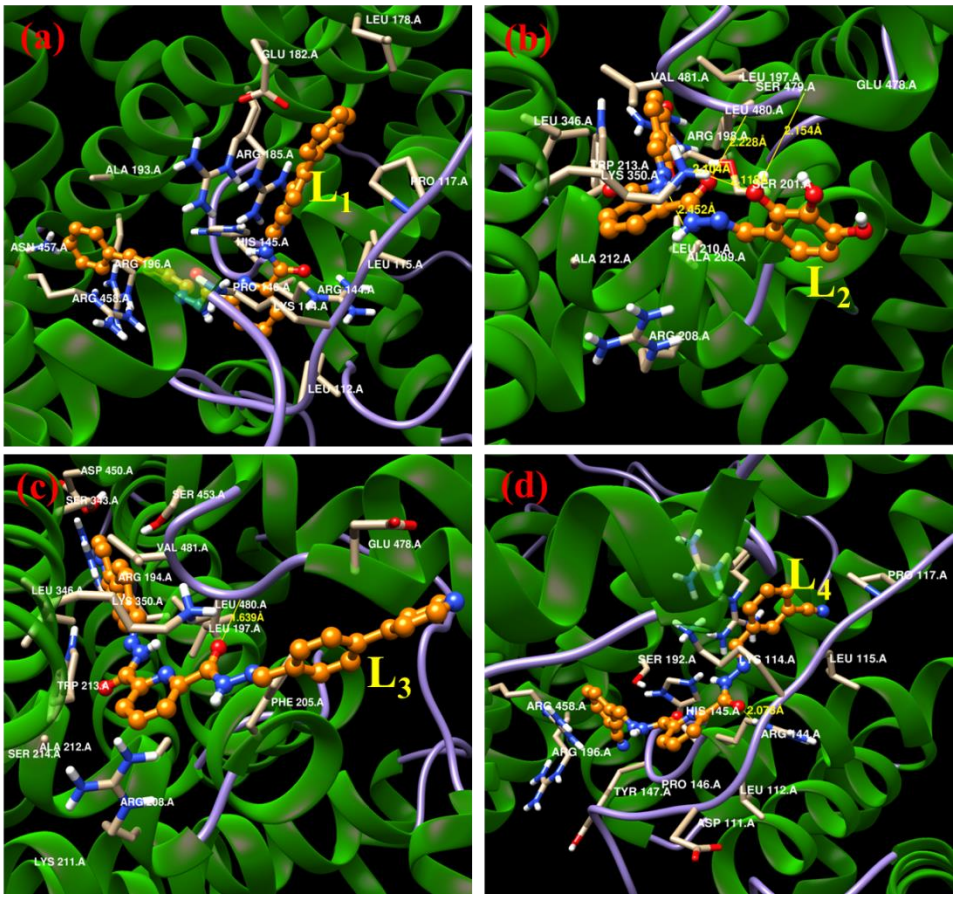

Figure 6.5. Molecular docking of ligand **L_1–L_4** with BSA (PDB: 4F5S). The proteins are shown as ribbons (α–helix green, β–sheet purple and random coil violet). The interacting residue displayed as a stick, the ligand depicted as a ball–and–stick (orange). Hydrogen bonds are shown as yellow line.

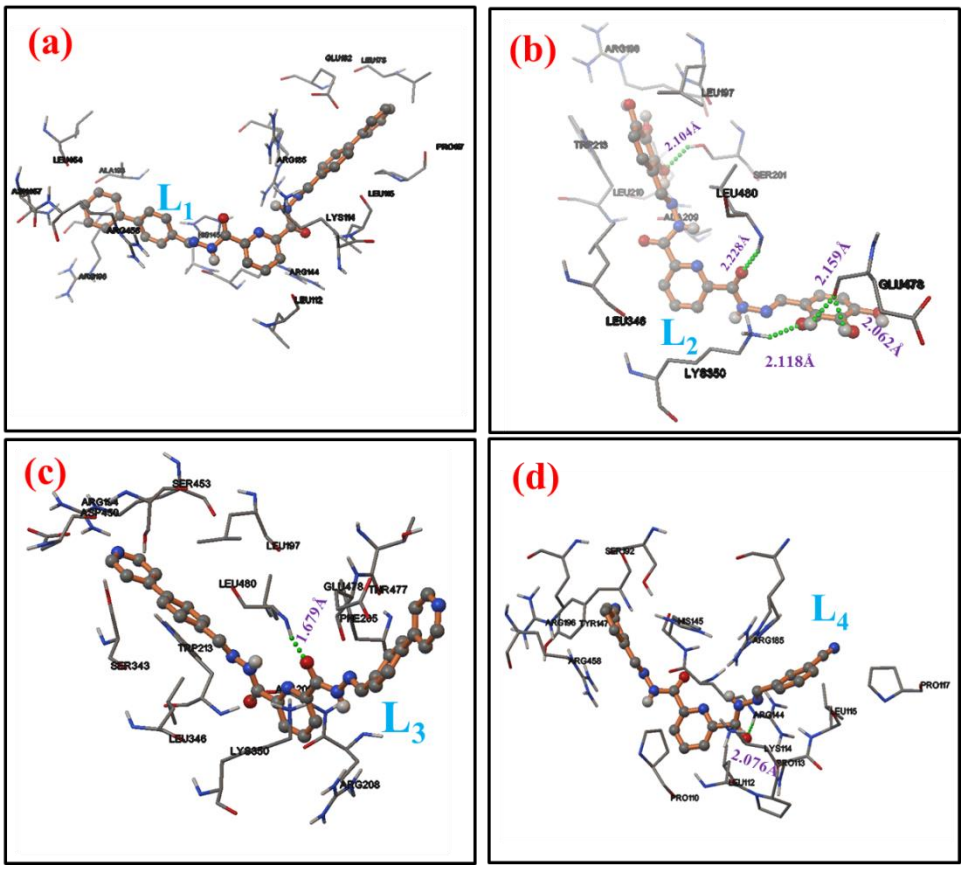

Figure 6.6. Molecular docking of ligand **L_1–L_4** with BSA (PDB: 4F5S). The interacting residue of BSA with Ligand (**L_1–L_4)** displayed as a stick, the all ligands depicted as a ball–and–stick (orange). Hydrogen bonds are shown as green dots.

6.2.5. Tryptophan quenching experiment

The tryptophan fluorescence quenching experiments was performed to study binding affinity of aroyl-hydrazones derivatives **L_1–L_4** with BSA. The fluorescence ability of BSA is primarily because of the presence of mostly aromatic amino acids such as tryptophan, phenylalanine, and tyrosine. However, alternation in the molecular environment nearby the fluorophores can be measured by the monitoring the change in the spectra of fluorescence in the absence as well in the presence of a quencher (ligand) which provide evidence for binding of ligands. Interaction of ligands with proteins is monitored by the intrinsic fluorescence intensity. The occurrence of fluorescence quenching may be due to dynamic quenching or static quenching. Dynamic quenching occurs

when the fluorophores and the quencher contact each other in their excited state. While in static quenching fluorophores and the quencher form a ground-state complex. In both situations, change in the fluorescence intensity is depending on the quencher concentration. The fluorescence spectrum of BSA at 340 nm indicates progressive reducing trends with increasing the ligand concentration. This may be due to binding of **L_1–L_4** to BSA cause conformational change in protein structure**.** The fluorescence quenching quantitatively analyzed by employing the Stern–Volmer equation *[31-32]*

$$\frac{F_0}{F} = 1 + k_q\tau_0[Q] = 1 + K_{sv}[Q] \qquad \text{(eq1)}$$

where F_0 and F denote fluorescence intensities in the absence and the presence of a quencher respectively, k_q is the bimolecular quenching rate constant, [Q] represent the concentration of the quencher (Ligand), τ_0 represent the fluorophore average lifetime in the absence of a quencher (10^{-8} s) *[33]* and K_{sv} is the linear Stern–Volmer quenching constant (M^{-1}). The fluorescence quenching spectra of BSA protein upon binding of ligands shown in **(Figure 6.7).** K_{sv} and K_q value obtained from the slope of quenching plot F_0/F vs ligand concentration **(inset in Figure 6.7)** are 9.42 × 10^3 M^{-1}, 9.42 × 10^{11} M^{-1} S^{-1} for **L_1**, 1.307 × 10^4 M^{-1}, 1.307 × 10^{12} M^{-1} S^{-1} for **L_2**, 3.06 × 10^3 M^{-1}, 3.06 × 10^{11} M^{-1} S^{-1} for **L_3**, 4.36 × 10^3 M^{-1}, 4.36 × 10^{11} M^{-1} S^{-1} for **L_4 (Figure 6.7, Table 6.4).** The k_q value, for dynamic quenching normally in the range 10^{10} M^{-1} s^{-1} *[34]*, but in case of **L_1–L_4** k_q value in the range of 10^{11} M^{-1} s^{-1} designating static quenching in these case. The binding constant (K_a) and the number of the binding site (n) can be obtained by employing the Scatchard equation *[35]*.

$$\log\left[\frac{F_O - F}{F}\right] = \log K_a + n\log[Q] \qquad \text{(eq2)}$$

F_0 and F denote the fluorescence emission intensities in the quencher's absence and presence respectively. K_a represents binding constant and n

denotes the number of binding sites. The intercept of the plot of log(F0 − F)/F versus log[Q] **(Figure 6.8, Table 6.4)** provide binding constant and value of slope provide a number of binding sites. The binding constant K_a of **L_1–L_4** are $3.92 \times 10^6\ M^{-1}$, $2.92 \times 10^6\ M^{-1}$, $3.00 \times 10^6\ M^{-1}$, $3.33 \times 10^6\ M^{-1}$ respectively. The binding affinity of ligands with BSA are in the order of **L_1> L_4> L_3> L_2**, which is an agreement with molecular docking binding constant results **(Figure 6.5, Figure 6.6, Table 6.3).** BSA protein binding result reveals that the addition of a phenyl ring in **L_1** remarkably improves the protein binding affinity, due to the phenyl ring stabilizes by hydrophobic interactions as **L_1** surrounded by mostly non-polar residues.

Table 6.4. Stern-Volmer quenching constant and binding constant of **L_1–L_4** with BSA protein**.**

Ligands	K_{sv} (M^{-1})	K_q ($M^{-1}S^{-1}$)	K_a (M^{-1})	n
L_1	9.42×10^3	9.42×10^{11}	3.92×10^6	0.99
L_2	1.307×10^4	1.307×10^{12}	2.92×10^6	0.77
L_3	3.06×10^3	3.06×10^{11}	3.00×10^6	0.86
L_4	4.36×10^3	4.36×10^{11}	3.33×10^6	0.93

$k_q = K_{SV}/\tau_0$ ($\tau_0 = 10^{-8}$ s).

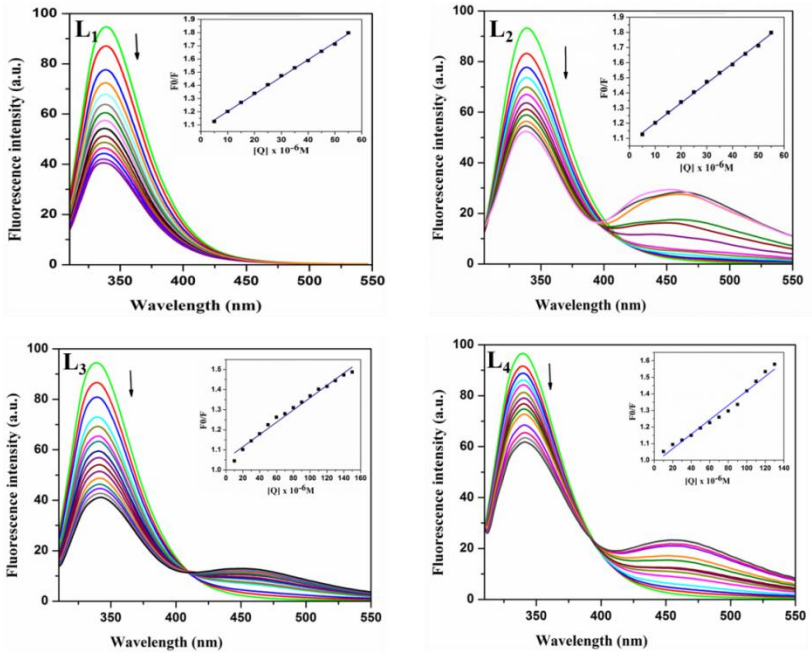

Figure 6.7. Fluorescence quenching spectra of BSA by ligand **L_1–L_4**. Inset: Corresponding Stern–Volmer plot

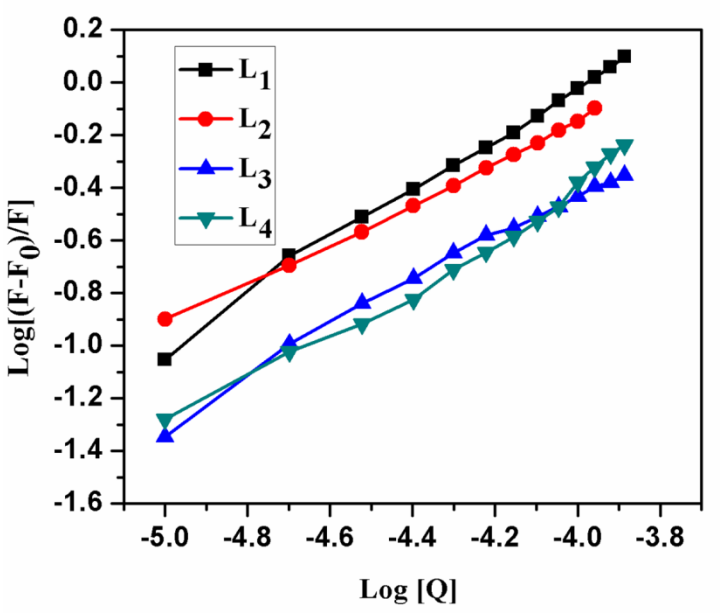

Figure 6.8 Scatchard plot for **L_1–L_4** with BSA protein binding

6.2.6. DNA binding study of L_1–L_4

DNA serves as a primary target for various drugs. DNA-binding is also one of the critical steps for the understanding of actual aroyl-hydrazone based drugs design. It helps in knowing the proper mechanisms which participate in the site-specific recognition of duplex DNA, and synthesis of aroyl-hydrazone based pharmaceutical molecules. Therefore the binding study of ligands **L_1–L_4** toward DNA is done by both theoretically by molecular docking and experimentally by ethidium bromide (EB) displacement method *[32]*.

The molecular docking of ligands **L_1–L_4** was performed with duplex DNA (PDB: 4O3M) *[36]* having Chain P:5'd(AGCGTCGA GATCCAAG)-3' and Chain T: 5'-d(CTTGGATCTCGACGCTCTCC CTTA)-3'. Docking plays a vital role in elucidating the drug- DNA interaction for the innovative discovery of rational drugs. Molecular docking of aroyl-hydrazone based ligands **L_1–L_4** with DNA was executed to predict the binding affinity and specific position of interaction. The best energetically favorable conformations have chosen which having the least

binding free energy and inhibition constant, which is considered as high binding affinity and more potent. (i) **L_1** stabilized by hydrogen bonding with nucleotide DG9 (N3–H···N3, 2.20 Å and N–H···N3, 1.998 Å) and DA10 (O···H–N2, 2.069 Å) as shown in **Figure 6.9 and Table 6.5**. (ii) Phenyl ring of **L_2** also stabilizes by π–π stacking interactions with DT10 base pair of duplex DNA. **L_2** stabilized by hydrogen bond with nucleotide DT7 (O–H···O2, 2.009 Å), DG9 (N3–H ···O1, 1.954 Å and N–H ···N1, 1.809 Å), DA10 (N3–H ···N3, 1.913 Å), DT9 (O ···H– N2, 2.156Å), DC10 (O ···H– N2, 1.91Å) represented in **Figure 6.9 and Table 6.5.** (iii) **L_3** also stabilized by both π–π stacking and hydrogen bond. **L_3** pyridine ring stabilizes by π–π stacking interactions with DC13 nitrogen base. Hydrogen-bonded nucleotides are DG7 (N–H···O, 2.131 Å), DG11 (N–H···N1, 1.83 Å), DA12 (N–H···O, 2.095 Å) as shown in **Figure 6.9 and Table 6.5.** (iv) **L_4** again form a hydrogen bond with various nucleotides such as DG9 (N–H···N1, 1.75 Å) and (N3–H···O, 1.923 Å), DA10 (N3–H···O, 1.99 Å), DC 10 (sugar O···N2–H, 2.107 Å) as depicted in **Figure 6.9 and Table 6.5**. Van der Waals interaction, Electrostatic Energy, hydrogen bonding, hydrophobic interaction, and π–π stacking interaction causes an increment in the binding affinity between ligand **L_1–L_4** and duplex DNA. The DNA binding affinity of ligands reveals that **L_3** bind very strongly with DNA than other three ligands in the order of **L_3>L_1>L_4>L_2 (Figure 6.9 and Table 6.5**). The ligands **L_1–L_3** intercalate in major groove whereas **L_4** intercalate in minor Groove of duplex DNA.

Table: 6.5 Molecular docking of L_1, L_2, L_3, and L_4 with dsDNA (PDB: 4O3M)

Ligands	Binding energy (Kcal/Mol)	Inhibition constant	Interacting residues	H–bonded residues
L_1	–11.27	5.5nM	Chain P: DG7, DA8, DG9, DA10, DT11 Chain T: DA6, DT7, DC8, DT9, DC10, DG11	DG9, DA10
L_2	–9.51	106.37nM	Chain P: DG7, DA8, DG9, DA10, DT11 Chain T: DT7, DT9, DC10	DG9, DC10, DT7, DA10, DT9
L_3	–11.92	1.82nM	Chain P: DT5, DC6, DG7, DA8, DG9, DA10 Chain T: DG9, DC10, DG11, DA12, DC13, DC15	DG7 DG11 DA12
L_4	–10.51	19.65nM	Chain P:DG7, DG9, DA10 Chain T: DT7, DC8, DT9, DC10, DG11	DG9, DA10

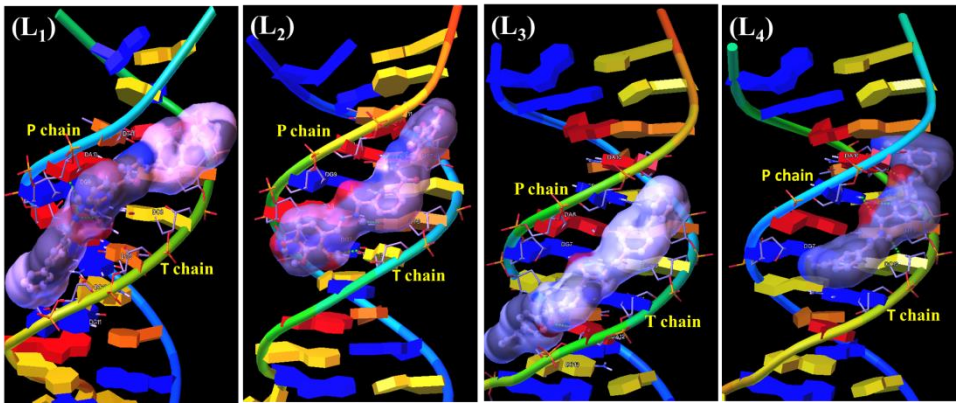

Figure 6.9. Molecular docking of ligand L_1–L_4 with duplex DNA (PDB: 4O3M). DNA represented as helix, ligand as ball and stick which is surrounded by msms.

The binding affinity order of aroyl-hydrazones derivatives **L_1–L_4** prediction by molecular docking studies were further authenticated experimentally by ethidium bromide (EtBr) fluorescence displacement titrations. EtBr is a planar cationic dye. The intrinsic fluorescence intensity of dsDNA is negligible, and also EtBr fluorescence intensity in Tris-HCl buffer is insignificant since it quenched by the solvent molecules. But when it intercalates between the adjacent base pair of DNA emits a strong fluorescent signal. When Ligand intercalates between DNA base pair, the probable binding site for EtBr decreased. Consequently, the fluorescence intensity of EtBr gets quenched. The fluorescence intensity of EtBr bound Calf thymus DNA (CT-DNA) remarkably decreases upon increasing the concentration of ligand **L_1–L_4,** which indicate that EtBr molecules dissociate from the DNA and replace by ligand binding. This may be due to the intercalation of ligands in DNA. The fluorescence quenching spectra depicted in **(Figure 6.10).** The quenching of EtBr bound to the DNA by ligand is in accordance with the linear Stern–Volmer equation *[31]*:

$$\frac{I_0}{I} = 1 + K_{SV}[Q]$$

The K_{sv} value is obtained from the slope of quenching plot I_0/I versus [ligand] **(inset in Figure 6.10),** The Stern–Volmer quenching constant (K_{sv}) value for the ligands **L_1–L_4** is 7.78×10^3 M^{-1}, 4.89×10^3 M^{-1}, 5.59×10^3 M^{-1}, 6.32×10^3 M^{-1} respectively. The binding constant (K_b) values of ligands obtained from the plot of log[(F0 − F)/F] vs. log[Q] using the Scatchard equation and Scatchard plot **(Figure 6.11, Table 6.6)** Binding constant of four ligands are as follow K_b; (**L_1**) 4.79×10^6 M^{-1}, (**L_2**) 3.97×10^6 M^{-1}, (**L_3**) 4.95×10^6 M^{-1}, (**L_4**) 4.17×10^6 M^{-1}. This data reflecting the binding affinity of ligands with CT DNA is in the order of **L_3>L_1>L_4>L_2**, which is an agreement with molecular docking binding constant results **(Figure 6.9 and Table 6.5).** DNA interaction result reveals that the

addition of a pyridine ring in $\mathbf{L_3}$ significantly improve the DNA binding strength, reasonably due to the pyridine ring stabilizes by π–π stacking interactions with nitrogen base.

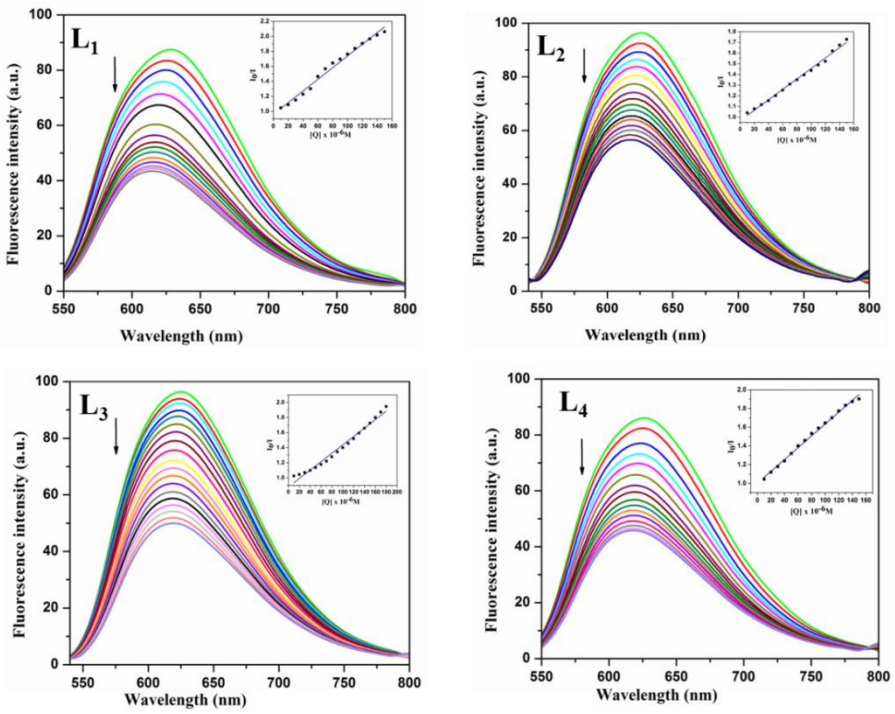

Figure 6.10. EtBr displacement assay ($\mathbf{L_1}$–$\mathbf{L_4}$) by change in the fluorescence intensity of EtBr with respect to conc. of ligands $\mathbf{L_1}$–$\mathbf{L_4}$. Inset: Corresponding Stern–Volmer plot.

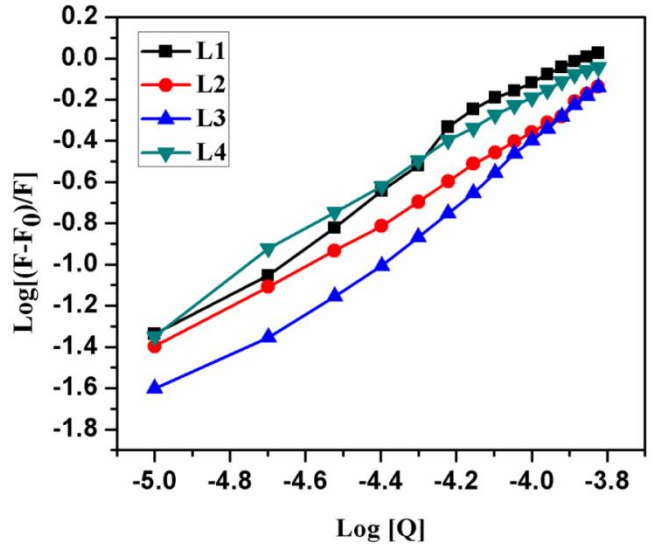

Figure 6.11. Scatchard plot for $\mathbf{L_1}$–$\mathbf{L_4}$ with DNA binding.

Table 6.6 Stern–Volmer quenching constant, binding constant of $\mathbf{L_1}$–$\mathbf{L_4}$ with calf thymus DNA

Ligands	K_{sv} (M^{-1})	K_a (M^{-1})
$\mathbf{L_1}$	7.78×10^3	4.79×10^6
$\mathbf{L_2}$	4.89×10^3	3.97×10^6
$\mathbf{L_3}$	5.59×10^3	4.95×10^6
$\mathbf{L_4}$	6.32×10^3	4.17×10^6

6.2.7. Density Functional Calculation

To understand electronic communication in $\mathbf{L_1}$-$\mathbf{L_4}$, theoretical calculations have been performed using DFT calculation. With reference to frontier molecular orbital theory, the energy of HOMO and LUMO orbital levels are very significant factors that affected bioactivity and play a vital role in various pharmacological processes. The energy and geometry optimization was accomplished using Gaussian 09 programme *[37]*. 6-31G basis set have been used throughout the calculation for carbon (C), Hydrogen (H), Oxygen (O) and Nitrogen (N) atoms. We believe that this basis set is accurate for energy and structure optimization of $\mathbf{L_1}$-$\mathbf{L_4}$. The frontier molecular orbitals of $\mathbf{L_1}$-$\mathbf{L_4}$ are illustrated in **Figure 6.12**. It is clearly seen in **Figure 6.12** that the electron density of highest occupied molecular orbitals (HOMO) of ligands $\mathbf{L_1}$-$\mathbf{L_4}$ located mainly on both the pedal part while in case of lowest unoccupied molecular orbitals (LUMO) is concentrated on the pyridyl group. The difference between the energy of the HOMO and LUMO orbitals (band gap) of $\mathbf{L_1}$-$\mathbf{L_4}$ are 3.72 eV, 3.89 eV, 3.90 eV, and 4.15 eV respectively. Among $\mathbf{L_1}$ to $\mathbf{L_4}$ the lowest band gap is observed in case of $\mathbf{L_1}$ while highest was found in case of $\mathbf{L_4}$, which means electronic communications between HOMO and LUMO orbitals of $\mathbf{L_1}$ will be easier in comparison to $\mathbf{L_4}$. Thus, to some extent, the DFT

calculation can explain the reason behind the strongly binding of $\mathbf{L_1}$ with protein and DNA and shows anti-influenza activities.

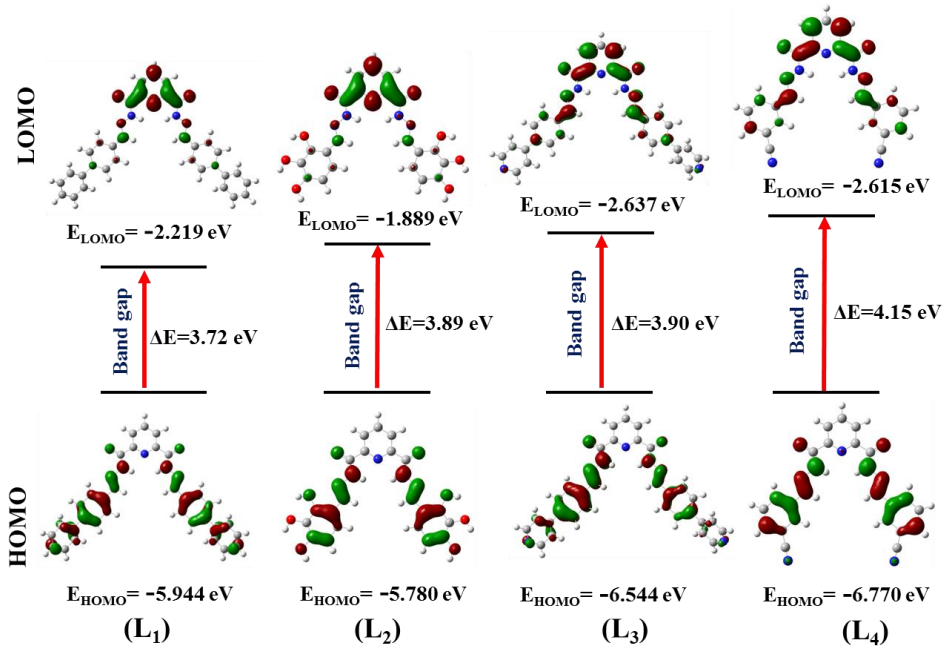

Figure 6.12. Frontier molecular orbitals of $\mathbf{L_1}$-$\mathbf{L_4}$ and their band gap.

6.3. Conclusions

In summary, we have designed and synthesized four new aroyl-hydrazones derivatives, **L_1–L_4** for their biological applications. Molecular docking and fluorescence emission titration results are in accordance with a strong interaction of **L_1–L_4** with Bovine serum albumin (BSA) protein in the order of **L_1>L_4>L_3>L_2** and with DNA in the order of binding **L_3>L_1>L_4>L_2**. **L_1** most strongly binds with BSA possibly due to addition phenyl ring stabilized by hydrophobic interaction as it mostly surrounded by hydrophobic residues. In case of DNA binding, **L_3** has the highest binding affinity, reasonably due to the additional pyridine ring in **L_3** is stabilizes by π–π stacking interactions with nitrogen base. Moreover, molecular docking of **L_1–L_4** was performed with twelve different proteins, which involve in disease proliferation. The results reveal that **L_1** and **L_2** exhibit unique binding affinity with viral protein i.e influenza A virus polymerase PB2 subunit and Hepatitis C Virus NS5B Polymerase respectively. However, **L_3** and **L_4** strongly bind with cancer-causing proteins i.e. TGF-beta receptor 1 and cancer-related EphA2 protein kinases respectively. Moreover, DFT results show better electronic communication in **L_1**. These promising results highlight the potential use of aroyl-hydrazones derivatives (**L_1–L_4**) as a new class of antiviral or anticancer agents.

6.4. Experimental Section

6.4.1. Materials

The synthesis of dipicolinic acid hydrazide was performed with reference to the reported methods *[28-29]*. The common reagents and solvents were obtained from S. D. Fine Chem. Ltd and Merck. Prior to use solvents; they are dried and distilled using standard literature procedures. 4-phenylbenzaldehyde, 2,3,4-trihydroxybenzaldehyde, 4-(4-Pyridyl) benzaldehyde, 3-cyanobenzaldehyde, CT-DNA, and BSA were procured from Sigma Aldrich Chemical Co., USA and used without any further purification. Ligand $\mathbf{L_2}$ was synthesized according to the literature *[38]*.

6.4.2. Physical Measurements:

All chemicals were reagent grade quality, purchased from commercial sources and were used without further purification. Melting points of the ligands $\mathbf{L_1}$–$\mathbf{L_4}$ were determined using aluminum block accepts three capillary tubes and mercury thermometer. ^{1}H NMR (400 MHz) and ^{13}C NMR (100 MHz) spectra were recorded on a Bruker Avance (III) instrument by using DMSO-d_6. ^{1}H NMR chemical shifts are reported in parts per million (ppm) relative to the solvent residual peak (DMSO-d_6, 2.50ppm). ^{13}C NMR chemical shifts are reported relative to the solvent residual peak (DMSO d_6, 39.52ppm). IR spectra [4000–400 cm−1] were recorded using Bio-Rad FTS 3000MX instrument on KBr pellets. The mass spectra of $\mathbf{L_1}$–$\mathbf{L_4}$ were recorded on a Bruker-Daltonics micro TOF-QII mass spectrometer. The elemental analyses were performed on a Thermo-Flash 2000 elemental analyzer. The UV-Vis absorption spectra were performed using dilute solutions in quartz cells (1 cm path length) on Varian UV/vis spectrophotometer (model: Cary 100). Fluorescence measurements were performed using fluoroMax-4 Spectrophotometer (HORIBA Scientific). The excitation and emission slits were 5/5 nm for the fluorescence emission measurements.

6.4.3. X-ray Crystallographic data collection and structure refinement of L_1–L_4

The single crystal of **L_1, L_2, L_3** and **L_4** were mounted on a Rigaku-Oxford Supernova CCD Diffractometer and the data were collected at 150 K or 293 K using graphite-monochromated Cu-Kα (λα = 1.54814 Å). The data was collected and evaluated by using the CrysAlisPro CCD software. Standard φ−ω scan techniques were used to collect and scale the data which was reduced by CrysAlisPro RED software. The crystal structures were solved by direct methods using SHELXS-97 and refined by full-matrix least squares with SHELXL-97 on F^2 *[39]*. The refinement of all non-H atoms were performed anisotropically and all the H atoms were placed in geometrically constrained positions and refined with isotropic temperature factors, generally 1.2 × Ueq of their parent atoms. The Diamond (*ver*. 3.1d) was used for the analysis of molecular drawings; hydrogen bonding interactions and mean-plane analysis. In **L_2**, one highly disordered solvent molecule is present in the asymmetric unit with partial occupancy in a special position, which cannot be resolved. Thus, to remove this disordered solvent molecule SQUEEZE was applied. Despite several attempts we were unable to generate better quality crystals for **L_4**. The existing alerts A and B are related to the week diffraction of crystal. The crystal and refinement data are summarized in **Table A9** and selected bond distances and angles are shown in **Table A10- A13.**

6.4.4. Synthesis and characterization

Synthesis of $C_{33}H_{25}N_5O_2$ (L_1): A solution of dipicolinic acid hydrazide (0.195 g, 1 mmol) and 4-phenylbenzaldehyde (0.364 g, 2.0 mmol) in 50 ml of methanol was refluxed. The white precipitate was obtained after 10 h. The precipitates were filtered off, washed with methanol and dried in a vacuum oven. Colorless crystals of **L_1** were obtained in 1:1 (v/v) methanol and acetone mixture within 5 days. Yield = 90%. Melting Point: 282 °C;

Anal. Calcd for $C_{33}H_{25}N_5O_2$: C, 75.70; H, 4.81; N, 13.38. Found: C, 75.12; H, 4.80; N, 13.55; ESI-MS calcd for $[M+H]^+$ $C_{33}H_{25}N_5O_2$, 524.5839, found 524.2235 **(Figure 6.13);** IR (KBr, cm^{-1}): 3229.92(w), 3028.32(w), 1699.03(vs), 1659.84(s), 1605.57(w), 1533.49(vs), 1515.28(s), 1485.82(s), 1366.42(w), 1232.75(s), 1159.17(s), 1077.00(w) depicted in **Figure 6.14)**; ^1H NMR δ_H (400 MHz, DMSO-d_6) 12.39 (s, 2H), 8.83 (s, 2H), , 8.38 (d, *J* = 8 Hz, 2H), 8.30 (t, *J* = 8 Hz, 1H), 7.93 (d, *J* = 8 Hz, 4H), 7.83 (d, *J* = 8 Hz, 4H), 7.75 (d, *J* = 8 Hz, 4H), 7.50 (t, *J* = 8 Hz, 4H), 7.40 (t, *J* = 8 Hz, 2H) shown in **Figure 6.15)**; ^{13}C NMR δ_C (100 MHz, DMSO-d_6) 159.45 (C = O), 149.70 (Py-C), 148.27 (C = N), 141.95 (Ar-C), 139.97 (Ar-C), 139.28 (Py-C), 133.22 (Ar-C), 129.03 (Ar-C), 127.92 (Ar-C), 127.12 (Ar-C), 126.71 (Ar-C), 125.50 (Py-C) shown in **Figure 6.16)**. The molar absorptivity coefficient (**ε**): 1.3×10^4 M^{-1} cm^{-1}.

Synthesis of $C_{21}H_{17}N_5O_8$ (L_2): **L_2** was synthesized by following the method specified above for **L_1** using 2,3,4-triihydroxybenzaldehyde (0.308 g, 2.0 mmol) instead of 4-phenylbenzaldehyde. Yellow colored crystals of **L_2** were obtained in water and acetone mixture 1:1 (v/v) within 10 days. Yield = 84%. Melting point: >350°C; Anal. Calcd for $C_{21}H_{17}N_5O_8$: C, 53.96; H, 3.67; N, 14.98. Found: C, 54.01; H, 3.61; N, 14.96; ESI-MS (ES^+) calcd for $[M+H]^+$ $C_{21}H_{17}N_5O_8$ 468.11, found 468.1 **(Figure 6.17);** IR (KBr, cm^{-1}): 3472.11(br), 3458.08(br), 3196.42(w), 1674.30(vs), 1634.69(vs), 1641.11(w), 1585.12(w), 1509.02(vs), 1448.42(w), 1374.13(w), 1263.85(s), 1234.54(s) shown in **Figure 6.18**; ^1H NMR δ_H (400 MHz, DMSO-d_6) 12.30 (s, 2H), 11.27 (s, 2H), 9.62 (s, 2H), 8.71 (s, 2H), 8.57 (s, 2H) , 8.34(d, *J* = 4 Hz, 2H) , 8.27 (t, *J* = 8 Hz, 1H), 6.91 (d, *J* = 8 Hz, 2H), 6.44(d, *J* = 8 Hz, 2H) spectra depicted in **Figure 6.19**; ^{13}C NMR δ_C (100 MHz, DMSO-d_6) 159.15 (C = O), 152.00 (Ar-C), 149.26 (Ar-C), 148.12 (Py-C), 147.78 (C = N), 140.15 (Py-C), 132.90 (Ar-C), 125.54 (Py-C), 121.29 (Ar-C), 111.00 (Ar-C), 108.03 (Ar-C) spectra shown in **Figure 6.20**. The molar absorptivity coefficient (**ε**): 1.1×10^4 M^{-1} cm^{-1}.

Synthesis of $C_{31}H_{23}N_7O_2$ (L_3): **L_3** was synthesized by following the method specified above for **L_1** using 4-(4-Pyridyl)benzaldehyde (0.366 g, 2.0 mmol) instead of 4-phenylbenzaldehyde. Light yellow colored crystals of **L_3** were obtained in 1:1 (v/v) ethanol and chloroform mixture within 2 days. Yield = 88%. Melting point: 328 °C; Anal. Calcd for $C_{31}H_{23}N_7O_2$: C, 70.84; H, 4.41; N, 18.66. Found: C, 70.82 ; H, 4.42; N, 18.67; ESI-MS calcd for $[M+H]^+$ $C_{31}H_{23}N_7O_2$ 526.19, found 526.20 (**Figure 6.21)**; IR (KBr, cm^{-1}): 3431.07(br), 3228.53(w), 3032.15(w), 1683.19(vs), 1596.28(s), 1539.15(s), 1369.66(w), 1160.15(s) depicted in **Figure 6.2**2; ^1H NMR δ_H (400 MHz, DMSO-d_6) 12.44 (s, 2H), 8.85 (s, 2H), 8.67 (d, *J* = 8 Hz, 4H), 8.38 (d, *J* = 8 Hz, 2H) , 8.30 (t, *J* = 8 Hz, 1H), 7.97 (t, *J* = 8 Hz, 8H), 7.78 (d, *J* = 4 Hz, 4H) spectra shown in **Figure 6.23**; ^{13}C NMR δ_C (100 MHz, DMSO-d_6) 159.72 (C = O), 150.34 (Py1-C), 149.30 (Py2-C), 148.39 (C = N), 146.15 (Py2-C), 138.72 (Py1-C), 135.09 (Ar-C), 129.64 (Ar-C), 128.00 (Ar-C), 127.40 (Ar-C), 125.61 (Py1-C), 121.16 (Py2-C) spectra depicted in **Figure 6.24**. The molar absorptivity coefficient (**ε**): 1.2×10^4 M^{-1} cm^{-1}.

Synthesis of $C_{23}H_{15}N_7O_2$ (L_4): **L_4** was synthesized by following the method specified above for **L_1** using 3-cyanobenzaldehyde (0.263 g, 2.0 mmol) instead of 4-phenylbenzaldehyde. White crystals of **L_4** were obtained in dimethylformamide (DMF) within 10 days. Yield = 76%. Melting point: 332 °C; Anal. Calcd for $C_{23}H_{15}N_7O_2$: C, 65.55; H, 3.59; N, 23.27. Found: C, 65.59; H, 3.61; N, 23.30; ESI-MS calcd for $[M+H]^+$ $C_{23}H_{15}N_7O_2$ 422.1287, found 422.1385 **(Figure 6.25);** IR (KBr, cm^{-1}): 3300.41(s), 3081.25(vw), 2229.63(s), 1694.81(vs), 1610.15(vw), 1525.08(s), 1481.22(w), 1453.93(w), 1416.00(w), 1316.74(s), 1290.96(s), 1169.78(s), 1083.32(s) shown in **(Figure 6.26)**; ^1H NMR δ_H (400 MHz, DMSO-d_6) 12.50 (s, 2H), 8.81 (s, 2H), 8.39(d, *J* = 8 Hz, 2H), 8.30(t, *J* = 8 Hz, 1H), 8.17 (t, *J* = 8 Hz, 4H), 7.94 (d, *J* = 8 Hz, 2H), 7.72(t, *J* = 8 Hz, 2H) spectra depicted in **(Figure 6.27)**; ^{13}C NMR δ_C (100 MHz, DMSO-d_6) 159.67 (C = O), 148.06 (Py-C), 147.74 (C=N), 140.12 (Py-C), 135.44

(Ar-C), 133.64 (Ar-C), 131.15 (Ar-C), 130.90 (Ar-C), 130.26 (Ar-C), 125.75 (Py-C), 118.33 (CN), 112.16 (Ar-C) spectra shown in **Figure 6.28)**. The molar absorptivity coefficient (**ε**): 8.1×10^4 M^{-1} cm^{-1}.

6.4.5. Molecular docking

In accordance with the literature survey, twelve different proteins which related to cancer, viral and bacterial diseases, one non-infectious protein BSA and one duplex DNA crystal structure were obtained from the Protein Data Bank (PDB). The proteins were studied are as follow: (i) Influenza A virus polymerase PB2 subunit (PDB: 2VY7); (ii) Hepatitis C Virus NS5B Polymerase (PDB: 2WCX); (iii) TGF-beta receptor 1 (PDB: 3FAA); (iv) Cancer Related EphA2 Protein Kinases (PDB:1MQB); (v), Dengue Virus NS2B/NS3 Protease (PDB: FOM); (vi) Human survivin an anti-apoptotic protein (PDB: 1XOX), (vii) Cancer-related Aurora-A Protein Kinase (PDB: 1MQ4), (viii) Type III Pantothenate Kinase (CoaX) from *Bacillus anthracis* (PDB:2H3G), (ix) RNA polymerase subunit structure from an avian influenza H5N1 virus (PDB: 3CM8) (x) HIV-1 integrase (PDB:2B4J) (xi) Cancer-related Focal Adhesion Kinase (PDB: 1MP8) (xii) FtsZ from *Bacillus subtilis* (PDB:2VAM); (xiii) Bovine serum albumin (PDB: 4F5S) and duplex DNA (PDB: 4O3M) having Chain P:5'D(AGCGTCGAGATCCAAG)-3' and Chain T: 5'-D(CTTGGATCTCGACGCTCTCCCTTA)-3'

In silico molecular docking was done by using AutoDock 4.2 software *[40-41]*. Lamarckian genetic algorithm (LGA) was used to calculate inhibition constant and binding energy of complex with the protein or dsDNA. The coordinates of $\mathbf{L_1}$–$\mathbf{L_4}$ were obtained from their crystal structures as a CIF file, converted into PDB format with the help of Mercury software. The receptor macro-molecules (proteins and dsDNA) were set rigid, whereas torsional bonds of ligand $\mathbf{L_1}$–$\mathbf{L_4}$ were set as flexible in order to explore the best possible binding sites. The co-crystallized inhibitors and water molecules were removed from all

proteins/DNA. In the case of duplex DNA (PDB: 4O3M), human Bloom's syndrome helicase protein which is attached with DNA is deleted from DNA structure. Polar hydrogen atoms were added followed by the assignment of Kollman and Gastegier charges on all biomolecules. The grid parameter file of all proteins and dsDNA were generated by MGL AutoDock Tool (ADT). After that, a huge grid-box was designed that enclosed entire protein/dsDNA motif. The center of the proteins/dsDNA structure was considered as the center of the grid-box. For all proteins/dsDNA, the spacing between grid points was set as a default value of 0.375. The Genetic Algorithms (GA) population size, the number of generations and the maximum number of energy evaluations remained as 150, 27 000 and 2 500 000 respectively. The same parameters were applied to all selected proteins/dsDNA. After completion of docking, 10 different conformations were obtained in each case. The best energetically favorable conformation was selected with the least inhibitory constant and binding energy. The best conformation was build and write as complex and saved as pdbqt. This pdbqt file open in Chimera 1.11 software *[42]* for a better depiction of the 3D image of final resultant conformation.

6.4.6. Protein binding study

Protein binding study of ligand **L_1–L_4** with the Bovine serum albumin (BSA) protein was carried out by fluorescence quenching titration experiment. BSA was excited at 295 nm and the emission peak was observed at ~337 nm. Tris-HCl buffer (pH = 7.2) was used to prepare the BSA stock solution (5 μM). The stock of concentrated solution of ligands was prepared by dissolving **L_1–L_4** separately in 4% DMSO and to obtain the required concentration **L_1–L_4** were further diluted with Tris-HCl buffer. Before measurements, the BSA and ligand were shaken properly and incubated for 10 minutes for proper binding of ligands with BSA protein.

6.4.7. DNA binding study using

For the binding of **L_1–L_4** with Calf thymus DNA (CT-DNA), 50 µM DNA solutions was prepared using Tris-HCl buffer (pH 7.4). To measure Ethidium bromide EtBr fluorescence displacement, 10µL of the EtBr in Tris-HCl solution (1 mM) was added in 2 mL of CT-DNA solution and placed in the dark environment for 3 hours at 4°C (DNA binding sites of ligands saturated with EtBr). The stock of concentrated solutions of ligands were prepared by dissolving **L_1–L_4** separately in 4% DMSO and to obtain the required concentration **L_1–L_4** were further diluted with Tris-HCl buffer. Then the solution of the aroyl-hydrazones based ligands **L_1–L_4** was titrated with DNA-EtBr mixture. The mixture was shaken and incubates for 20 min before measuring spectra. In all the experiments DNA-EtBr concentration kept constant while slowly increasing the concentration of ligands. The EtBr bound DNA was excited at wavelength 520nm (λ_{ex} 520 nm) and the maximum fluorescence spectra were obtained at the emission wavelength of 626 nm.

NMR, Mass, FTIR spectra of compounds L_1, L_2, L_3 and L_4

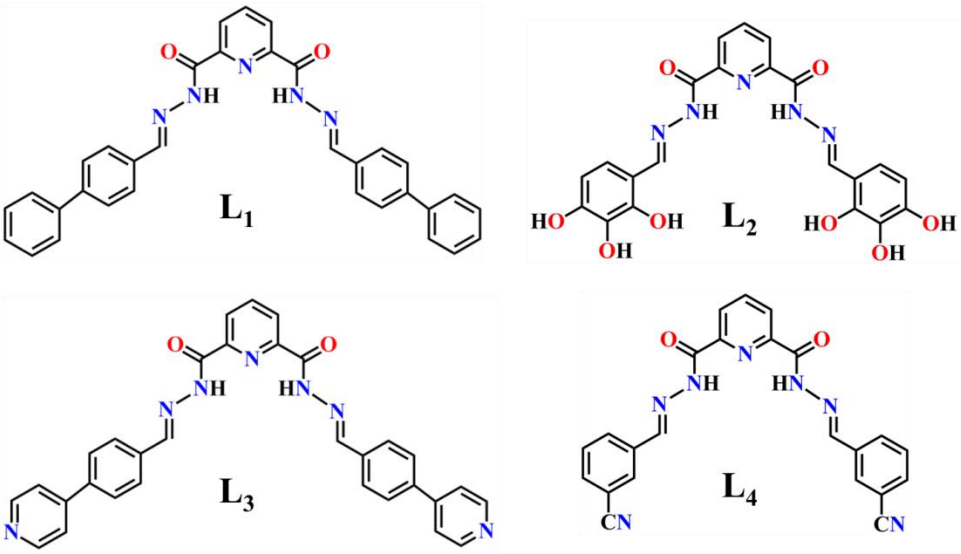

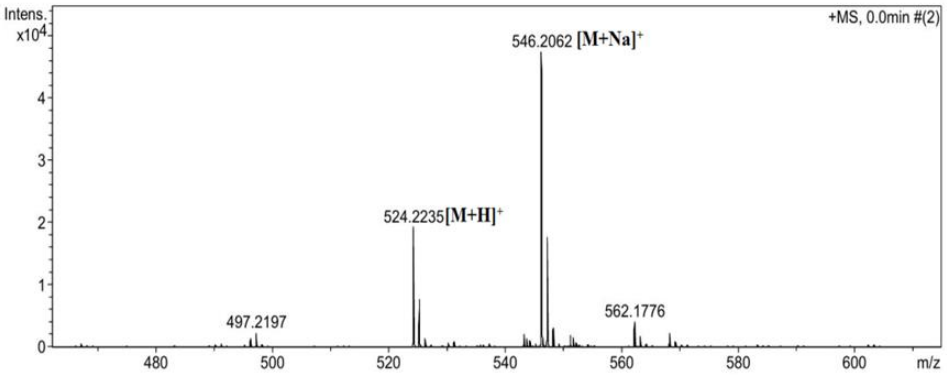

Figure 6.13. ESI–MS spectrum of L_1

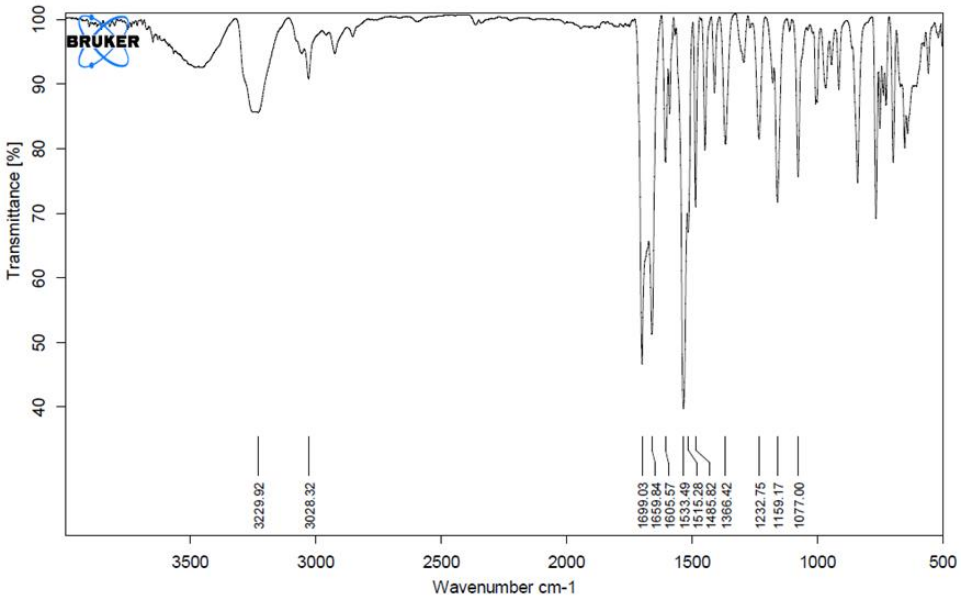

Figure 6.14. FTIR spectrum of $\mathbf{L_1}$

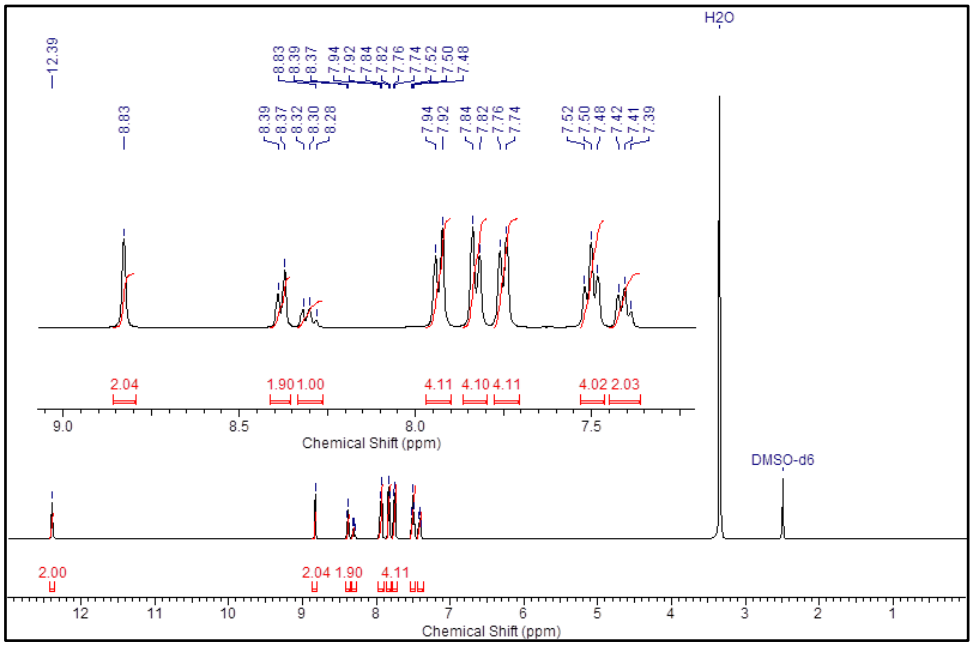

Figure 6.15. ^{1}H NMR spectrum of $\mathbf{L_1}$ in DMSO-d_6

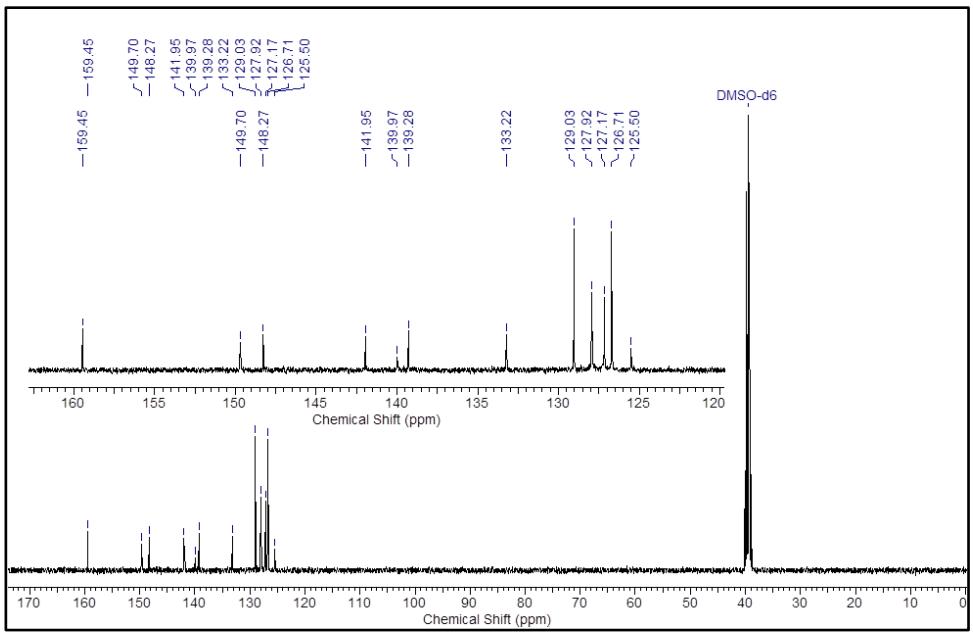

Figure 6.16. ^{13}C NMR spectrum of $\mathbf{L_1}$ in DMSO-d_6

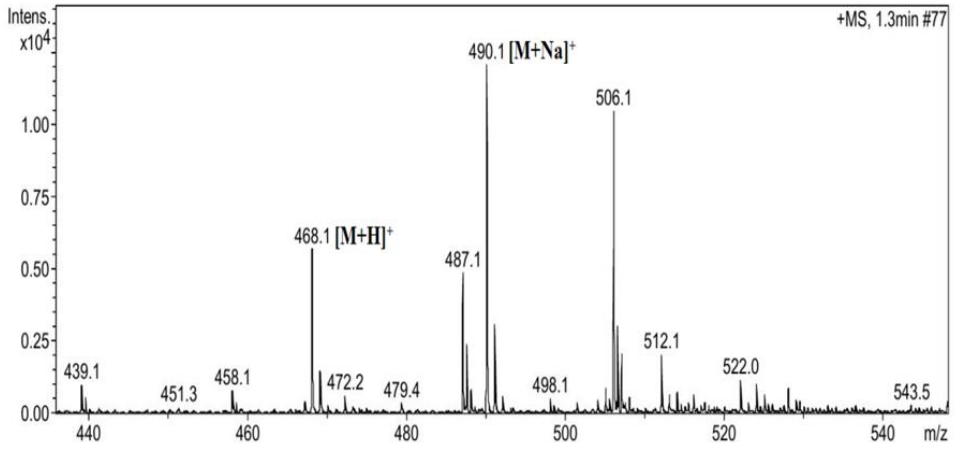

Figure 6.17. ESI–MS spectrum of $\mathbf{L_2}$

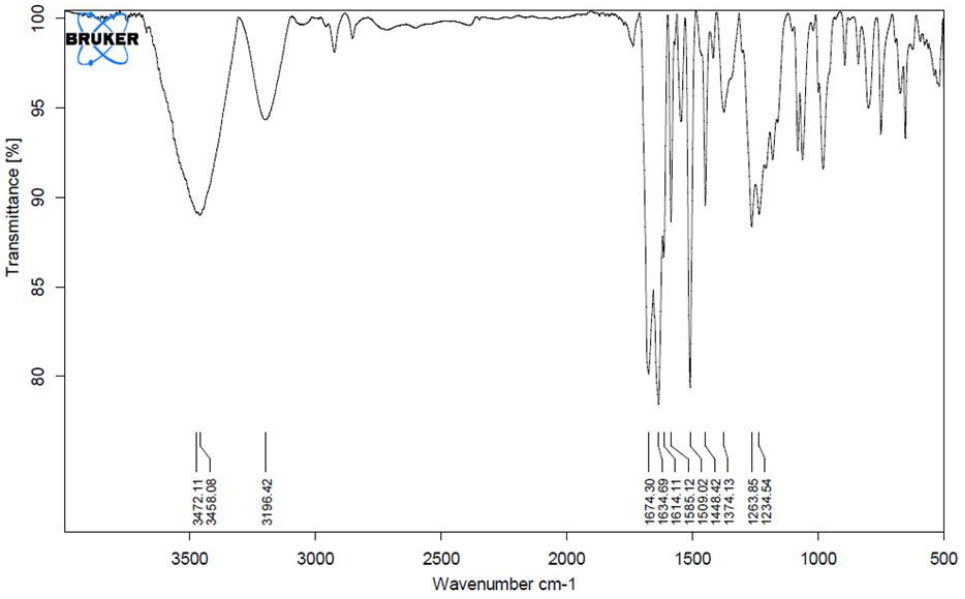

Figure 6.18. FTIR spectrum of $\mathbf{L_2}$

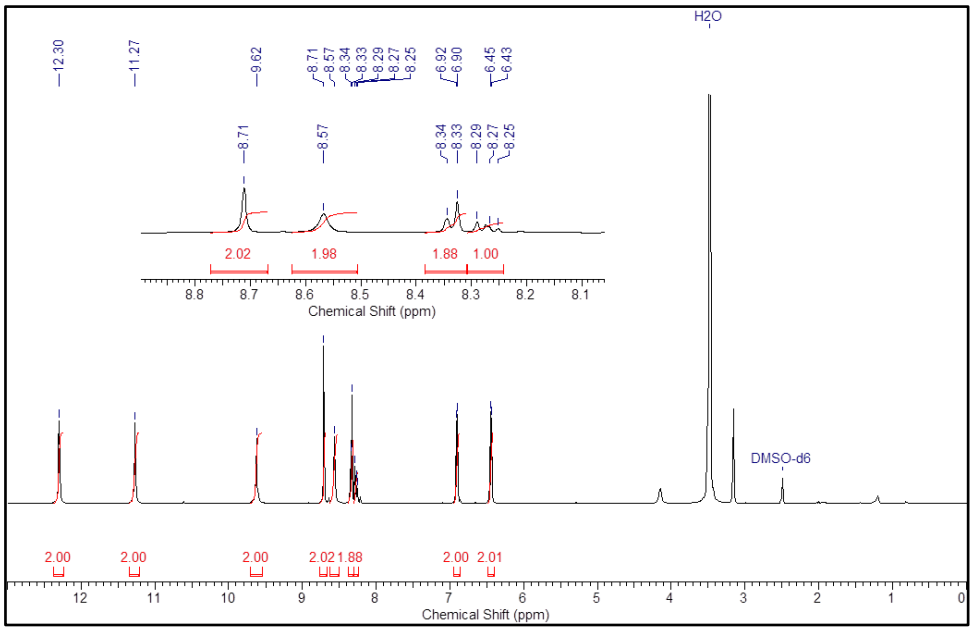

Figure 6.19. ^{1}H NMR spectrum of $\mathbf{L_2}$ in DMSO-d_6

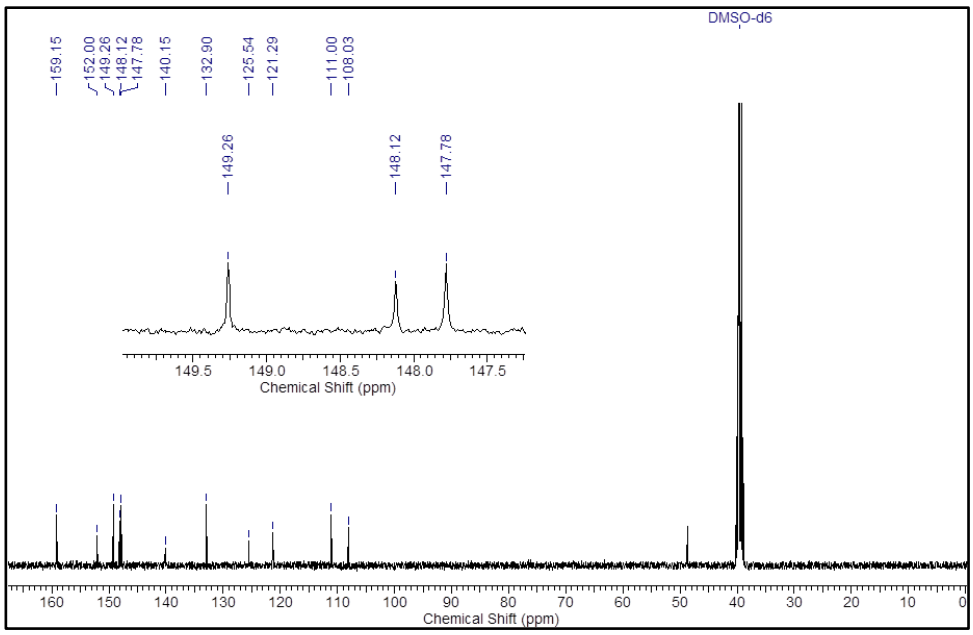

Figure 6.20. ^{13}C NMR spectrum of $\mathbf{L_2}$ in DMSO-d_6

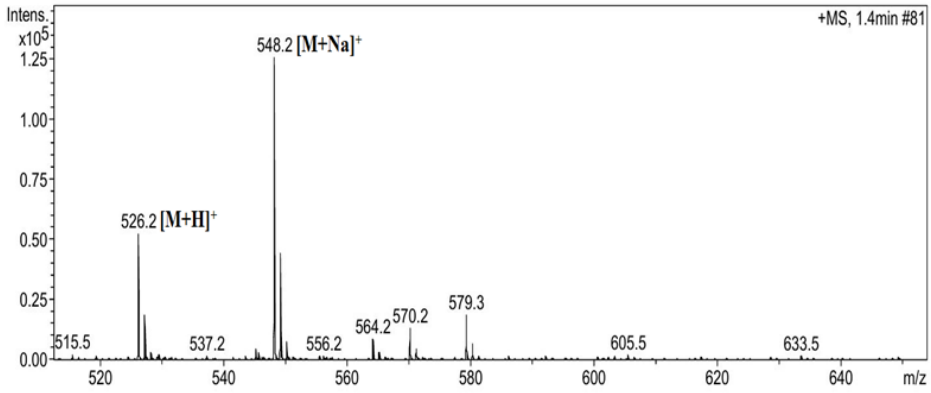

Figure 6.21. ESI–MS spectrum of $\mathbf{L_3}$

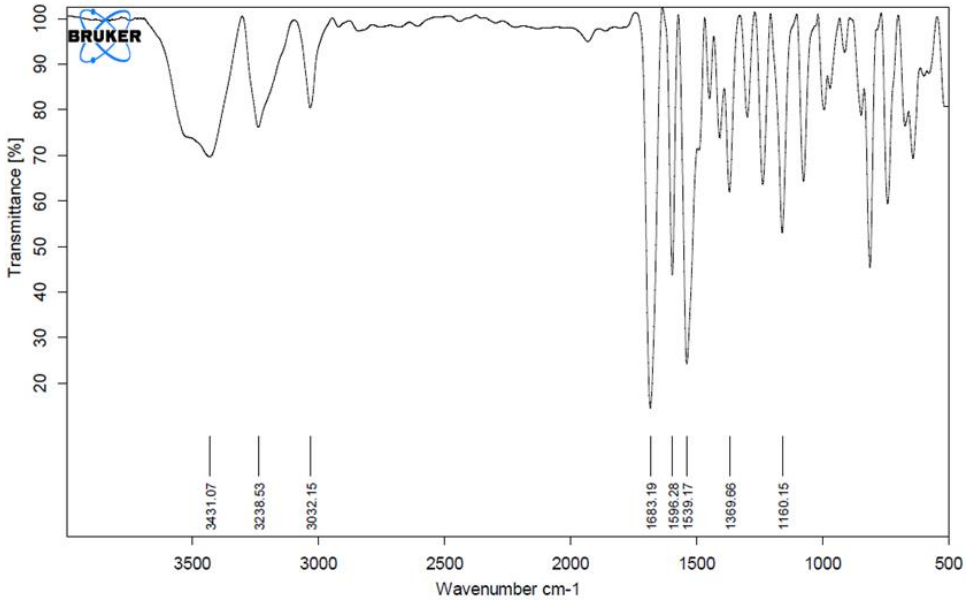

Figure 6.22. FTIR spectrum of $\mathbf{L_3}$

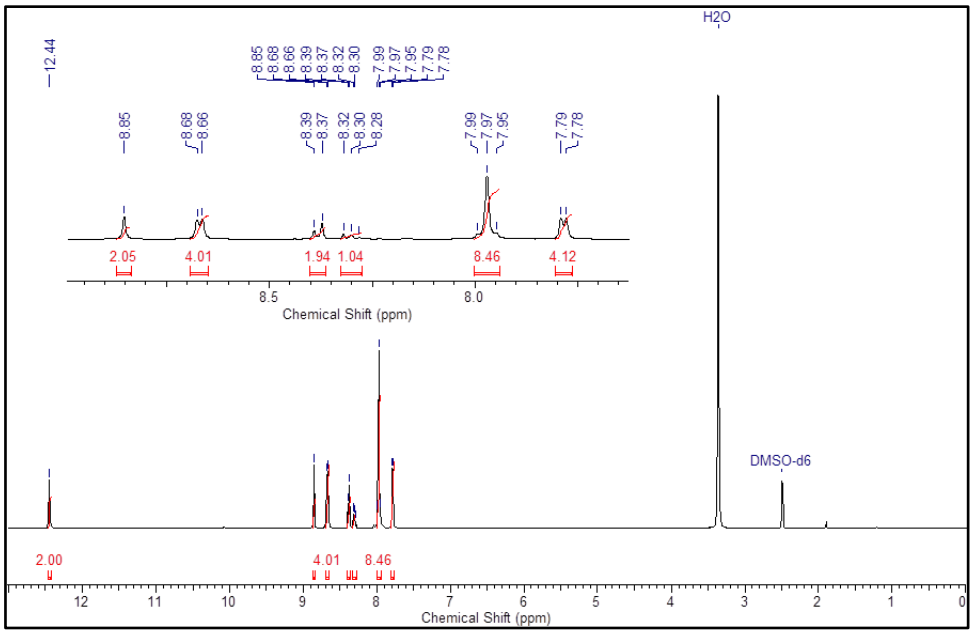

Figure 6.23. ^{1}H NMR spectrum of $\mathbf{L_3}$ in DMSO-d_6

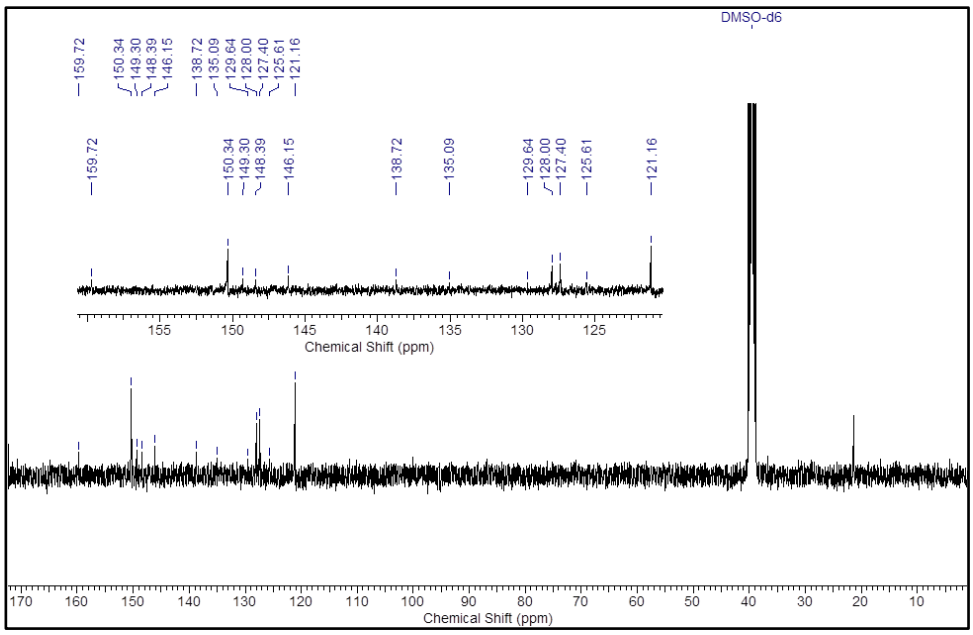

Figure 6.24. ^{13}C NMR spectrum of $\mathbf{L_3}$ in DMSO-d_6

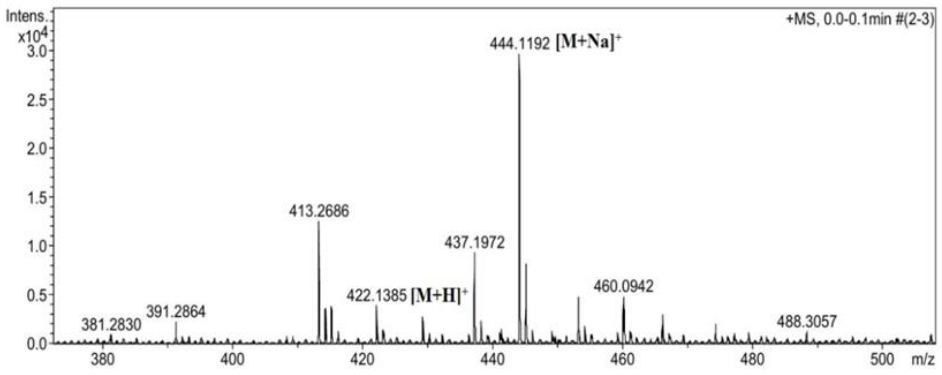

Figure 6.25. ESI–MS spectrum of $\mathbf{L_4}$

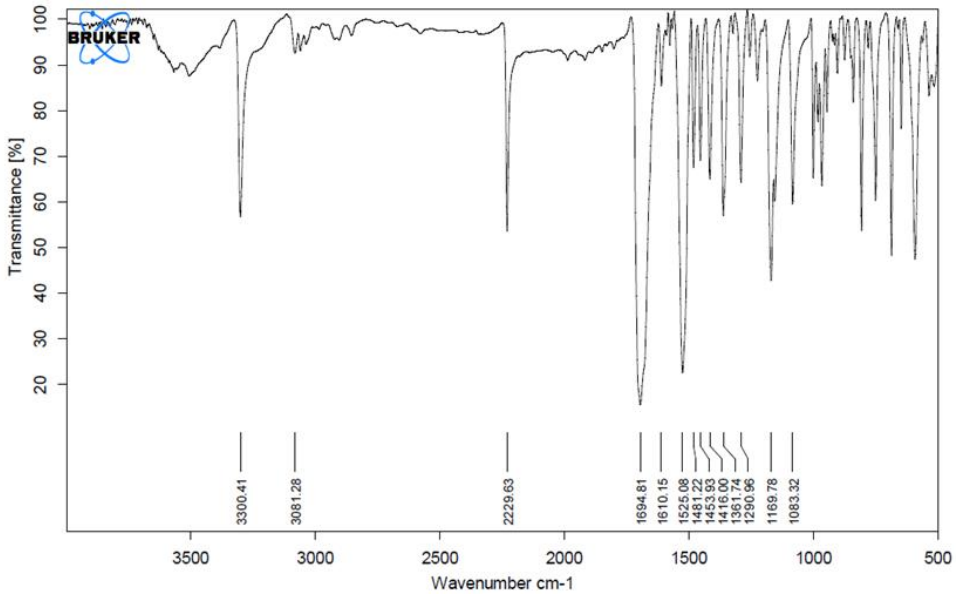

Figure 6.26. FTIR spectrum of **L_4**

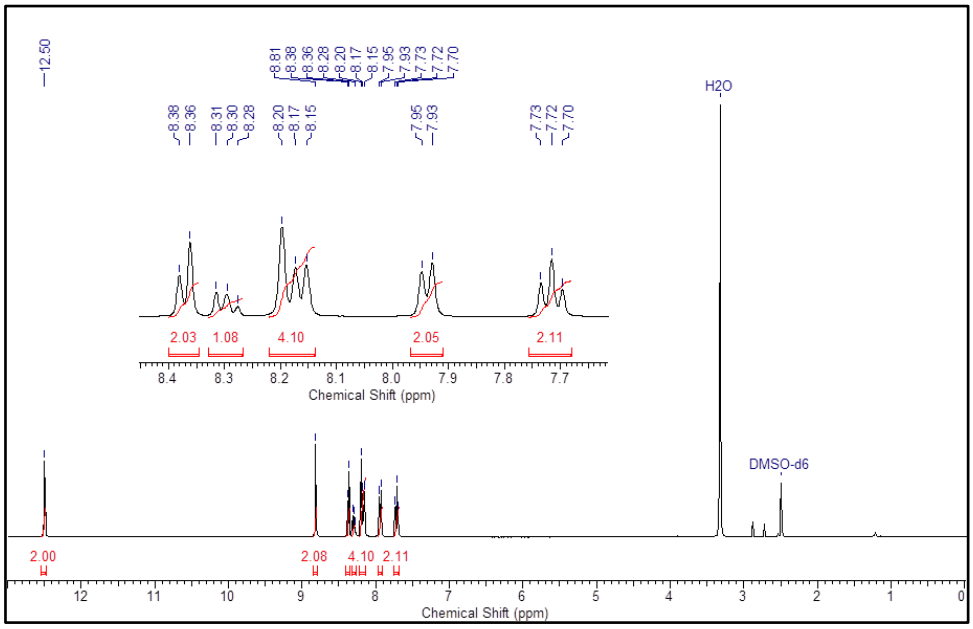

Figure 6.27. ^{1}H NMR spectrum of **L_4** in DMSO-d_6

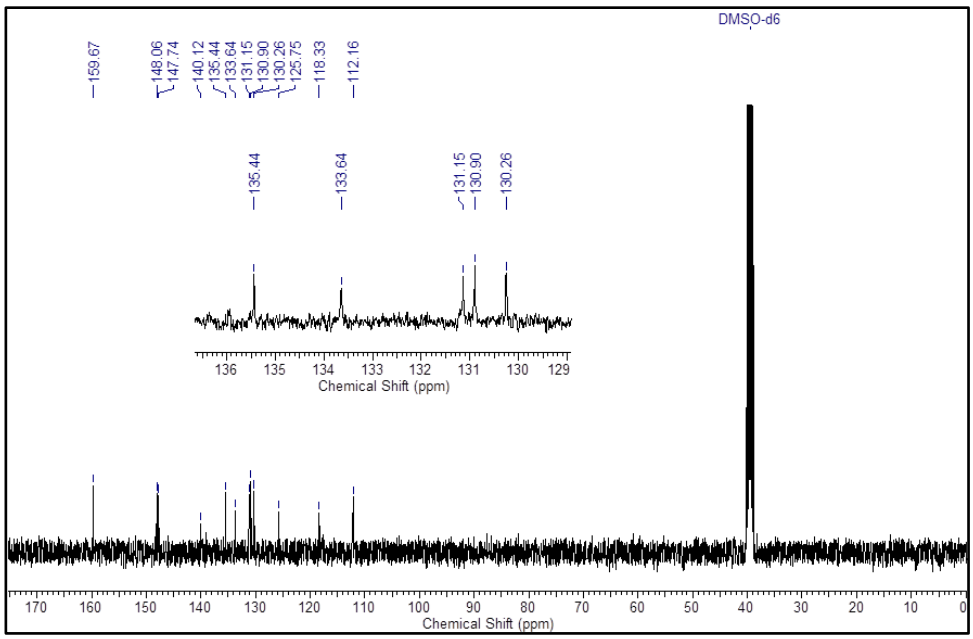

Figure 6.28. ^{13}C NMR spectrum of **L$_4$** in DMSO-d_6

6.5. References

[1]. Ramachandran, E., Gandin, V., Bertani, R., Sgarbossa, P., Natarajan, K., Bhuvanesh, N. S. P., Venzo, A., Zoleo, A., Glisenti, A., Dolmella, A., Albinati, A., Marzano, C. (2018), Synthesis, characterization and cytotoxic activity of novel copper(II) complexes with aroylhydrazone derivatives of 2-Oxo-1,2-dihydrobenzo[h]quinoline-3-carbaldehyde, J. Inorg. Biochem., 182, 18-28 (DOI: 10.1016/j.jinorgbio.2018.01.016).

[2]. Angelusiu, M. V., Barbuceanu, S. F., Draghici, C., Almajan, G. L. (2010), New Cu(II), Co(II), Ni(II) complexes with aroyl-hydrazone based ligand. Synthesis, spectroscopic characterization and in vitro antibacterial evaluation, Eur. J. Med. Chem., 45, 2055-2062 (DOI: 10.1016/j.ejmech.2010.01.033).

[3]. Pape, V. F., Toth, S., Furedi, A., Szebenyi, K., Lovrics, A., Szabo, P., Wiese, M., Szakacs, G. (2016), Design, synthesis and biological evaluation of thiosemicarbazones, hydrazinobenzothiazoles and arylhydrazones as anticancer agents with a potential to overcome multidrug resistance, Eur. J. Med. Chem., 117, 335-354 (DOI: 10.1016/j.ejmech.2016.03.078).

[4]. Kajal, A., Bala, S., Sharma, N., Kamboj, S., Saini, V. (2014), Therapeutic Potential of Hydrazones as Anti-Inflammatory Agents, Int. J. Med. Chem., 2014, 11 (DOI: 10.1155/2014/761030).

[5]. Kucukguzel, S. G., Mazi, A., Sahin, F., Ozturk, S., Stables, J. (2003), Synthesis and biological activities of diflunisal hydrazide-hydrazones, Eur. J. Med. Chem., 38, 1005-1013 (DOI: 10.1016/ejmech.2003.08.004).

[6]. Ragavendran, J. V., Sriram, D., Patel, S. K., Reddy, I. V., Bharathwajan, N., Stables, J., Yogeeswari, P. (2007), Design and synthesis of anticonvulsants from a combined phthalimide-GABA-

anilide and hydrazone pharmacophore, Eur. J. Med. Chem., 42, 146-151 (DOI: 10.1016/j.ejmech.2006.08.010).

[7]. Abdelrahman, M. A., Salama, I., Gomaa, M. S., Elaasser, M. M., Abdel-Aziz, M. M., Soliman, D. H. (2017), Design, synthesis and 2D QSAR study of novel pyridine and quinolone hydrazone derivatives as potential antimicrobial and antitubercular agents, Eur. J. Med. Chem., 138, 698-714 (DOI: 10.1016/j.ejmech.2017.07.004).

[8]. Vogel, S., Kaufmann, D., Pojarova, M., Muller, C., Pfaller, T., Kuhne, S., Bednarski, P. J., von Angerer, E. (2008), Aroyl hydrazones of 2-phenylindole-3-carbaldehydes as novel antimitotic agents, Bioorg. Med. Chem., 16, 6436-6447 (DOI: 10.1016/j.bmc.2008.04.071).

[9]. Wang, Z., Kang, D., Chen, M., Wu, G., Feng, D., Zhao, T., Zhou, Z., Huo, Z., Jing, L., Zuo, X., Daelemans, D., De Clercq, E., Pannecouque, C., Zhan, P., Liu, X. (2018), Design, synthesis, and antiviral evaluation of novel hydrazone-substituted thiophene[3,2-d]pyrimidine derivatives as potent human immunodeficiency virus-1 inhibitors, Chem. Biol. Drug Des., 92, 2009-2021 (DOI: 10.1111/cbdd.13373).

[10]. Vanucci-Bacque, C., Carayon, C., Bernis, C., Camare, C., Negre-Salvayre, A., Bedos-Belval, F., Baltas, M. (2014), Synthesis, antioxidant and cytoprotective evaluation of potential antiatherogenic phenolic hydrazones. A structure-activity relationship insight, Bioorg. Med. Chem., 22, 4269-4276 (DOI:10.1016/j.bmc.2014.05.034).

[11]. Tarendeau, F., Crepin, T., Guilligay, D., Ruigrok, R. W., Cusack, S., Hart, D. J. (2008), Host determinant residue lysine 627 lies on the surface of a discrete, folded domain of influenza virus polymerase PB2 subunit, PLoS Pathog., 4, e1000136 (DOI:10.1371/journal.ppat.1000136).

[12]. Pautus, S., Sehr, P., Lewis, J., Fortuné, A., Wolkerstorfer, A., Szolar, O., Guilligay, D., Lunardi, T., Décout, J.-L., Cusack, S. (2013), New 7-Methylguanine Derivatives Targeting the Influenza Polymerase PB2 Cap-Binding Domain, J. Med. Chem., 56, 8915-8930 (DOI:10.1021/jm401369y).

[13]. He, X., Zhou, J., Bartlam, M., Zhang, R., Ma, J., Lou, Z., Li, X., Li, J., Joachimiak, A., Zeng, Z., Ge, R., Rao, Z., Liu, Y. (2008), Crystal structure of the polymerase PAC–PB1N complex from an avian influenza H5N1 virus, Nature, 454, 1123 (DOI:10.1038/nature07120

[14]. Cohen, J. (1999), The scientific challenge of hepatitis C, Science, 285, 26-30.

[15]. Chan, S. T., Ou, J. J. (2017), Hepatitis C Virus-Induced Autophagy and Host Innate Immune Response, Viruses, 9, (DOI:10.3390/v9080224).

[16]. Sarbah, S. A., Younossi, Z. M. (2000), Hepatitis C: an update on the silent epidemic, J. Clin. Gastroenterol., 30, 125-143 (PMID:10730918).

[17]. Martin Hernando, J. I., Ontoria, J. M., Malancona, S., Attenni, B., Fiore, F., Bonelli, F., Koch, U., Di Marco, S., Colarusso, S., Ponzi, S., Gennari, N., Vignetti, S. E., Del Rosario Rico Ferreira, M., Habermann, J., Rowley, M., Narjes, F. (2009), Optimization of thienopyrrole-based finger-loop inhibitors of the hepatitis C virus NS5B polymerase, ChemMedChem, 4, 1695-1713 (DOI: 10.1002/cmdc.200900184).

[18]. Sesmero, E., Thorpe, I. F. (2015), Using the Hepatitis C Virus RNA-Dependent RNA Polymerase as a Model to Understand Viral Polymerase Structure, Function and Dynamics, Viruses, 7, 3974-3994 (DOI: 10.3390/v7072808).

[19]. Hewawasam, P., Tu, Y., Gao, M., Hanumegowda, U., Knipe, J., Lemm, J. A., Parker, D. D., Rigat, K. L., Roberts, S. B., Meanwell, N. A., Kadow, J. F. (2016), Discovery and preclinical evaluation of

potent, orally bioavailable, metabolically stable cyclopropylindolobenzazepine acylsulfonamides as thumb site 1 inhibitors of the hepatitis c virus NS5B RNA-dependent, RNA polymerase, Bioorg. Med. Chem. Lett., 26, 936-940 (DOI: 10.1016/j.bmcl.2015.12.058).

[20]. Zhou, Z., Liu, T., Zhang, J., Zhan, P., Liu, X. (2018), Influenza A virus polymerase: an attractive target for next-generation anti-influenza therapeutics, Drug. Discov. Today, 23, 503-518 (DOI: 10.1016/j.drudis.2018.01.028).

[21]. Huang, D. T., Lu, C. Y., Shao, P. L., Chang, L. Y., Wang, J. Y., Chang, Y. H., Lai, M. J., Chi, Y. H., Huang, L. M. (2017), In vivo inhibition of influenza A virus replication by RNA interference targeting the PB2 subunit via intratracheal delivery, PloS one, 12, e0174523 (DOI: 10.1371/journal.pone.0174523).

[22]. Simon, S., Roy, D., Schindler, M. (1994), Intracellular pH and the control of multidrug resistance, Proc. Natl. Acad. Sci. U. S. A., 91, 1128-1132.

[23]. Bonafoux, D., Chuaqui, C., Boriack-Sjodin, P. A., Fitch, C., Hankins, G., Josiah, S., Black, C., Hetu, G., Ling, L., Lee, W. C. (2009), 2-Aminoimidazoles inhibitors of TGF-beta receptor 1, Bioorg. Med. Chem. Lett., 19, 912-916 (DOI: 10.1016/j.bmcl.2008.11.119).

[24]. Haque, S., Morris, J. C. (2017), Transforming growth factor-beta: A therapeutic target for cancer, Hum. Vaccin. Immunother., 13, 1741-1750 (DOI: 10.1080/21645515.2017.1327107).

[25]. Nowakowski, J., Cronin, C. N., McRee, D. E., Knuth, M. W., Nelson, C. G., Pavletich, N. P., Rogers, J., Sang, B. C., Scheibe, D. N., Swanson, R. V., Thompson, D. A. (2002), Structures of the cancer-related Aurora-A, FAK, and EphA2 protein kinases from nanovolume crystallography, Structure, 10, 1659-1667 (DOI: 10.1016/S0969-2126(02)00907-3).

[26]. Mercurio, F. A., Leone, M. (2016), The Sam Domain of EphA2 Receptor and its Relevance to Cancer: A Novel Challenge for Drug Discovery?, Curr. Med. Chem., 23, 4718-4734 (DOI: 10.2174/0929867323666161101100722).

[27]. Zhou, Y., Yamada, N., Tanaka, T., Hori, T., Yokoyama, S., Hayakawa, Y., Yano, S., Fukuoka, J., Koizumi, K., Saiki, I., Sakurai, H. (2015), Crucial roles of RSK in cell motility by catalysing serine phosphorylation of EphA2, Nat. Commun., 6, 7679 (DOI: 10.1038/ncomms8679).

[28]. Maja, M., Milan, C., Sanja Zec, Z. (2012), Synthesis and Antioxidant Evaluation of Schiff Bases Derived from 2,6-Pyridinedicarboxylic Acid, Lett. Org. Chem., 9, 401-410 (DOI: 10.2174/157017812801322480).

[29]. Molnar, M., Pavić, V., Šarkanj, B., Čačić, M., Vuković, D., Klenkar, J. (2017), Mono- and bis-dipicolinic acid heterocyclic derivatives – thiosemicarbazides, triazoles, oxadiazoles and thiazolidinones as antifungal and antioxidant agents, Heterocycl. Commun., 23, 35 (DOI: 10.1515/hc-2016-0078).

[30]. Kumari, P., Verma, S. K., Mobin, S. M. (2018), Water soluble two-photon fluorescent organic probes for long-term imaging of lysosomes in live cells and tumor spheroids, Chem. Commun., 54, 539-542 (DOI: 10.1039/c7cc07812a).

[31]. Boaz, H., Rollefson, G. K. (1950), The Quenching of Fluorescence. Deviations from the Stern-Volmer Law, J. Am. Chem. Soc., 72, 3435-3443 (DOI: 10.1021/ja01164a032).

[32]. Saini, A. K., Kumari, P., Sharma, V., Mathur, P., Mobin, S. M. (2016), Varying structural motifs in the salen based metal complexes of Co(ii), Ni(ii) and Cu(ii): synthesis, crystal structures, molecular dynamics and biological activities, Dalton. Trans., 45, 19096-19108 (DOI: 10.1039/C6DT03573F).

[33]. Zheng, K., Liu, F., Xu, X.-M., Li, Y.-T., Wu, Z.-Y., Yan, C.-W. (2014), Synthesis, structure and molecular docking studies of dicopper(ii) complexes bridged by N-phenolato-N′-[2-(dimethylamino)ethyl]oxamide: the influence of terminal ligands on cytotoxicity and reactivity towards DNA and protein BSA, New J. Chem., 38, 2964-2978 (DOI: 10.1039/C4NJ00092G).

[34]. Das, M., Nasani, R., Saha, M., Mobin, S. M., Mukhopadhyay, S. (2015), Nickel(ii) complexes with a flexible piperazinyl moiety: studies on DNA and protein binding and catecholase like properties, Dalton. Trans., 44, 2299-2310 (DOI: 10.1039/C4DT02675F).

[35]. Singh, A., Kumari, P., Raghuvanshi, A., Mobin, S. M., Mathur, P. (2018), Ferrocene-substituted bis(ethynyl)anthracene compounds as anticancer agents, Appl. Organomet. Chem., 32, e4071 (DOI:10.1002/aoc.4071).

[36]. Swan, M. K., Legris, V., Tanner, A., Reaper, P. M., Vial, S., Bordas, R., Pollard, J. R., Charlton, P. A., Golec, J. M., Bertrand, J. A. (2014), Structure of human Bloom's syndrome helicase in complex with ADP and duplex DNA, Acta Crystallogr. D Biol. Crystallogr., 70, 1465-1475 (DOI: 10.1107/s139900471400501x).

[37]. Frisch, M. J., Trucks, G. W., Schlegel, H. B., Scuseria, G. E., Robb, M. A., Cheeseman, J. R., Scalmani, G., Barone, V., Petersson, G. A., Nakatsuji, H., Li, X., Caricato, M., Marenich, A. V., Bloino, J., Janesko, B. G., Gomperts, R., Mennucci, B., Hratchian, H. P., Ortiz, J. V., Izmaylov, A. F., Sonnenberg, J. L., Williams, Ding, F., Lipparini, F., Egidi, F., Goings, J., Peng, B., Petrone, A., Henderson, T., Ranasinghe, D., Zakrzewski, V. G., Gao, J., Rega, N., Zheng, G., Liang, W., Hada, M., Ehara, M., Toyota, K., Fukuda, R., Hasegawa, J., Ishida, M., Nakajima, T., Honda, Y., Kitao, O., Nakai, H., Vreven, T., Throssell, K., Montgomery Jr., J. A., Peralta, J. E., Ogliaro, F., Bearpark, M. J., Heyd, J. J., Brothers, E. N., Kudin, K. N., Staroverov, V. N., Keith, T. A., Kobayashi, R., Normand, J.,

Raghavachari, K., Rendell, A. P., Burant, J. C., Iyengar, S. S., Tomasi, J., Cossi, M., Millam, J. M., Klene, M., Adamo, C., Cammi, R., Ochterski, J. W., Martin, R. L., Morokuma, K., Farkas, O., Foresman, J. B., Fox, D. J. Gaussian 16 Rev. B.01, Wallingford, CT, 2016.

[38]. Jung, S. H., Hyun, T. K., Kim, J.-Y., Jung, J. H. (2015), High selective fluorescence imaging of cesium distribution in Arabidopsis using a bis(trihydroxyphenyl)-appended fluorescent probe with a turn-on system, RSC Adv., 5, 26662-26665 (10.1039/C5RA03371C).

[39]. Sheldrick, G. M. (2015), Crystal structure refinement with SHELXL, Acta Crystallogr. C Struct. Chem., 71, 3-8 (DOI: 10.1107/s2053229614024218).

[40]. Morris, G. M., Huey, R., Lindstrom, W., Sanner, M. F., Belew, R. K., Goodsell, D. S., Olson, A. J. (2009), AutoDock4 and AutoDockTools4: Automated docking with selective receptor flexibility, J. Comput. Chem., 30, 2785-2791 (DOI: 10.1002/jcc.21256).

[41]. Morris, G. M., Lim-Wilby, M. (2008), Molecular docking, Methods Mol. Biol., 443, 365-382 (10.1007/978-1-59745-177-2_19).

[42]. Pettersen, E. F., Goddard, T. D., Huang, C. C., Couch, G. S., Greenblatt, D. M., Meng, E. C., Ferrin, T. E. (2004), UCSF Chimera visualization system for exploratory research and analysis, J. Comput. Chem., 25, 1605-1612 (DOI: 10.1002/jcc.20084).

CHAPTER 7

Conclusions and Future Outlook

The present thesis work describes the perspectives of developing new Schiff base fluorescent organic ligands as organelles targeting probe. The probes used for targeting specific organelles including lysosomes, Endoplasmic reticulum and mitochondria. Fluorescent probe used for bio-imaging in live cells and tumor spheroids. 3D tumor spheroids possess numerous features that mimic *in vivo* tumors. Short wavelength excitation probes leading to cellular auto-fluorescence resulting in photodamage and photobleaching. Schiff base probes for bio-imaging have one of the important properties that they are excited by two-photon, owing to the low background interference, minimal photodamage of cells or tissues, penetration depth (4500 μm) and near-infrared light (700–1100 nm) excitation wavelengths. Furthermore, A novel photostable mesoionic carbene based highly fluorescent Pd(II) complex was synthesized as an endoplasmic reticulum tracker in live cells and tumor spheroid. The employment of fluorescent probes as a tracker can become a great contribution to the medical community and scientific community including industries.

We successfully demonstrated elastic bending properties of a new Schiff base crystal. The powder XRD and Raman studies indicate high retention of crystallinity and chemical bonds even under stress (bend) conditions which imply that the bending is due to the intermolecular hydrogen bonding interactions and C–H···π interactions.. The elastic crystals were found to be consistent in MeOH, EtOH and ACN solvents. Inspite of having elastic properties; in solution state, it also fluorescence and used for mitochondria imaging in live cells. The elastic solid-state crystalline materials can plays significant role in the field of crystal engineering and for the design of organic flexible materials, flexible electronic devices and optics.

Moreover, new aroyl-hydrazone derivatives were synthesized and their various biological applications exploited. Molecular docking studies of aroyl-hydrazone derivatives can be explore the unique binding properties with influenza A virus polymerase PB2 subunit and shows potential for use in anti-influenza therapy. These aroyl-hydrazone derivatives can be explore the pharmacological and biological significance for the development of new drug entities in the future.

ANNEXURE 1

Table A1–A18

Chapter 2

Table: A1 Crystallographic data and structural refinements of **L-lyso**

Identification code	**L-lyso**
Empirical formula	$C_{21}H_{22}N_2O_2$
Formula weight	334.40
Temperature/K	150(2)
Crystal system	orthorhombic
Space group	*P*na2_1
a/Å	10.467(2)
b/Å	6.9909(13)
c/Å	23.485(5)
α/°	90
β/°	90
γ/°	90
Volume/$Å^3$	1718.5(6)
Z	4
ρcalcg/cm3	1.293
μ/mm^{-1}	0.084
F(000)	712.0
Crystal size/mm^3	0.210 × 0.180 × 0.130
Radiation	MoKα (λ = 0.71073)
2Θ range for data collection/°	6.08 to 57.942
Index ranges	$-13 \leq h \leq 14$, $-9 \leq k \leq 9$, $-31 \leq l \leq 30$
Reflections collected	15729
Independent reflections	4042 [R_{int} = 0.1491, R_{sigma} = 0.1060]
Data/restraints/parameters	4042/5/228
Goodness-of-fit on F^2	1.336
Final R indexes [I>=2σ (I)]	R_1 = 0.1550, wR_2 = 0.3837
Final R indexes [all data]	R_1 = 0.1912, wR_2 = 0.4130
Largest diff. peak/hole / e $Å^{-3}$	0.68/-0.49
Flack parameter	2.2(10)
CCDC	**1570338**

Table: A2 Selected bond lengths (Å) and bond angles (°) of **L-lyso**

Bond lengths (Å)		**Bond angles (°)**	
O1–C1	1.363 (14)	C11–N1–C10	125.1 (9)
O2–C13	1.302 (12)	C15–N2–C18	120.9 (9)
N1–C11	1.305 (13)	C15–N2–C20	123.2 (9)
N1–C10	1.445 (13)	C18–N2–C20	115.9 (9)
N2–C15	1.341 (14)	C2–C1–O1	123.1 (10)
N2–N18	1.466 (14)	C2–C1–C10	119.6 (10)
N2–C20	1.481 (14)	O1–C1–C10	117.3 (9)
C1–C10	1.391(14)	C9–C10–C1	121.5 (10)
C9–C10	1.374 (14)	C9–C10–N1	122.2 (9)
C11–C12	1.403 (14)	C1–C10–N1	116.3 (8)
C12–C13	1.432 (13)	N1–C11–C12	123.6 (9)
		O2–C13–C14	119.5 (9)
		O2–C13–C12	121.7 (9)
		C14–C13–C12	118.8 (9)
		N2–C15–C14	122.8 (9)
		N2–C15–C16	119.7 (9)
		N2–C18–C19	113.5 (10)
		N2–C20–C21	112.5 (9)

Chapter 3

Table: A3 Crystallographic data and structural refinements of **ERLp**

Identification code	**ERLp**
Empirical formula	$C_{19}H_{17}NO_3$
Formula weight	307.33
Temperature/K	298
Crystal system	monoclinic
Space group	$P2_1/n$
a/Å	8.31350(10)
b/Å	7.85760(10)
c/Å	24.1360(3)
α/°	90
β/°	99.4900(10)
γ/°	90
Volume/Å^3	1555.09(3)
Z	4
ρ_{calc}g/cm3	1.313
μ/mm^{-1}	0.721
F(000)	648.0
Crystal size/mm^3	0.7 × 0.4 × 0.3
Radiation	CuKα (λ = 1.54184)
2Θ range for data collection/°	7.428 to 142.728
Index ranges	$-6 \leq h \leq 10$, $-9 \leq k \leq 9$, $-28 \leq l \leq 29$
Reflections collected	10584
Independent reflections	2988 [R_{int} = 0.0214, R_{sigma} = 0.0151]
Data/restraints/parameters	2988/0/214
Goodness-of-fit on F^2	1.036
Final R indexes [I>=2σ (I)]	R_1 = 0.0450, wR_2 = 0.1197
Final R indexes [all data]	R_1 = 0.0463, wR_2 = 0.1215
Largest diff. peak/hole / e Å^{-3}	0.17/-0.30
CCDC	**1854514**

Table: A4 Selected bond lengths (Å) and bond angles (°) of **ERLp**

Bond lengths (Å)		Bond angles (°)	
C1–C2	1.4047 (16)	C4– C1 –C2	119.15(11)
C1–C4	1.3799 (17)	O2– C1– C2	116.43(10)
C1–O2	1.3613 (14)	O2– C1– C4	124.38(11)
C2–C7	1.3776 (16)	C7– C2– C1	119.83(10)
C2–O1	1.3670 (13)	O1– C2– C1	115.01(10)
C3–O1	1.4189 (16)	O1–C2–C7	125.14(10)
C4–C5	1.3942 (18)	C1–C4–C5	120.76(11)
C5–C6	1.3785 (17)	C6–C5–C4	120.11(11)
C6–C7	1.3969 (15)	C5–C6–C7	119.34(11)
C6–C8	1.5070 (15)	C5–C6–C8	124.80(10)
C8– N1	1.4549 (14)	C7–C6–C8	115.81(10)
C9–C10	1.4044 (16)	C2–C7–C6	120.79(11)
C9–N1	1.3081 (14)	N1–C8–C6	115.77(10)
C10–C11	1.4274 (16)	N1–C9–C10	126.15(10)
C10–C15	1.4590 (15)	C9–C10–C11	119.61(10)
C11–C12	1.4371 (18)	C9–C10–C15	119.76(10)
C11–O3	1.2801 (14)	C11–C10–C15	120.59(10)
C12–C13	1.349(2)	C10–C11–C12	117.73(11)
		O3–C11–C10	121.69(11)
		O3–C11–C12	120.58(11)
		C13–C12–C11	121.43(12)
		C9–N1–C8	122.32(10)
		C2–O1–C3	117.08(10)

Table: A5 Crystal data and structure refinement for Pd (II) complex **(1)**.

Identification code	**1**
CCDC	1573135
Empirical formula	$C_{16}H_{18}I_2N_4Pd$
Formula weight	626.54
Temperature/K	293(2)
Crystal system	monoclinic
Space group	$P2_1/n$
a/Å	10.7786(5)
b/Å	8.1520(3)
c/Å	23.4486(10)
α/°	90
β/°	99.338(4)
γ/°	90
Volume/Å^3	2033.06(15)
Z	4
ρ_{calc}g/cm^3	2.047
μ/mm^{-1}	3.953
F(000)	1176.0
Crystal size/mm^3	0.25 × 0.23 × 0.2
Radiation	MoKα (λ = 0.71073)
2Θ range for data collection/°	6 to 57.682
Index ranges	$-14 \le h \le 13$, $-10 \le k \le 11$, $-29 \le l \le 31$
Reflections collected	11043
Independent reflections	4670 [R_{int} = 0.0283, R_{sigma} = 0.0267]
Data/restraints/parameters	4670/0/211
Goodness-of-fit on F^2	1.045
Final R indexes [I>=2σ (I)]	R_1 = 0.0434, wR_2 = 0.1117
Final R indexes [all data]	R_1 = 0.0488, wR_2 = 0.1154
Largest diff. peak/hole / e Å^{-3}	1.80/-1.33

Table: A6 Bond Lengths and Bond Angles for Pd (II) complex **(1)**.

Bond Length/Å		**Bond Angles/°**	
Pd1− I2	2.5935(5)	I2 −Pd1 −I1	176.52(2)
Pd1− I1	2.6107(5)	N4 −Pd1 −I2	90.46(12)
Pd1− N4	2.100(4)	N4 −Pd1 −I1	91.59(12)
Pd1− C9	1.968(5)	C9 −Pd1 −I2	87.89(14)
N3 −N2	1.337(6)	C9 −Pd1 −I1	90.13(14)
N3 −C9	1.363(6)	C9 −Pd1 −N4	177.77(17)
N3 −C11	1.464(7)	N2 −N3 −C9	114.2(4)
N1 −C8	1.368(6)	N2 −N3 C−11	117.8(4)
N1 −N2	1.319(6)	C9 −N3 −C11	128.0(4)
N1 −C10	1.470(7)	C8 −N1 −C10	129.8(5)
C8 −C5	1.473(7)	N2 −N1 −C8	112.7(4)
C8 −C9	1.387(7)	N2 −N1 −C10	117.4(4)
N4 −C12	1.325(8)	N1 −C8 −C5	123.4(4)
N4−C16	1.327(7)	N1 −C8 −C9	106.3(4)
C5− C4	1.388(7)	C9 −C8 −C5	130.3(4)
C5 − C6	1.384(8)	C12 −N4 −Pd1	122.5(4)
C4 −C3	1.377(8)	C12 −N4 −C16	116.5(5)
C6 −C7	1.393(9)	C16 −N4 −Pd1	121.0(4)
C7 −C2	1.394(10)	N1 −N2 −N3	103.5(4)
C2 −C3	1.368(10)	C4 −C5 −C8	121.2(5)
C2 −C1	1.501(9)	C6 −C5 −C8	119.9(5)
C13 −C12	1.383(9)	C6 −C5− C4	118.9(5)
C13 −C14	1.349(10)	C3 −C4 −C5	120.4(6)
C14 −C15	1.349(10)	C5 −C6 −C7	119.7(6)
C16 −C15	1.376(9)	N3 −C9 −Pd1	124.5(4)
		N3 −C9 −C8	103.4(4)
		C8 −C9 −Pd1	132.1(3)
		C6 −C7 −C2	121.2(6)
		C7 −C2 −C1	121.2(7)
		C3 −C2 −C7	117.9(6)
		C3 −C2 −C1	120.9(7)
		C2 −C3 −C4	121.7(6)
		C14 −C13 −C12	119.6(7)
		N4 −C12 −C13	122.8(6)
		C13 −C14 −C15	118.4(6)
		N4 −C16 −C15	123.2(6)
		C14 −C15 −C16	119.5(6)

Chapter 5

Table: A7 Crystallographic parameters of **H_2L**

Identification code	**H_2L**
Empirical formula	$C_{21}H_{15}NO_2$
Formula weight	313.34
Temperature/K	293(2)
Crystal system	orthorhombic
Space group	$P2_12_12_1$
a/Å	6.2484(11)
b/Å	12.728(2)
c/Å	19.126(5)
α/°	90
β/°	90
γ/°	90
Volume/Å^3	1521.1(5)
Z	4
ρ_{calcg}/cm^3	1.368
μ/mm^{-1}	0.088
F(000)	656.0
Crystal size/mm^3	0.6 × 0.06 × 0.04
Radiation	MoKα (λ = 0.71073)
2Θ range for data collection/°	6.402 to 57.844
Index ranges	$-8 \le h \le 8$, $-11 \le k \le 16$, $-22 \le l \le 25$
Reflections collected	12246
Independent reflections	3649 [R_{int} = 0.4989, R_{sigma} = 0.8252]
Data/restraints/parameters	3649/0/218
Goodness-of-fit on F^2	0.877
Final R indexes [I>=2σ (I)]	R_1 = 0.0996, wR_2 = 0.1174
Final R indexes [all data]	R_1 = 0.4637, wR_2 = 0.2097
Largest diff. peak/hole / e Å^{-3}	0.22/-0.23
Flack parameter	3.4(10)
CCDC	**1935588**

Table: A8 Selected bond distances (Å) and bond angle (°) of $\mathbf{H_2L}$

bond lengths (Å)		bond angles (°)	
N1–C10	1.400(14)	C11–N1–C10	123.9(13)
N1–C11	1.288(15)	O1–C1–C10	110.5(13)
O1–C1	1.371(14)	C2–C1–O1	126.6(14)
O2–C13	1.280(14)	C2–C1–C10	122.7(14)
C1–C2	1.344(16)	C1–C2–C3	118.4(15)
C1–C10	1.449(18)	C10–C9–C8	122.8(15)
C2–C3	1.427(17)	N1–C10–C1	115.7(13)
C3–C4	1.425(18)	C9–C10–N1	127.0(14)
C3–C8	1.427(18)	C9–C10–C1	117.3(14)
C7–C8	1.404(18)	N1–C11–C12	123.6(15)
C8–C9	1.403(17)	C11– 12–C13	119.4(15)
C9–C10	1.388(16)	C21–C12–C11	122.1(15)
C11–C12	1.425(17)	C21–C12–C13	118.5(15)
C12–C13	1.434(18)	C15–C14–C13	120.6(15)
C12–C21	1.419(19)	C15–C14–C19	121.6(15)
C13–C14	1.468(17)	O2–C13–C12	122.2(15)
C14–C15	1.402(17)	O2–C13–C14	117.9(15)
C14–C19	1.414(19)	C12–C13–C14	119.9(15)
C15–C16	1.384(17)	C21–C20–C19	122.4(16)
C20–C21	1.348(18)	C20–C21–C12	121.4(16)

Chapter 6

Table: A9 Crystallographic parameters of **L_1–L_4**.

Identification code	**L_1**	**L_2**	**L_3**	**L_4**
Empirical formula	C_{33} H_{27} N_5 O_3	$C_{10.50}$ $H_{10.50}$ $N_{2.50}O_5$	C_{33} H_{31} N_7 O_4	C_{26} H_{22} N_8 O_4
Formula weight	541.59	251.71	589.65	510.51
Temperature/K	150(2) K	293(2) K	150(2) K	293(2) K
Wavelength	1.5418 A	1.5418 A	0.71073 A	1.5418 A
Crystal system, Space group	Triclinic, *P -1*	Monoclinic, *C2/c*	Monoclinic, *P 21/c*	Triclinic, *P -1*
a (Å)	10.1674(3)	23.281(5) (14)	23.0525(11)	7.6087(17)
b (Å)	10.3568(5)	13.731(3) (5)	10.4701(5)	13.553(3)
c (Å)	14.4668(6)	8.5073(15) (2)	12.7208(7)	14.344(3)
$\alpha/^{o}$	71.840(4)	90	90	115.81(2)
$\beta/^{o}$	69.606(4)	99.538(19)	103.858	97.686(17)
$\gamma/^{o}$	86.751(3)	90	90	97.698(18)
Volume ($Å^3$)	1354.46(10)	2682.0(9)	2980.9(3)	1288.7(5)
Z, Density (calculated)	2, 1.328 Mg/m^3	8, 1.247 Mg/m^3	4, 1.314	2, 1.316
Absorption coefficient	0.703 mm^{-1}	0.866 mm^{-1}	0.089	0.769
F(000)	568	1048	1240	532
Theta range for data collection	3.431 to71.354°	3.751 to 39.986°	2.895 to 25.000	3.505 to 39.989
Index ranges	-12<=h<=8, -12<=k<=12, -17<=l<=16	-19<=h<=19, -11<=k<=11, -7<=l<=7	-27<=h<=27, -12<=k<=12, -15<=l<=15	-6<=h<=5, -11<=k<=11, -11<=l<=11
Reflections collected, Unique	8948, 5142 [R(int) = 0.0145]	3191 / 821 [R(int) = 0.0833]	20316 / 5228 [R(int) = 0.0792]	3095 / 1566 [R(int) = 0.0362]
Data/restraints/parameters	5142 / 0 / 374	821 / 2 / 176	5228 / 0 / 410	1566 / 0 / 346
Goodness-of-fit on F^2	1.023	1.082	1.137	2.487
Final R indices [I>=2σ (I)]	R1 = 0.0349, wR2 = 0.0956	R1 = 0.0814, wR2 = 0.2222	R1 = 0.0585, wR2 = 0.1566	R1 = 0.2493, wR2 = 0.5641
R indices [all data]	R1 = 0.0363, wR2 = 0.0973	R1 = 0.1024, wR2 = 0.2414	R1 = 0.0894, wR2 = 0.1711	R1 = 0.2702, wR2 = 0.5835
CCDC number	**1893001**	**1893024**	**1893025**	**1896817**

Table: A10 Selected bond distances (Å) and bond angle (º) of $\mathbf{L_1}$

Bond distances (Å)		**Bond angle (º)**	
N(1)–C(5)	1.335(4)	N(1)–C(5)–C(6)	116.69(9)
C(5)–C(6)	1.502(5)	C(5)–C(6)–O(1)	122.37(10)
O(1)–C(6)	1.225(3)	O(1)–C(6)–N(2)	124.88(11)
N(2)–C(6)	1.347(5)	C(5)–C(6)–N(2)	112.75(9)
N(2)–N(3)	1.376(3)	C(6)–N(2)–N(3)	121.06(9)
N(3)–N(7)	1.284(5)	N(2)–N(3)–C(7)	114.06(9)
C(7)–C(8)	1.459(6)	N(3)–C(7)–C(8)	121.95(10)
N(1)–C(1)	1.334(4)	N(1)–C(1)–C(20)	117.27(9)
C(1)–C(20)	1.501(4)	C(1)–C(20)–O(2)	121.39(10)
O(2)–C(20)	1.228(3)	O(2)–C(20)–N(4)	124.55(10)
C(20)–N(4)	1.351(4)	C(20)–N(4)–N(5)	118.63(9)
N(4)–N(5)	1.381(2)	N(4)–N(5)–C(21)	115.29(9)
N(5)–C(21)	1.280(4)	N(5)–C(21)–C(22)	120.63(10)
C(21)–C(22)	1.463(4)	C(1)–N(1)–C(5)	117.64(10)

Table: A11 Selected bond distances **(**Å) and bond angle (°) of **L_2**

Bond distances (Å)		**Bond angle (°)**	
O(1)–C(4)	1.201(12)	C(1)#1–N(1)–C(1)	119.6(13)
O(2)–C(7)	1.365(10)	C(4)–N(2)–N(3)	119.5(10)
O(3)–C(8)	1.388(10)	C(5)–N(3)–N(2)	116.5(9)
O(4)–C(9)	1.383(12)	N(1)–C(1)–C(2)	121.8(10)
N(1)–C(1)#1	1.341(10)	N(1)–C(1)–C(4)	119.2(9)
N(1)–C(1)	1.341(10)	C(2)–C(1)–C(4)	118.9(9)
N(2)–C(4)	1.342(12)	N(2)–C(4)–C(1)	110.7(11)
N(2)–N(3)	1.398(10)	N(3)–C(5)–C(6)	119.5(10)
N(3)–C(5)	1.287(11)	C(6)–C(7)–O(2)	120.5(11)
C(1)–C(2)	1.375(13)	O(3)–C(8)–C(9)	118.6(12)
C(1)–C(4)	1.494(14)	C(10)–C(9)–O(4)	127.3(13)
C(2)–C(3)	1.365(10)	O(4)–C(9)–C(8)	113.6(13)
C(5)–C(6)	1.432(12)	C(2)–C(1)–C(4)	118.9(9)
		C(3)–C(2)–C(1)	117.2(9)

Table: A12 Selected bond distances (Å) and bond angle (º) of $\mathbf{L_3}$

Bond distances (Å)		**Bond angle (º)**	
O(1)–C(19)	1.232(3)	C(1)–N(1)–C(5)	116.7(2)
O(2)–C(6)	1.227(3)	C(6)–N(2)–N(3)	119.1(2)
N(1)–C(1)	1.337(3)	C(6)–N(2)–H(2)	120.4
N(1)–C(5)	1.340(3)	N(3)–N(2)–H(2)	120.4
N(2)–C(6)	1.338(4)	C(7)–N(3)–N(2)	116.6(3)
N(2)–N(3)	1.376(3)	C(19)–N(4)–N(5)	119.7(2)
N(3)–C(7)	1.264(4)	C(19)–N(4)–H(4)	120.2
N(4)–C(19)	1.338(4)	C(20)–N(5)–N(4)	116.2(2)
N(4)–N(5)	1.380(3)	C(15)–N(6)–C(14)	115.2(4)
N(5)–C(20)	1.272(4)	N(1)–C(1)–C(2)	123.3(3)
N(6)–C(15)	1.318(6)	N(1)–C(1)–C(19)	117.1(3)
N(6)–C(14)	1.317(6)	O(2)–C(6)–N(2)	124.3(3)
N(7)–C(28)	1.326(4)	O(2)–C(6)–C(5)	120.9(3)
N(7)–C(27)	1.338(4)	N(2)–C(6)–C(5)	114.7(3)

Table: A13 Selected bond distances (Å) and bond angle (º) of $\mathbf{L_4}$

Bond distances (Å)		Bond angle (º)	
O(1)–C(6)	1.18(2)	C(1)–N(1)–C(5)	115(2)
O(2)–C(15)	1.17(3)	C(6)–N(2)–N(3)	120(2)
N(1)–C(1)	1.31(3)	C(7)–N(3)–N(2)	117(2)
N(1)–C(5)	1.35(3)	C(15)–N(4)–N(5)	122(2)
N(2)–C(6)	1.34(3)	C(16)–N(5)–N(4)	113(2)
N(2)–N(3)	1.38(3)	N(1)–C(1)–C(2)	123(2)
N(3)–C(7)	1.26(3)	N(1)–C(1)–C(15)	118(3)
N(4)–C(15)	1.31(3)	N(1)–C(5)–C(6)	113(3)
N(4)–N(5)	1.39(2)	O(1)–C(6)–N(2)	126(3)
N(7)–C(23)	1.13(4)	O(1)–C(6)–C(5)	118(3)
N(6)–C(14)	1.06(4)	N(2)–C(6)–C(5)	117(2)
C(1)–C(2)	1.34(3)	N(3)–C(7)–C(8)	122(3)
C(1)–C(15)	1.60(3)	N(6)–C(14)–C(12)	170(4)
C(2)–C(3)	1.40(3)	O(2)–C(15)–N(4)	128(3)
		O(2)–C(15)–C(1)	121(3)

Table: A14 molecular docking of $\mathbf{L_1}$ with various cancers, viral and bacterial disease causing proteins.

Protein (PDB ID)	Full name of protein	Binding energy (Kcal/Mol)	Inhibition constant	Interacting residues
3FAA	TGF–beta receptor 1 (Transforming growth factor β–R1)	–10.95	9.45nM	Chain A: Ile211, Gly212, Lys213, Ala230, Glu245, Tyr249, Leu260, Phe262, Leu278, Ser280, Tyr282, His283, Glu284, Gly286, Ser287
2FOM	Dengue Virus NS2B/NS3 Protease	–10.84	11.33nM	Chain A: 0 Chain B: His51, Lys73, Lys74, Asp75, Trp83, Leu85, Val147, Gly148, Asn152, Gly153,Val154
2WCX	Hepatitis C Virus NS5B Polymerase	–10.51	19.78nM	Chain A: Lys51, Ser218, Asp220, Thr221, Arg222, Cys223, Phe224, Thr287, Ser288, Asn291, Gly317, Asp318, Gly351, Asp352, Pro354, Gln355
1MQB	Cancer Related Ephrin A2 (ephA2) Receptor Protein Kinase	–10.03	44.21nM	Ala644, Lys646, Tyr735, Val736, His737, Arg738, Asp739, Arg743, Asn744, Leu746, Ser756, Asp757, Gly759, Lys778
1XOX	Human survivin (Antiapoptotic protein)	–9.67	81.14nM	Phe13, Lys15, Arg18, Glu29, Thr34, Glu36, Arg37, Glu40, Phe86, Lys90, Phe93, Leu96, Phe101, Leu104
1MQ4	Cancer–related Aurora–A Protein Kinase	–9.6	91.54nM	Arg137,Leu139, Gly142, Lys143, Phe144, Lys162, Leu164, Leu169, Val174, Gln177, Leu178, Ala213, Gly216, Thr217, Arg220, Glu260, Asp274
2H3G	Type III Pantothenate Kinase (CoaX) from Bacillus Anthracis	–9.37	134.61nM	Asp6,Asn9,Val13,Arg27,Thr132,Ala133, Gly221,Gly222,Lys225,Pro239,Thr242
3CM8	RNA polymerase subunit structure from an avian influenza H5N1 virus	–9.32	148.2nM	Chain A: Ser277, Lys574, Trp577, Glu580, Met581, Arg583, Ser648, Ala651, Pro653, Asn696, Asp697,Pro698 Chain B : 0
2B4J	HIV–1 integrase	–9.11	208.3nM	Chain A: Glu87, Gln168, Lys173, Thr174, Gln177, Met178, Phe181 Chain C: Lys360, Leu363, Ile365, Lys402, Ile403
1MP8	Cancer–related Focal Adhesion Kinase (FAK)	–8.65	458.04nM	Ile428, Lys454, Glu471, Met475, Gly505, Glu506, Arg545, Asp546, Leu553, Asp564, Pro585, Met589, Phe599
2VAM	FtsZ from Bacillus subtilis	–7.54	–2.98μM	Ile31,Glu34,Val35, Gln36, Gly37, Val38, Ile201, Ala202, Pro204, Asn208

Table: A15 molecular docking of $\mathbf{L_2}$ with various cancers, viral and bacterial disease causing proteins.

Protein (PDB ID)	Full name of proteins	Binding energy (Kcal/Mol)	Inhibition constant	Interacting residues
3FAA	TGF–beta receptor 1 (Transforming growth factor β–R1)	–7.48	3.27 µM	Ala230, Lys232,Glu245, Tyr249, Leu260, His283, Gly286, Ser287, Phe289, Asp290, Lys337,Asp351
2FOM	Dengue Virus NS2B/NS3 Protease	–8.37	732.63nM	Chain A: 0 Chain B: Thr120, Leu128, Pro132, Ser135, Tyr150, Gly151, Gly153, Val154
1MQB	Cancer Related Ephrin A2 (ephA2) Receptor Protein Kinase	–6.32	23.15µM	Ala731, Asn732, Asn734, Arg738, Arg792, Phe794, Ser796, Lys863, Phe864, Ala865
1XOX	human survivin (Antiapoptotic protein)	–8.08	1.2µM	Phe13, Arg18, Arg37, Glu40, Asp72, Pro73, Ile74, Phe86, Val89, Lys90, Lys91,Gln92, Phe93, Leu96
1MQ4	cancer–related Aurora–A Protein Kinase	–8.7	419.55nM	Leu139, Lys143, Phe144,Val147, Lys162, Leu164, Tyr212, Ala213, Asp274
2H3G	Type III Pantothenate Kinase (CoaX) from Bacillus Anthracis	–7.04	6.93 µM	Asp6, Val7, Val65, Gly89, Pro90, Gly91, Arg104, Val106, Gly107, Ala108, Asp109, Arg110
3CM8	RNA polymerase subunit structure from an avian influenza H5N1 virus	–7.16	5.6 µM	Chain A: Arg279, Lys281, Asn561, Trp577, Asn647, Ser648, Ala651, Glu656, Ser659 Chain A: 0
2B4J	HIV–1 integrase	–6.5	17.16 µM	Chain A: Glu87,Val88, Lys173, Thr174, Gln177,Val184,Lys185, Chain C: Ile365
1MP8	Cancer–related Focal Adhesion Kinase (FAK)	–8.33	787.06nM	Arg426, Ile428, Gln432, Ala452, Lya454, Glu471, Val484, Met499, Leu501, Cys502, Thr503, Gly505, Leu553,Asp564
2VY7	Influenza A virus polymerase PB2 subunit	–8.1	1.16 µM	Trp564, Leu599, Arg604, Gly608, Phe610, Asp611, Gln614, Ile615, Leu648, Arg650
2VAM	FtsZ from Bacillus subtilis (plays a central role in prokaryotic cell division)	–7.14	5.84 µM	Asn25, Ala71, Met 105, Gly107, Gly108, Thr109, Gly110,Thr133, Arg143, Asn166,Leu180,Phe183, Asp187

Table: A16 molecular docking of L_3 with various cancers, viral and bacterial disease causing proteins.

Protein (PDB ID)	Full name of protein	Binding energy (Kcal/Mol)	Inhibition constant	Interacting residues
2FOM	Dengue Virus NS2B/NS3 Protease	–10.35	25.71nM	Chain A: 0 Chain B: Trp50, Arg54, Val72, Lys73, Lys74, Leu76, Trp83, Leu85, Thr118, Thr120, Ile123, Gly148, Asn152, Val154
2WCX	Hepatitis C Virus NS5B Polymerase	–9.38	132.6nM	Chain A: Ile160, Phe162, Arg168, Val179, Tyr191, Phe193, Gln194, Tyr195, Ser196, Gly283, Val284, Leu285, Ser288, Cys289, Tyr448,
1MQB	Cancer Related Ephrin A2 (ephA2) Receptor Protein Kinase	–9.23	171.64nM	Ala644,Lys646, Tyr735,Val736, His737, Arg738, Asp739, Arg743, Asn744, Leu746, Asp757, Gly759, Lys778
1XOX	Human survivin (Antiapoptotic protein)	–8.68	436.21 nM	Phe13, Arg18, Glu29, Thr34, Pro35, Glu36, Glu40, Phe86, Lys90, Lys91, Phe93, Leu96, Phe101, Leu104
1MQ4	Cancer–related Aurora–A Protein Kinase	–9.56	97.84nM	Leu139, Gly140, Lys141, Lys143, Phe144, Val147, Lys162, Gln177, Leu178, Tyr212, Ala213
2H3G	Type III Pantothenate Kinase (CoaX) from Bacillus Anthracis	–9.15	197.39nM	His25, Arg27, Arg110, Asp129, Thr132, Ala133, Thr220, Gly221, Gly222, Pro239, Phe240, Thr242
3CM8	RNA polymerase subunit structure from an avian influenza H5N1 virus	–8.16	1.04 µM	Chain A:Pro303, Lys356, Thr357, Val 463, Tyr464, Thr467, Ala468, Ala472, Ala475, Pro484, Ile486, Arg582 Chain B: 0
2B4J	HIV–1 integrase	–8.18	1.01 µM	Chain A: Glu85, Ala86, Arg107, Gln168, Gln177, Met178, Phe181 Chain C: Lys360, Ile365, Lys402
1MP8	Cancer–related Focal Adhesion Kinase (FAK)	–8.66	450.49nM	Arg426, Ile428, Ala452, Lys454, Val484, Met499, Glu501, Cys505, Glu506, Asp546, Arg550, Asn551, Leu553, Asp564
2VY7	(influenza A virus polymerase PB2 subunit)	–10.36	25.31nM	Trp564, Leu599, Gly608, Phe610, Gln614, Ile615, Ser634, Leu648, Val649, Arg650
2VAM	FtsZ from Bacillus subtilis (plays a central role in prokaryotic cell division)	–8.22	940.1nM	Lys79, Gly112, Pro115, Gln119, Lys122, Gly125, Ala126, Leu127, Ala153, Lys215

Table: A17 molecular docking of $\mathbf{L_4}$ with various cancers, viral and bacterial disease causing proteins.

Protein (PDB ID)	Full name of protein	Binding energy (Kcal/ Mol)	Inhibition constant	Interacting residues
3FAA	TGF–beta receptor 1 (Transforming growth factor β–R1)	–9.08	221.45nM	Ile211, Lys232, Tyr249, Leu278, Val279, Ser280, Tyr282, His283, Glu284, Ser287, Lys 337, Asp351,
2FOM	Dengue Virus NS2B/NS3 Protease	–9.62	88.56nM	Chain A: 0 Chain B: Ile36, His51, Val52, Arg54, Leu128, Pro132, Gly151, Gly153, Tyr161
2WCX	Hepatitis C Virus NS5B Polymerase	–8.81	350.68nM	Ser180, Thr181, Pro183, Gln184, Tyr191, Phe193, Gln194, Tyr195, Ser196, Pro197, Tyr448
1XOX	Human survivin (Antiapoptotic protein)	–9.46	115.42nM	Phe13, Arg18, Arg37, Glu40, Pro37, Ile74, Val89, Lys90, Lys91, Phe93, Leu96
1MQ4	Cancer–related Aurora–A Protein Kinase	–9.51	107.35nM	Leu139, Lys141, Gly142, Lys143, Val147, Ala160, Lys162, Leu164, Gln177, Leu178, Leu194, Leu210, Glu211, Tyr212, Ala213, Leu263, Asp274, Gly276
2H3G	Type III Pantothenate Kinase (CoaX) from Bacillus Anthracis	–9.9	55.42 nM	Asp6,Val7, Gly8, Asn11, Ala12, Val13, Arg27, Phe130, Gly131, Thr132, Gly153, Met155, Ile156, Glu159, Gly222, Leu223
3CM8	RNA polymerase subunit structure from an avian influenza H5N1 virus	–8.82	342.44nM	Chain A: Ser280, Lys281, Phe282, Asn466, Trp577, Gly578, Met581,Arg583, Cys584, Gln587, Ser644, Ser648, Leu649 Chain B: 0
2B4J	HIV–1 integrase	–7.84	1.79µM	Chain A: 0 Chain C:Ile359, Lys360, Leu363, Thr399, Lys402, Arg405, Phe406, Lys407, Val408
1MP8	Cancer–related Focal Adhesion Kinase (FAK)	–8.79	363.23nM	Arg426, Ile428, Gln432, Ala452, Lys454, Val484, Met499, Glu500, Leu501, Cys502, Gly505, Glu506, leu553
2VY7	Influenza A virus polymerase PB2 subunit	–7.95	1.49 µM	Chain A: Trp552, Ile554, Arg555, Asn556, Trp557,Glu558, Thr674, Leu675, Ile676
2VAM	FtsZ from Bacillus subtilis	–8.14	1.08 µM	Ile31, Glu34, Val35, Gly37, Val38, Tyr40, Ile201, Ala202, Asn208, Phe211

Table: A18 Permissions for re-producing the materials

Figure 1.6	Confocal microscopy fluorescence images of 5 μM **CPM.** (a) LysoTracker Green DND-26 (1 μM) (b) co-stained in SMMC-7721 cells. (c) Merged image. (d) The correlation of **CPM** and LysoTracker Green DND-26 intensities (A = 0.93).	Reproduced from Ref. [31]: Chapter 1, with permission from Royal Society of Chemistry.
Figure 1.7	TPM imaging of Zn(II) ions in live NIH 3T3 cells:	Reproduced from Ref. [43]: Chapter 1, with permission from Royal Society of Chemistry.
Figure 1.8	Co-localization of fluorescence of **4d** (as Zn^{2+} sensor) with LysoTracker Deep Red in NIH 3T3 cells:	Reproduced from Ref. [43]: Chapter 1, with permission from Royal Society of Chemistry.
Figure 1.9	**Figure 1.9.** (a) HL-7720 cells incubated with 30 μM Cu^{2+} for 30 min at 37ºC, then 15 μM RHAT **(5b)** for 15 min. (b) Addition of 50 nM Lyso-Tracker DND-26 for 10 min. (c) Overlay of (a) and (b).	Reproduced from Ref. [49]: Chapter 1, with permission from the Elsevier.
Figure 1.10	Confocal fluorescence images of RHAT **(5d)** showing Cu^{2+} ions sensing in live HL-7720 cells.	Reproduced from Ref. [49]: Chapter 1, with permission from the Elsevier.
Figure 1.12	Co-localization experiment of **ERp** (2.5 μM) with various organellespecific markers in Hela cells.	Reproduced from Ref. [78]: Chapter 1, with permission from Royal Society of Chemistry.
Figure 1.13	Fluorescence images of HeLa cells using tunicamycin (40 mg ml^{-1}) treated for 3 h before **ERp** (2.5 μM) for 20 min. GFP-tubulin (C-10613; Thermo) has to be incubated overnight at 37 ºC before the experiment.	Reproduced from Ref. [78]: Chapter 1, with permission from Royal Society of Chemistry.
Figure 1.14	Co-localization of **ELP1** with organelles trackers showing vesicle transport from ER to Lysosomes	Reproduced from Ref. [81]: Chapter 1, with permission from Royal Society of Chemistry.

Figure 1.23	Molecular docking of the phthalimide derivative **1** with DNA.	Reproduced from Ref. [131]: Chapter 1, with permission from Springer Publishing group.
Figure 1.24	Molecular docking of plumbagin (**1**) and plumbagin hydrazides (**2-5**) into the active site of p50 subunit of NF-kB protein.	Reproduced from Ref. [132]: Chapter 1, with permission from Elsevier.
Figure 1.25	Frontier molecular orbital energy level and distribution in compound 2g, Oseltamivir acid, and Oseltamivir.	Reproduced from Ref. [136]: Chapter 1, with permission from Springer Publishing group.
Figure 1.26	Comparison of the frontier orbital distribution and the direction of electron transfer of compound 2g and oseltamivir acid.	Reproduced from Ref. [136]: Chapter 1, with permission from Springer Publishing group.
Figure 1.27	The different elastic stages in the successive bending in H_3L.	Reproduced from Ref. [140]: Chapter 1, with permission from Royal Society of Chemistry.